ITG Turbulence Saturation and Near-Resonant Heat Flux Reduction in Gyrokinetic Dimits-Shift Analysis

by

Ping-Yu Li

A dissertation submitted in partial fulfillment
of the requirements for the degree of
Doctor of Philosophy
(Physics)

at the
University of Wisconsin-Madison
2021

Date of Final Oral Exam: 9/17/2021
The dissertation is approved by the following members of the Final Oral Committee:
Paul W. Terry, Professor, Physics
John Sarff, Professor, Physics
Chris Hegna, Professor, Engineering Physics
Carl Sovinec, Professor, Engineering Physics
M.J. Pueschel, Lecturer, Applied Physics, Eindhoven University of Technology

Acknowledgements

Many thanks to my advisor, Paul Terry, for guiding me through my Ph.D. life. I have learned not just a whole bunch of turbulence theory but also how to take care of my family from him. I also thank M.J. Pueschel for teaching me a lot about gyrokinetics, and the nitty-gritty about making slides and writing papers. And thanks to the faculty and staff in UW-Madison Physics Department for helping me pursuing my dream.

I would also thank Garth Whelan for helping me get my Ph.D. research on track in my early Ph.D. life and teaching me a lot about the US. Many thanks to Adrian Fraser for having useful discussions together about math and physics while we were still both working in the Cascave. Another big thanks to Shu-Wei Tsao for helping me on GENE code modifications and more discussions about physics and of course life in the US as foreigners.

Also thanks to all of my friends for giving me helps and laughter in Madison. More thanks to my family members for supporting me studying abroad.

Finally, I would like to thank my wife, Hsin-Wei, for accompanying me and supporting me all these days, and also thanks to my infant son, Darius, for giving me more fun during my Ph.D. life.

Contents

1 Introduction 1

1.1 Drift Waves and ITG Instability 1

1.2 Statistical Closure and Triplet Correlation Time 4

1.3 Zonal Flows and Stable Modes 10

1.4 Thesis Summary and Outline 11

2 Assessing Physics of Ion Temperature Gradient Turbulence via Hierarchical Reduced-Model Representations 17

2.1 Introduction 18

2.2 Model Hierarchy 22

2.2.1 Two-Field Fluid Model 23

2.2.2 Primitive Model of Three-wave Interaction 26

2.2.3 Models Based on Statistical Closures 27

2.3 Tests of Time-Average Behavior 33

2.3.1 Three-Wave Interaction 33

2.3.2 Analytic Scaling Relations 41

2.3.3 Cascade Interactions 43

2.3.4 Qualification Related to Wavenumber Range 45

2.4 Conclusions 50

3 Mode Oscillations Under Zonal-Flow-Catalyzed Interactions and ITG Predator-Prey Model Building 59

3.1 Introduction 59

3.2 Three-Wave Truncation of toroidal fluid Model 61

3.3 Role of the Zonal Flow in Three-Wave Interaction 63

3.4 Predator-Prey Model Built on Saturation Theory 71

3.5 Conclusion 79

3.A Coefficients for Predator-Prey model 81

4 Saturation Physics of Threshold Heat-Flux Reduction 90

4.1 Introduction 91

4.2 Comparative Turbulence Analysis 97

4.3 Threshold Fluid Model 102

4.4 Relationships between Turbulent Correlations 108

4.5 Nonlinear Saturation Relations 116

4.6 Heat Flux Solutions 121

4.7 Conclusions 130

5 The Role of Mode Resonances in Regulating Zonal-Flow-Moderated Plasma Microturbulence 137

5.1 Introduction 138

5.2 Saturation Theory for zonal-flow-Dominated Systems 142

5.3 Symmetry breaking in ITG turbulence 146

5.4 Nonlinear frequency broadening 150

5.5 Resonance breaking 154
5.6 Saturation theory in Quasilinear model building 158
5.7 Summary 168

6 The Coupling Coefficients 174

6.1 Coupling Coefficients in Analytic Form 175
6.2 Coupling Coefficient Numerical Calculation 177

7 Conclusions and Future Work 182

7.1 Conclusions 182
7.2 Future Work 183

List of Figures

1.1 The constant-density surface moving in an electron drift wave due to the $E \times B$ velocity. (Wesson J. (2004) *Tokamaks*) 2

1.2 Toroidal ITG instability cartoon. The Bad curvature and temperature gradient cause charge separation which leads to $E \times B$ feed back that enlarges perturbation. (Fusion Wiki) 3

1.3 The stable mode is excited through the nonlinearity after the unstable mode has grown to a certain level. The amplitude of the stable in the quasi-stationary state ($t \gtrsim 20$) is comparable to that of the unstable mode. 11

1.4 Thesis road map. A Saturation theory for toroidal ITG fluid model is tested under different level of approximations in wavenumber space and frequency in chapter 2. Chapters 3 and 4 show the applications of saturation theory in predator-prey model building and Dimits shift respectively described in chapter 2 on fluid model. The triplet correlation time and resonance picture derived from chapter 4 are examined with gyrokinetic simulations in chapter 5, these ideas are also implemented in quasilinear model in this chapter. Coupling coefficient is shown to play an important role in turbulence saturation in fluid theory in chapter 2, the method to calculate such quantity in gyrokinetics is proposed and tested in chapter 6. 12

2.1 Model hierarchy for nonlinear physics of ion temperature gradient turbulence, with more comprehensive treatments at the top. The left-hand pathway represents approximations to the treatment of nonlinear interactions in wavenumber space. The right-hand pathway represents approximation in the treatment of the temporal domain in the context of a statistical closure. 24

2.2 Scalings of $|v_z'|^2$, $|\beta_1|^2$, and $|\beta_2|^2$ as a function of ν from a) numerical solutions of the primitive three-wave interaction equations and b) the full two-field fluid model. 35

2.3 Scalings of $|v_z'|^2$, $|\beta_1|^2$, and $|\beta_2|^2$ as a function of ν for the zero-dimensional (single wavenumber) inversion of the energy balance equations from statistical closure theory. This solution is represented by the box labeled *Analytic scaling relations* in Fig. 2.1. 37

2.4 Scalings of $|v_z'|^2$, $|\beta_1|^2$, $|\beta_2|^2$, $|\beta_1''|^2$, and $|\beta_2''|^2$ as a function of ν for three interacting waves from inversion of the energy balance equations of statistical closure theory. The triplet correlation time is given by Eq. (2.14) with no eddy-damping contribution. 39

2.5 Time histories of $|v_z'|^2$, $|\beta_1|^2$, $|\beta_2|^2$, $|\beta_1''|^2$, and $|\beta_2''|^2$ from the primitive three-wave equations, Eqs. (2.3) - (2.5). Timescales for both the mode energies and the zonal kinetic energy are much shorter than linear wave periods. 40

2.6 Scalings of $|v_z'|^2$, $|\beta_1|^2$, $|\beta_2|^2$, $|\beta_1''|^2$, and $|\beta_2''|^2$ as a function of ν for three interacting waves from inversion of the energy balance equations of statistical closure theory. The triplet correlation time includes nonlinear corrections from Eqs. (2.17) - (2.19). 41

2.7 Schematics of mode couping in a radial wavenumber cascade mediated by a single zonal flow with wavenumber $-k_x'$. 45

2.8 Scalings of a) $|v_z'|^2$ and b) $|\beta_1|^2$, $|\beta_2|^2$, $|\beta_1''|^2$, and $|\beta_2''|^2$ as functions of ν, showing comparison between solutions of full fluid model (points) and the cascade closure model (solid traces). For this result $k_x' = 0.2$, $k_x = 0.2$, and $k_y = 0.2$. 46

2.9 Scalings of a) $|v_z'|^2$ and b) $|\beta_1|^2$, $|\beta_2|^2$, $|\beta_1''|^2$, and $|\beta_2''|^2$ as functions of η, showing comparison between solutions of full fluid model (points) and the cascade closure model (solid traces). For this result $k_x' = 0.2$, $k_x = 0.2$, and $k_y = 0.2$. 47

2.10 Scalings of a) $|v_z'|^2$ and b) $|\beta_1|^2$, $|\beta_2|^2$, $|\beta_1''|^2$, and $|\beta_2''|^2$ as functions of η, showing comparison between solutions of full fluid model (points) and the cascade closure model (solid traces). For this result $k_x' = 0.15$, $k_x = 0.15$, and $k_y = 0.2$. 49

3.1 (a) The energy goes back and forth between the eigenmodes of k and k''. (b) Strong zonal flow leads to large energy exchange rate between modes and fast mode oscillations. Weak zonal flow leads small energy exchange rate and staggering mode oscillations. 64

3.2 The trace of the eigenmodes on the complex plane. They go in their own near-closed loop with some fixed phases difference between them. 68

3.3 By adding extra 20% of dampings on the stable modes, the saturation level becomes lower, the zonal flow now has a more static amplitude . 69

3.4 By adding extra 20% of dampings on the stable modes, the zonal flow and the total non-zonal energy oscillates coherently with a little phase difference between them. However, this is not a predator-prey dynamics. 70

3.5 The zonal flow acts as a predator and the total non-zonal energy acts like a prey, forming a predator-prey system. The oscillation amplitudes damp down to a set of fixed points, this could be the result of constraint over imposing. 74

3.6 The oscillation amplitudes damp down as time goes by, but the amplitudes increase when the phase restart kicks in with a period of 10τ, therefore, the amplitudes do not attenuate to zero. 75

3.7 (a) With restarting period = τ. (b) Withe restarting period = 0.1τ. There is no real difference between these two settings, none of them shows the obvious attenuation of the oscillation when the system reaches the steady state, which are both different from the case with restarting period = 10τ. 76

3.8 The typical Lotka-Volterra type predator-prey model shows a steady and coherent predator-prey oscillation. 77

3.9 (a) With restarting period 78

4.1 The energy drive and energy dissipation averaged over z and time, and summed over k_y as a function of k_x. Over the wavenumbers plotted, the energy dissipation rate is much larger within the unstable range than outside it. The absolute values of the total area under both curves are ≈ 4.78. 93

4.2 Time history of $Q_{\mathrm{i}}^{\mathrm{es}}$ and Φ_{ZF} for saturated ITG turbulence from gyrokinetic simulations for $\omega_{T\mathrm{i}} = 5.5$, $\omega_{T\mathrm{i}} = 6.5$, and $\omega_{T\mathrm{i}} = 7$. The NLCG is at $\omega_{T\mathrm{i}} \approx 6.5$. 97

4.3 The time-averaged energy spectra of the ITG turbulence for saturated gyrokinetic simulations for a) $\omega_{T\mathrm{i}} = 5.5$ and b) $\omega_{T\mathrm{i}} = 7$. The NLCG is at $\omega_{T\mathrm{i}} \approx 6.5$. Both show strong band structure in the k_x direction, and modes are only strongly excited in the low-k regime. To better see how energy is distributed the $k_y = 0$ energy is plotted at 0.01 of its actual value in a), while the $k_y = 0$ energy is plotted at 0.1 of its actual value in b). 99

4.4 The time-averaged rate of direct energy transfer from $(k_x, k_y) = (0, 0.2)$ to grid cells for a) $\omega_{T\mathrm{i}} = 5.5$ and b) $\omega_{T\mathrm{i}} = 7$ at saturated state. The prominent horizontal bands for $k_y = 0.2$ represent the major energy transfer channel is the zonal-flow-catalyzed energy transfer. . . 100

4.5 The time-averaged energy transfer in the zonal-flow mediated entropy cascade beginning at modes with $k_x = 0$ and different k_y to higher k_x for a) $\omega_{T\mathrm{i}} = 5.5$ and b) $\omega_{T\mathrm{i}} = 7$ at saturated state. 101

4.6 Growth rate at $\mathbf{k} = (0, 0.25)$ (magenta), analytic heat flux (blue) and simulated heat flux (black) as a functions of η for $\epsilon = 1.25$, $\nu = 0.001$ and $\chi = 0$. Eddy damping is neglected in the triplet correlation time factors of the analytic formula. The heat flux predicted from the analytic formula showing unphysical behavior close to the linear threshold. 125

4.7 Triplet correlation time (blue) and coupling coefficient C_{1F2} (red) as a function of η for the same parameters as Fig. 4.6. Eddy damping is neglected in $|\tau|$. The triplet correlation time increases dramatically just above the linear threshold, which leads to the spike of the heat flux in close-threshold region. 125

4.8 Growth rate (magenta), analytic heat flux (blue), and simulated heat flux (black) as functions of η for $\epsilon = 1.25$, $\nu = 0.001$, and $\chi = 0$, with eddy damping included in the analytic formula. 127

4.9 Triplet correlation time (blue) and coupling coefficient C_{1F2} (red) as a function of η for the same parameters as Fig. 4.4 with eddy damping included in τ. The triplet correlation time decreases monotonically as η increases, which eliminates the unphysical behavior. 128

4.10 Heat flux as a function of η for $\epsilon = 0.625$ and $\epsilon = 1.25$ analytic theory (triangles and circles), numerical solution (inverted triangles and crosses). 129

5.1 (a) Zonal flow shearing rate $\omega_s = \sum_{k_x} k_x^2 |\Phi_{ZF}|$ as a function of temperature gradient $\omega_{T\mathrm{i}}$. (b)Ratio of zonal flow shearing rate to growth rate of the most unstable mode γ as a function of $\omega_{T\mathrm{i}}$. Vertical lines denote the linear (dashed-dotted) and nonlinear (dashed) critical gradients. The shearing rate increases as ω_T increases, the shearing rate is always larger than the growth rate of the most unstable mode. 139

5.2 The zonal field spectrum for various ω_{T_i} above and within the Dimits regime. The high-k_x zonal flow contributes nearly nothing to the shearing rate within in the Dimits regime. Note that k_x has the unit ρ_0^{-1}, the inverse of gyroradius 140

5.3 Histogram of heat fluxes in the quasi-stationary state for (a) $\omega_{T_\mathrm{i}} = 5$, with skewness = 1.446 and excess kurtosis = 1.219, and (b) $\omega_{T_\mathrm{i}} = 8$, with skewness = 0.681 and excess kurtosis = -0.97. The histogram above the Dimits regime is closer to a Guassian distribution, implying that the nonlinear interactions involving non-zonal wavenumbers are more excited above the Dimits regime. 141

5.4 If we raise the gradient to induce larger fluctuation and stronger turbulence, the nonlinear frequency will also be enlarged, which will lead to smaller lifetime of the nonlinear energy transfer. The system will therefore end up at a more turbulent state, which deviates from the prediction based only on linear physics. 146

5.5 Schematic of how unstable and stable eigenvalues are affected by a combination of increased gradient drive (red) and radiative damping (blue): the original eigenvalue (black circles) experiences stronger growth/damping for the unstable/stable ITG mode due to increased $\omega_{T\mathrm{i}}$ (black crosses), while both modes are damped when adding the radiative damping term (blue triangles). These effects can be balanced to ensure close to no change of the unstable mode relative to the original eigenvalue. 148

5.6 The red curve is the growth rate spectrum with $D_{\mathrm{rad}} = 0$ and $\omega_{T_{\mathrm{i}}} = 8$. The blue curve is the one with $D_{\mathrm{rad}} = 0.02338$, $\omega_{T_{\mathrm{i}}} = 8$, and second order hyper diffusion in y direction with magnitude = 0.1338 to suppress the growth rate in the high k regime. The growth rate spectra are nearly identical. 149

5.7 Time traces of ion electrostatic heat flux for a simulation with artificial radiative damping (red) and increased gradient drive, and for the reference simulation (black). Adding radiative damping leads to 60% more heat flux even though the linear growth rate spectrum is well matched between the two cases. 149

5.8 Heat flux spectra simulations with (a) $D_{\mathrm{rad}} = 0$ and (b) $D_{\mathrm{rad}} = 0.02338$. with matched growth rate spectra for the unstable ITG mode. 150

5.9 Frequency spectrum for (a) $\omega_{T_\mathrm{i}} = 5$ at $k_y = 0.15$, (b) $\omega_{T_\mathrm{i}} = 8$ at $k_y = 0.15$, (c) $\omega_{T_\mathrm{i}} = 5$ at $k_y = 0.2$, (d) $\omega_{T_\mathrm{i}} = 8$ at $k_y = 0.2$. Black dotted lines denote linear frequencies, whereas red dotted lines in (a) and (c) are intermittency frequencies obstained from nonlinear simulations. The red curve in (b) and (d) are Lorentzian fits to the frequency spectra. Frequency spectra are wider above the Dimits regime. The frequency spectra with same k_y are almost identical within the Dimits regime 151

5.10 Re(Φ_k) as a function of time for (a) $\omega_{T\mathrm{i}} = 5$ for $k = (0, 0.15)$ and $k = (0.0834, 0.15)$, and for (b) $\omega_{T\mathrm{i}} = 8$ for $k = (0, 0.15)$ and $k = (0.0834, 0.15)$. Modes above the Dimits regime are less coherent. . . . 153

5.11 Cross-correlation functions C for modes at $k = (0, 0.15)$ and $k = (0.0834, 0.15)$, as well as $k = (0, 0.15)$ and $k = (0., 0.2)$, within the Dimits regime (a) $\omega_{T\mathrm{i}} = 5$ and above the Dimits regime (b) $\omega_{T\mathrm{i}} = 8$. Within the Dimits regime, C is extremely large at the correlated stage 154

5.12 The ratio between the correlated signal and the decorrelated signal (peak signal-to-noise ratio) of the cross-correlation function versus $\omega_{T\mathrm{i}}$. The coherency between the electrostatic potential at two wavenumbers coupled through the zonal flow decreases as $\omega_{T\mathrm{i}}$ increases. 155

5.13 The correlation time measured from Fig. 5.11 as a function of $\omega_{T\mathrm{i}}$. The trend is about the same as Fig. 5.12, the correlation time decreases as $\omega_{T\mathrm{i}}$ increases. 156

5.14 Heat flux as a function of temperature gradient for the standard scenario (blue), as well as for cases with artificially introduced weak (red) and strong (magenta) zonal dissipation. The dashed line is the NLCG and the dashed-dotted line is LCG. 157

5.15 Heat flux for the standard Dimits shift scan (blue circle), as well as with two levels of zonal frequency $\Delta\omega_{\mathrm{z}}$, low (red triangle) and high (magenta triangle). Both cases with artificial zonal frequencies reduce the extent of Dimits shift. The case with strong artificial frequency removes the Dimits shift almost entirely. The dashed line is the NLCG and the dashed-dotted line is LCG. 158

5.16 ω_s for the standard Dimits shift scan (blue circle), as well as with two levels of zonal frequency $\Delta\omega_{\mathrm{z}}$, low (red triangle) and high (magenta triangle). The artificial zonal frequency does not reduce the shearing rate. The dashed line is the NLCG and the dashed-dotted line is LCG.159

5.17 Zonal flow peak frequency $\omega^{\mathrm{ZF}}_{\mathrm{peak}}$ and half width $\Delta\omega^{\mathrm{ZF}}$ versus $\omega_{T_{\mathrm{i}}}$ at $k = (0.0834, 0)$. The zonal flow peak frequencies is much smaller than the instability frequency and growth rate. The same applies to the half width $\Delta\omega^{\mathrm{ZF}}$. The resolution is defined as two times the smallest increment of ω. 160

5.18 Quasilinear and nonlinear (red square) fluxes versus temperature gradient in kinetic-electron Cyclone Base Case. The standard quasilinear model (purple circle) overpredicts fluxes below $\omega_T \approx 5$, while the improved model using $\tau_{k,k'}(k'_x = 0.1)$ (blue diamond) recoversthe nonlinear heat flux in the Dimits regime. 163

5.19 Quasilinear and nonlinear (red square) fluxes versus density gradient for a collisionless TEM case. The standard quasilinear model (purple circle) overpredicts fluxes greatly, while the τ factor improves the model significantly. The choice of k'_x is less relevant. 164

5.20 Quasilinear and nonlinear fluxes (red square) versus density gradient for a collisional TEM case. The standard quasilinear model (purple circle) hugely overpredicts fluxes, while the τ factor does improve the model significantly but the discrepancy remains. 165

5.21 Quasilinear and nonlinear fluxes versus temperature gradient for a low collisionality ITG case for JET. The standard quasilinear model (purple circle) performs decently well, while the τ factor improves the model a bit more. 166

5.22 The quasilinear model with (a) $\mathrm{Re}(\tau)$ and (b) $|\tau|$. The standard quasilinear model performs well in NCSX ITG case. The model with $\mathrm{Re}(\tau)$ performs poorly. However, the model with $|\tau|$ tracks the nonlinear heat flux almost exactly. 167

5.23 The quasilinear model with (a) $\mathrm{Re}(\tau)$ and (b) $|\tau|$. The standard quasilinear model performs well in CMOD ITG case. Both models with $\mathrm{Re}(\tau)$ or $|\tau|$ shows some but insignificant improvement. 167

5.24 The quasilinear model with (a) $\mathrm{Re}(\tau)$ and (b) $|\tau|$. The standard quasilinear model performs well in SPARC ITG case. All models tracks the nonlinear result closely. 168

List of Tables

2.1 Triplet correlations times for the zonal coupling of two unstable modes (τ_{1F1}) and a stable and unstable pair (τ_{1F2}). Triplet correlation times are evaluated at $k'_x = 0.2$, $k_x = 0.2$, and three values of k'_y. 49

2.2 Coupling coefficients for $k'_x = 0.2$, $k_x - 0.2$, and various values of $k'_y = k_y$. Terms retained in Eqs. (A1) - (A4) are proportional to C_{1F2}. The coefficient C_{F12} introduces terms proportional to squares of mode energies. 50

6.1 The absolute value of the coupling coefficients $|C|$ for different pairs of eigenmodes for the adiabatic-electron Cyclone Base Case between the most unstable mode at $k = (0, 0.3)$, the zonal mode at $k' = (0.083, 0)$, and the sideband at $k'' = (-0.083, 0.3)$, where γ_z and γ_{side} are the growth rates for the zonal modes and sidebands. Several coupling coefficients are orders of magnitudes larger than the others, allowing for a reduction of the problem dimension. 180

Abstract

Microturbulence is caused by gyroradius-scale instabilities such as the Ion-Temperature-Gradient-driven (ITG) instability, Trapped Electron Mode (TEM), Kinetic Ballooning Mode (KBM), etc. Understanding how these instabilities saturate and form turbulence is important for the efficient operation and optimization of magnetic confinement fusion devices in the quest for sustained fusion energy. The objective of this thesis is to understand the important factors and mechanisms that saturate ITG turbulence and to utilize said understanding to build reduced models that capture key physical behavior , resolving which would otherwise require a complex full-physics approach.

Zonal-flow-catalyzed interactions that involve large-scale stable, unstable modes and zonal flows are crucial for the saturation of curvature-driven ITG turbulence. A corresponding saturation theory is built based on a fluid model and implemented and tested numerically. The crudest saturation theory drops the non-zonal interactions and also the nonlinear corrections to frequencies, while also truncating the wavenumber space to obtain scalings for the saturation level with a triplet correlation time based on linear frequencies and coupling coefficients. It is then discovered that nonlinear interactions can cause nonnegligible modifications on the mode oscillations for systems with higher turbulence level. Furthermore, the k_x direction in wavenumber space needs to be resolved in order to break the symmetry between modes and build up the zonal flow, which is shown in both time-dependent and time-independent research. A two-predator-prey model based on the saturation theory, and with no free parameters, is also constructed. This will help build a predator-prey model from first principles, which has the potential to further understanding of the limit-cycle oscillations observed in L-H transitions.

The importance of large-scale stable modes and the triplet correlation time derived from saturation theory is tested in gyrokinetics. Numerical results show that the resonance between the stable and unstable modes through the coupling with zonal flows corresponds to long nonlinear interaction lifetimes, or large triplet correlation times, which increases nonlinear energy transfer and leads to strong turbulence suppression beyond any purely linear estimates.

The triplet correlation time is further used to improve the standard quasilinear transport model for fast heat-flux prediction in gyrokinetics, which shows significant improvement in cases that demonstrate heat-flux onset upshift from the linear critical gradient. The role of the coupling coefficient in gyrokinetics is discussed and initial efforts to calculate the coupling coefficient are described.

Chapter 1

Introduction

In order to develop nuclear fusion as a viable energy source, a thorough understanding of magnetically confined plasmas is required. Decades of research have enabled an encompassing view of plasma instability mechanisms, but our understanding of the properties of nonlinear saturation of those instabilities, which is essential for operation and optimization of fusion devices, is still incomplete. Drift waves, which are ubiquitous in plasmas, can become unstable under various conditions. The ion-temperature-gradient-driven (ITG) instability is one of the key drivers of turbulent transport in fusion devices. This thesis builds on a modern view of ITG turbulence saturation, where includes zonal flow and large-scale stable modes and are important players in the nonlinear redistribution of energy. In this chapter, the mechanisms underlying drift waves and ITG modes are presented. Afterwards, I will introduce statistical closure, a mathematical tool to describe chaotic nonlinear systems. Finally, zonal flows and stable modes will be discussed.

1.1 Drift Waves and ITG Instability

Consider a slab of plasma with a uniform magnetic field pointing into the page and density gradient pointing toward the right, as shown in Fig. 1.1. When there is a

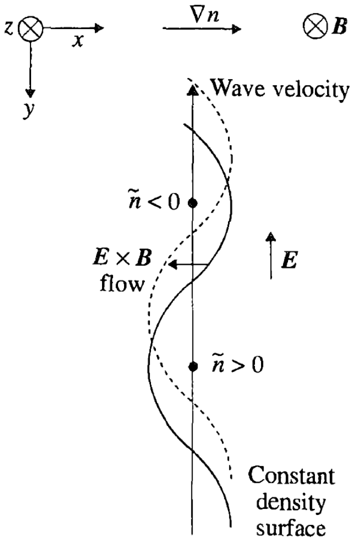

Figure 1.1: The constant-density surface moving in an electron drift wave due to the $E \times B$ velocity. (Wesson J. (2004) *Tokamaks*)

small perturbation in the plasma, the density gradient on the constant-x plane will force the low-inertia electrons to generate an electric field to establish force balance, and therefore

$$\tilde{\phi} = \frac{T_e \tilde{n}_e}{e n_e} \tag{1.1}$$

where $\tilde{\phi}$ is the perturbed electrostatic potential in the y direction, e is the electron charge, T_e and n_e are the equilibrium temperature and density, respectively, and $\tilde{n}_e$ is the perturbed electron density. This provides the $E \times B$ drift velocity that is $\pi/2$ out of phase with the density, and the resulting wave propagates in the y direction. The dispersion relation of this wave can be derived from the ion continuity equation

$$\frac{\partial n_i}{\partial t} = -\nabla \cdot n_i \mathbf{v}_i \tag{1.2}$$

By assuming $\tilde{n}_i \propto e^{-i\omega t}$ and that $v_{E\times B}$ is the dominant velocity, one can derive the first order equation

$$i\omega \tilde{n}_i = v_{E\times B} \frac{dn}{dx} \tag{1.3}$$

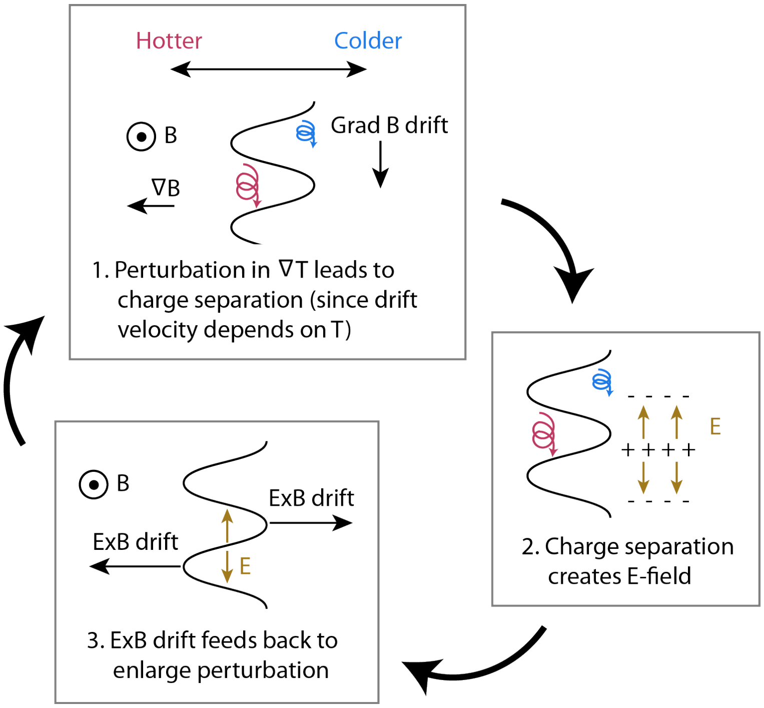

Figure 1.2: Toroidal ITG instability cartoon. The Bad curvature and temperature gradient cause charge separation which leads to $E \times B$ feed back that enlarges perturbation. (Fusion Wiki)

where $v_{E\times B} = -\frac{1}{B}\frac{\partial\tilde{\phi}}{\partial y}$. Using quasineutrality $\tilde{n}_e = \tilde{n}_i$, we can equate Eq. (1.1) and Eq. (1.3) and derive the dispersion relation

$$\omega = \omega_{*e} \equiv -\frac{k_y T_e}{eBn}\frac{dn}{dr} = k_y v_* \tag{1.4}$$

The velocity v_* is called the diamagnetic drift velocity, and the wave described here is called the drift wave. Drift waves driven linearly unstable are called the drift-wave instabilities. One important drift-wave instability that is driven by the ion temperature gradient is called the ITG instability. A specific case where the ITG instability relies on bad curvature is called toroidal ITG instability, a central research subject of this thesis.

The toroidal ITG instability occurs when the drift wave passes through the region where the magnetic field curvature gradient points in the same direction as the pressure gradient (temperature gradient). Due to the fact that the drift speed of the drift wave depends on the temperature, the spatial temperature difference causes charge separation and creates an electric field which creates $E \times B$ drift that enlarges the wave amplitude as shown in Fig. 1.2. The more detailed calculation can be seen in gyrokinetics calculations, which will not be presented here.[26]

1.2 Statistical Closure and Triplet Correlation Time

The plasma is composed of an extremely large number of charged particles, making it impossible to track all particles' motions. However, it is possible to capture relevant behavior of the plasma, utilizing what is called the ensemble average, the average of all particle motions over a suitable statistical ensemble. However, taking the ensemble average makes calculations more intractable and systems of equations not closed, which is required to obtain unique solutions.

Consider the simple example [1],

$$\frac{\partial y}{\partial t} + iby = 0 \tag{1.5}$$

with the initial condition $y(t=0) = 1$, where b is a random variable that is constant in time but different for different particles. Solving this equation directly, one obtains the solution $y = e^{-ibt}$. The ensemble-averaged solution therefore is

$$\langle y \rangle = \left\langle e^{-ibt} \right\rangle = \int_{-\infty}^{\infty} e^{-ibt} P(b) db \tag{1.6}$$

where $P(b)$ is the probability density for y. Note that the ensemble average of two or more functions can be written as

$$\langle f_1(x_1) f_2(x_2) \cdots f_n(x_n) \rangle = \int f_1(x_1) f_2(x_2) \cdots f_n(x_n) P(x_1, x_2, \cdots, x_n) dx_1 dx_2 \cdots dx_n \, , \tag{1.7}$$

Returning to the original problem, if one takes the ensemble average before solving the equation, obtaining a solution will not be as straight forward,

$$\begin{array}{rr} \frac{\partial\langle y\rangle}{\partial t}+i\left\langle by\right\rangle=0, & \langle y(t=0)\rangle=1, \\ \frac{\partial\langle by\rangle}{\partial t}+i\left\langle b^2y\right\rangle=0, & \langle by(t=0)\rangle=\langle b\rangle\,, \\ \frac{\partial\left\langle b^2y\right\rangle}{\partial t}+i\left\langle b^3y\right\rangle=0, & \left\langle b^2y(t=0)\right\rangle=\left\langle b^2\right\rangle, \\ \vdots & \vdots \end{array} \tag{1.8}$$

Note that $\langle b^n\rangle$ denotes the n-th moment of b, and can also be written as $\langle b_1 b_2\cdots b_n\rangle$. The ensemble averaged y is unknown, as is $\langle by\rangle$. In order to solve the evolution equation for $\langle y\rangle$, one requires the evolution equation for $\langle by\rangle$. However, in order to solve $\langle by\rangle$, one needs to know what $\langle b^2y\rangle$ is. Therefore, this set of equations can never be solved as is because the solution for the last equation of the infinite series is required. Therefore, a closure needs to be imposed on the equations to terminate the series and obtain the approximated answer. Note that the term closure describes a group of mathematical relations that makes the equations solvable with a finite number of terms. For instance, one may attempt to solve the above equations with the zeroth order approximation that b and y are statistically independent, i.e. $P(a,b)=P(a)P(b)$, along with a set of relations for b

$$\langle b^n\rangle=\begin{cases} 0 & (n \text{ odd}) \\ (\frac{1}{2}\langle b^2\rangle)^{n/2}n!/(n/2)! & (n \text{ even}) \end{cases} \tag{1.9}$$

which is the result if one assume the probability density is Gaussian, $P(b)=e^{-b^2/2}/\sqrt{2\pi}$. One can then derive different orders of closure approximations

$$\begin{array}{c} \langle by\rangle=\langle b\rangle\langle y\rangle=0, \\ \left\langle b^2y\right\rangle=\left\langle b^2\right\rangle\langle y\rangle\,, \\ \left\langle b^3y\right\rangle=3\left\langle b^2\right\rangle\langle by\rangle\,, \\ \vdots \end{array} \tag{1.10}$$

Note that one can not impose all of these closure approximations at the same time, but only chose to cloose the equations at a specific order. The corresponding solutions for these closure equations at different order are

$$\begin{gathered}\langle y\rangle = 1\\ \langle y\rangle = \cos\left(\langle b^2\rangle^{1/2}\, t\right)\\ \langle y\rangle = \tfrac{2}{3} + \tfrac{1}{3}\cos\left(\sqrt{3}\,\langle b^2\rangle^{1/2}\, t\right)\\ \vdots\end{gathered} \tag{1.11}$$

The solution converges to the exact solution $\langle y\rangle = e^{-\frac{1}{2}\langle b^2\rangle t^2}$ solved directly from Eq. (1.6). Compare to Eq. 1.11, we can also find the solution for $\langle y(t)\rangle$ with Taylor expansion in t with Eq. 1.9

$$\begin{aligned}\langle y(t)\rangle &= \langle y(t=0)\rangle + t\,\langle y'(t=0)\rangle + \frac{t^2}{2}\,\langle y''(t=0)\rangle + \cdots\\ &= 1 + \sum_{n=1}^{\infty}(-i)^n\,\langle b^n\rangle\, t^n/n!\\ &= 1 + \sum_{n=1}^{\infty}(-\frac{1}{2}\,\langle b^2\rangle\, t^2)^n/n!\end{aligned} \quad . \tag{1.12}$$

which is the Taylor expansion of the exact solution. Eq. (1.12) converges more slowly to the exact solution than does Eq. (1.11). Also, for $t > 2/\langle b^2\rangle^{1/2}$, Eq. 1.12 converges poorly and required a substantial number of terms to be retained. This makes statistical closure better option for finding the approximate solution for systems whose exact solutions are close to Gaussian.

One may question why it is necessary to use statistical closure since the exact solution from the above example is straightforward to derive. In linear systems, the exact solutions are often quite accessible. However, exact solutions for nonlinear systems are generally impossible to derive, and statistical closure can be useful in deriving approximate solutions for turbulent systems.

Consider another example of a generic scalar-evolution equation with a quadratic nonlinearity [2]

$$\frac{\partial a_k}{\partial t} + \gamma_k a_k = \sum_{k'} C_{k,k'}\, a_{k'}\, a_{k-k'}\ , \tag{1.13}$$

where k and k' are wavenumbers, $C_{k,k'}$ is the coupling coefficient for the nonlinearity, and γ_k is the linear growth rate. The evolution equation for $|a_k|^2$, often related to energy evolution, which can be expressed as

$$\frac{\partial |a_k|^2}{\partial t} + 2\gamma_k |a_k|^2 = 2\mathrm{Re} \sum_{k'} C_{k,k'} a_{k'} a_{k-k'} a_k^* \tag{1.14}$$

It is possible to use a quasilinear approximation to expand the nonlinearity and solve for the lowest-order solution. However, the quasilinear approximation can fail to find an appropriate solution when the system is turbulent and the nonlinearity is strong. On the other hand, statistical closure can provide a better alternative under such condition; to obtain it, one first takes the ensemble average of Eq. (1.15),

$$\frac{\partial |a_k|^2}{\partial t} + 2\gamma_k |a_k|^2 = 2\mathrm{Re} \sum_{k'} C_{k,k'} \left\langle a_{k'} a_{k-k'} a_k^* \right\rangle \tag{1.15}$$

To solve this equation, one composes the evolution equation of the third-order moment

$$\begin{aligned} \frac{\partial}{\partial t} \left\langle a_{k'} a_{k-k'} a_k^* \right\rangle + \left(\gamma_k^* + \gamma_{k'} + \gamma_{k-k'}\right) \left\langle a_{k'} a_{k-k'} a_k^* \right\rangle = \sum_{k''} \Big\{ C_{k,k''}^* \left\langle a_{k''}^* a_{k-k''}^* a_{k'} a_{k-k'} \right\rangle \\ + C_{k',k''} \left\langle a_{k''} a_{k'-k''} a_k^* a_{k-k'} \right\rangle + C_{k-k',k''} \left\langle a_{k''} a_{k-k'-k''} a_k^* a_{k'} \right\rangle \Big\} . \end{aligned} \tag{1.16}$$

Equation 1.19 is not closed, and the specification of the fourth order moments is required to find the solution, stopping it from connecting the equations to the bottomless abyss. Similar to the previous example, one may close the equations by assuming the fluctuations are close to Gaussian at the level of the fourth-order moments, but not the third-order moment; this approach is known as the quasinormal closure. The assumption of near-Gaussian fluctuation leads to result that the as at different wavenumbers are statistically independent at zeroth-order, that is, $\langle a_k a_{k'} \rangle = \langle a_k \rangle \langle a_{k'} \rangle$ if $k \neq \pm k'$. Note that a_{-k} survives because $a_{-k} = a_k^*$, which is dependent on a_k. Furthermore, the chaotic behavior of the complex function a suggests $\langle a\rangle = 0$, which can be shown by integrating it over the complex phase in the ensemble average. This is known as a random phase average. It follows that $\langle a_k a_{k'}\rangle = \langle a_k\rangle\langle a_{k'}\rangle = 0$ if $k \neq -k'$, and even $\langle a_k a_k\rangle = 0$. The only pair that is not ensemble-averaged to zero is $\langle a_k a_{-k}\rangle = \langle a_k a_k^*\rangle = |a_k|^2$, where the two fluctuations are correlated and also cancel out the complex phase. In Eq. (1.16), k'' can be k' or $k-k'$ to make the first term on the right-hand side non-zero. Similarly, k'' can be k or $k'-k$ for the second term, and k or $-k'$ for the third term. The final result for Eq. (1.16) after closure is

$$\begin{aligned}\left[\frac{\partial}{\partial t} + (\gamma_k^* + \gamma_{k'} + \gamma_{k-k'})\right]\langle a_{k'}a_{k-k'}a_k^*\rangle &= C^*_{k,k'}|a_{k'}|^2|a_{k-k'}|^2 + C^*_{k,k-k'}|a_{k'}|^2|a_{k-k'}|^2 \\ + C_{k',k}|a_k|^2|a_{k-k'}|^2 + C_{k',-k+k'}|a_k|^2|a_{k-k'}|^2 &+ C_{k-k',k}|a_k|^2|a_{k'}|^2 + C_{k-k',-k'}|a_k|^2|a_{k'}|^2 \ .\end{aligned} \tag{1.17}$$

Due to the symmetry between k' and $k-k'$ in the nonlinearity, $C_{k,k'} = C_{k,k-k'}$, therefore, $C^*_{k,k'} = C^*_{k,k-k'}$, $C_{k',k} = C_{k',-k+k'}$, and $C_{k-k',k} = C_{k-k',-k'}$. Thus, Eq. (1.19) can be simplified to

$$\begin{aligned}\left[\frac{\partial}{\partial t} + (\gamma_k^* + \gamma_{k'} + \gamma_{k-k'})\right]\langle a_{k'}a_{k-k'}a_k^*\rangle &= 2C^*_{k,k'}|a_{k'}|^2|a_{k-k'}|^2 \\ &+ 2C_{k',k}|a_k|^2|a_{k-k'}|^2 + 2C_{k-k',k}|a_k|^2|a_{k'}|^2 \ .\end{aligned} \tag{1.18}$$

By using the method of Green's function, one can invert Eq. (1.18) to obtain an expression for the third-order moment

$$\begin{aligned}\langle a_{k'}a_{k-k'}a_k^*\rangle = 2\int_{t_0}^{t} dt' e^{-(\gamma_k^*+\gamma_{k'}+\gamma_{k-k'})(t-t')}&\left[C^*_{k,k'}|a_{k'}|^2|a_{k-k'}|^2\right. \\ &\left.+ C_{k',k}|a_k|^2|a_{k-k'}|^2 + C_{k-k',k}|a_k|^2|a_{k'}|^2\right] \ .\end{aligned} \tag{1.19}$$

Thus, the final closed form for Eq. (1.15)

$$\begin{aligned}\frac{\partial|a_k|^2}{\partial t} + 2\gamma_k|a_k|^2 = 4\mathrm{Re}\sum_{k'}\int_{t_0}^{t} dt' e^{-(\gamma_k^*+\gamma_{k'}+\gamma_{k-k'})(t-t')}&\left[C^*_{k,k'}|a_{k'}|^2|a_{k-k'}|^2\right. \\ &\left.+C_{k',k}|a_k|^2|a_{k-k'}|^2 + C_{k-k',k}|a_k|^2|a_{k'}|^2\right] \qquad (1.20) \\ = 4\mathrm{Re}\sum_{k'}\int_{t_0}^{t} dt' e^{-(\gamma_k^*+\gamma_{k'}+\gamma_{k-k'})(t-t')}\left[C^*_{k,k'}|a_{k'}|^2|a_{k-k'}|^2 + 2C_{k',k}|a_k|^2|a_{k-k'}|^2\right]&\end{aligned}$$

Here, everything is expressed in terms of $|a|^2$, meaning a finite number of equations leads to a unique solution. The physical meaning of Eq. (1.21) is that the time evolution of $|a_k|^2$ depends on the collective effects from the combinations of $|a|^2$s throughout the time history. On the other hand, $|a_k|^2$ can also absorb or release energy efficiently by interacting with large amplitude modes. If the linear timescale is much larger than the nonlinear timescale for the evolution of $|a|^2$, one can extract the $|a|^2$s on the right-hand-side of the equation and integrate only the propagator, yielding

$$\frac{\partial |a_k|^2}{\partial t} + 2\gamma_k |a_k|^2 = 4\text{Re}\sum_{k'} (\hat{\gamma}_k^* + \hat{\gamma}_{k'} + \hat{\gamma}_{k-k'})^{-1} \left[C_{k,k'}^* |a_{k'}|^2 |a_{k-k'}|^2 + 2C_{k',k} |a_k|^2 |a_{k-k'}|^2\right] \tag{1.21}$$

where $\hat{\gamma} = \gamma + \Delta\gamma$, and $\Delta\gamma$ is the nonlinear correction. $\tau \equiv (\hat{\gamma}_k^* + \hat{\gamma}_{k'} + \hat{\gamma}_{k-k'})^{-1}$ is called the triplet correlation time, which is the timescale of the response function, more precisely, the lifetime of the nonlinear interaction. Large τ represents long interaction time between modes and leads to strong nonlinear interaction; from Eq. (1.21), it is evident that large τ can result in low saturation levels for $|a_k|^2$. Note that in the statistical-closure hierarchy, the core assumption is that the $|a|^2$ are close to Gaussian, which is true for strongly turbulent systems, however, closure hierarchy allows deviations from Gaussian making it applicable to weak turbulence. Conversely, the quasilinear approximation expands the variables around the mean, which makes it more appropriate for weak-turbulence systems but inapplicable for strong-turbulence cases. More discussion about how to utilize the triplet correlation time and the statistical closure in an ITG fluid model in different turbulent regimes will be forthcoming in the following Chapters.

1.3 Zonal Flows and Stable Modes

Zonal flows are large-scale band structures often observed in scenarios such as planetary systems and certain regimes of turbulence in fusion devices. In magnetized plasmas, the varying potential Φ generates an $v_{E\times B}$ flow with *zonal* referring to variation only in the radial direction in toroidal geometry. Note that zonal flows do not arise from linear physics; rather, they are pumped nonlinearly, thus accessing energy injected by the instability.

Zonal flows can suppress the turbulence and transport. A common cartoon interpretation of the underlying physics is that the spatially varying velocity of the zonal flow suppresses the turbulence by shearing fluctuations and delivering energy from large scale turbulence to the small-scale dissipative range of wavenumbers. However, this picture is at best incomplete, as the zonal flow can catalyze the interactions between large-scale modes, including damped modes at large, linearly unstable scales, which are also referred to as stable modes [17]. In Fig. 1.3, the initial perturbations start at a very low amplitude, where linear terms dominate over any nonlinear contributions. The stable mode is damped exponentially in the beginning while the unstable mode is growing exponentially; the stable mode is later pumped up significantly through the nonlinearity to a level that is comparable to that of the unstable mode. The model used to produce Fig. 1.3 is the Horton-Holland model [15, 31], which is a toroidal ITG fluid model with strong zonal flow that dominates the nonlinear interactions. Based on these observations, it is important to take zonal-flow-catalyzed interactions between stable and unstable modes into account in predicting the turbulence saturation level and the heat flux.

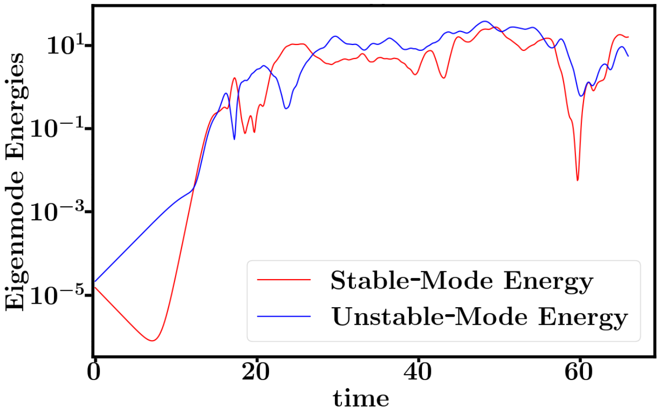

Figure 1.3: The stable mode is excited through the nonlinearity after the unstable mode has grown to a certain level. The amplitude of the stable in the quasi-stationary state ($t \gtrsim 20$) is comparable to that of the unstable mode.

1.4 Thesis Summary and Outline

The main objective of the thesis is to investigate how toroidal ITG turbulence is saturated and how to utilize this knowledge.

In chapter 2, a saturation theory for the ITG fluid model. A discussed above will be presented saturation formula for the eigenmode amplitudes and the zonal flow will be derived under the assumptions that zonal-flow-catalyzed nonlinear interactions between stable and unstable modes are dominant, that the zonal pressure decouples from the system, and that the system is turbulent, implying that statistical closure is applicable. The technique of wavenumber truncation is tested first. Then, an improved saturation formula with nonlinearity-affected eigenmode frequency and one with zonal flow energy cascade included are derived and tested. The validation and qualification of the model is also discussed in this chapter. Extensions and applications of this theory are presented in later chapters according to the outline given in Fig. 1.4.

In chapter 3, the time-dependent behavior of the wavenumber-truncated Horton-

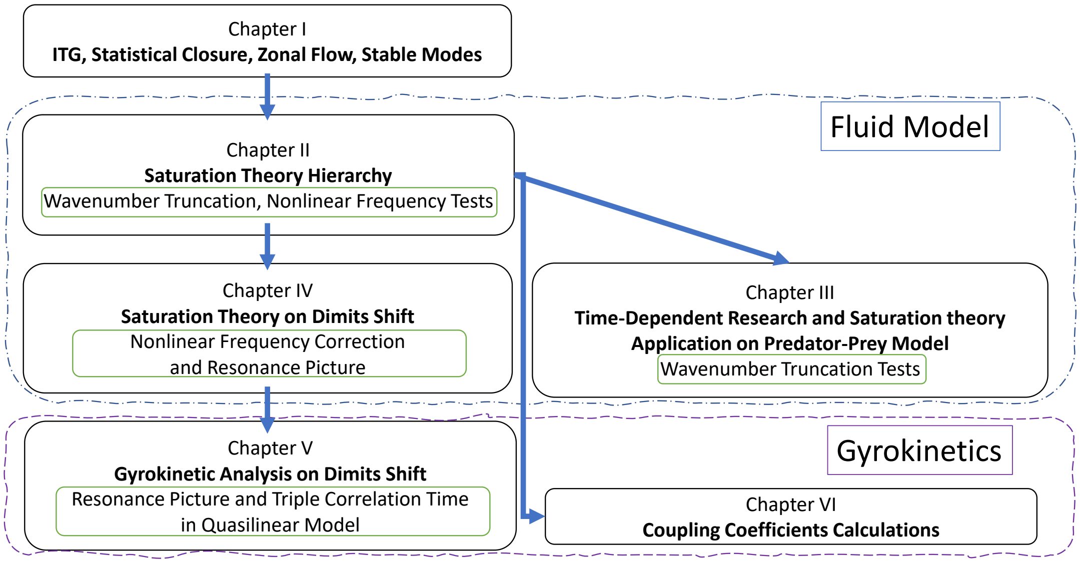

Figure 1.4: Thesis road map. A Saturation theory for toroidal ITG fluid model is tested under different level of approximations in wavenumber space and frequency in chapter 2. Chapters 3 and 4 show the applications of saturation theory in predator-prey model building and Dimits shift respectively described in chapter 2 on fluid model. The triplet correlation time and resonance picture derived from chapter 4 are examined with gyrokinetic simulations in chapter 5, these ideas are also implemented in quasilinear model in this chapter. Coupling coefficient is shown to play an important role in turbulence saturation in fluid theory in chapter 2, the method to calculate such quantity in gyrokinetics is proposed and tested in chapter 6.

Holland model is analyzed and tested. It is shown that the asymmetry between the stable and unstable mode drives a zonal flow, and a numerical experiment is performed by adding artificial damping on the stable modes. A two-predator-prey model is built based thereupon, but with the symmetry broken by including multiple wavenumbers to simulate the zonal-flow energy cascade; the saturation theory described in chapter 2 is also utilized to reduce the model to three variables.

In chapter 4, the saturation theory is applied to a modified ITG fluid model that captures the linear instability threshold and shows heat flux suppression near the linear threshold, mimicking the full-physics gyrokinetic situation. The nonlinear frequency is again included to improve the saturation model. From the analysis, it is concluded that a resonance between the stable and unstable modes leads to a large triplet correlation time, and therefore produces the strong zonal-flow-catalyzed interaction which successfully removes the energy from the unstable mode and yields a low saturation level and heat flux.

In chapter 5, the ideas derived from the fluid-model saturation theory are tested with numerical experiments in gyrokinetic simulations of a scenario with nonlinear critical gradient upshift. It is shown that the stable modes, zonal-flow-catalyzed nonlinear interactions, and the resonance between the stable and unstable modes are indeed the root cause of the observed turbulence suppression. These concepts are then used to improve the standard quasilinear model, a reduced model to predict heat flux. It is shown that the introduced modifications improve the model significantly, demonstrating for several cases with and without nonlinear critical gradient upshift excellent predictive capability.

In chapter 6, a brief introduction on coupling coefficients and how to calculate them is presented. The coefficients are then calculated for the a standard gyrokinetic scenario. This constitutes an essential step towards a reduced description of coupling coefficients for deployment in quasilinear transport models.

Bibliography

[1] R.H. Kraichnan, J. Math. Phys. **2**, 124 (1961).

[2] P.W. Terry, Concepts in Plasma Turbulence from the Perspective of Classical Hydrodynamic Turbulence: course notes for Physics 805, University of Wisconsin-Madison, 2020.

[3] W. Horton, Rev. Mod. Phys. **71**, 735 (1999).

[4] P.W. Terry, Rev. Mod. Phys. **72**, 109 (2000).

[5] A.M. Dimits, G. Bateman, M.A. Beer, B.I. Cohen, W. Dorland, G.W. Hammett, C. Kim, J.E. Kinsey, M. Kotschenreuther, A.H. Kritz et al., Phys. Plasmas, **7**, 969 (2000).

[6] P.W. Terry, P.-Y. Li, M.J. Pueschel, and G.G. Whelan, Phys. Rev. Lett. **126**, 025004 (2021).

[7] P.W. Terry, B.J. Faber, C.C. Hegna, V.V. Mirnov, M.J. Pueschel, and G.G. Whelan, Phys. Plasmas **25**, 012308 (2018).

[8] C. Holland, P.H.Diamond, S. Champeaux, E. Kim, O. Gurcan, M.N. Rosenbluth, G.R. Tynan, N. Crocker, W. Nevins, and J. Candy, Nucl. Fusion **43**, 761 (2003).

[9] K. Makwana, P.W. Terry, and J.-H. Kim, Phys. Plasmas **19**, 062310 (2012).

[10] K. Makwana, P.W. Terry, M.J. Pueschel, and D.R. Hatch, Phys. Rev. Lett. **112**, 095002 (2014).

[11] M. Stransky, Phys. Plasmas **18**, 052302 (2011).

[12] P.W. Terry, K.D. Makwana, M.J. Pueschel, D.R. Hatch, F. Jenko, and F. Merz, Phys. Plasmas **21**, 122303 (2014).

[13] P.H. Diamond, S.-I. Itoh, K. Itoh, and T.S. Hahm, Plasma Phys. Control. Fusion **47**, R35 (2005).

[14] F. Jenko, W. Dorland, M. Kotschenreuther, and B.N. Rogers, Phys. Plasmas **7**, 1904 (2000).

[15] G. Hammett, UCLA Winter School, Center for Multiscale Plasma Dynamics, Los Angeles, CA, Jan. 2007.

[16] G.G. Whelan, Ph.D. Dissertation, Univ. of Wisconsin-Madison, 2019.

[17] W. Horton, D.-I. Choi, and W.M. Tang, Phys. Fluids **24**, 1077 (1981).

[18] A.J. Wootton, M.E. Austin, R.D. Bengtson, J.A. Boedo, R.V. Bravenec, D.L. Brower, J.Y. Chen, G.Cima, P.H. Diamond, R.D. Durst et al., Plasma Phys. Control. Fusion **30**, 1479 (1988).

[19] S.A. Orszag, J. Fluid Mech. **41**, 363 (1970).

[20] R.H. Kraichnan, J. Fluid Mech. **5**, 497 (1959).

[21] P.W. Terry and W. Horton, Phys. Fluids **26**, 206 (1983).

[22] M.J. Pueschel, M. Kammerer and F. Jenko, Phys. Plasmas **15**, 102310 (2008).

[23] M.J. Pueschel, P.-Y. Li and P.W. Terry, Nucl. Fusion **61**, 054003 (2021).

[24] D.R. Ernst, J. Lang, W.M. Nevins, M. Hoffman, Y. Chen, W. Dorland, and S. Parker, Phys. Plasmas **16**, 055906 (2009).

[25] R. Gatto, P.W. Terry, and D.A. Baver, Phys. Plasma **13**, 022306 (2006).

[26] Merz F. (2008) Dissertation title : *GYROKINETIC SIMULATION OF MULTIMODE PLASMA TURBULENCE*

Chapter 2

Assessing Physics of Ion Temperature Gradient Turbulence via Hierarchical Reduced-Model Representations

Abstract

The saturation physics of ion temperature gradient (ITG) turbulence is probed by studying how amplitudes and scalings with key parameters vary across a hierarchy of reduced models. The models derive from nonlinear fluid equations for toroidal ITG turbulence under approximations to the mode coupling interactions in wavenumber space and the representation of turbulent decorrelation. Mode coupling approximations include local-in-wavenumber treatments like the spectral density of flux in quasilinear theory, a truncation to three nonlinearly interacting waves, and the interactions in a cascade to high radial wavenumber mediated by a single zonal flow. Turbulent decorrelation treatments are based on the triplet correlation time with and without eddy damping. Model fidelity is assessed by the scalings and magnitudes of the squared amplitudes of unstable mode, stable mode, and zonal flow with respect to the flow-damping rate and temperature gradient. It is shown that all models reproduce fundamental scalings provided they incorporate the coupling of unstable mode, stable mode and zonal flow. Accurate amplitude prediction requires eddy damping in the triplet correlation time and proper representation of the zonal-flow drive by interactions associated with the radial wavenumber cascade.

In this chapter, I will introduce the saturation theory presented in Ref. [30] and also its qualifications and different order of approximations, which constitute a model hierarchy. The knowledge presented in this chapter is the basis for investigations that will be discussed in the following chapters. One set of approximations involves truncation of wavenumber space for the fluid model, which is also being studied in time-dependent analyses of chapter 3. Moreover, the scaling formula for the turbulence level in saturated state derived in this chapter will be utilized in chapter 3. The Dimits shift seen in various systems will also be checked from the view of saturation theory in chapter 4. In chapter 6, we will come back to the coupling coefficients calculations presented in this chapter for gyrokinetics.

2.1 Introduction

The containment of hot plasmas by magnetic fields is highly sensitive to the turbulence driven by the gradients that necessarily accompany confinement [1]. Consequently, the successful realization of fusion energy in magnetically confined plasmas is critically dependent on predicting and controlling turbulence driven losses [2]. An essential part of predicting and controlling these losses is understanding the turbulence that drives them. Turbulence in confined plasmas involves complex motions sensitive to geometry-independent instabilities [3], nonlinear multiscale evolution [4], and multiscale sinks of fluctuation energy [5]. Despite intense study and steady progress, understanding of turbulence remains limited. These realities make it desirable to employ a variety of strategies for understanding turbulence. This chapter addresses a strategy based on model hierarchies for turbulence that has been widely recommended [6, 7] but whose use in physics understanding has been limited.

Model hierarchies naturally arise in prediction, where the needs for high fidelity and rapid real-time solution come into tension. Because greater fidelity generally comes with more intense computation and longer run times, model hierarchies allow this trade off to be adjusted. Indeed, there is a long history of seeking to reliably model turbulent transport with the quasilinear approximation, a highly reduced model with respect to nonlinear physics, in which a significant reliance on linear inputs produces rapid predictions [8, 9]. However, the value of reduced models transcends the need for prediction. Because reduced models enable rapid solution by eliminating the modeling of physics that is assumed to be less critical in predictions, model hierarchies can be used to probe physics, i.e., approximations that affect or remove physics can be used to assess the importance and role of that physics in the turbulence. For their role in both prediction and understanding, model hierarchies relate to the primacy hierarchy of verification and validation [6] and are therefore an important aspect of verification and validation. In a well validated hierarchy it should be possible to know in quantitative terms the trade off between fidelity and speed of computation, including for predictions outside an empirical database.

We examine here a model hierarchy that has been developed to understand and describe ion temperature gradient (ITG) turbulence [10], a key player in dominant transport losses in a variety of magnetic confinement devices, including tokamaks [11], stellarators [12], and the reversed field pinch [13]. This hierarchy is built on a fluid model for the toroidal branch of ITG turbulence that qualitatively replicates many features of ITG turbulence [14]. These include the spectrum [15], spectral energy transfer [15, 16] and its catalyzation by zonal flows [17], saturation by stable modes [18], and the transport phenomena of nonlinear finite-β stabilization [19, 20] and the critical-gradient upshift [11, 21, 22], both of which are tied to resonance of the dominant nonlinear interaction time. The hierarchy is created by introducing a number of approximations relating to turbulence behavior and properties that are intermediate to the fluid model and the quasilinear approximation. Relative to a more complete hierarchy that includes gyro Landau fluid models [23], gyrokinetics [24], and full kinetics [25], this hierarchy occupies a model range of more significant reduction. This means that the hierarchy tends to probe physics content with more extensive impacts, i.e., removing one piece of physics can affect multiple aspects of the turbulent behavior. Moreover, the effects are sizable. In the case of the hierarchy studied here, impacted effects include nonlinear finite-β stabilization, the critical gradient upshift, gross turbulence levels, zonal flow levels, scalings with key parameters, and the timescales of time histories. In contrast hierarchies in the model range of least reduction tend to affect phenomena of more narrow reach or more subtle gradations of behavior. Examples include the residual flow [26] in early comparisons of gyrokinetic and gyro Landau fluid codes [11], and turbulence levels within factors of a few [27].

The turbulence physics exposed by variations across our hierarchy includes the decorrelation of turbulent interactions, with representations of the associated timescale that involve the triplet correlation time and eddy damping rates; the multiplicity of coupling of turbulent fluctuations as it relates to the wavenumber spectrum; and mode-coupling channel hegemony. The last two categories are less familiar but relate to truncations of interactions in wavenumber space that can affect the multiplicity of fluctuation states accessible in a turbulent system, and the types of mode coupling interactions that dominate turbulent energy transfer. The latter, in particular, is exposed by a qualification analysis, an exercise in verification and validation that delineates domains of applicability [6]. Here the qualification is tied not to validation tolerances, but to physics retained or excluded by choice of domain.

With respect to nonlinear physics, the quasilinear approximation is an extreme reduction. It can provide a satisfactory representation of transport phenomena when an an overall transport level set by a single nonlinear simulation of a comprehensive model like gyrokinetics is independent of, or at worst weakly dependent on parameters whose variation is important in the modeling. Were this not the case, a costly nonlinear run would have to carried out for every change of relevant parameters. Extensive experience and careful tailoring of linear inputs have shown cases where this type of reduction can be made to work. Situations where it doesn't work have been more sparsely studied and reported. The quasilinear approximation will provide a reference point for our hierarchy but will not be investigated here because we have recently completed several studies aimed at exploring and expanding the physics content of quasilinear theory in situations where it has been unable to model parameter scans. These exercises have demonstrated the importance of the triplet correlation time in finite-β nonlinear stabilization [20] and the critical gradient upshift of ITG turbulence [21]. This quantity, which is a nonlinear correlation time of the interaction between the unstable ITG mode, a zonal-flow fluctuation, and a stable-mode fluctuation at a triplet of interacting wavenumbers, can in some cases be approximated by the linear frequencies and growth/damping rates of each member of the triplet. Recent work has also shown that coupling coefficients between these fluctuations can also affect key transport scalings [28]. In both of these cases there is a less severe reduction to quasilinear theory, which will be studied here, that includes the triplet correlation time and the coupling coefficients, and can be approximated with linear inputs.

This chapter is organized as follows. The model hierarchy is introduced in Sec. 2.2, along with the approximations that delineate its members and their inter relationships. Comparative measurements across this hierarchy are described in Sec. 2.3, as are measurements relating to qualification of wavenumber space truncations. These analyses all pertain to time-independent solutions of hierarchy members, appropriate for steady state turbulence. Behavior of time-dependent solutions will be described elsewhere. The conclusions are given in Sec. 2.3.2. An appendix contains the most lengthy set of model equations.

2.2 Model Hierarchy

We introduce in Fig. 2.1 a model hierarchy for ITG turbulence and transport. For reference the hierarchy is bounded by models that will not be studied here — at the top of the figure is gyrokinetics, representing a more comprehensive model [29]; at the bottom is the quasilinear approximation, representing a more reduced model. This hierarchy is ordered by nonlinear physics. The two-field fluid model appearing just under gyrokinetics is a set of coupled nonlinear partial differential equations for ion vorticity and pressure. The quasilinear approximation is a mixing length transport flux that is generally furnished with linear inputs, with the exception of a single numerical run of a comprehensive nonlinear model like gyrokinetics, which sets an overall level. Note that the two-field fluid model has simplified linear physics and could be taken as more reduced than quasilinear theory if the hierarchy were ordered according to linear physics. This hierarchy is not inclusive of every approximation in use or that otherwise could be conceived. For example, gyro-Landau-fluid models [23], which would be intermediate to gyrokinetics and the two-field fluid model, are not represented.

Reduced models are in frequent use, often in studies that employ a single model to pursue specific objectives. Model comparisons often involve a pair of models, not a hierarchy. Here we wish to understand how turbulence properties are represented by multiple models with graded approximations. The left-hand branch in Fig. 2.1 represents approximations in the treatment of the spatial representation of turbulent interactions. The right-hand pathway represents approximations related to the temporal representation of interactions. Relative to the two-field fluid model, the quasilinear approximation makes severe reductions with respect to both of these representations, and can be thought of as a zero-dimensional projection of both the spatial and temporal domains, at least in its standard representations. It is therefore instructive to study intermediate approximations.

2.2.1 Two-Field Fluid Model

The two-field fluid model referred to in Fig. 2.1 is the least reduced model considered in the hierarchy. In keeping with historical precedent we will refer to this as a *primitive model* because as a less reduced model it is less processed. The model is given by

$$\frac{\partial p_k}{\partial t} + ik_y(1+\eta)\phi_k + \chi k_\perp^4 p_k = -\sum_{k'}(\mathbf{k}'\times\hat{\mathbf{z}}\cdot\mathbf{k})\phi_{k'}p_{k-k'} \tag{2.1}$$

$$[\delta(k_y)+k_\perp^2]\frac{\partial \phi_k}{\partial t} + ik_y\phi_k - ik_y\epsilon p_k + \nu k_\perp^2\phi_k = -\frac{1}{2}\sum_{k'}(\mathbf{k}'\times\hat{\mathbf{z}}\cdot\mathbf{k})[(k-k')_\perp^2 - k_\perp'^2]\phi_{k'}\phi_{k-k'}, \tag{2.2}$$

where p_k and ϕ_k are Fourier amplitudes of pressure and electrostatic potential fluctuations, ν and χ are coefficients of collisional dissipation, $\eta = L_n/L_{Ti}$ is the ratio of density and ion temperature gradient scale lengths, and $\epsilon = L_n/R$ is the ratio of density scale length to toroidal major radius, which quantifies the ratio of diamagnetic drift frequency to the frequency of magnetic ∇B and curvature drifts. Equations (4.8) and (4.9) are rendered in the ballooning representation of toroidal geometry. The eigenmodes are assumed to be strongly localized to the outboard

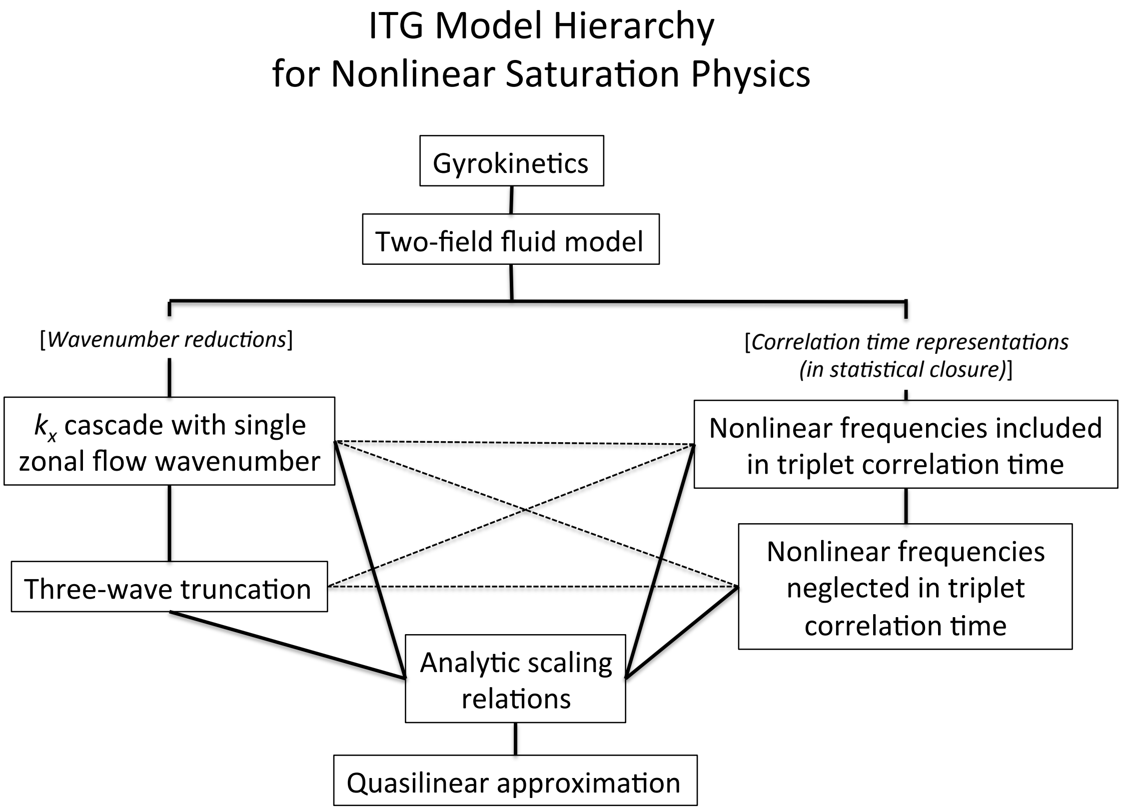

Figure 2.1: Model hierarchy for nonlinear physics of ion temperature gradient turbulence, with more comprehensive treatments at the top. The left-hand pathway represents approximations to the treatment of nonlinear interactions in wavenumber space. The right-hand pathway represents approximation in the treatment of the temporal domain in the context of a statistical closure.

midplane, so that terms in the eigenmode potential that depend on angular distance along the field line from the outboard midplane, including those that describe the parallel ion flow, are small. The Fourier wavenumbers k_x and k_y arise from radial and poloidal derivatives, with $k_x = \varphi_0 \hat{s} k_y$ the radial wavenumber of the ballooning representation. Here $\hat{s} = (r/q)dq/dr$ is the magnetic shear, q is the safety factor, and φ_0 is a displacement of mode structure along the magnetic field measured from the outboard midplane. The electrons are adiabatic, with their response given by $\delta(k_y)$, where $\delta(k_y) = 0$ for $k_y = 0$, and $\delta(k_y) = 1$ for $k_y \neq 0$. Equations (4.8) and (4.9) are normalized with the ion sound gyroradius ρ_s for the perpendicular length scale, L_n for the parallel length scale, and L_n/C_s for the time scale, where C_s is the ion sound speed. Our analyses of the hierarchy will be based on the ITG fluid model first used to derive saturation scaling relations [30]. A newer version reproduces the kinetic threshold of linear instability and was used to study the critical gradient upshift [21, 28]. Both versions saturate via the same mechanism, differing only in the value of the linear critical gradient.

Models in the hierarchy of Fig. 2.1 that make approximations with respect to the spatial domain (left branch) involve the treatment of Fourier space. We consider here models that reduce the Fourier space of standard numerical solutions. The latter discretize the spatial domain, thereby producing a finite number of modes and mode interactions. This can be further reduced by considering limited numbers of mode interactions associated with energy transfer channels. The least reduced involves a sequence of wavenumbers tied to a cascade. For ITG turbulence, gyrokinetic simulations show that the cascade is dominated by the interaction of turbulence with the zonal flow at its peak radial wavenumber [5, 17]. This produces a cascade in radial wavenumber at the k_y values of $k_x = 0$ modes that dominate the instability drive [20]. A more severe reduction of wavenumber coupling interactions truncates them to three wavenumbers. This is the maximal reduction that preserves energy conservation by the nonlinearity, allowing saturated solutions that are meaningful with respect to energy transfer in wavenumber space. Both of these reductions are rooted in the physics of ITG turbulence saturation, which as observed in gyrokinetic simulations, involves energy transfer from the unstable ITG mode through a zonal flow to a stable mode at comparable scale [17]. This localizes energy and energy transfer to large scales, and involves three-wave interactions of the unstable mode, the zonal flow, and a stable mode.

2.2.2 Primitive Model of Three-wave Interaction

The equations for the three-wave truncation involve three wavenumbers and the three modes just mentioned. Although truncating the number of interacting modes, this model preserves the symmetries of mode coupling coeffficients necessary to ensure energy conservation in the interaction. Accordingly this model is also designated as primitive. The interaction is described by five equations,

$$\dot{\beta}_j + i\omega_j\beta_j = \sum_{l=1}^{2} C_{jFl}^{(k,k')} v'_z \beta''_l, \tag{2.3}$$

$$\dot{\beta}''_j + i\omega''_j\beta''_j = \sum_{l=1}^{2} C_{jFl}^{(k'',-k')} v'_z \beta_l, \tag{2.4}$$

$$\dot{v}'_z + \nu v'_z = \sum_{j=1}^{2}\sum_{l=1}^{2} C_{Fjl}^{(k',k)} \beta_j \beta''_l, \tag{2.5}$$

where j assumes the values of 1 or 2, $\beta_{1(2)}$ is the amplitude of the unstable (stable) mode at wavenumber k, $\beta''_{1(2)}$ is the amplitude of the unstable (stable) mode at wavenumber $k'' = k - k'$, and v'_z is the zonal flow at wavenumber k' (with $k'_y = 0$).

The nonlinear coupling coefficients $C_{jFl}^{(k,k')}$, and $C_{Fjl}^{(k',k)}$ are given by

$$C_{jFl}^{(k,k')} = \frac{(-1)^{j-1}}{[R_1(k) - R_2(k)]} \frac{(-ik_y)}{2} \left[R_l(k'') - \frac{R_{3-j}(k)[k_\perp''^2 - k_\perp'^2]}{1 + k_\perp^2} \right], \tag{2.6}$$

$$C_{Fjl}^{(k',k)} = \frac{-ik_y[k_\perp''^2 - k_\perp^2]}{2}, \tag{2.7}$$

where

$$R_{1,2}(k) = \frac{\omega_{1,2}(1 + k_\perp^2) - k_y + i\nu k_\perp^2}{k_y \epsilon}, \tag{2.8}$$

and

$$\omega_{1,2} = -\frac{i}{2} \left(\frac{\nu k_\perp^2 + ik_y}{\delta + k_\perp^2} \right) \pm \frac{i}{2} \left\{ \left(\frac{\nu k_\perp^2 + ik_y}{\delta + k_\perp^2} \right)^2 + \frac{4(1+\eta)k_y^2 \epsilon}{\delta + k_\perp^2} \right\}^{1/2}. \tag{2.9}$$

The coefficient $C_{jFl}^{(k'',-k')}$ can be generated from $C_{jFl}^{(k,k')}$ by the mapping $k \rightarrow k''$, $k' \rightarrow -k'$, and $k'' \rightarrow k$. The last two expressions give the eigenvector components and eigenvalues, and have assumed that the dissipation rate $k_\perp^4 \chi$ is negligible compared to $k_\perp^2 \nu$, given the localization of fluctuation energy to the small wavenumber range $k_\perp^2 \ll 1$.

2.2.3 Models Based on Statistical Closures

The right branch of Fig. 2.1 represents physics associated with the effect of nonlinearity on the temporal evolution of fluctuations. Turbulence, and its representation by nonlinear evolution equations like gyrokinetics or Eqs. (4.8) and (4.9), have random behavior that manifests itself in finite temporal and spatial correlations. Energy transfer between scales, which saturates instabilities, is proportional to the lifetime of the correlation between fluctuations involved in the energy transfer. In the quasilinear approximation the only timescale is the growth rate of the instability. In the situations mentioned in Sec. 2.1 where quasilinear theory fails (i.e., the critical gradient upshift and finite-β nonlinear stabilization) the linear growth rate is not a sufficiently accurate measure of the correlation time associated with nonlinear spectral interactions. Statistical closures provide a representation of these interactions that explicitly treats this correlation time. Closures are therefore well suited for studying model reductions that improve the timescale treatment of spectral transfer relative to quasilinear theory. The exploration of approximations related to the turbulent correlation time has received considerable attention in large Reynolds-number hydrodynamic turbulence. For example, an interaction correlation time based on viscous damping was shown to produce unphysical negative energy excursions despite a treatment of the nonlinearity that preserves energy conservation [32]. It was found that closures based on eddy damping (whose timescale is the inverse eddy turnover time) can remove such excursions, but still produce a spectrum that is too shallow if the sweeping time of the largest eddies dominates the eddy turnover time [33, 34].

In ITG turbulence near the linear critical gradient, aspects of weak turbulence come into play. Weak turbulence is regime where linear timescales legitimately dominate the fluctuation interaction time [35]. A hallmark of such a regime is a correlation time that depends on the mismatch of the three frequencies involved in the triplet interaction dictated by the wavenumber constraint $\mathbf{k} = \mathbf{k}' + (\mathbf{k} - \mathbf{k}')$ intrinsic to quadratic nonlinearities. In this regime the nonlinear timescale (or eddy damping rate) is small for two reasons. First, the eddy damping rate depends on turbulence amplitude, which is small near the instability threshold. Second, the eddy damping rate has one more factor of wavenumber than linear wave frequencies. In systems like ITG turbulence where the long-wavelength instability promptly accesses stable-mode sinks at comparable scales, excitations do not reach the smaller scales where the eddy damping rate starts to dominate. In this regime, the interaction time must involve the frequency mismatch of the three interacting waves [36] and is appropriately called the triplet correlation time [30]. However, when the complex frequencies of the three waves sum to zero, or are close to meeting this resonance condition, the eddy damping must be included in the triplet correlation time [28]. We examine the effect of different representations of the triplet correlation time on ITG turbulence by comparing numerical solutions of Eqs. (4.8) - (4.9) with closure calculations utilizing these representations.

In Fig. 2.1, between the quasilinear approximation and the two branches of the diagram, lies a model labeled *Analytic scaling relations*. This refers to analytic expressions for ITG turbulence levels and the heat flux that were derived in Refs. [30] and [28] from Eqs. (4.8) and (4.9). These relations are based on statistical closure theory, and therefore use either of the models in the right-hand branch of Fig. 2.1. Moreover, because they involve analytic expressions, they approximate the wavenumber sums arising from nonlinearities in a Fourier representation. These approximations generally assume that wavenumber interactions are localized to the long wavelength unstable range, and that wavenumber-dependent quantities can be evaluated at typical wavenumbers in this range. The closure can be applied to equations for the interaction of three waves, as with Eqs. (2.3) - (2.5). Although the three-wave closure equations are not amenable to analytic solution they are readily solved numerically, and are a useful reference point for a discussion of analytical saturation expressions. The closure equations are formulated for quadratic fluctuation correlations and assuming a steady state, are written

$$-\mathrm{Im}\omega_1 \frac{|\beta_1|^2}{|v_z'|^2} = \mathrm{Re}\Big\{ C_{1F2}^{(k,k')} \tau_{2F1} \Big[C_{1F1}^{(k,k')*} \langle \beta_1''^* \beta_2'' \rangle + C_{1F2}^{(k,k')*} |\beta_2''|^2$$

$$+ C_{2F1}^{(k'',-k')}|\beta_1|^2 + C_{2F2}^{(k'',-k')}\langle\beta_1^*\beta_2\rangle\Big]\Big\}, \tag{2.10}$$

$$-\mathrm{Im}\omega_2\frac{|\beta_2|^2}{|v_z'|^2} = \mathrm{Re}\Big\{C_{2F1}^{(k,k')}\tau_{1F2}\Big[C_{2F2}^{(k,k')*}\langle\beta_1''\beta_2''^*\rangle + C_{2F1}^{(k,k')*}|\beta_1''|^2$$

$$+ C_{1F2}^{(k'',-k')}|\beta_2|^2 + C_{1F1}^{(k'',-k')}\langle\beta_1\beta_2^*\rangle\Big]\Big\}, \tag{2.11}$$

$$i(\omega_2 - \omega_2^*)\langle\beta_1^*\beta_2\rangle = \mathrm{Re}\Big\{C_{2F2}^{(k,k')}\tau_{2F1}^*\Big[C_{1F1}^{(k,k')*}\langle\beta_1''^*\beta_2''\rangle + C_{1F2}^{(k,k')*}|\beta_2''|^2$$

$$+ C_{2F1}^{(k'',-k')}|\beta_1|^2 + C_{2F2}^{(k'',-k')}\langle\beta_1^*\beta_2\rangle\Big]\Big\} + \Big\{C_{1F1}^{(k,k')*}\tau_{1F2}^*\Big[C_{2F2}^{(k,k')}\langle\beta_1''^*\beta_2''\rangle$$

$$+C_{2F1}^{(k,k')}|\beta_1''|^2 + C_{1F2}^{(k'',-k')*}|\beta_2|^2 + C_{1F1}^{(k'',-k')*}\langle\beta_1^*\beta_2\rangle\Big]\Big\}, \tag{2.12}$$

$$\nu = \mathrm{Re}\Big\{C_{F12}^{(k',k)}\tau_{2F1}^*\Big[C_{1F1}^{(k,k')}\langle\beta_1''\beta_2''^*\rangle + C_{1F2}^{(k,k')}|\beta_2''|^2 + C_{2F1}^{(k'',-k')*}|\beta_1|^2 + C_{2F2}^{(k'',-k')*}\langle\beta_1^*\beta_2\rangle\Big]\Big\}$$

$$+\mathrm{Re}\Big\{C_{F21}^{(k',k)}\tau_{1F2}^*\Big[C_{2F2}^{(k,k')}\langle\beta_1''^*\beta_2''\rangle + C_{2F1}^{(k,k')}|\beta_1''|^2 + C_{1F2}^{(k'',-k')*}|\beta_2|^2 + C_{1F1}^{(k'',-k')*}\langle\beta_1^*\beta_2\rangle\Big]\Big\}, \tag{2.13}$$

where the triplet correlation time enters explicitly as

$$\tau_{jFm} = \frac{1}{i(\omega_j'' + \omega_1' - \omega_m^*)}, \tag{2.14}$$

and the subscript F indicates that the corresponding wavenumber is zonal, i.e., its y component vanishes. There are three additional equations for $|\beta_1''|^2$, $|\beta_2''|^2$, and $\langle\beta_1''^*\beta_2''\rangle$ that are not written, but can be obtained from Eqs. (2.10) - (2.12) by appropriate transmutation of the wavenumber triad. Equation (2.13) is the zonal flow energy balance. Note that when the two subscripts of τ_{jFm} are not equal (with values 1 and 2), the wavenumber triad $\mathbf{k}$, $\mathbf{k}'$, and $\mathbf{k} - \mathbf{k}'$ is designated as the zonal-flow-catalyzed triad or zonal-flow-catalyzed interaction.

This set of equations represents the minimum wavenumber truncation that conserves energy in the interaction between the unstable and stable modes, and the zonal flow. Because the zonal flow mediates all turbulent couplings, $|v_z'|^2$ drops out of Eq. (2.13). The remaining equations form a linear system for the energies $|\beta_1|^2$, $|\beta_2|^2$,

$\langle\beta_1^*\beta_2\rangle$, $|\beta_1''|^2$, $|\beta_2''|^2$, and $\langle\beta_1''^*\beta_2''\rangle$. With the complex-valued cross correlations written in terms of their real and imaginary parts, the system can be written $\mathbf{MA} = 0$, where $\mathbf{M}$ is the 8×8 matrix whose elements are generated by the couplings of Eqs. (2.10) - (2.12), and $\mathbf{A}$ is the vector whose components are the eight energies. Solving $\mathrm{Det}(\mathbf{M}) = 0$ yields eigenvalues, which specify $|v_z'|^2$ in terms of model parameters via the couplings and the triplet correlation time. Solving for the eigenvector specifies ratios of energies. The zonal-flow energy balance sets an overall energy level through the linear combination of energies in Eq. (2.13).

Equations (2.10) - (2.13) are reduced to the zero-dimensional k-space representation similar to quasilinear theory by assuming that fluctuation levels are comparable at k and k''. The linear system $\mathbf{MA} = 0$ then becomes a 4×4 problem for $|\beta_1|^2$, $|\beta_2|^2$, $\mathrm{Re}\langle\beta_1^*\beta_2\rangle$, and $\mathrm{Im}\langle\beta_1^*\beta_2\rangle$. An example of analytic scaling relations obtained from this procedure is given in Eqs. (46) and (50) of Ref. [30], which express levels the zonal flow and the turbulence,

$$|v_z'|^2 = \frac{4.08\gamma_1}{\mathrm{Re}[\tau_{1F2}]|C_{iFj}|^2}, \tag{2.15}$$

and

$$|\beta_2|^2 = \frac{\nu}{18.32\mathrm{Re}[\tau_{1F2}]|C_{F12}||C_{iFj}|}, \tag{2.16}$$

where γ_1 is the growth rate from Eq. (2.9), and $\chi = 0$ is assumed. The coupling coefficients C_{F12} and C_{iFj} and triplet correlation time are evaluated a typical wavenumber triad in the unstable range. The coupling coefficients and triplet correlation time represent nonlinear effects absent from quasilinear theory, placing this model above quasilinear theory in Fig. 2.1. These expressions set overall levels, as indicated by the numerical coefficients in Eqs (2.15) and (2.16). They also specify scalings with respect to model parameters through the other factors in the expressions. These relations from the 4×4 matrix solution represent the hierarchy level of the box labeled *Analytic scaling relations* in Fig. 2.1.

The 4×4 and 9×9 problems can be expected to have the same scalings only if all combinations of coupling coefficients and triplet correlation time in Eqs. (2.10) - (2.12) have the same scalings as the factor $\mathrm{Re}[\tau_{1F2}]|C_{iFj}|^2$ of Eq. (2.15); and the combinations of Eq. (2.13) have the same scalings as the factor $\mathrm{Re}[\tau_{1F2}]|C_{F12}||C_{iFj}|$ of Eq. (2.16). Arguments to this effect were made in Ref. [30] but have not been verified. If this assertion is shown to be valid it establishes a scaling invariance property across hierarchy levels in wavenumber-space truncations, provided mode coupling interactions are restricted to the zonal-flow catalyzed triplet. There are, of course, many other mode coupling interactions available in the full two-field fluid model of Eqs. (4.8) and (4.9). These are generally referred to as non-zonal interactions and their number is much larger than the number of interactions involving the zonal flow. It has been argued on the basis of observations in gyrokinetics and the fluid model that the non-zonal interactions represent a subdominant saturation channel [37, 16]. If the scalings of Eqs. (2.15) and (2.16) match those of numerical solutions of the full fluid model it demonstrates that the zonal interactions are indeed dominant, not just in energy transfer but in the overall scalings of the saturated state. It also adds additional evidence to a growing list [28] that the role of zonal flows in saturation is not compatible with turbulence suppression by the shear of the zonal flow.

In the next section the scalings of saturation levels with the physical parameters of Eqs. (4.8) and (4.9) will be shown to be the same across the hierarchy, i.e., whether generated from numerical solutions of Eqs. (4.8) and (4.9), Eqs. (2.3) and (2.5), Eqs. (2.10) and (2.13), or evaluation of Eqs (2.15) and (2.16). This confirms that the reduced models intermediate to the two-field fluid model and the quasilinear model produce correct scalings. Consequently they represent physically meaningful improvements to quasilinear theory. This provides confidence that the improvements producing better scalings than quasilinear theory for finite-β nonlinear stabilization and the critical gradient upshift are rooted in essential physics captured in Eqs. (2.15) and (2.16). At different levels of this hierarchy, however, very different results are obtained for fluctuation and transport levels, with better matches to the two-field fluid model obtained as one ascends the hierarchy.

2.3 Tests of Time-Average Behavior

Equations (4.8) and (4.9) are time-dependent turbulent evolution equations that describe the evolution of the ITG instability, and account for sinks of fluctuation energy in the form of nonlinearly excited stable modes and collisional dissipation. If Eqs. (4.8) and (4.9) are multiplied by p_k^* and ϕ_k^*, energy evolution equations are obtained, and rapid wave-phase information is removed. After saturation of the linear instability a steady state is reached in which average energy levels can be obtained from time-independent solutions with $\partial/\partial t \rightarrow 0$. Such time-average behavior is the focus of this chapter.

2.3.1 Three-Wave Interaction

We begin by considering hierarchal models based on the interaction of three turbulent modes with wavevectors $\mathbf{k}$, $\mathbf{k}'$, and $\mathbf{k}-\mathbf{k}'$. This interaction is the minimal truncation of wavenumber space such that energy is conserved in mode coupling and random behavior is possible. Moreover when chosen to be the zonal-flow catalyzed triad, it represents the essential coupling of ITG saturation. We examine fluctuation levels and the scalings with key parameters. Obtaining correct scalings with respect to model parameters is an important target for reduced models. When a scaling is not reproduced in quasilinear theory, physics not included in the linear growth rate and perpendicular fluctuation scale is important. The critical-gradient upshift is an example, where the temperature-gradient dependence of τ_{1F2} and C_{iFj} in Eqs. (2.15) and (2.16) is important. This scaling and its relationship to quasilinear theory have been explored elsewhere [21], as has scaling with respect to plasma β [31]. Here we focus on scalings with the flow damping rate ν. The heat flux scales with ν in gyrokinetic ITG turbulence with collisional flow damping [38]. Moreover, ν affects the resonance of the frequency mismatch in τ, and therefore the critical gradient upshift. We also focus on the turbulence levels, especially the ratios of mode energy levels $|\beta_2|^2/|\beta_1|^2$ and $|\beta_1|^2/|v_z|^2$. These ratios are highly sensitive to saturation physics, and therefore important in assessing how model approximations treat essential physics.

We start with the ν scaling of the primitive three-wave interaction equations, Eqs. (2.3) - (2.5), in comparison with the full two-field fluid model, Eqs. (4.8) and (4.9), as shown in Fig. 2.2. For the three-wave truncation the wavenumbers are $\mathbf{k} = (0.2, 0.2)$ and $\mathbf{k}' = (0.15, 0)$. We observe that for both models the zonal-flow and mode energies have scalings of ν to a positive power. The scaling of the mode energies is stronger than that of the zonal kinetic energy. These scalings are consistent with the analytical scaling relations of the zero-dimensional truncation, Eqs. (2.15) and (2.16), as seen from the following: the triplet correlation time scales as ν^{-1} because the real parts of the frequencies cancel out [16]. The mode energies have an additional factor of ν from the numerator of Eq. (2.16). The zonal kinetic energy has a factor of γ_1 in its numerator, but neither γ_1 nor C_{iFj} have anything other

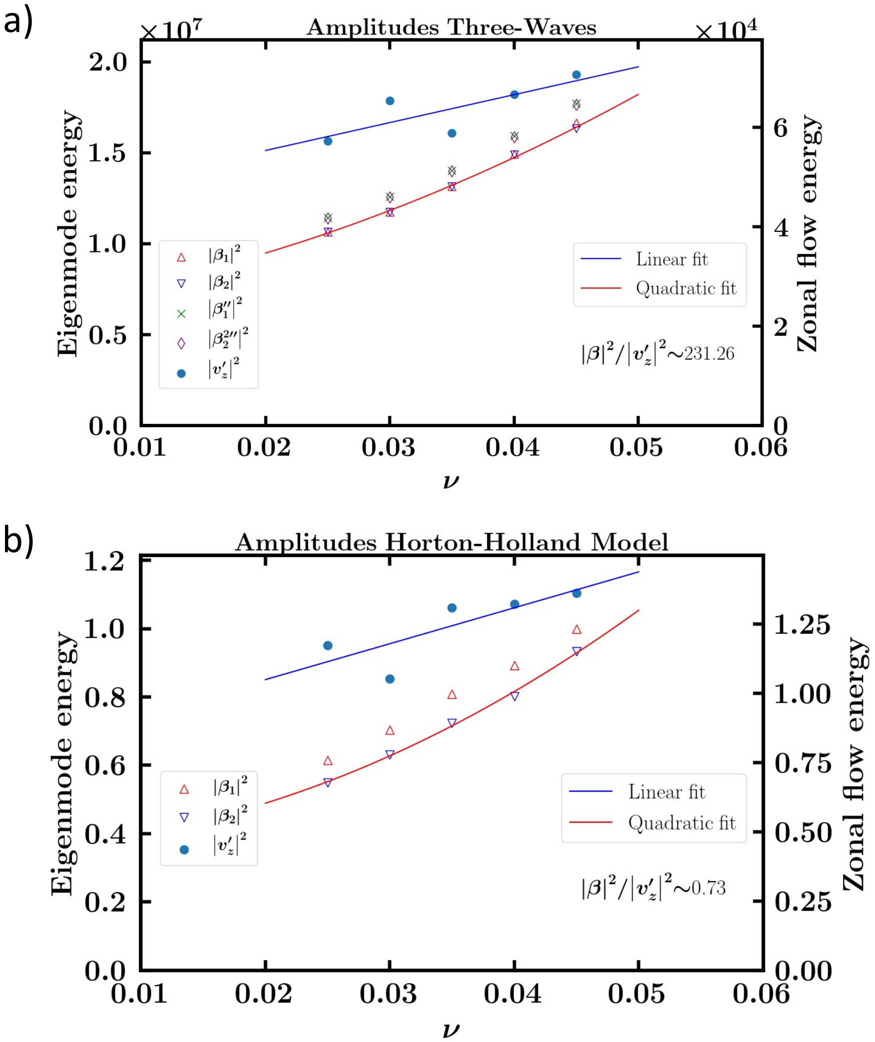

Figure 2.2: Scalings of $|v_z'|^2$, $|\beta_1|^2$, and $|\beta_2|^2$ as a function of ν from a) numerical solutions of the primitive three-wave interaction equations and b) the full two-field fluid model.

than week dependence on ν because they are dominated by the diamagnetic-drift and magnetic frequencies. Consequently $|v_z'|^2$ scales roughly as ν, while $|\beta_1|^2$ and $\beta_2|^2$ scale roughly as ν^2. Fits to linear and quadratic variations are shown in Fig. 2.2, and track the scalings of the numerical solutions for both the full wavenumber space and the three-wave truncation. Note that the three-wave truncation has no zonal pressure evolution, whereas the full system does. The fact that both systems follow the same scaling confirms earlier assertions that the zonal pressure does not affect saturation.

For comparison with the scalings of the primitive models of Fig. 2.2, we show in Fig. 2.3 the scalings of the zero-dimensional model that comes from numerical solution of the 4×4 matrix producing Eqs. (2.15) and (2.16). The matrix is generated from Eqs. (2.10) - (2.13) by evaluating all fields at a common wavenumber $\mathbf{k}$, i.e., $|\beta_1''|^2 \rightarrow |\beta_1|^2$, $|\beta_2''|^2 \rightarrow |\beta_2|^2$, and $\langle \beta_1''^* \beta_2'' \rangle \rightarrow \langle \beta_1^* \beta_2 \rangle$. The coupling coefficients and τ factors are evaluated for a wavenumber triad $\mathbf{k}$, $\mathbf{k}'$, and $\mathbf{k}-\mathbf{k}'$ in the low wavenumber range of instability. This procedure evaluates all coupling coefficients in Eqs. (2.10) - (2.13) and provides more accurate values for the numerical coefficients than those given in Eqs. (2.15) and (2.16). Linear and quadratic behavior are readily apparent, indicating that the same scaling occurs throughout the hierarchy.

In Fig. 2.2 the amplitudes are several orders of magnitude larger in the three-wave solution than in the full fluid model. A clue to this behavior resides in the ratio of mode energy to zonal kinetic energy $|\beta_1|^2/|v_z'|^2$. For the three-wave truncation this ratio is several hundred, while for the full mode coupling representation the ratio is order unity. Because the zonal flow regulates the fluctuation level via the interaction with the stable mode, the much weaker zonal flow of the three-wave truncation leads to proportionately larger fluctuation levels. In Sec. 2.3.2 we will show that a

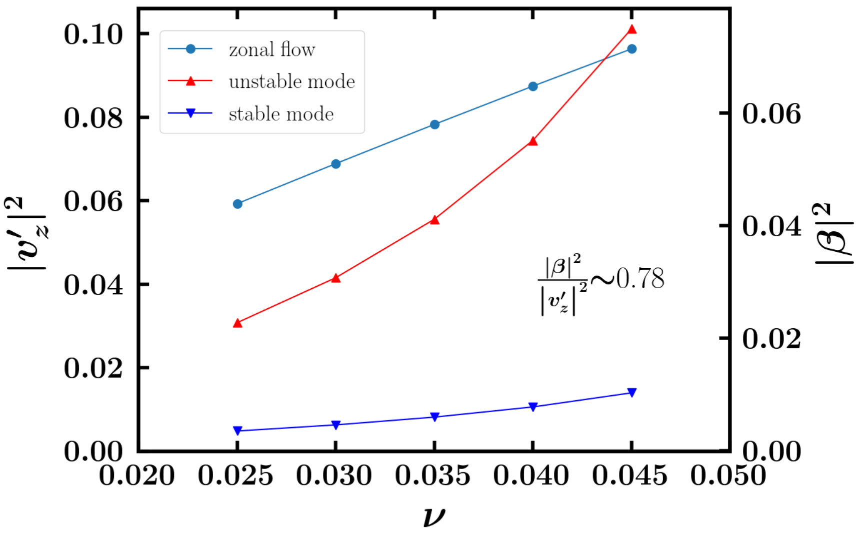

Figure 2.3: Scalings of $|v_z'|^2$, $|\beta_1|^2$, and $|\beta_2|^2$ as a function of ν for the zero-dimensional (single wavenumber) inversion of the energy balance equations from statistical closure theory. This solution is represented by the box labeled *Analytic scaling relations* in Fig. 2.1.

single triplet interaction produces a weaker excitation of the zonal flow than a series of coupled triplet interactions with fluctuations at multiple wavenumbers driving the same zonal flow. Given the intrinsic differences in mode coupling between the three-wave truncation and the full mode-coupling representation, we will first study approximations of turbulent decorrelation in three-wave systems, assessing how well the approximations replicate the numerical solution of the primitive three-wave equations. A separate study will focus on the enlargement of mode coupling interactions relative to the three-wave truncation that enables more accurate modeling of amplitudes.

We now examine reduced models of the three-wave interaction associated with representations of the nonlinear correlation time from statistical closure theory. Closure theory, which is generally portrayed as a procedure for calculating mean quantities in turbulence, performs an important function in model reductions by encoding the temporal correlation properties of the turbulence in a calculable function. Spectral energy transfer is governed by a correlation of fluctuations at three wavenumbers. As such, the triplet correlation time, Eq. (2.14), represents the duration of the turbulent correlation that governs spectral transfer.

We first examine the ν scaling and amplitudes of the three-wave interaction from closure theory, i.e., from Eqs. (2.10) - (2.14) and the related equations for $|\beta_1''|^2$, $|\beta_2''|^2$, and $\langle\beta_1''^*\beta_2''\rangle$. The numerical evaluation solves the 8×8 matrix inversion problem, maintaining energy conservation and the symmetry relationships between coupling coefficients. The results are shown in Fig. 2.4. The scalings with ν closely match $|v_z|^2 \propto \nu$ and $\beta_j|^2 \propto \nu^2$, and are essentially the same as those of Figs. 2.2 and 2.3. The ratio $|\beta_1|^2/|v_z|^2$ has been reduced from its value of ~ 200 for the primitive three-field equations by over three orders of magnitude. While this value is close to that of the primitive fluid equations [Fig. 2.2 b)], that agreement is fortuitous. The benchmark is to Fig. 2.2 a), since this is a three-wave system. The source of this discrepancy lies in the turbulent correlation time, which is represented by the triplet correlation time τ_{jFm} of Eq. (2.14).

Figure 5 shows time histories from the nonlinear evolution of the zonal-flow and mode energies for the primitive three-wave equations [Eqs. (2.3) - (2.5)]. The mode energies have periods of order of 0.1, while the period of the zonal kinetic energy is order unity. However the linear mode frequencies have periods and growth times that are several orders of magnitude larger. For the parameters of Fig. 2.5 the complex frequency of the unstable mode is $\omega_1 = 0.0913 + i0.0779$. This indicates that a triplet correlation time τ_{jlm} constructed from linear frequencies, as in Eq. (2.14), is not a valid approximation for three-wave models based on statistical closure, and that nonlinear frequency corrections must be included. Such corrections are related

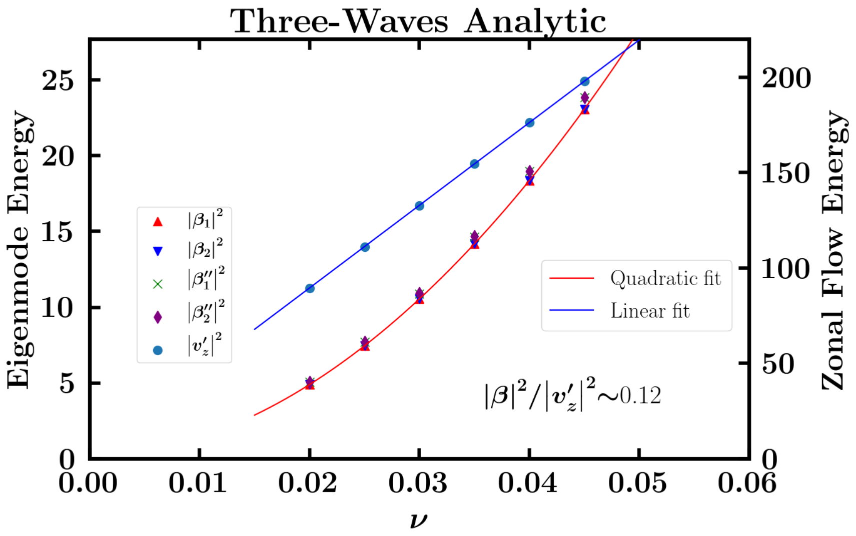

Figure 2.4: Scalings of $|v_z'|^2$, $|\beta_1|^2$, $|\beta_2|^2$, $|\beta_1''|^2$, and $|\beta_2''|^2$ as a function of ν for three interacting waves from inversion of the energy balance equations of statistical closure theory. The triplet correlation time is given by Eq. (2.14) with no eddy-damping contribution.

to the eddy turnover time. In the previous section we argued that eddy damping corrections are not essential for reasonable estimates of the triplet correlation time. However, as born out by simulations, this is true of models with a full wavenumber space, like the full fluid model or even gyrokinetics. In the three-wave system the much larger amplitudes seen in Fig. 2.2 lead to much larger eddy damping rates, and these dominate the triplet correlation time.

We use the Eddy Damped Quasi Normal Markovian closure to calculate the eddy damping rates. The details are not given here but can be found in Ref. [28]. The full nonlinear frequencies of stable and unstable modes with eddy damping corrections are given by $\hat{\omega}_j = \omega_j + \Delta\omega_j$, where $\Delta\omega_j$ are the eddy damping rates given by

$$\Delta\omega_1 = \frac{-iC_{1F2}^{(k)}}{i\hat{\omega}_2'' - i\hat{\omega}_1^* + i\hat{\omega}_1'} \left[C_{2F1}^{(k'')} |v_z'|^2 + C_{F12}^{(k')} |\beta_2''|^2 + C_{F11}^{(k'')} \langle \beta_1''^* \beta_2'' \rangle \right], \tag{2.17}$$

$$\Delta\omega_2 = \frac{-iC_{2F1}^{(k)}}{i\hat{\omega}_1'' - i\hat{\omega}_2^* + i\hat{\omega}_1'} \left[C_{1F2}^{(k'')} |v_z'|^2 + C_{F21}^{(k')} |\beta_1''|^2 + C_{F22}^{(k'')} \langle \beta_1'' \beta_2''^* \rangle \right], \tag{2.18}$$

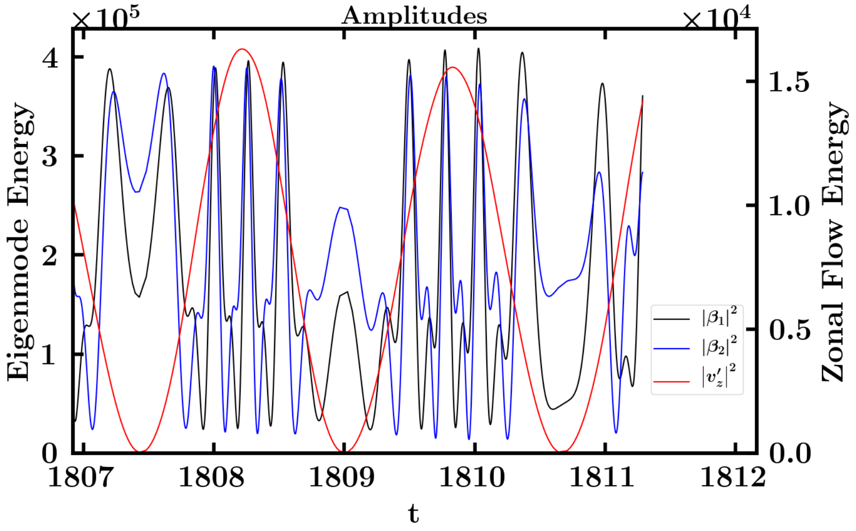

Figure 2.5: Time histories of $|v_z'|^2$, $|\beta_1|^2$, $|\beta_2|^2$, $|\beta_1''|^2$, and $|\beta_2''|^2$ from the primitive three-wave equations, Eqs. (2.3) - (2.5). Timescales for both the mode energies and the zonal kinetic energy are much shorter than linear wave periods.

and $\hat{\omega}_1 = \nu + \Delta\nu$ is the nonlinear zonal-flow damping rate with the eddy contribution given by

$$\Delta\nu = -\frac{C_{F12}^{(k')}}{i\hat{\omega}_2''^* - i\hat{\omega}_1 + i\hat{\omega}_1'^*}\left[C_{2F1}^{(k'')*}|\beta_1|^2 + C_{1F2}^{(k)}|\beta_2''|^2 + C_{2F2}^{(k'')*}\langle\beta_1\beta_2^*\rangle + C_{1F1}^{(k)}\langle\beta_1''\beta_2''^*\rangle\right]$$

$$-\frac{C_{F21}^{(k')}}{i\hat{\omega}_1''^* - i\hat{\omega}_2 + i\hat{\omega}_1'^*}\left[C_{1F2}^{(k'')*}|\beta_2|^2 + C_{2F1}^{(k)}|\beta_1''|^2 + C_{1F1}^{(k'')*}\langle\beta_1^*\beta_2\rangle + C_{2F2}^{(k)}\langle\beta_1''^*\beta_2''\rangle\right]. \quad (2.19)$$

We now repeat the solution of the closed three-wave equations with τ_{jFm} given by $\tau_{jFm} = 1/i(\hat{\omega}_j'' + \hat{\omega}_l' - \hat{\omega}_m^*)$. The results are given in Fig. 2.6. We note that the amplitudes are much larger than their values for the case without nonlinear frequencies in the triplet correlation time [Fig. 2.4], consistent with the larger eddy damping rates. The amplitudes are ~ 1.6 times larger than those of the primitive three-wave solution, while the ratio $|\beta|^2/|v_z'|^2$ is ~ 1.7 times larger. The linear and quadratic scalings of $|v_z'|^2$ and $\beta_j|^2$ with ν are retained. To recap this subsection, we find that solutions of the three-wave system differ from the system with a full

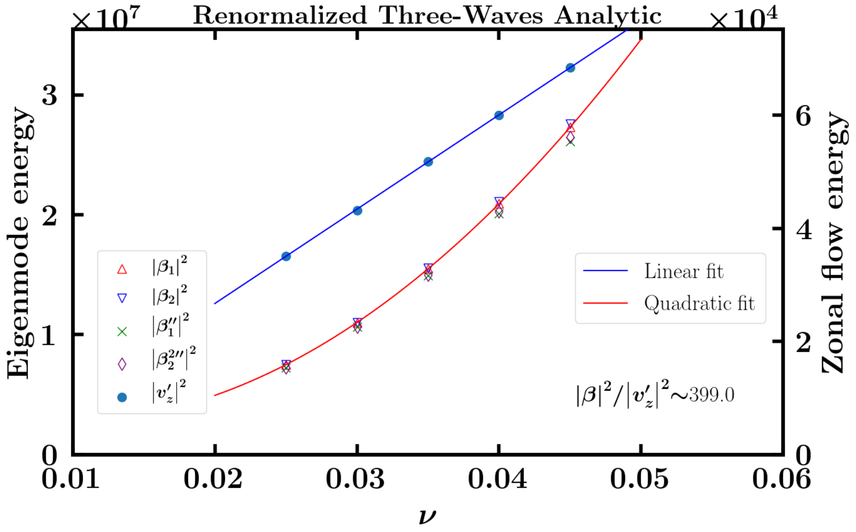

Figure 2.6: Scalings of $|v_z'|^2$, $|\beta_1|^2$, $|\beta_2|^2$, $|\beta_1''|^2$, and $|\beta_2''|^2$ as a function of ν for three interacting waves from inversion of the energy balance equations of statistical closure theory. The triplet correlation time includes nonlinear corrections from Eqs. (2.17) - (2.19).

wavenumber space by having very high amplitudes and correspondingly high eddy damping rates. The closure theory, which can be solved as a linear 8×8 problem, reproduces the ν scaling and the ratio of turbulent energy to zonal kinetic energy if eddy damping corrections are included in the triplet correlation time.

2.3.2 Analytic Scaling Relations

The results of the zero dimensional 4×4 matrix solution that yields the analytic scaling relations of Eqs. (2.15) and (2.16) were briefly presented in Fig. 2.3 of Sec. 2.3.1. We return to this figure to further discuss its content. It was already noted that this model recovers the general scaling of $|v_z'|^2 \sim \nu$ and $|\beta_j|^2 \sim \nu^2$. This is significant, because Eqs. (2.15) and (2.16) have been used to model the critical-gradient upshift in a version of the two-field fluid model with correct threshold physics, and they have motivated modifications to quasilinear theory in gyrokinetic modeling of both the critical-gradient upshift and finite-β nonlinear stabilization. The comparison of the scalings in Fig. 2.3 with the scalings of the other models, but especially the primitive models of Fig. 2.2, provides verification of the models of the hierarchy, including the analytic scaling relations, with respect to scaling behavior.

An interesting feature of Fig. 2.3 concerns the levels of the mode and zonal-flow energies. The values of $|\beta_j|^2$ and $|v_z'|^2$, and the ratio $|\beta_j|^2/|v_z'|^2$ are closer to the results of the full model [Fig. 2.2 a)] than are the energies of Fig. 2.2 b) to those of Fig. 2.2 a). This is despite the fact that the primitive three-wave equations represent a model that is less reduced than the analytical scaling relations. This feature of Fig. 2.3 is an example of fortuitous agreement, a potential aspect of model performance and comparisons that is known to arise, and which verification and validation are intended to uncover [6]. A clue that this is the case is the mode energy ratio $|\beta_2|^2/|\beta_1|^2$. This ratio is very close to unity for every model of the hierarchy except the zero-dimensional model of Fig. 2.3 where the ratio ranges from $\sim$0.12 to $\sim$0.16. Careful analysis of the fluid model shows that

$$\frac{|\beta_2|^2}{|\beta_1|^2} = \frac{\gamma_1}{|\gamma_2|} + (\text{higher order}), \tag{2.20}$$

where *higher order* refers to terms that are very small in a ratio of ν to the mode frequency or growth rate raised to a power considerably larger than unity [28]. This results has also been observed in gyrokinetics [39]. The ratio $\gamma_1/|\gamma_2|$ is close to unity because of near conjugate symmetry for small collisionality. Moreover, there is symmetry in the various coupling coefficients of Eqs. (4.8) and (4.9), which leads to Eq. (2.20), the smallness of the higher order terms, and the fact that that the result does not depend on the nonlinearities.

The symmetries of the coupling coefficients are retained in the three-wave primitive model and produce cancellations and near cancellations of nonlinear terms that lead to the very large amplitudes of Fig. 2.2 a). However, such cancellations are lost in the analytical scaling relations because the coupling coefficients C_{iFj} and C_{ijF} and their interrelationships are replaced by a single factor of $|C_{1F2}|$ in Eqs. (2.15) and (2.16). This reduces the amplitudes but at the same time also violates the symmetries that lead to Eq. (2.20), therefore producing a ratio of $|\beta_2|^2/|\beta_1|^2$ that is no longer close to unity. Consequently the lower amplitudes of Fig. 2.3 are a fortuitous consequence of discarding important information that misleadingly yields better amplitude agreement with a less reduced model. Because $|C_{1F2}|$ has the same scalings as C_{iFj} and C_{ijF}, it is only amplitudes and not scalings that are affected.

2.3.3 Cascade Interactions

We now consider approximations in the wavenumber domain that address the physical origins of the amplitude discrepancy between the solutions of the primitive models for the three-wave interaction and the full fluid-model interaction. We specifically investigate the mode coupling that maintains the zonal flow, noting that if the zonal flow is weaker, turbulence amplitudes become larger. The zonal flow is maintained in stationary turbulence by the zonal-flow-catalyzed interaction. This interaction involves an unstable mode, a stable mode, and the zonal flow, with the coupling occurring through a variety of wavenumber combinations. In gyrokinetics energy transfer is dominated by a single zonal flow $\mathbf{k}' = (-k'_x, 0)$ that couples to a sequence of turbulent modes $\mathbf{k} = (jk'_x, k_y)$, and $\mathbf{k}'' = ((j+1)k'_x, k_y)$ satisfying $\mathbf{k} = \mathbf{k}' + \mathbf{k}''$, where j is an integer. The sequence generates a cascade in harmonics of k'_x. The longest wavelength mode corresponds to $j = 0$, a so-called streamer $\mathbf{k} = (0, k_y)$ that can be thought of as the outer scale of the cascade. Different values of k_y each produce a cascade in k_x. This is not the only energy-transfer channel of the system, but it carries most of the energy. This channel is depicted in Fig. 2.7 a), which shows a sequence of turbulent modes whose position in the vertical direction corresponds to k_y, all coupling with the same zonal flow. The dominance of zonal-flow mediated cascades is evident in Figs. 2 and 3 of Ref. [28]. Given that mode coupling drives the zonal flow, the interactions of a cascade in k_x for a single k_y allows all the modes (jk'_x, k_y) to pump a given zonal flow, resulting in a higher zonal flow level. Moreover, symmetries in a single triplet interaction are broken because a given wavenumber (jk'_x, k_y) interacts with two different triplets, one with $((j+1)k'_x, k_y)$ and one with $((j-1)k'_x, k_y)$ through the zonal flow $\mathbf{k}' = (-k'_x, 0)$ and its complex conjugate $\mathbf{k}' = (k'_x, 0)$, respectively.

The three-wave closure equations, Eqs. (2.10) - (2.13), were solved for a sequence of triplets with $\mathbf{k} = (jk'_x, k_y)$ and $\mathbf{k}' = (\pm k'_x, 0)$ where $0 \leq j \leq 4$. Over this range of k_x, a large fraction (over 95%) of the cascading energy is removed by stable modes, and levels change very little if modes at higher k_x are included. Figure 7 b) shows the wavevectors involved in three of the triplets in this sequence, associated with $j = 0, 1, 2$. For $j_{\max} = 4$ there are five triplet interactions linked through nearest neighbors in $\mathbf{k}$, with 21 real equations. As with Eqs. (2.10) - (2.13) the zonal-flow equation decouples to provide an overall saturation level, with solution of a 20×20 matrix providing the zonal flow and energy ratios. The equations are written in Appendix A.

Figure 8 shows the solution of this system for a scan over ν with $k'_x = 0.2$, $k_y = 0.2$, $\eta = 3$, $\epsilon = 0.1$, and $\chi = 0.01$. The points represent numerical solution of the full fluid model, Eqs. (4.8) and (4.9), with a resolution of 256×128. The solid lines are solutions of the closure equations for the cascade interactions. This numerical evaluation of expressions representing analytical solution of turbulent energy balance

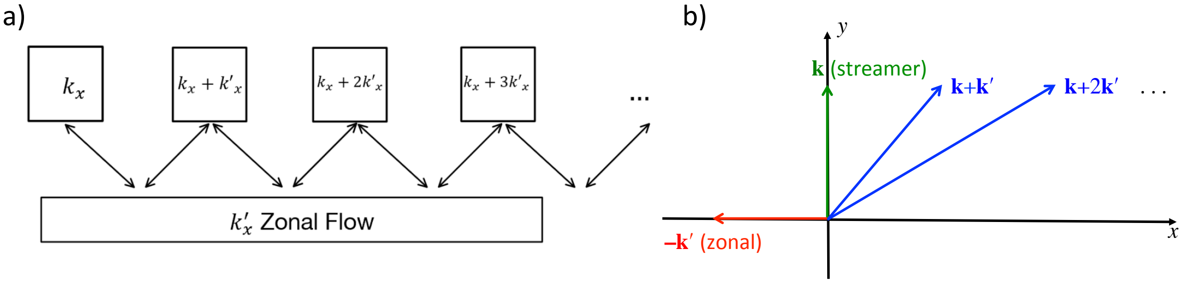

Figure 2.7: Schematics of mode couping in a radial wavenumber cascade mediated by a single zonal flow with wavenumber $-k'_x$.

equations yields amplitudes that are close to those of full fluid model. In the case of the zonal kinetic energy the agreement is better than 25%. For the mode energies the two solutions are identical near $\nu = 0.04$, and differ by at most a factor of 3 at the lowest collisionality. The cascade model is able to produce realistic values for the ratios $|\beta_2|^2/|\beta_1|^2$ and $|\beta_1|^2/|v'_z|^2$. This indicates that the multiple interactions of the cascade are important for setting reasonable levels, through breaking of strong symmetry in the three-wave system at low collisionality, and through a multiplicity of mode coupling for the zonal-flow drive. For the same cascade system, Fig. 2.9 shows a scan in drive strength η for $\nu = 0.03$. It should be noted that the cascade closure model involves the inversion of a matrix with 20 eigenmodes. Most of these roots are unphysical because they produce complex values for quantities that are real, or negative values for quantities that are positive definite. The solution in Figs. 2.8 and 2.9 corresponds to a root that is physical and produces meaningful values relative to the full fluid model.

2.3.4 Qualification Related to Wavenumber Range

Qualification in the context of verification and validation is the *theoretical specification of the expected domain of applicability of a conceptual model and/or approximations*

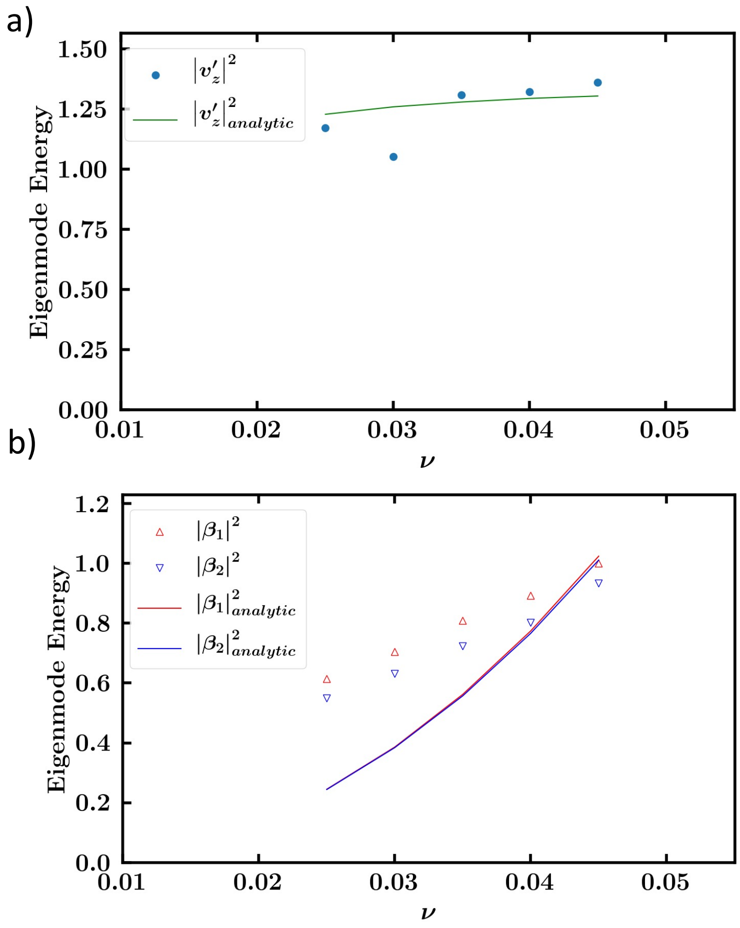

Figure 2.8: Scalings of a) $|v_z'|^2$ and b) $|\beta_1|^2$, $|\beta_2|^2$, $|\beta_1''|^2$, and $|\beta_2''|^2$ as functions of ν, showing comparison between solutions of full fluid model (points) and the cascade closure model (solid traces). For this result $k_x' = 0.2$, $k_x = 0.2$, and $k_y = 0.2$.

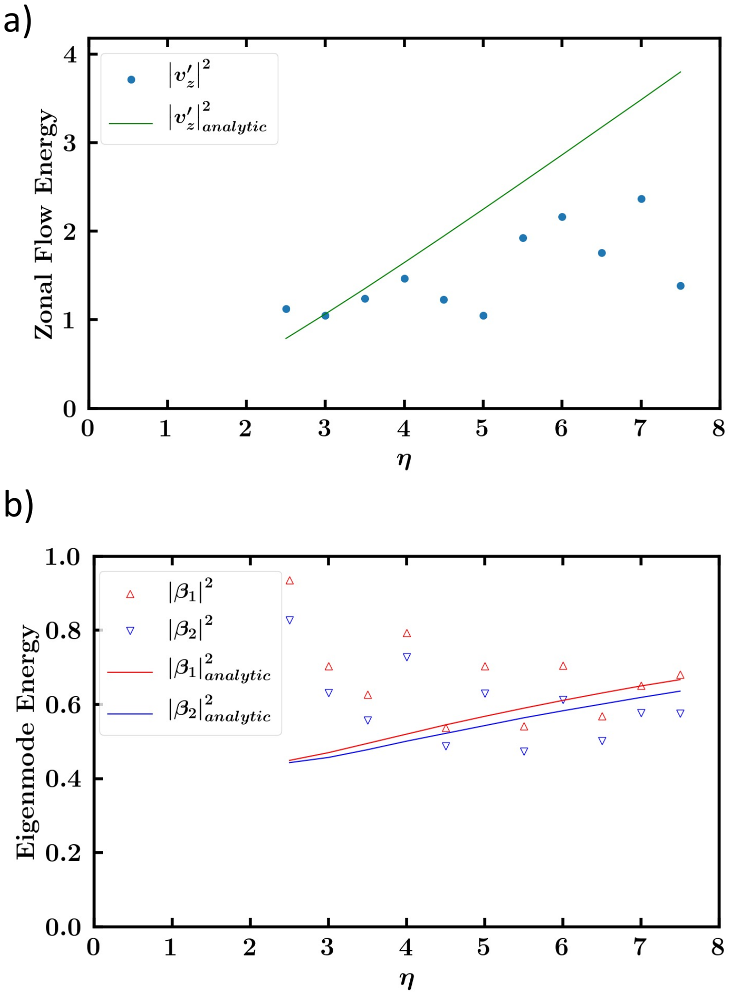

Figure 2.9: Scalings of a) $|v_z'|^2$ and b) $|\beta_1|^2$, $|\beta_2|^2$, $|\beta_1''|^2$, and $|\beta_2''|^2$ as functions of η, showing comparison between solutions of full fluid model (points) and the cascade closure model (solid traces). For this result $k_x' = 0.2$, $k_x = 0.2$, and $k_y = 0.2$.

made in its derivation [6]. Closure theory produces equations that can be more difficult to solve or require more computational resources than primitive equations from which the closure is derived. The closure equations became tractable for the solutions described in Figs. 2.8 and 2.9 because of two key approximations that linearized the energy balance equations of Appendix A and allowed a matrix inversion solution. These approximations do either of two things. First they allow mode coupling to be restricted to the zonal-flow catalyzed interaction, permitting the neglect of the greater number of couplings with non-zonal modes or couplings with two unstable modes. Second, they allow the neglect in Eqs. (A1) - (A4) of terms that involve the product of two mode energies (instead of a mode energy and a zonal kinetic energy). These approximations clearly delineate a domain of applicability, providing qualification of the cascade closure model.

The zonal-flow catalyzed interaction becomes dominant if the combination of triplet correlation time, coupling coefficients, and amplitudes makes its energy transfer rate larger than the rate of other interactions [16]. Because amplitudes are set by the energy balances in accordance with parameter values, we examine how parameter values affect the assumptions relating to coupling coefficients and triplet correlation time. The triplet correlation time establishes a preference for zonal-flow catalyzed interactions when $\tau_{1F2} > \tau_{1F1}$, i.e., when zonal couplings between the unstable and stable mode have a longer triplet correlation time than zonal couplings between two unstable modes. Table 1 shows τ_{1F2} and τ_{1F1} for k_y' ranging from 0.1 to 0.4. At $k_y' = 0.1$ τ_{1F1} is considerably larger than τ_{1F2}, violating an approximation used in obtaining Eqs. (A1) - (A4). This result is consistent with and provides an explanation for the observation in gyrokinetics that the zonal energy transfer rate between unstable modes becomes larger than the zonal energy transfer rate between the unstable and stable modes for $k_x < 0.15$ (see Fig. 2.1 of Ref. [31]). Figure 10 shows the ν scan in the low wavenumber range, where it is seen that the agreement between the solution of the full fluid model and the cascade closure model is not as good as it is at higher k, especially in the level of the zonal kinetic energy.

Equations (A1) - (A4) neglect terms proportional to the product of mode energies by assuming that $C_{Fmn} \ll C_{lFn}$. Because $C_{Fmn} \sim k^3$ and $C_{lFn} \sim k$ this is a good approximation in the low wavenumber instability range, but will break down as

	$k'_y = 0.1$	$k'_y = 0.2$	$k'_y = 0.4$
τ_{1F1}	$-115.9607 - i5.8287$	$-21.1006 - i0.2957$	$-7.9619 - i0.0677$
τ_{1F2}	$33.0177 + i0.0392$	$32.7193 + i0.0756$	$31.7357 + i0.6381$

Table 2.1: Triplet correlations times for the zonal coupling of two unstable modes (τ_{1F1}) and a stable and unstable pair (τ_{1F2}). Triplet correlation times are evaluated at $k'_x = 0.2$, $k_x = 0.2$, and three values of k'_y.

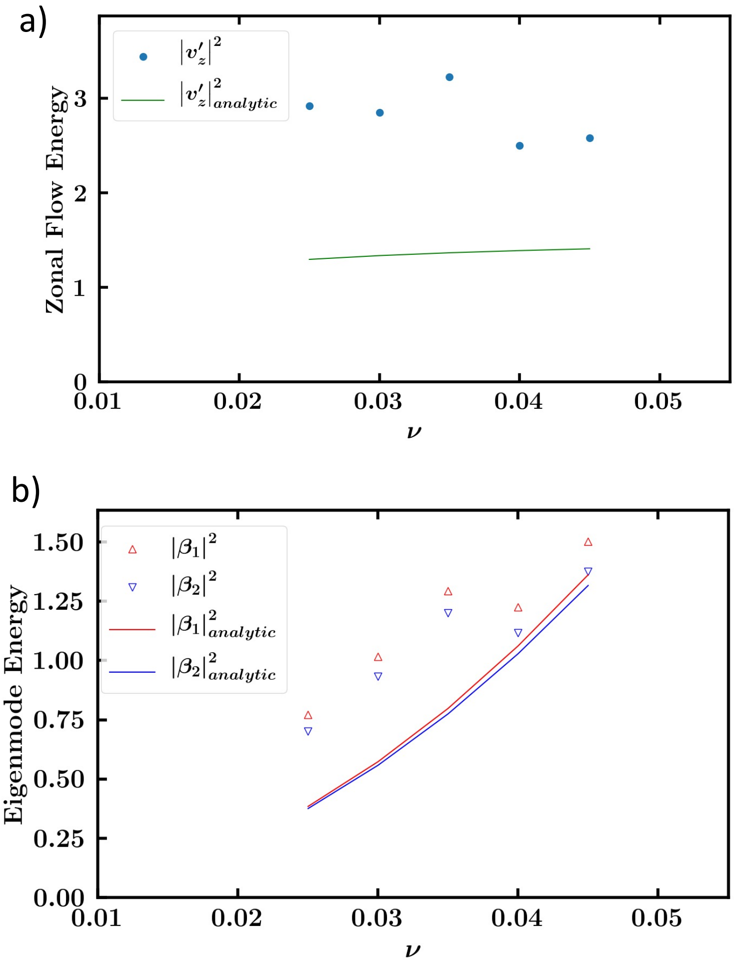

Figure 2.10: Scalings of a) $|v'_z|^2$ and b) $|\beta_1|^2$, $|\beta_2|^2$, $|\beta''_1|^2$, and $|\beta''_2|^2$ as functions of η, showing comparison between solutions of full fluid model (points) and the cascade closure model (solid traces). For this result $k'_x = 0.15$, $k_x = 0.15$, and $k_y = 0.2$.

	$k'_y = 0.1$	$k'_y = 0.2$	$k'_y = 0.4$	$k'_y = 0.8$
C_{1F2}	$-115.9607 - i5.8287$	$-21.1006 - i0.2957$	$-7.9619 - i0.0677$	blah
C_{F12}	$33.0177 + i0.0392$	$32.7193 + i0.0756$	$31.7357 + i0.6381$	blah

Table 2.2: Coupling coefficients for $k'_x = 0.2$, $k_x - 0.2$, and various values of $k'_y = k_y$. Terms retained in Eqs. (A1) - (A4) are proportional to C_{1F2}. The coefficient C_{F12} introduces terms proportional to squares of mode energies.

k approaches unity. Table 2 shows that C_{F12} is no longer smaller than C_{1F2} for $k_y = 0.8$. These results indicate that the cascade closure model is valid only in the wavenumber range $0.2 < k < 0.8$. This is the range of wavenumbers in which stable modes mediate saturation. Energy transfer beyond this range is observed to have little effect on turbulence properties.

2.4 Conclusions

The turbulence saturation physics of ion temperature gradient turbulence has been investigated by use of a model hierarchy that exposes the importance of different physical processes in model fidelity. This study is important because 1) it assesses the means through which zonal-flow catalyzed transfer, the well established saturation mechanism for ITG turbulence, governs turbulence properties, including finite-β nonlinear stabilization and the critical-gradient upshift (Dimits shift); 2) it supports the use of saturation physics based on stable-mode excitation as the basis for optimization of 3D fields in stellarators to reduce turbulent transport [40]; 3) it bolsters the evidence that zonal-flow shearing is not the primary saturation mechanism in ITG turbulence; and 4) it provides an illustration of the use of model hierarchies in verification and validation. The models in this hierarchy include a nonlinear fluid model for toroidal ITG turbulence, models based on reductions of mode-coupling interactions in wavenumber space, models that explicitly treat turbulent decorrelation, and analytic scaling relations. Relationships in performance relative to gyrokinetics and quasilinear theory, as explored elsewhere, frame this work.

The study of model performance across the hierarchy reveals what physical processes affect different aspects of model behavior. It was found that the scaling of turbulence and zonal-flow levels with physical parameters is replicated in models across the hierarchy, including the analytic saturation relations derived from statistical closure theory. The latter form the basis for explanations of finite-β nonlinear stabilization and the critical gradient upshift. Levels of turbulent energy and zonal kinetic energy are sensitive to approximations over the hierarchy. Three-wave truncations, even at the level of primitive equations, miss mode-coupling multiplicities critical in setting levels, and are hypersensitive to symmetries in nonlinear coupling. These effects weaken the zonal-flow drive and produce unrealistically high turbulence levels. The large amplitudes produce a nonlinear decorrelation rate that is much larger than what it is in systems with more appropriate mode coupling multiplicities. Three-wave closure-theory models with eddy damping expressions provide a reasonable match to the ratio of zonal kinetic energy and mode energy in the primitive three-wave system but still fail to replicate overall amplitudes. A minimal mode-coupling representation that reproduces the amplitudes of the full fluid model is achieved by including a finite sampling of the radial wavenumber cascade associated with a single zonal flow. Five radial modes retained in the numerical evaluation of analytic closure balances produces a good match with mode energy and zonal kinetic energy levels.

The hierarchy models based on the zonal-flow catalyzed interaction ignore non zonal interactions, zonal flow mediated interactions of unstable modes with other unstable modes, and interactions with zonal pressure. A qualification exercise shows good fidelity with the full fluid model within a wavenumber band $0.2 < k_y < 0.8$. Below this band zonal-flow mediated interactions between unstable modes are important. Above this band zonal-flow catalyzed interactions involving the polarization drift become important. The latter are readily retained in the saturation balance of closure theory, but they depend on a product of mode energies that makes the balances nonlinear and invalidates the linearized matrix inversion solution that produces expressions like Eqs. (2.15) and (2.16).

This study provides other insights. It shows that quasilinear theory can provide a reasonable model for scaling behavior, but only in situations in which the turbulent correlation time and the nonlinear coupling coefficients between unstable mode, stable mode, and zonal flow do not depend on a scanned parameter. There are ways to modify reduced models like quasilinear theory with linear-physics-based estimates of the nonlinear correlation time and coupling coefficients [31, 28, 22]. In gyrokinetic modeling the nonlinear correlation time in the from of the triplet correlation time has been successfully modeled in a variety of cases. The coupling coefficients can be extracted from linear solutions but require matrix manipulation techniques. Work on this operation will be reported elsewhere. This work shows that fortuitous agreement between reduced models and more complete models can and does occur. A model hierarchy is very useful for detecting this behavior and understanding the physics related to its occurance.

Acknowledgments

This work was supported by U.S. Department of Energy Grant DE-FG02-89ER-53291.

Appendix: Cascade Equations

The equations studied in Sec. 2.3.4 are a sequence of three-wave equations all coupled to a zonal flow at one $|k_x'|$. The interactions involve wavenumbers

$$\mathbf{k} = (jk_x', k_y), \tag{2.21}$$

$$\mathbf{k}' = (k_x', 0) \text{ and } (-k_x', 0), \tag{2.22}$$

$$\mathbf{k} - \mathbf{k}' = ((j \pm 1)k_x', k_y), \tag{2.23}$$

where j is an integer that ranges from $j_{\min} = 0$ to $j_{\max} > 0$, k_x' is a positive number, the $+$ branch of Eq. (23) is for the interaction with the zonal flow at $\mathbf{k}' = (-k_x', 0)$ and the $-$ branch is for interaction with the zonal flow at $\mathbf{k}' = (k_x', 0)$. Each mode $\mathbf{k}$ couples to its nearest neighbors at $j + 1$ and $j - 1$, except the mode at $j_{\max}$, which only couples to $j_{\max} - 1$, and the mode at $j_{\min}$, which only couples to $j_{\min} + 1$. Because $k_x = 0$ is typically the most unstable mode, this sequence of interactions can be thought of as modeling a forward cascade in k_x at one k_y. The energy transfer diagnostic in GENE shows that this is the most prominent energy transfer channel in ITG turbulence.

The equations are

$$\begin{aligned}
-\mathrm{Im}\omega_1(k)|\beta_1(k)|^2 = \mathrm{Re}\Bigg\{ \Bigg[& C_{1F2}^{(k,k')} \Big(i\omega_2(k-k') + \nu - i\omega_1(k)^* \Big)^{-1} |v_z(k')|^2 \\
& \Big[C_{1F1}^{(k,k')*} \langle \beta_1(k-k')^* \beta_2(k-k') \rangle \\
& + C_{1F2}^{(k,k')*} |\beta_2(k-k')|^2 + C_{2F1}^{(k-k',-k')} |\beta_1(k)|^2 + C_{2F2}^{(k-k',-k')} \langle \beta_1(k)^* \beta_2(k) \rangle \Big] \Bigg] (1 - \delta_{j,j_{\min}}) \\
& + \Bigg[k_x' \to -k_x' \Bigg] (1 - \delta_{j,j_{\max}}) \Bigg\},
\end{aligned} \tag{2.24}$$

$$\begin{aligned}
-\mathrm{Im}\omega_2(k)|\beta_2(k)|^2 = \mathrm{Re}\Bigg\{ \Bigg[& C_{2F1}^{(k,k')} \Big(i\omega_1(k-k') + \nu - i\omega_2(k)^* \Big)^{-1} |v_z(k')|^2 \\
& \Big[C_{2F2}^{(k,k')} \langle \beta_1(k-k') \beta_2(k-k')^* \rangle
\end{aligned}$$

$$+C_{2F1}^{(k,k')*}|\beta_1(k-k')|^2 + C_{1F2}^{(k-k',-k')}|\beta_2(k)|^2 + C_{1F1}^{(k-k',-k')}\langle\beta_1(k)\beta_2(k)^*\rangle\Big]\Bigg](1-\delta_{j,j_{\min}})$$

$$+\Bigg[k'_x \to -k'_x\Bigg](1-\delta_{j,j_{\max}})\Bigg\}, \tag{2.25}$$

$$i\Big(\omega_2(k)-\omega_1(k)^*\Big)\langle\beta_1(k)^*\beta_2(k)\rangle = \Bigg\{\Bigg[C_{2F2}^{(k,k')}\Big(i\omega_2(k-k')+\nu-i\omega_1(k)^*\Big)^{-1}|v_z(k')|^2$$

$$\Big[C_{1F1}^{(k,k')*}\langle\beta_1(k-k')^*\beta_2(k-k')\rangle + C_{1F2}^{(k,k')*}|\beta_2(k-k')|^2 + C_{2F1}^{(k-k',-k')}|\beta_1(k)|^2$$

$$+C_{2F2}^{(k-k',-k')}\langle\beta_1(k)^*\beta_2(k)\rangle\Big] + C_{1F1}^{(k,k')*}\Big(-i\omega_1(k-k')^*+\nu+i\omega_2(k)\Big)^{-1}|v_z(k')|^2$$

$$\Big[C_{2F2}^{(k,k')}\langle\beta_1(k-k')^*\beta_2(k-k')\rangle + C_{2F1}^{(k,k')}|\beta_1(k-k')|^2$$

$$+C_{1F2}^{(k-k',-k')}|\beta_2(k)|^2 + C_{1F1}^{(k-k',-k')}\langle\beta_1(k)\beta_2(k)^*\rangle\Big]\Bigg](1-\delta_{j,j_{\min}})$$

$$+\Bigg[k'_x \to -k'_x\Bigg](1-\delta_{j,j_{\max}})\Bigg\}, \tag{2.26}$$

$$\nu = \mathrm{Re}\Bigg\{\sum_{j=j_{\min}+1}^{j_{\max}}\Bigg[C_{F12}^{(k',k)}\Big(-i\omega_2(k-k')^*+\nu+i\omega_1(k)\Big)^{-1}\Big[C_{1F1}^{(k,k')}\langle\beta_1(k-k')\beta_2(k-k')^*\rangle$$

$$+C_{1F2}^{(k,k')}|\beta_2(k-k')|^2 + C_{2F1}^{(k-k',-k')*}|\beta_1(k)|^2 + C_{2F2}^{(k-k',-k')*}\langle\beta_1(k)\beta_2(k)^*\rangle\Big]$$

$$+C_{F21}^{(k',k)}\Big(-i\omega_1(k-k')^*+\nu+i\omega_2(k)\Big)^{-1}\Big[C_{2F2}^{(k,k')}\langle\beta_1(k-k')^*\beta_2(k-k')\rangle$$

$$+C_{2F1}^{(k,k')}|\beta_1(k-k')|^2 + C_{1F2}^{(k-k',-k')*}|\beta_2(k)|^2 + C_{1F1}^{(k-k',-k')*}\langle\beta_1(k)^*\beta_2(k)\rangle\Big]\Bigg]$$

$$+\sum_{j=j_{\min}}^{j_{\max}-1}\Bigg[k'_x \to -k'_x\Bigg]\Bigg\} \tag{2.27}$$

where $k_x \to -k'_x$ in large square brackets signifies that the expression preceding it in large square brackets is repeated with the substitution $k'_x \to -k'_x$. Each of Eqs. (2.24)-(2.26) represent $|j_{\min}| + j_{\max} + 1$ equations for the allowed values of j. If Eq. (2.26) is split into equations for the real and imaginary parts of $\langle\beta_1^*\beta_2\rangle$, there are a total of $4(|j_{\min}| + j_{\max} + 1) + 1$ coupled equations in the system. For Figs. 2.8 and 2.9 $k'_x = 0.2$, $k_y = 0.2$, $j_{\min} = 0$, and $j_{\max} = 4$.

Bibliography

[1] W. Horton, Rev. Mod. Phys. **71**, 735 (1999).

[2] J.D. Callen, Phys. Fluids B **2**, 2896 (1990).

[3] P. Helander, J.H.E. Proll, and G.G. Plunk, Phys. Plasmas **20**, 122505 (2013).

[4] N.T. Howard, C. Holland, A.E. White, M. Greenwald, and J. Candy, Nuclear Fusion **56**, 014004 (2016).

[5] D.R. Hatch, P.W. Terry, F. Jenko, F. Merz, M.J. Pueschel, W.M. Nevins, and E. Wang, Phys. Plasmas **18**, 055706 (2011).

[6] P.W. Terry, M. Greenwald, J.-N. Leboeuf, G.R. McKee, D.R. Mikkelsen, W.M. Nevins, D.E. Newman, and D.P. Stotler, Phys. Plasmas **15**, 062503 (2008).

[7] M. Greenwald, Phys. Plasmas **17**, 058101 (2010).

[8] R.E. Waltz, G.D. Kerbel, and J. Milovich, Phys. Plasmas **1**, 2229 (1994).

[9] C. Bourdelle, X. Garbet, F. Imbeaux, A. Casati, N. Dubuit, R. Guirlet, and T. Parisot., Phys. Plasmas **14**, 112501 (2007).

[10] B. Coppi, M.N. Rosenbluth, and R.Z. Sagdeev, Phys. Fluids **10**, 582 (1967).

[11] A.M. Dimits, G. Bateman, M.A. Beer, B.I. Cohen, W. Dorland, G.W. Hammett, C. Kim, J.E. Kinsey, M. Kotschenreuther, A.H. Kritz, et al., Phys. Plasmas **7**, 969 (2000).

[12] P. Helander, T. Bird, F. Jenko, R. Kleiber, G.G. Plunk, J.H.E. Proll, J. Riemann, and P. Xanthopoulos, Nucl. Fusion **55**, 053030 (2015).

[13] D. Carmody, M.J. Pueschel, J.K. Anderson, and P.W. Terry, Phys. Plasmas **22**, 012504 (2015).

[14] W. Horton, D.-I. Choi, and W.M. Tang, Phys. Fluids **24**, 1077 (1981).

[15] C. Holland, P.H. Diamond, S. Champeaux, E. Kim, O. Gurcan, M.N. Rosenbluth, G.R. Tynan, N. Crocker, W.M. Nevins, and J. Candy, Nuclear Fusion **43**, 761 (2003).

[16] K.D. Makwana, P.W. Terry, and J.-H. Kim, Phys. Plasmas **19**, 062310 (2012).

[17] K.D. Makwana, P.W. Terry, M.J. Pueschel, and D.R. Hatch, Phys. Ref. Lett. **112**, 095002 (2014).

[18] P.W. Terry, D.A. Baver, and S. Gupta, Phys. Plasmas **13**, 022307 (2006).

[19] M.J. Pueschel and F. Jenko, Phys. Plasmas **17**, 062307 (2010).

[20] G.G. Whelan, M.J Pueschel, P.W. Terry, J. Citrin, I.J. McKinney, W. Guttenfelder, and H. Doerk, Phys. Plasmas **26**, 082302 (2019).

[21] P.W. Terry, P.-Y. Li, M.J. Pueschel, and G.G. Whelan, Phys. Rev. Lett. **126**, 025004 (2021).

[22] M.J. Pueschel, P.-Y. Li, and P.W. Terry, Nuclear Fusion **61**, 054003 (2021).

[23] M.A. Beer and G.W. Hammett, Phys. Plasmas **3**, 4046 (1998).

[24] F. Jenko, W. Dorland, M. Kotschenreuther, and B.N. Rogers, Phys. Plasmas **7**, 1904 (2000).

[25] R.D. Sydora, J. Comp. Appl. Math. **109**, 243 (1999).

[26] M.N. Rosenbluth and F.L. Hinton, Phys. Rev. Lett. **80**, 724 (1998).

[27] J. Chowdhury, W. Wan, Y. Chen, S.E. Parker, R.J. Groebner, C. Holland, and N.T. Howard, Phys. Plasmas **21**, 112503 (2014).

[28] P.-Y. Li, P.W. Terry, M.J. Pueschel, and G.G. Whelan, submitted to Phys. Plasmas.

[29] J.A. Krommes, Annu. Rev. Fluid Mech. **44**, 175 (2012).

[30] P.W. Terry, B.J. Faber, C.C. Hegna, V.V. Mirnov, M.J. Pueschel, and G.G. Whelan, Phys. Plasmas **25**, 012308 (2018).

[31] G.G. Whelan, M.J. Pueschel, and P.W. Terry, Phys. Rev. Lett. **120**, 175002 (2018).

[32] S.A. Orszag, J. Fluid Mech. **41**, 363 (1970).

[33] R.H. Kraichnan, J. Fluid Mech. **5**, 497 (1959).

[34] R.H. Kraichnan, J. Fluid Mech. **88**, 355 (1978).

[35] R.Z. Sagdeev and A.A. Galeev, *Nonlinear Plasma Theory*, (Benjamin, New York, 1969).

[36] D.A. Baver, P.W. Terry, R. Gatto, and E. Fernandez, Phys. Plasmas **9**, 3318 (2002).

[37] D.R. Hatch, M.J. Pueschel, F. Jenko, W.M. Nevins, P.W. Terry, and H. Doerk, Phys. Plasmas **20**, 0112307 (2013).

[38] Z. Lin, T.S. Hahm, W.W. Lee, W.M. Tang, and P.H. Diamond, Phys. Rev. Lett. **83**, 3645 (1999).

[39] P.W. Terry, K.D. Makwana, M.J. Pueschel, D.R. Hatch, F. Jenko, and F. Merz, Phys. Plasmas **21**, 122303 (2014).

[40] C.C. Hegna, P.W. Terry, and B.J. Faber, Phys. Plasmas **25**, 022511 (2018).

Chapter 3

Mode Oscillations Under Zonal-Flow-Catalyzed Interactions and ITG Predator-Prey Model Building

In this chapter, the wavenumber truncation of the fluid model is also checked with time-dependent simulations. These augment and complement the time-independent behavior examined in chapter 2. A two-predator-prey model is built based on the saturation formula discussed in chapter 2 in order to avoid heuristic derivations with a number of free parameters which characterize predator-prey models typically found in the literature.

3.1 Introduction

Zonal flows are known to exist in various fluid systems such as planetary atmospheres and fusion devices. When zonal flows are prominent, there is often turbulence suppression in these self-regulated systems. For example, strong $E \times B$ mean flow and zonal flow are known to be present in the plasma edge in the high confinement regime (H-mode) of toroidal fusion devices, in contrast to the low confinement regime (L-mode)[6, 7]. While zonal flows are involved in various mechanisms that suppress turbulence, the shearing machnism that delivers energy from large scale turbulence to the small scale regime is the most familiar[3]. However, numerous results from gyrokinetic and fluid simulations have shown that zonal-flow-catalyzed nonlinear energy transfer to stable modes plays the most important role in turbulence saturation for curvature-driven ion temperature gradient (ITG) turbulence[24, 5]. This process has been overlooked in most theories. The saturation theory based on the zonal-flow-catalyzed nonlinear energy transfer that couples the large scale unstable and stable modes as the major energy transfer channel is shown to reproce the essentail features of the curvature-driven ITG heat flux observed in simulations. Therefore, theories and models that have the presence of strong zonal flows should carefully account for this mechanism before reaching any conclusion.

On the other hand, it was also discovered in L-H transition experiments that the $E \times B$ mean flow and zonal flow oscillates undergo limit-cycle with drift wave turbulence. Such oscillations can often be modeled with predator-prey like dynamics[6, 7]. Models built for such limit-cycle oscillations primarily treat the zonal flow as predator and the drift wave turbulence as prey, suggesting that the zonal flow is a major energy sink. Again, the effect of the large scale stable modes and zonal-flow-catalyzed nonlinear energy transfer is neglected in these models[5, 2, 4]. Moreover, because those models are built with simple variables with several free parameters to fit different systems, a quantitative connection to first principles is lacking. Therefore, we seek a way to derive a predator-prey model, starting from a fluid model that is simplified from a more complicated model, and involves large-scale stable modes. Only a model constructed in this fashion will have dynamical behavior that is consistent with the dominant energy transfer between unstable modes, stable models, and the zonal flow.

In this chapter, we first introduce in Sec. 3.2 a truncated model that is derived from a more complete fluid model after transformation to the eigenmode decomposition. The time dependent behavior of the zonal flow under the truncated model will be discussed in Sec. 3.3. A predator-prey model built on the saturation theory, the simple fluid model, and the observations from Sec. 3.3 will be introduced in Sec. 3.4. Section 3.5 provides concluding remarks.

3.2 Three-Wave Truncation of toroidal fluid Model

The predator-prey model we will introduce is based on a wavenumber space truncation of a simple fluid model for toroidal ITG trubulence first derived in Ref. [1] and later modified in Ref. [12]. This model has stable modes as important energysinks and zonal flows as crucial nonlinear interaction catalysts[13, 14]. The model describes a set of coupled evolution equations for ion pressure and vorticity with adiabatic electrons,

$$\frac{\partial p_k}{\partial t} + ik_y(1+\eta)\phi_k + \chi k_\perp^4 p_k = -\sum_{k'}(k' \times \hat{z} \cdot k)\phi_{k'} p_{k-k'} \tag{3.1}$$

$$\left[\delta(k_y) + k_\perp^2\right] \frac{\partial \phi_k}{\partial t} + ik_y\phi_k - ik_y\epsilon p_k + \nu k_\perp^2 \phi_k = -\frac{1}{2}\sum_{k'}(k' \times \hat{z} \cdot k)[(k-k')_\perp^2 - k_\perp'^2]\phi_{k'}\phi_{k-k'} \tag{3.2}$$

where $\mathbf{k} = (k_x, k_y)$, p_k and ϕ_k are Fourier amplitudes of pressure and electrostatic potential, $\delta(k_y)$ is the adiabatic electron response with $\delta = 1$ if $k_y \neq 0$ and $\delta = 0$ if $k_y = 0$, ν and χ are coefficients for collisional dissipation, $\eta = L_n/L_{T_\mathrm{i}}$ is the ratio of density and ion temperature gradient scale lengths, $\epsilon = L_n/R$ is a magnetic curvature parameter, and R is the major radius.

To account for energy injection and loss from fluctuations in the system, it is convenient to express the model in terms of the linear eigenmodes. The eigenvalues, or the eigenmode frequencies, of the linear operators can be expressed as

$$\begin{cases} \omega_{1,2} = -\frac{i}{2}\left(\chi k_\perp^4 + \frac{\nu k_\perp^2 + ik_y}{\delta + k_\perp^2}\right) \pm \frac{i}{2}\left\{\left(\chi k_\perp^4 - \frac{\nu k_\perp^2 + ik_y}{\delta + k_\perp^2}\right)^2 + \frac{4(1+\eta)k_y^2\epsilon}{\delta + k_\perp^2}\right\}^{1/2} & ,\ k_y \neq 0 \\ \omega_1 = -i\nu,\ \omega_2 = -i\chi k_x^4 & ,\ k_y = 0 \end{cases} . \tag{3.3}$$

where 1 and 2 corresponds to plus and minus sign, respectively. The fields p_k and ϕ_k can also be expressed in terms of eigenvectors

$$\begin{pmatrix} p_k \\ \phi_k \end{pmatrix} = \beta_1(k)\begin{pmatrix} R_1(k) \\ 1 \end{pmatrix} + \beta_2(k)\begin{pmatrix} R_2(k) \\ 1 \end{pmatrix} , \tag{3.4}$$

where $R_{1,2}(k) = \frac{\omega_{1,2}(1+k_\perp^2) - k_y + i\nu k_\perp^2}{k_y \epsilon}$ and $\beta_{1,2}(k)$ are eigenmode amplitudes. For the remainder of this chapter we will drop the $\chi k_\perp^4$ and keep the $\nu k_\perp^2$ for the case with $k_\perp^2 \ll 1$. If we express the nonlinear interactions in terms of the linear eigenmodes, the nonlinear equations for the eigenmodes will become

$$\begin{aligned} \dot{\beta}_l + i\omega_l\beta_l = \sum_{k', k'_y \neq 0, k_y} C_{lmn}^{(k,k')}\beta'_m\beta''_n + \sum_{k'_x}\Bigg\{\left[C_{lFn}^{(k,k')}v'_z\beta''_n + C_{lPn}^{(k,k')}p'_z\beta''_n\right]\Bigg|_{k'_y=0} \\ + \left[C_{lmF}^{(k,k')}\beta'_m v''_z + C_{lmP}^{(k,k')}\beta'_m p''_z\right]\Bigg|_{k'_y=k_y}\Bigg\} , \end{aligned} \tag{3.5}$$

$$\dot{v}_z + \nu v_z = \sum_{k'} C_{Fmn}^{(k,k')}\beta'_m\beta''_n\,\Big|_{k_y=0} , \tag{3.6}$$

$$\dot{p}_z + \chi k_x^2 p_z = \sum_{k'} C_{Pmn}^{(k,k')}\beta'_m\beta''_n\,\Big|_{k_y=0} , \tag{3.7}$$

where l, m and n are either 1 or 2. $v_z = ik\phi_{k_y=0}$ and p_z are zonal flow and zonal pressure at $k_y = 0$ respectively, $\beta_l = \beta(k)\,\big|_{k_y\neq 0}$, $\beta'_l = \beta_l(k')$, $\beta''_l = \beta_l(k'' = k - k')$, and C_{lmn}, C_{lFn}, C_{Fmn}, C_{lmF}, C_{lPn}, C_{Pmn}, and C_{lmP} are coupling coefficients where F and P denote coupling to zonal flow and zonal pressure respectively.

In order to build a predator-prey model based on the fluid model, we first truncate the fluid model into a simpler set of equations which contain an energy source, energy sink and the zonal flow. The model which has the most severe wavenumber truncation based on the two-field fluid model that has explicitly coupled wavenumbers with conserved energy transfer is the three-wave model. The three-wave model includes two pairs of eigenmodes $\beta_{1,2}(k)$ and $\beta_{1,2}(k''=k-k')$ and a zonal flow $v_z'=v_z(k')$ that couples the eigenmodes. The energy transfer catalyzed by zonal pressure is much weaker than that catalyzed by the zonal flow, and therefore the zonal pressure is largely decoupled from the system and can be dropped from the equations. The truncated model can be expressed as

$$\left\{\begin{array}{r}
\dot{\beta}_1+i\omega_1\beta_1=C^{(k,k')}_{1F1}v_z'\beta_1''+C^{(k,k')}_{1F2}v_z'\beta_2'' \\
\dot{\beta}_2+i\omega_2\beta_2=C^{(k,k')}_{2F1}v_z'\beta_1''+C^{(k,k')}_{2F2}v_z'\beta_2'' \\
\dot{\beta}_1''+i\omega_1''\beta_1''=C^{(k'',-k')}_{1F1}v_z'^{*}\beta_1+C^{(k'',-k')}_{1F2}v_z'^{*}\beta_2 \\
\dot{\beta}_2''+i\omega_2''\beta_2''=C^{(k'',-k')}_{2F1}v_z'^{*}\beta_1+C^{(k'',-k')}_{2F2}v_z'^{*}\beta_2 \\
\dot{v}_z'+\nu v_z'=C^{(k',k)}_{F11}\beta_1\beta_1''^{*}+C^{(k',k)}_{F12}\beta_1\beta_2''^{*}+C^{(k',k)}_{F21}\beta_2\beta_1''^{*}+C^{(k',k)}_{F22}\beta_2\beta_2''^{*}
\end{array}\right. , \tag{3.8}$$

where

$$C^{(k,k')}_{lFn}=\frac{(-1)^{l-1}}{R_1(k)-R_2(k)}\frac{-ik_y}{2}\left[R_m(k')-R_n(k'')+\frac{R_{3-l}(k)[k_\perp''^2-k_\perp'^2]}{1+k_\perp^2}\right] , \tag{3.9}$$

and

$$C^{(k',k)}_{Fmn}=\frac{ik_y(k^2-k''^2)}{2} . \tag{3.10}$$

$C^{(k'',-k')}_{lFn}$ can be calculated from Eq. 3.9 by replacing k with k'' and k' with $-k'$. According to Eq. 3.10, the evolution equation for v_z can be simplified to

$$\dot{v}_z'+\nu v_z'=C^{(k',k)}_{F11}\left(\beta_1+\beta_2\right)\left(\beta_1''^{*}+\beta_2''^{*}\right) . \tag{3.11}$$

3.3 Role of the Zonal Flow in Three-Wave Interaction

The role of zonal flows is usually assumed only to involve shear suppression of the turbulence, which enhances energy transfer from large scale to dissipative small scales. However, mounting evidence has shown that in some cases zonal flows can

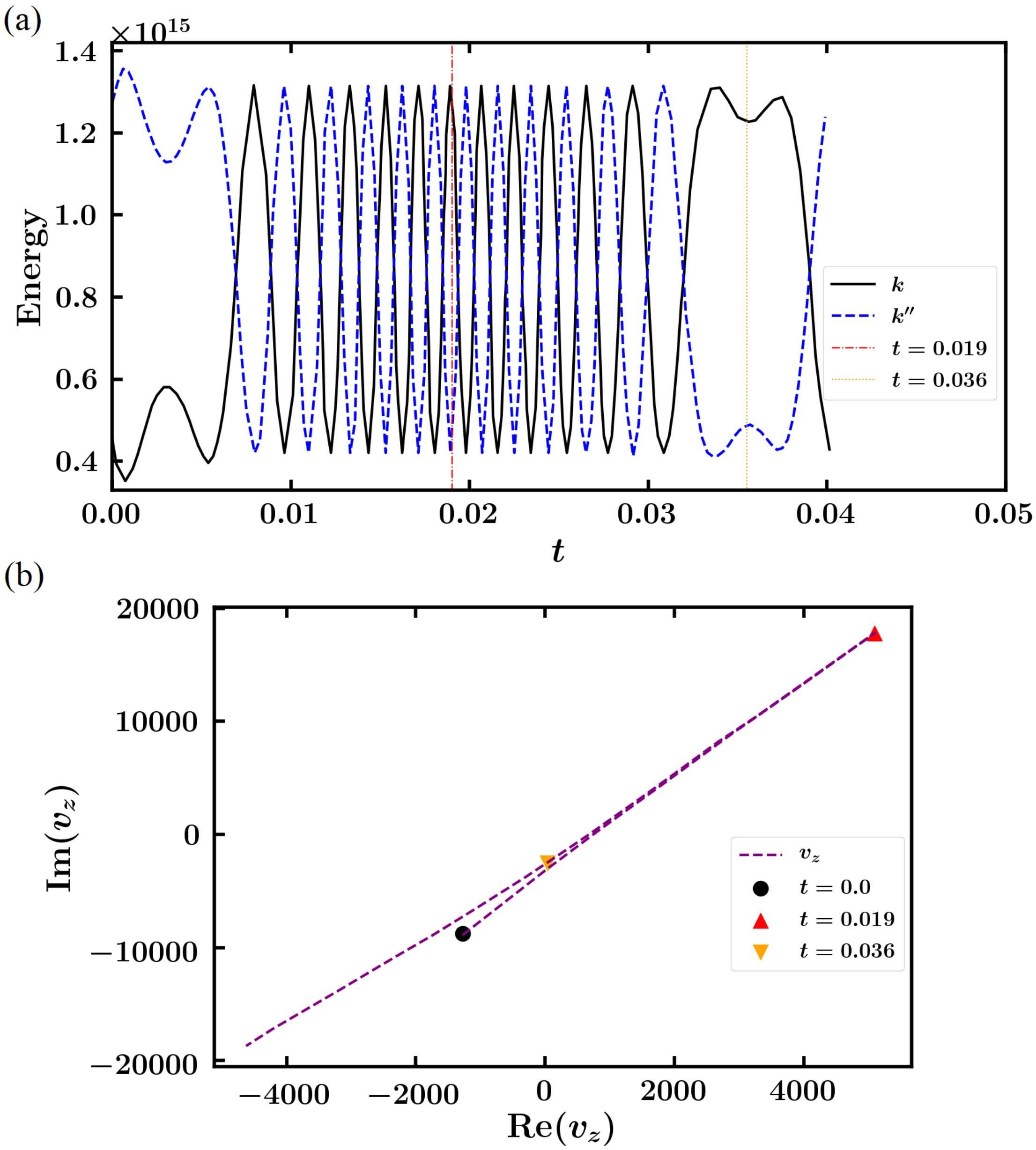

Figure 3.1: (a) The energy goes back and forth between the eigenmodes of k and k''. (b) Strong zonal flow leads to large energy exchange rate between modes and fast mode oscillations. Weak zonal flow leads small energy exchange rate and staggering mode oscillations.

act more like catalysts that help transfer the energy from sources to sinks at large scale. This evidence has been gleaned from gyrokinetics toroidal ITG turbulence[5] and numerical solutions of the toroidal fluid model[13, 14, 30, 24]. The zonal flow in the three-wave truncation of the fluid model also shows such behavior, which we will see in the following paragraphs.

We have performed numerical solutions of the three-wave model with the parameters $k = (0.05, 0.1)$, $k' = (0.075, 0)$, $\nu = 0.035$, $\eta = 5$, $\epsilon = 0.1$. Figure 3.1(a) shows the oscillations of the eigenmode energies at k and k'' when the turbulence is saturated, and Figure 3.1(b) shows the time trace of the zonal flow v_z in the complex plane. The system shows extremely fast energy oscillation between different wavenumbers. The time scale is ~ 0.001 or the frequency is ~ 1000 equivalently. The observed frequency is much larger than the eigenmodes linear frequencies which are typically ~ 0.1. This suggests the the oscillations are not governed by the linear physics, instead, extremely high saturation levels lead to dominating nonlinear effects and frequencies. The high saturation levels can be explained by the high degree of symmetry in the coefficients that govern coupling strength between the stable, and unstable modes at different wavenumbers. The dynamics of the zonal flow is described by Eqs. 3.8, 3.9, and 3.11. If we take the time derivative of Eq. 3.11, we get

$$\ddot{v}'_z + \nu \dot{v}'_z = C_{F11}^{(k',k)} \left[(\beta_1 + \beta_2) \left(\dot{\beta}_1''^* + \dot{\beta}_2''^* \right) + \left(\dot{\beta}_1 + \dot{\beta}_2 \right) (\beta_1''^* + \beta_2''^*) \right] . \tag{3.12}$$

$\left(\dot{\beta}_1 + \dot{\beta}_2 \right)$ and $\left(\dot{\beta}_1''^* + \dot{\beta}_2''^* \right)$ can be derived from Eq. 3.8 by summing over the evolution equations,

$$\begin{array}{c} (\dot{\beta}_1 + \dot{\beta}_2) = -(i\omega_1\beta_1 + i\omega_2\beta_2) + (C_{1F1}^{(k,k')} + C_{2F1}^{(k,k')}) v'_z \beta_1'' \\ +(C_{1F2}^{(k,k')} + C_{2F2}^{(k,k')}) v'_z \beta_2'' \\ (\dot{\beta}_1'' + \dot{\beta}_2'') = -(i\omega_1''\beta_1'' + i\omega_2''\beta_2'') + (C_{1F1}^{(k'',-k')} + C_{2F1}^{(k'',-k')}) v_z'^* \beta_1 \\ +(C_{1F2}^{(k'',-k')} + C_{2F2}^{(k'',-k')}) v_z'^* \beta_2 \end{array} . \tag{3.13}$$

From Eq. 3.9, the combined coupling coefficients can be further simplified as follows,

$$C^{(k,k')}_{1F1} + C^{(k,k')}_{2F1} = C^{(k,k')}_{1F2} + C^{(k,k')}_{2F2} = \frac{-ik_y}{2(1+k_\perp^2)}(k''^2_\perp - k'^2_\perp) = D^k \tag{3.14}$$

$$C^{(k'',-k')}_{1F1} + C^{(k'',-k')}_{2F1} = C^{(k'',-k')}_{1F2} + C^{(k'',-k')}_{2F2} = \frac{-ik''_y}{2(1+k''^2_\perp)}(k^2_\perp - k'^2_\perp) = D^{k''}\ . \tag{3.15}$$

The nonlinearities contributed by the pressure cancel out while the ones from vorticity add, which indicates that the pressure nonlinearity does not deliver energy to the zonal flow but from the unstable mode to the stable mode. The vorticity nonlinearity delivers energy from both the stable and unstbale modes to the zonal flow. Therefore, by using Eq. 3.15, Eq. 3.13 can be rewritten as

$$\begin{aligned} (\dot{\beta}_1 + \dot{\beta}_2) &= -(i\omega_1\beta_1 + i\omega_2\beta_2) + D^k v'_z(\beta''_1 + \beta''_2) \\ (\dot{\beta}''_1 + \dot{\beta}''_2) &= -(i\omega''_1\beta''_1 + i\omega''_2\beta''_2) + D^{k''} v'^*_z(\beta_1 + \beta_2) \end{aligned} \tag{3.16}$$

By inserting Eq. 3.16 into Eq. 3.12, we obtain

$$\begin{aligned} \ddot{v}'_z + \nu\dot{v}'_z =& C^{(k',k)}_{F11}\big[(i\omega''^*_1\beta''^*_1 + i\omega''^*_2\beta''^*_2)(\beta_1 + \beta_2) - (i\omega_1\beta_1 + i\omega_2\beta_2)(\beta''^*_1 + \beta''^*_2) \\ &+ v'_z(D^k|\beta''_1 + \beta''_2|^2 + D^{k''*}|\beta_1 + \beta_2|^2)\big] \end{aligned} . \tag{3.17}$$

As in other studies [21, 28, 30], we introduce an ordering parameters for small wavenumber and collisional damping, defining $k \sim \hat{\epsilon}^2$ and $\nu \sim k \sim \hat{\epsilon}^2$. Under this ordering, $\omega^*_2 - \omega_1 \sim \omega''^*_2 - \omega''_1 \sim \omega''^*_2 - \omega_1 \sim \omega''^*_1 - \omega_2 \sim \mathcal{O}(\hat{\epsilon}^6)$. The $(i\omega''^*_1\beta''^*_1 + i\omega''^*_2\beta''^*_2)(\beta_1 + \beta_2) - (i\omega_1\beta_1 + i\omega_2\beta_2)(\beta''^*_1 + \beta''^*_2)$ term can be rewritten as $i(\omega''^*_1 - \omega_1)\beta_1\beta''^*_1 + i(\omega''^*_2 - \omega_1)\beta_1\beta''^*_2 + i(\omega''^*_1 - \omega_2)\beta_2\beta''^*_1 + i(\omega''^*_2 - \omega_2)\beta_2\beta''^*_2$, from which we see that it is nearly zero due to the symmetry between the eigenmodes. Therefore, the term $v'_z(D^k|\beta''_1 + \beta''_2|^2 + D^{k''*}|\beta_1 + \beta_2|^2)$ dominates the right hand side of Eq. 3.17. When the turbulence is saturated, i.e., when $|\beta''_1 + \beta''_2|^2$ and $|\beta_1 + \beta_2|^2$ are quasi-stationary, and we are in a regime where the nonlinearities of the zonal-flow evolution equation dominate linear damping, Eq. 3.17 becomes a damped harmonic oscillator. This is because D^k, $D^{k''}$ and $C^{(k',k)}_{F11}$ are pure imaginary and $(D^k + D^{k''*})C^{(k',k)}_{F11} < 0$.

This explains why the zonal flow almost goes in a straight line and returns when it is away from the origin in Fig. 3.1(b). As for Fig. 3.1(a), the energy level of the zonal flow is much lower than the eigenmodes, which gives it a much longer oscillation period. Consequently, the zonal flow acts as an intermediary between the eigenmodes rather than an energy sink and predator. Energy then oscillates between the eigenmodes at wavenumbers k and k'', with a phase shift of 180°. Another observation from Fig. 3.1(a) is that the oscillation frequencies of the eigenmode energies depend on the magnitude of the zonal flow. At $t = 0.019$, when the zonal flow magnitude reaches its maximum, the oscillations of the eigenmode energies are also most rapid. On the contrary, when the zonal flow passes through the point near the origin at $t = 0.036$, the energy exchange stagnates. This also indicates that frequencies depend on the magnitude of the nonlinearities.

Figure 3.2 shows time traces of all the eigenmodes and the zonal flow on the complex plane. The eigenmodes circulate in near-closed loops with fixed phases between them. The phase between these eigenmodes can also be calculated from the from Eqs. 3.8, 3.9, and 3.11. The difference between the $C_{1Fn}^{(k,k')}$ and $-C_{2Fn}^{(k,k')}$ is of order $\nu k_\perp^2$ which is $\hat{\epsilon}^6$ smaller than $C_{lFn} \sim k \sim \hat{\epsilon}^2$, therefore, the right hand side of the evolution equations of the stable and unstable modes are almost identical but with a minus sign difference. In the regime where the nonlinearities dominate, the phase between β_1 and β_2 will therefore be π. On the other hand, the difference between $C_{1Fn}^{(k,k')}$ and $C_{1Fn}^{(k'',-k')}$ is also $\mathcal{O}(\hat{\epsilon}^4)$, which is much smaller than $C_{lFn} \sim k \sim \hat{\epsilon}^2$. The evolution equations for k and k'' are basically the same but with $v'_z \to v'^*_z$. If we let $\beta_1 = \beta_1''^* e^{i\theta}$, $\beta_2 = \beta_2''^* e^{i\theta}$ (phase locked between β_1 and β_2, so the phase difference between β_2 and $\beta_2''^*$ is also θ), and $v'_z = |v'_z|e^{i\phi}$, and insert these relations into Eq. 3.8, we can obtain that the only solution with phase locking between β_1

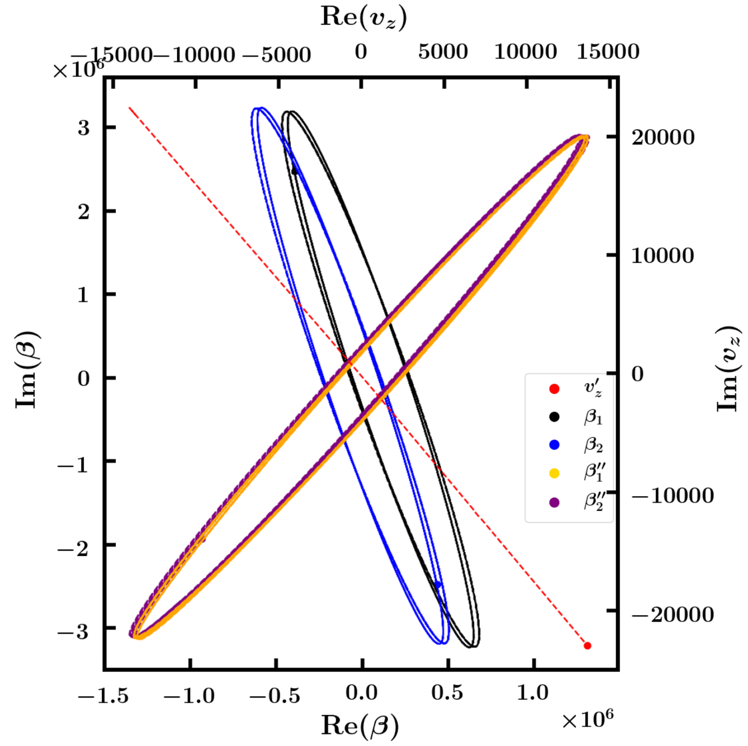

Figure 3.2: The trace of the eigenmodes on the complex plane. They go in their own near-closed loop with some fixed phases difference between them.

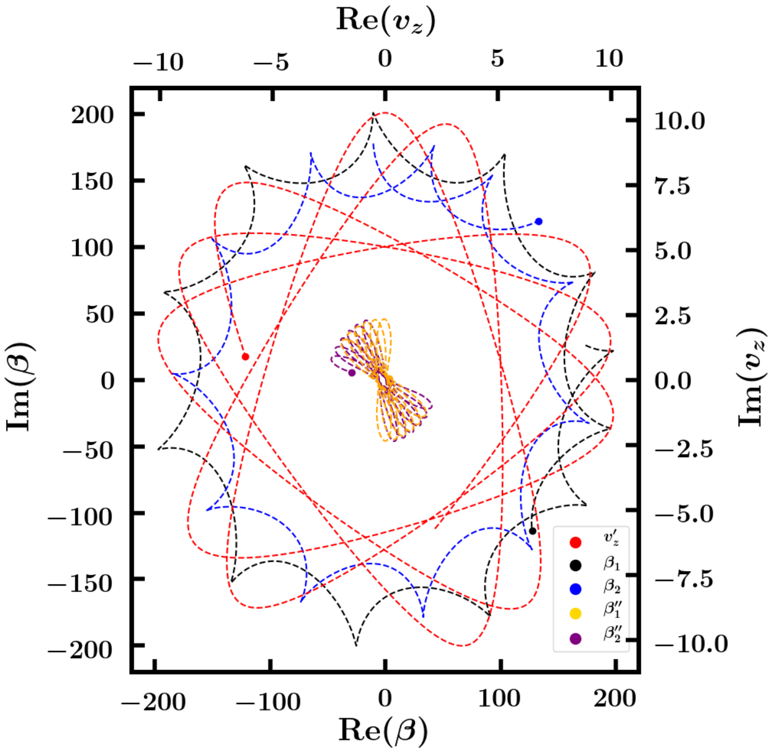

Figure 3.3: By adding extra 20% of dampings on the stable modes, the saturation level becomes lower, the zonal flow now has a more static amplitude

and β_1'' is $\theta = \phi$. We have shown that the large degree of symmetry between the eigenmodes makes the zonal flow oscillate around the origin with small amplitude compared to the eigenmodes, instead of having a large static amplitude that allows the zonal flow to consume the energy from the eigenmodes like a predator. This suggests that a relationship between the eigenmodes and the zonal flow that is closer to predator and prey may arise if symmetry is broken with artificial damping on the stable mode. Figure. 3.3 shows the time trace of the eigenmodes and the zonal flow on the complex plane for the case damping rate on the stable modes at k and k' is increased by 20%. The amplitudes of the eigenmodes and the zonal flow are significantly lower, zonal flow also acquires a more static non-zero amplitude, and the ratio β/v_z' is much lower. Another interesting observation from Figure. 3.3 is

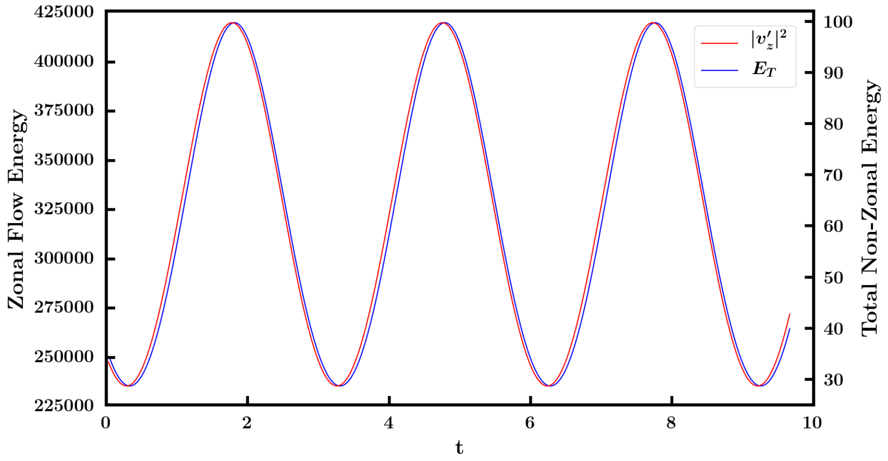

Figure 3.4: By adding extra 20% of dampings on the stable modes, the zonal flow and the total non-zonal energy oscillates coherently with a little phase difference between them. However, this is not a predator-prey dynamics.

that the asymmetry between the stable and unstable modes not only builds up a static zonal flow, it also breaks the symmetry between k and k'', which leads to relatively smaller β''s. Without the artificial damping, the zonal flow acts like an intermediary for energy transfer back and forth between k and k''. On the contrary, when a static zonal flow is built up, there is a preferred direction of the energy transfer in the k space, which leads to the asymmetry of amplitudes between the βs and the β''s. However, breaking the symmetry in order to create a static zonal flow does not give us the predator-prey oscillation we expected, as shown in Fig. 3.4. The non-zonal energy E_T in Fig. 3.4, expressed as

$$E_T = \sum_{k,k''} \Big[\left(1 + k_\perp^2 + |R_1|^2\right) |\beta_1|^2 + \left(1 + k_\perp^2 + |R_2|^2\right) |\beta_2|^2 \\ +2\left(1 + k_\perp^2\right) \mathrm{Re}\langle \beta_1^* \beta_2 \rangle + 2\mathrm{Re}\langle R_1^* \beta_1^* R_2 \beta_2 \rangle \Big] \,. \tag{3.18}$$

We see that the zonal flow and the total non-zonal energy oscillate coherently with a very small phase lag between them. This is in contrast with having the total non-zonal energy lead in the oscillations which would be more typical of a predator-prey oscillation. Here, the zonal flow leads the oscillation, albeit by only a small fraction of a period. This suggests that the zonal flow is still acting like an intermediary and passing the energy back and forth between modes, only with a preferred direction for the energy transfer. We conclude that three-wave model is much too simplified to capture the properties needed for predator-prey-like behavior. However, we do learn that the asymmetries between the stable and unstable modes drive up the zonal flow to a static amplitude, which can lead to an energy-flow-direction preference. Also, the three-wave model is the zero dimensional truncation of the two dimensional fluid model, and obviously loses effects from the associates with the energy cascade mediated by the zonal flow. In two dimensional space, a single zonal flow interacts with $2 \times m \times n$ number of eigenmodes(m is the number of points for x, n is the number of points for y) while it can only interact with 4 eigenmodes in the three-wave model. The significant increase in the number of interactions can pump up the zonal flow markedly compared to the three-wave model. We will take advantage of this feature to build a more complete predator-prey model in Sec. 3.4.

3.4 Predator-Prey Model Built on Saturation Theory

In Sec. 3.3, we showed that the three-wave model does not produce predator-prey-like behavior because it lacks the mechanism for pumping the zonal flow to a large steady value. Here, we will preserve the effect of the energy cascade over an extended wavenumber range, keeping the summation in Eqs. 3.5 and 3.6 instead of truncating to three wavenumbers. However, Eqs. 3.5 and 3.6 are evolution equations for amplitude, and we need to know the relative amplitude between the eigenmodes to evaluate the sum. Fortunately, the saturation theory described in Refs. [30, 28] provides the closed form of Eqs. 3.5 and 3.6 expressed in terms of amplitude squared as well as the scalings with key parameters of the eigenmode amplitude squared. Therefore, we can take advantage of the equations derived from the saturation theory and build a simple model for predator-prey dynamics in the saturated state. The model is composed of three variables, the total unstable mode energy E_U, the total stable mode energy E_S, and the total zonal flow energy E_z. Based on the closed equations of saturation theory, we can build the model with the three following equations

$$\begin{aligned}
\frac{dE_U}{dt} &= 2\gamma_U E_U + \left(C_{U1}E_U + C_{U2}E_S + C_{U3}\sqrt{E_U E_S}\right) E_Z \\
\frac{dE_S}{dt} &= -2\gamma_S E_S + \left(C_{S1}E_U + C_{S2}E_S + C_{S3}\sqrt{E_U E_S}\right) E_Z \\
\frac{dE_Z}{dt} &= -2\nu E_Z + \left(C_{U1}E_U + C_{U2}E_S + C_{U3}\sqrt{E_U E_S}\right) E_Z
\end{aligned} \tag{3.19}$$

where the γs are the ensemble-averaged energy growth and damping rates, and the Cs are the ensemble averaged nonlinear coupling coefficients for the energies. The coefficients and the variables in Eq. 3.19 are extracted from wavenumber sums, consistent with the saturation theory. According to the saturation formula of Ref. [30], the ensemble-averaged eigenmode amplitude and zonal kinetic energy go as $|\beta|^2 \sim \frac{\nu}{\mathrm{Re}(\tau)|C_{iFj}||C_{Fmn}|}$ and the zonal flow $|v_z|^2 \sim \frac{\gamma_1}{\mathrm{Re}(\tau)|C_{iFj}|^2}$, where $\tau = -i(\omega_2'' + \omega_1' - \omega_1^*)^{-1}$ is the triplet correlation time for the triplet interaction between the unstable mode at k, the zonal flow at k', and the stable mode at k'', and γ_1 is the growth rate of the unstable mode at k. With these formulas, we can derive the relation between the unstable modes or stable modes at two different wave number,

$$|\beta_{i,k}|^2 = |\beta_{i,k_{ref}}|^2 \frac{[\mathrm{Re}(\tau)|C_{iFj}||C_{Fmn}|]_{k_{ref}}}{[\mathrm{Re}(\tau)|C_{iFj}||C_{Fmn}|]_{k}} \ , \tag{3.20}$$

where $i = 1, 2$ the unstable or stable mode. We can do the same thing for the zonal flows, obtaining

$$|v_{z,k}|^2 = |v_{z,k_{ref}}|^2 \left[\frac{\gamma_1}{\mathrm{Re}(\tau)|C_{iFj}|^2}\right]_k \left[\frac{\mathrm{Re}(\tau)|C_{iFj}|^2}{\gamma_1}\right]_{k_{ref}} . \tag{3.21}$$

where the k_{ref} is the reference wavenumber. With the help of Eqs. 3.20 and 3.21, we can now calculate the coefficients in Eq. 3.19. First of all, the total unstable mode energy E_U can be expressed as

$$E_U = \sum_k |\beta_{1,k}|^2 \left(1 + k^2 + |R_{1k}|^2\right) = \left|\beta_{1,k_{ref}}\right|^2 C_{U0} \ , \tag{3.22}$$

where

$$C_{U0} = \left[\mathrm{Re}\left(\tau\right)|C_{iFj}|\,|C_{Fmn}|\right]_{k_{ref}} \sum_{k_y \neq 0} \frac{1 + k^2 + |R_1|^2}{\mathrm{Re}\left(\tau\right)|C_{iFj}|\,|C_{Fmn}|} . \tag{3.23}$$

We can also do the same thing for the total stable mode energy and zonal flow energy,

$$\begin{aligned} E_S &= \sum_k |\beta_{2,k}|^2 \left(1 + k^2 + |R_{2k}|^2\right) = \left|\beta_{2,k_{ref}}\right|^2 C_{S0} \ , \\ E_Z &= \sum_{kx, ky \neq 0} |v_z|^2 = \left|v_{z,k_{ref}}\right|^2 C_{Z0} \ , \end{aligned} \tag{3.24}$$

where

$$\begin{aligned} C_{S0} &= \left[\mathrm{Re}\left(\tau\right)|C_{iFj}|\,|C_{Fmn}|\right]_{k_{ref}} \sum_{k_y \neq 0} \frac{1 + k^2 + |R_2|^2}{\mathrm{Re}\left(\tau\right)|C_{iFj}|\,|C_{Fmn}|} \ , \\ C_{Z0} &= \left[\frac{\mathrm{Re}\left(\tau\right)|C_{iFj}|^2}{\gamma_1}\right]_{k_{ref}} \sum_{k_x, k_y = 0} \frac{\gamma_1}{\mathrm{Re}\left(\tau\right)|C_{iFj}|^2} . \end{aligned} \tag{3.25}$$

The calculation for γ_U, γ_S, C_{U1}, C_{U2}, C_{U3}, C_{S1}, C_{S2}, C_{S3} C_{Z1}, C_{Z2} and C_{Z3} are essentially the same with an extra assumption that the phase between the stable and unstable modes is assumed to be fixed. The details of these calculations are found in the appendix. Figure. 3.5 shows the simulation result for Eq. 3.19 with $\nu = 0.02$, $\epsilon = 0.1$, $\eta = 3$, $chi = 0.01$, and $k_{ref} = (0, 0.15)$ and $k'_{ref} = (0.15, 0)$.

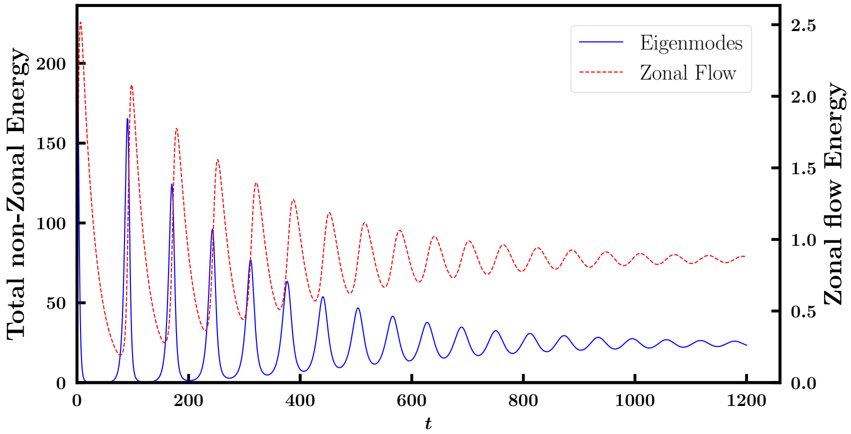

Figure 3.5: The zonal flow acts as a predator and the total non-zonal energy acts like a prey, forming a predator-prey system. The oscillation amplitudes damp down to a set of fixed points, this could be the result of constraint over imposing.

For the terms with the k_{ref} label, the summation of the nonlinearities is for k_x from -1.5 to 1.5, with $k_{x,min} = 0.05$. The total non-zonal energy E_T is given by $E_U + E_S$. Also, the phase between the stable and unstable modes are generated by using random number generator. The two-predator and prey oscillation shows a fixed time delay for the zonal flow. The oscillation phase between the total energy and the zonal flow reaches a number close to $\pi/2$ as the oscillation amplitudes damp to fixed points. The damping of the oscillations is not expected in a typical predator-prey model. This could be the result of imposing a fixed phase between the stable and unstable modes. The original set of equations have fixed amplitudes solutions, but the complex phases can remain unsettled. This is seen in solutions for the βs as looping trajectories in the complex plane, instead of fixed points to which the system converges. If this is the cause of the delay, we can relax the phase constraint by restarting the phase once in a while. Figure. 3.6 shows the predator-prey oscillation if we reset the phase by a random increment at a period $\sim 10\tau$, where τ is the average triplet correlation time of the system, which is on the order

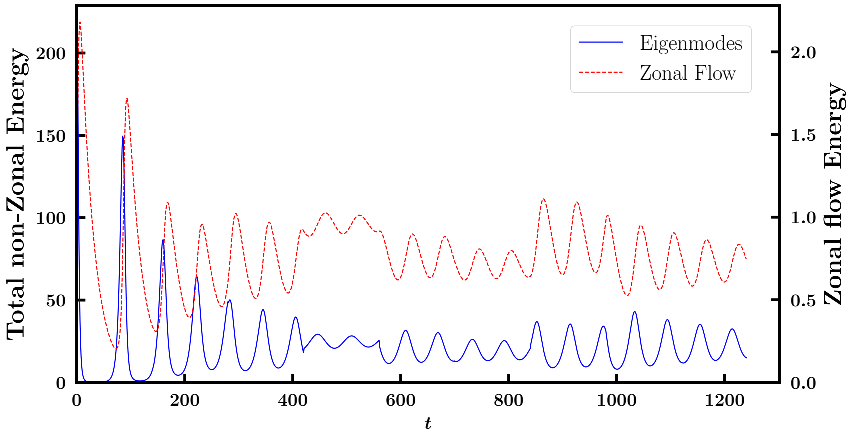

Figure 3.6: The oscillation amplitudes damp down as time goes by, but the amplitudes increase when the phase restart kicks in with a period of 10τ, therefore, the amplitudes do not attenuate to zero.

of 10 time units. The oscillation amplitudes for the E_T and E_Z damp as time goes by, however, the amplitudes increases when the phase restart kicks in. This remedy mimics the randomness of the nonlinear systems and also prevents the oscillations from damping to a set of fixed points.

Figure. 3.7 shows the oscillation of two different periods for phase resets, τ and 0.1τ. Both figures show that by introducing a phase reset period that is equal to or shorter than the triplet correlation time can keep the system's oscillation amplitudes at a roughly constant level. There is no clear difference between Figure. 3.7(a) and Figure. 3.7(b), which support the idea that the life time of the nonlinear interaction is smaller or equal to the triplet correlation time τ in a system with turbulence, and that an overly large nonlinear interaction life time will lead to unphysically large energy transfer rate, leading to significant turbulence suppression.

Another interesting observation from this model is that if we zero out E_S at each time step, we can recover the standard Lotka-Volterra type predator-prey model, where the zonal flow is the predator and the unstable mode is the prey. Figure. 3.8

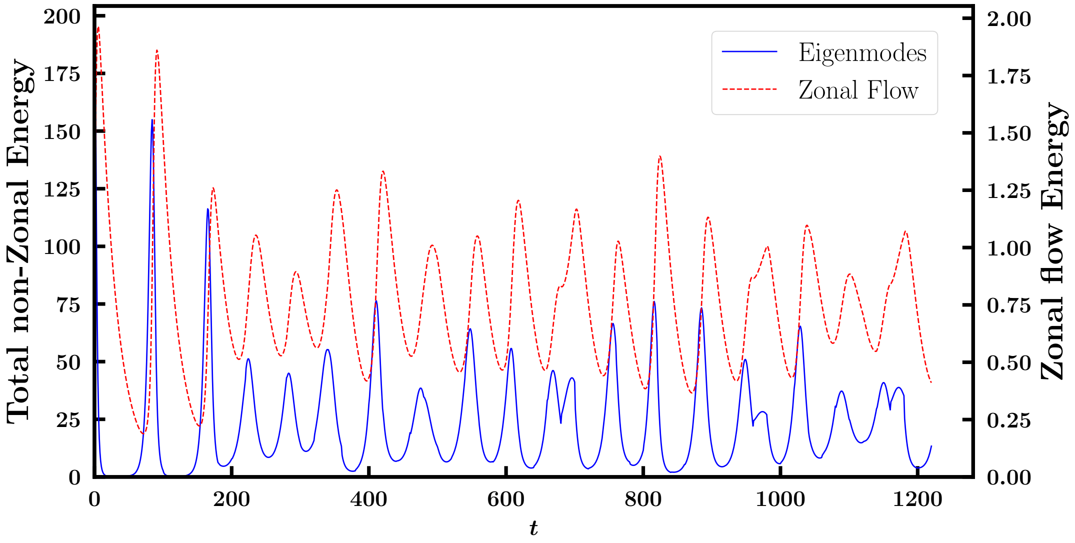

(a)

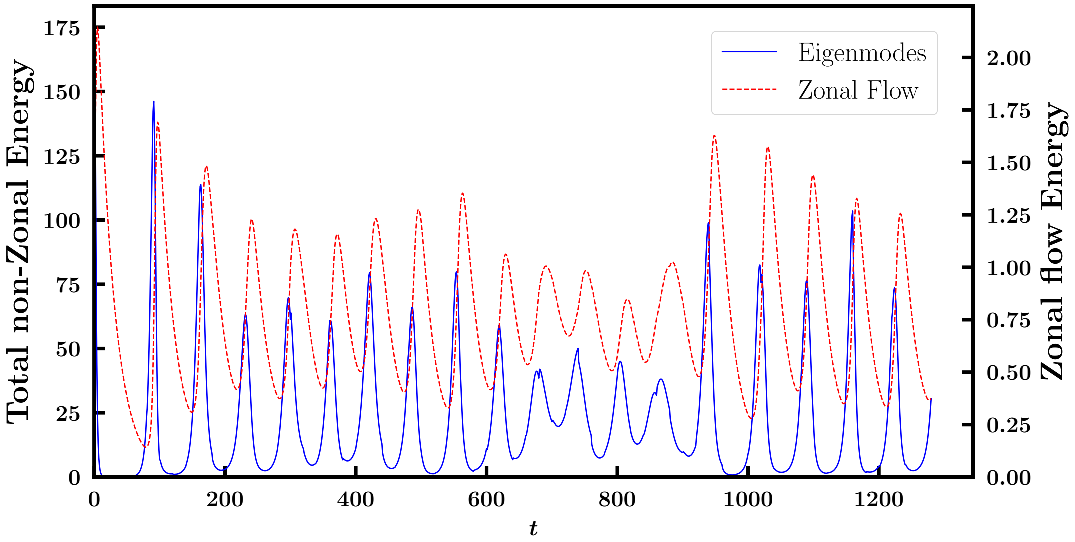

(b)

Figure 3.7: (a) With restarting period = τ. (b) Withe restarting period = 0.1τ. There is no real difference between these two settings, none of them shows the obvious attenuation of the oscillation when the system reaches the steady state, which are both different from the case with restarting period = 10τ.

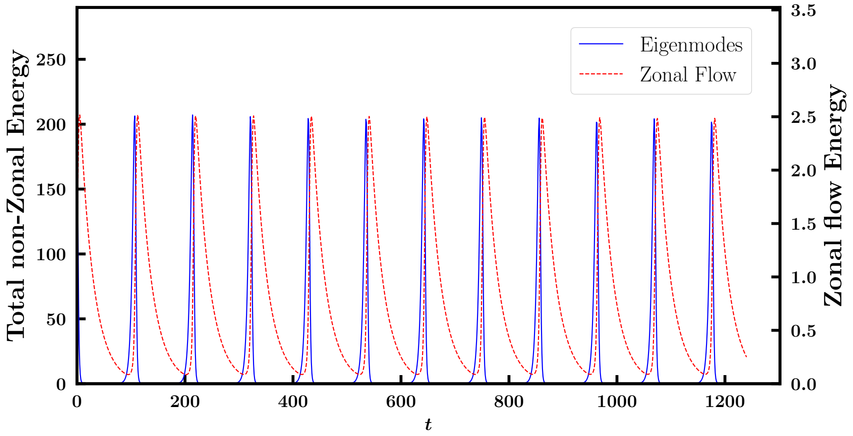

Figure 3.8: The typical Lotka-Volterra type predator-prey model shows a steady and coherent predator-prey oscillation.

shows the result of this model without stable modes, the oscillations are stable and coherent with their amplitudes being almost fixed. It might appear that the case without the stable mode is a better candidate for a realistic predator-prey dynamics. However, this is not the case when it comes to the stiffness of the saturation level, that is, the system should converge and oscillate around the saturation level no matter what initial condition is given. Figure. 3.9(a) shows the result with an initial condition for the case with stable modes and a phase reset period of 0.1τ. Figure 3.9(b) shows the result for the standard Lotka-Volterra type predator-prey model. In the case with stable mode the oscillation converges to an amplitude that is similar to those with smaller initial energies, which is how a typical nonlinear system oscillating about nonlinear balance should respond to such kicks. On the other hand, the standard Lotka-Volterra type predator-prey model keeps the large amplitude oscillation without changing the oscillation by much, failing to capture a key feature expected of a nonlinear balance has. Therefore, the model with the stable mode included can be used to describe an actual system more precisely.

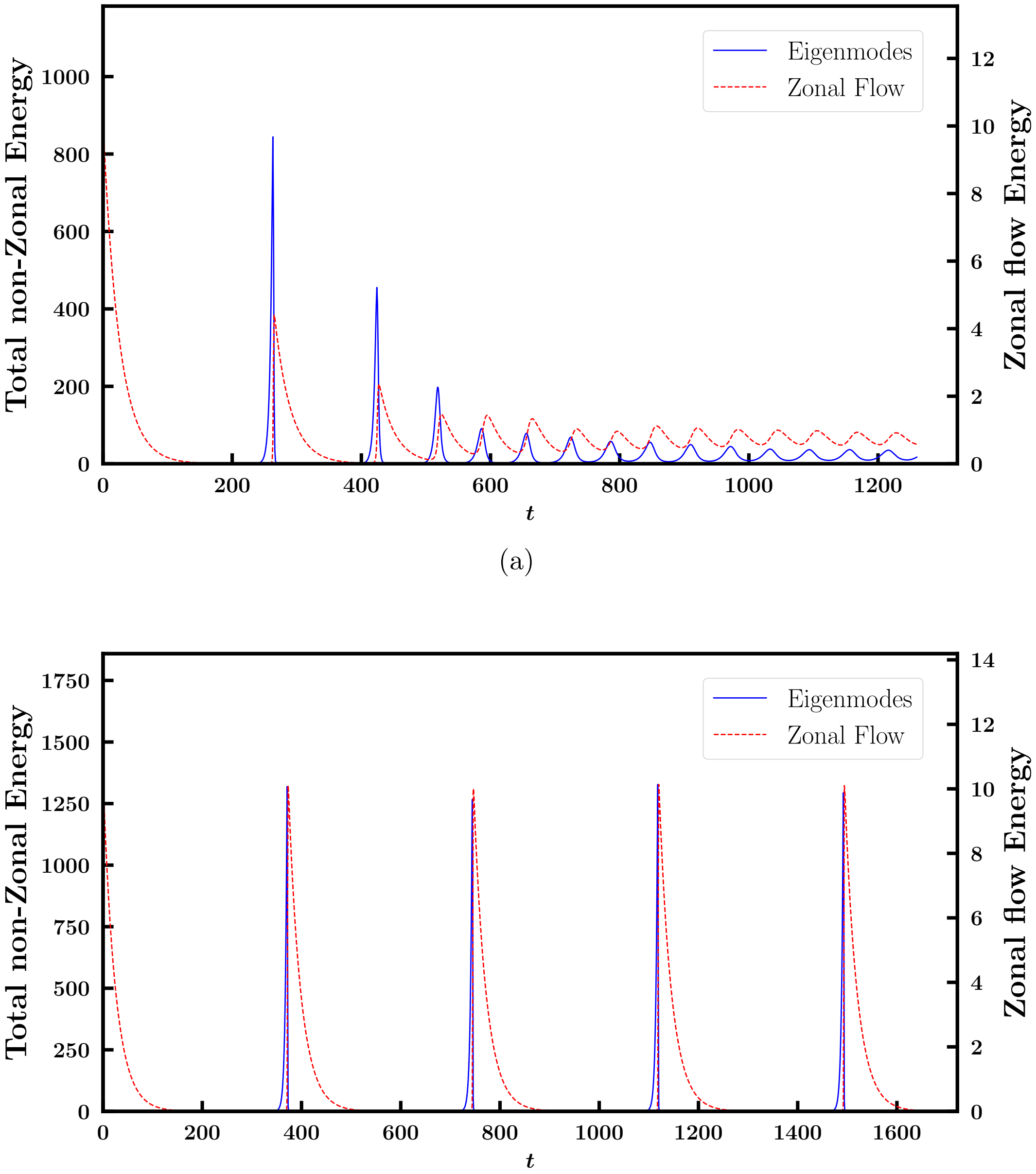

(a)

(b)

Figure 3.9: (a) With restarting period

3.5 Conclusion

Procedures for building predator-prey models from a more complicated fluid system is studied. Our first example was a direct wavenumber truncation of the fluid model that includes two pairs of stable and unstable modes at two wavenumbers and a zonal flow. In this three-wave model, the zonal flow oscillates around the origin on the complex plane and does not acquire a static non-zero amplitude. As such, it acts as an intermediary, helping the energy oscillate between the eigenmodes at two different wavenumbers. Such behavior is the consequence of the large symmetry between the stable and unstable modes and also the symmetry between the eigenmodes at different large-scale wavenumbers. The zonal flow has no preferred direction and can not form a static flow. This does not behave like typical predator-prey oscillations. To improve the model, we create a more static-amplitude zonal flow by breaking the symmetry between the stable and unstable modes, adding artificial damping to the stable modes. The static zonal flow tips the symmetry between the eigenmodes at two different wavenumbers and makes the energy larger for the eigenmodes on one side. However, even though the zonal flow becomes more static with the help from symmetry breaking, it still lacks the characteristic phase lag of oscillations in a predator-prey system. To address this issue, we took a step backward in degree of reduction and kept the summation over wavenumbers instead of truncating the system to three waves.

With help from the ITG saturation theory of Refs. [30, 28], we transformed the eigenmode evolution equations into a set of closed equations expressed in terms of β^2s, then we evaluate the summation by applying the saturation formula for βs and the zonal flow v_z. With this procedure, the set of equations are simplified into three equations composed of the total unstable mode energy E_U, the total stable mode energy E_S, and the total zonal flow energy E_Z. This simple two-predator-prey model demonstrates the typical predator prey oscillation with the zonal flow lagging behind the total non-zonal energy. Nevertheless, the oscillation attenuates and converges to a fixed point if the complex phase between the stable and unstable modes is fixed throughout the simulation. One way to solve this problem is to reassign new random numbers to the complex phases at regular intervals. This procedure relaxes an artificial constraint and keeps the predator-prey dynamics going . An interesting illustration of the role of the stable mode is to remove it, which leads to the Lotka-Volterra type predator-prey model. The oscillation continues without the need of phase restart, however, the oscillation amplitude depends on the initial condition and won't converge to a oscillation around the stationary solution. In contrast, when the stable mode is retained, the oscillation amplitude has a physically meaningful dependence on the initial amplitude. Therefore, the model with the stable mode included has the benefit of tracking the stiffness of the actual nonlinear model. This study addresses the important question of what is required for modeling limit cycle behavior in complex turbulent systems when realistic saturation physics is retained. In this regard, the success of prior predator-prey models in matching the gross features of observed limit-cycle behavior is misleading. Predator-prey models have a form that can be heuristically matched to the relationship between turbulent fields and mean shear flows under the physics of shear suppression. However, this happenstance does not apply to zonal flows, which are a large-scale component of the fluctuation spectrum. Neither shear suppression nor the relationship of mean flows to turbulence is consistent with the role of zonal flows in saturating ITG turbulence. Zonal flows instead catalytically enable transfer to stable modes as the primary mechanism supporting steady state saturation. We have shown that limit cycle behavior is possible in models accounting for the dominant energy transfer mediating saturation but artificial constraints associated with symmetries of the energy transfer under low order reductions must be treated. We have provided a derivation and demonstration of a predator-prey type model consistent with this physics.

3.A Coefficients for Predator-Prey model

The derivation of the coefficients of this model follows the same procedure as the calculation for Es. For E_U the evolution equation is

$$\begin{aligned}\gamma_U E_U &= 2\sum_k \left|\beta_{1k}\right|^2 \left(1+k^2+\left|R_{1k}\right|^2\right)\gamma_{1k} \\ &= \left|\beta_{1ref}\right|^2 \left[\mathrm{Re}\left(\tau\right)\left|C_{iFj}\right|\left|C_{Fmn}\right|\right]_{k_{ref}} \sum_{k_y\neq 0} \frac{1+k^2+\left|R_1\right|^2}{\mathrm{Re}\left(\tau\right)\left|C_{iFj}\right|\left|C_{Fmn}\right|}\gamma_{1k}\ .\end{aligned} \tag{3.26}$$

Since $E_U = \left|\beta_{1ref}\right|^2 C_{U0}$,

$$\gamma_U = \frac{2}{C_{U0}}\left[\left[\mathrm{Re}\left(\tau\right)\left|C_{iFj}\right|\left|C_{Fmn}\right|\right]_{k_{ref}} \sum_{k_y\neq 0} \frac{1+k^2+\left|R_1\right|^2}{\mathrm{Re}\left(\tau\right)\left|C_{iFj}\right|\left|C_{Fmn}\right|}\gamma_{1k}\right]\ . \tag{3.27}$$

The balance involving the damped mode damping rate is similar,

$$\gamma_S = \frac{2}{C_{S0}}\left[\left[\mathrm{Re}\left(\tau\right)\left|C_{iFj}\right|\left|C_{Fmn}\right|\right]_{k_{ref}} \sum_{k_y\neq 0} \frac{1+k^2+\left|R_2\right|^2}{\mathrm{Re}\left(\tau\right)\left|C_{iFj}\right|\left|C_{Fmn}\right|}\gamma_{2k}\right]\ . \tag{3.28}$$

There are cross terms between the stable and unstable modes in the nonlinearities, and we therefore need some treatment for the cross phase. In the quasi-stationary stage, the phases between the stable and unstable modes can be assumed to be locked, and thus we denoted the cross phase as ϕ_k for each wavenumber. Also, for simplicity, the triplet correlation times are defined as $\tau = -i(\omega_2''+\omega_1'-\omega_1^*)^{-1}$, $\tau_{lmn} = \tau_{lmn}^{(k,k')}\left(i\omega_l''+i\omega_m'-i\omega_n^*\right)^{-1}$, and $\tau_{lmnp} = \tau_{lmnp}^{(k,k'')} = \left(i\omega_l'+i\omega_m''-i\omega_n^*\right)^{-1}$. By summimg these equations over wavenumber, the nonlinear part of the unstable modes with scalings applied can be written as

$$
\begin{aligned}
N_U = 2\sum_{k,k'} &\left(1+k^2+|R_1|^2\right) \mathrm{Re}\Bigg\{ \left[\frac{\gamma_1}{\mathrm{Re}\left(\tau\right)\left|C_{iFj}\right|^2}\right]_{k'} \\
&\Bigg[C_{1F2}^{(k,k')}\tau_{211}\Bigg[\left(C_{2F1}^{(k'',-k')}+C_{21F}^{(k'',k)}\right)\frac{\left[\mathrm{Re}\left(\tau\right)\left|C_{iFj}\right|\left|C_{Fmn}\right|\right]_{k_{ref}}}{\left[\mathrm{Re}\left(\tau\right)\left|C_{iFj}\right|\left|C_{Fmn}\right|\right]}\left|\beta_{1ref}\right|^2 \\
&+\left(C_{2F2}^{(k'',-k')}+C_{22F}^{(k'',k)}\right)\frac{\left[\mathrm{Re}\left(\tau\right)\left|C_{iFj}\right|\left|C_{Fmn}\right|\right]_{k_{ref}}}{\left[\mathrm{Re}\left(\tau\right)\left|C_{iFj}\right|\left|C_{Fmn}\right|\right]}\left\langle\beta_1^*\beta_2\right\rangle_{k_{ref}} \\
&+\left(C_{1F2}^{(k,k')*}\right)\frac{\left[\mathrm{Re}\left(\tau\right)\left|C_{iFj}\right|\left|C_{Fmn}\right|\right]_{k_{ref}}}{\left[\mathrm{Re}\left(\tau\right)\left|C_{iFj}\right|\left|C_{Fmn}\right|\right]_{k''}}\left|\beta_{2ref}\right|^2 \\
&+\left(C_{1F1}^{(k,k')*}\right)\frac{\left[\mathrm{Re}\left(\tau\right)\left|C_{iFj}\right|\left|C_{Fmn}\right|\right]_{k_{ref}}}{\left[\mathrm{Re}\left(\tau\right)\left|C_{iFj}\right|\left|C_{Fmn}\right|\right]_{k''}}\left\langle\beta_1^*\beta_2\right\rangle_{k_{ref}}\Bigg]\left|v'_{zk_{ref}}\right|^2\Bigg]_{k'_y=0} \\
&+\left[\frac{\gamma_1}{\mathrm{Re}\left(\tau\right)\left|C_{iFj}\right|^2}\right]_{k''} \\
&\Bigg[C_{12F}^{(k,k')}\tau_{211p}\Bigg[\left(C_{2F1}^{(k',-k'')}+C_{21F}^{(k',k)}\right)\frac{\left[\mathrm{Re}\left(\tau\right)\left|C_{iFj}\right|\left|C_{Fmn}\right|\right]_{k_{ref}}}{\left[\mathrm{Re}\left(\tau\right)\left|C_{iFj}\right|\left|C_{Fmn}\right|\right]}\left|\beta_{1ref}\right|^2 \\
&+\left(C_{2F2}^{(k',-k'')}+C_{22F}^{(k',k)}\right)\frac{\left[\mathrm{Re}\left(\tau\right)\left|C_{iFj}\right|\left|C_{Fmn}\right|\right]_{k_{ref}}}{\left[\mathrm{Re}\left(\tau\right)\left|C_{iFj}\right|\left|C_{Fmn}\right|\right]}\left\langle\beta_1^*\beta_2\right\rangle_{k_{ref}} \\
&+\left(C_{12F}^{(k,k')*}\right)\frac{\left[\mathrm{Re}\left(\tau\right)\left|C_{iFj}\right|\left|C_{Fmn}\right|\right]_{k_{ref}}}{\left[\mathrm{Re}\left(\tau\right)\left|C_{iFj}\right|\left|C_{Fmn}\right|\right]_{k'}}\left|\beta_{2ref}\right|^2 \\
&+\left(C_{11F}^{(k,k')*}\right)\frac{\left[\mathrm{Re}\left(\tau\right)\left|C_{iFj}\right|\left|C_{Fmn}\right|\right]_{k_{ref}}}{\left[\mathrm{Re}\left(\tau\right)\left|C_{iFj}\right|\left|C_{Fmn}\right|\right]_{k'}}\left\langle\beta_1^*\beta_2\right\rangle_{k_{ref}}\Bigg]\left|v''_{zk_{ref}}\right|^2\Bigg]_{k'_y=k_y}\Bigg\}\,.
\end{aligned}
\tag{3.29}
$$

From this expression, we extract the coefficients C_{Uj} as

$$
\begin{aligned}
C_{U1} =&\frac{2}{C_{U0}C_{Z0}}\sum_{k,k'}\left(1+k^2+|R_1|^2\right)\Bigg\{\left[\frac{\gamma_1}{\mathrm{Re}\left(\tau\right)\left|C_{iFj}\right|^2}\right]_{k'} \\
&\mathrm{Re}\left\{C_{1F2}^{(k,k')}\tau_{211}\left[\left(C_{2F1}^{(k'',-k')}+C_{21F}^{(k'',k)}\right)\frac{\left[\mathrm{Re}\left(\tau\right)\left|C_{iFj}\right|\left|C_{Fmn}\right|\right]_{k_{ref}}}{\left[\mathrm{Re}\left(\tau\right)\left|C_{iFj}\right|\left|C_{Fmn}\right|\right]}\right]\right\}_{k_y=0} \\
&+\left[\frac{\gamma_1}{\mathrm{Re}\left(\tau\right)\left|C_{iFj}\right|^2}\right]_{k''}\mathrm{Re}\Bigg\{C_{12F}^{(k,k')}\tau_{211p} \\
&\left[\left(C_{2F1}^{(k',-k'')}+C_{21F}^{(k',k)}\right)\frac{\left[\mathrm{Re}\left(\tau\right)\left|C_{iFj}\right|\left|C_{Fmn}\right|\right]_{k_{ref}}}{\left[\mathrm{Re}\left(\tau\right)\left|C_{iFj}\right|\left|C_{Fmn}\right|\right]}\right]\Bigg\}_{k'_y=k_y}\Bigg\}\,,
\end{aligned}
\tag{3.30}
$$

$$
\begin{aligned}
C_{U2} =& \frac{2}{C_{S0}C_{Z0}} \sum_{k,k'} \left(1+k^2+\left|R_1\right|^2\right) \Bigg\{ \left[\frac{\gamma_1}{\mathrm{Re}\left(\tau\right)\left|C_{iFj}\right|^2}\right]_{k'} \\
& \mathrm{Re}\Bigg\{ C_{1F2}^{(k,k')}\tau_{211} \left[\left(C_{1F2}^{(k,k')*}\right) \frac{\left[\mathrm{Re}\left(\tau\right)\left|C_{iFj}\right|\left|C_{Fmn}\right|\right]_{k_{ref}}}{\left[\mathrm{Re}\left(\tau\right)\left|C_{iFj}\right|\left|C_{Fmn}\right|\right]_{k''}} \right] \Bigg\}_{k_y=0} \\
& + \left[\frac{\gamma_1}{\mathrm{Re}\left(\tau\right)\left|C_{iFj}\right|^2}\right]_{k''} \mathrm{Re}\Bigg\{ C_{12F}^{(k,k')}\tau_{211p} \\
& \left[\left(C_{12F}^{(k,k')*}\right) \frac{\left[\mathrm{Re}\left(\tau\right)\left|C_{iFj}\right|\left|C_{Fmn}\right|\right]_{k_{ref}}}{\left[\mathrm{Re}\left(\tau\right)\left|C_{iFj}\right|\left|C_{Fmn}\right|\right]_{k'}} \right] \Bigg\}_{k'_y=k_y} \Bigg\} ,
\end{aligned}
\tag{3.31}
$$

and

$$
\begin{aligned}
C_{U3} =& \frac{2}{C_{Z0}\sqrt{C_{U0}C_{S0}}} \sum_{k,k'} \left(1+k^2+\left|R_1\right|^2\right) \Bigg\{ \left[\frac{\gamma_1}{\mathrm{Re}\left(\tau\right)\left|C_{iFj}\right|^2}\right]_{k'} \\
& \mathrm{Re}\Bigg\{ C_{1F2}^{(k,k')}\tau_{211} \Bigg[\left(C_{2F2}^{(k'',-k')} + C_{22F}^{(k'',k)}\right) \frac{\left[\mathrm{Re}\left(\tau\right)\left|C_{iFj}\right|\left|C_{Fmn}\right|\right]_{k_{ref}}}{\left[\mathrm{Re}\left(\tau\right)\left|C_{iFj}\right|\left|C_{Fmn}\right|\right]} e^{i\phi} \\
& + \left(C_{1F1}^{(k,k')*}\right) \frac{\left[\mathrm{Re}\left(\tau\right)\left|C_{iFj}\right|\left|C_{Fmn}\right|\right]_{k_{ref}}}{\left[\mathrm{Re}\left(\tau\right)\left|C_{iFj}\right|\left|C_{Fmn}\right|\right]_{k''}} e^{i\phi''} \Bigg] \Bigg\}_{k_y=0} \\
& + \left[\frac{\gamma_1}{\mathrm{Re}\left(\tau\right)\left|C_{iFj}\right|^2}\right]_{k''} \mathrm{Re}\Bigg\{ C_{12F}^{(k,k')}\tau_{211p} \\
& \Bigg[\left(C_{2F2}^{(k',-k'')} + C_{22F}^{(k',k)}\right) \frac{\left[\mathrm{Re}\left(\tau\right)\left|C_{iFj}\right|\left|C_{Fmn}\right|\right]_{k_{ref}}}{\left[\mathrm{Re}\left(\tau\right)\left|C_{iFj}\right|\left|C_{Fmn}\right|\right]} e^{i\phi} \\
& + \left(C_{11F}^{(k,k')*}\right) \frac{\left[\mathrm{Re}\left(\tau\right)\left|C_{iFj}\right|\left|C_{Fmn}\right|\right]_{k_{ref}}}{\left[\mathrm{Re}\left(\tau\right)\left|C_{iFj}\right|\left|C_{Fmn}\right|\right]_{k'}} e^{i\phi'} \Bigg] \Bigg\}_{k'_y=k_y} \Bigg\} .
\end{aligned}
\tag{3.32}
$$

The nonlinear part of the stable modes can be rewritten as,

$$
\begin{aligned}
N_S =& 2\sum_{k,k'} \left(1+k^2+|R_2|^2\right) \Bigg\{ \left[\frac{\gamma_1}{\mathrm{Re}\left(\tau\right)|C_{iFj}|^2}\right]_{k'} \\
&\mathrm{Re}\Bigg\{ C_{2F1}^{(k,k')}\tau_{112}\Bigg[\left(C_{1F2}^{(k'',-k')} + C_{12F}^{(k'',k)}\right) \frac{\left[\mathrm{Re}\left(\tau\right)|C_{iFj}|\,|C_{Fmn}|\right]_{k_{ref}}}{\left[\mathrm{Re}\left(\tau\right)|C_{iFj}|\,|C_{Fmn}|\right]} \left|\beta_{2ref}\right|^2 \\
&+ \left(C_{1F1}^{(k'',-k')} + C_{11F}^{(k'',k)}\right) \frac{\left[\mathrm{Re}\left(\tau\right)|C_{iFj}|\,|C_{Fmn}|\right]_{k_{ref}}}{\left[\mathrm{Re}\left(\tau\right)|C_{iFj}|\,|C_{Fmn}|\right]} \langle\beta_1\beta_2^*\rangle_{k_{ref}} \\
&+ \left(C_{2F1}^{(k,k')*}\right) \frac{\left[\mathrm{Re}\left(\tau\right)|C_{iFj}|\,|C_{Fmn}|\right]_{k_{ref}}}{\left[\mathrm{Re}\left(\tau\right)|C_{iFj}|\,|C_{Fmn}|\right]_{k''}} \left|\beta_{1ref}\right|^2 \\
&+ \left(C_{2F2}^{(k,k')*}\right) \frac{\left[\mathrm{Re}\left(\tau\right)|C_{iFj}|\,|C_{Fmn}|\right]_{k_{ref}}}{\left[\mathrm{Re}\left(\tau\right)|C_{iFj}|\,|C_{Fmn}|\right]_{k''}} \langle\beta_1\beta_2^*\rangle_{k_{ref}} \Bigg] \left|v'_{zk_{ref}}\right|^2 \Bigg\}_{k'_y=0} \\
&+ \left[\frac{\gamma_1}{\mathrm{Re}\left(\tau\right)|C_{iFj}|^2}\right]_{k''} \mathrm{Re}\Bigg\{ C_{21F}^{(k,k')}\tau_{112p} \\
&\Bigg[\left(C_{1F2}^{(k',-k'')} + C_{11F}^{(k',k)}\right) \frac{\left[\mathrm{Re}\left(\tau\right)|C_{iFj}|\,|C_{Fmn}|\right]_{k_{ref}}}{\left[\mathrm{Re}\left(\tau\right)|C_{iFj}|\,|C_{Fmn}|\right]} \left|\beta_{2ref}\right|^2 \\
&+ \left(C_{1F1}^{(k',-k'')} + C_{11F}^{(k',k)}\right) \frac{\left[\mathrm{Re}\left(\tau\right)|C_{iFj}|\,|C_{Fmn}|\right]_{k_{ref}}}{\left[\mathrm{Re}\left(\tau\right)|C_{iFj}|\,|C_{Fmn}|\right]} \langle\beta_1\beta_2^*\rangle_{k_{ref}} \\
&+ \left(C_{22F}^{(k,k')*}\right) \frac{\left[\mathrm{Re}\left(\tau\right)|C_{iFj}|\,|C_{Fmn}|\right]_{k_{ref}}}{\left[\mathrm{Re}\left(\tau\right)|C_{iFj}|\,|C_{Fmn}|\right]_{k'}} \left|\beta_{1ref}\right|^2 \\
&+ \left(C_{21F}^{(k,k')*}\right) \frac{\left[\mathrm{Re}\left(\tau\right)|C_{iFj}|\,|C_{Fmn}|\right]_{k_{ref}}}{\left[\mathrm{Re}\left(\tau\right)|C_{iFj}|\,|C_{Fmn}|\right]_{k'}} \langle\beta_1^*\beta_2\rangle_{k_{ref}} \Bigg] \left|v''_{zk_{ref}}\right|^2 \Bigg\}_{k'_y=k_y} \Bigg\} .
\end{aligned}
\tag{3.33}
$$

The coefficients C_{Sj} are therefore given by

$$
\begin{aligned}
C_{S1} =& \frac{2}{C_{U0}C_{Z0}} \sum_{k,k'} \left(1+k^2+|R_2|^2\right) \Bigg\{ \left[\frac{\gamma_1}{\mathrm{Re}\left(\tau\right)|C_{iFj}|^2}\right]_{k'} \\
&\mathrm{Re}\Bigg\{ C_{2F1}^{(k,k')}\tau_{112} \left[\left(C_{2F1}^{(k,k')*}\right) \frac{\left[\mathrm{Re}\left(\tau\right)|C_{iFj}|\,|C_{Fmn}|\right]_{k_{ref}}}{\left[\mathrm{Re}\left(\tau\right)|C_{iFj}|\,|C_{Fmn}|\right]_{k''}} \right] \Bigg\}_{k_y=0} \\
&+ \left[\frac{\gamma_1}{\mathrm{Re}\left(\tau\right)|C_{iFj}|^2}\right]_{k''} \\
&\mathrm{Re}\Bigg\{ C_{21F}^{(k,k')}\tau_{112p} \left[\left(C_{22F}^{(k,k')*}\right) \frac{\left[\mathrm{Re}\left(\tau\right)|C_{iFj}|\,|C_{Fmn}|\right]_{k_{ref}}}{\left[\mathrm{Re}\left(\tau\right)|C_{iFj}|\,|C_{Fmn}|\right]_{k'}} \right] \Bigg\}_{k'_y=k_y} \Bigg\}
\end{aligned}
\tag{3.34}
$$

$$
\begin{aligned}
C_{S2} =& \frac{2}{C_{S0}C_{Z0}} \sum_{k,k'} \left(1+k^2+|R_2|^2\right) \Bigg\{ \left[\frac{\gamma_1}{\mathrm{Re}\left(\tau\right)|C_{iFj}|^2}\right]_{k'} \\
& \mathrm{Re}\Bigg\{ C_{2F1}^{(k,k')}\tau_{112}\left[\left(C_{1F2}^{(k'',-k')}+C_{12F}^{(k'',k)}\right)\frac{\left[\mathrm{Re}\left(\tau\right)|C_{iFj}|\,|C_{Fmn}|\right]_{k_{ref}}}{\left[\mathrm{Re}\left(\tau\right)|C_{iFj}|\,|C_{Fmn}|\right]}\right]\Bigg\}_{k_y=0} \\
& + \left[\frac{\gamma_1}{\mathrm{Re}\left(\tau\right)|C_{iFj}|^2}\right]_{k''} \\
& \mathrm{Re}\Bigg\{ C_{21F}^{(k,k')}\tau_{112p}\left[\left(C_{1F2}^{(k',-k'')}+C_{12F}^{(k',k)}\right)\frac{\left[\mathrm{Re}\left(\tau\right)|C_{iFj}|\,|C_{Fmn}|\right]_{k_{ref}}}{\left[\mathrm{Re}\left(\tau\right)|C_{iFj}|\,|C_{Fmn}|\right]}\right]\Bigg\}_{k'_y=k_y}\Bigg\} ,
\end{aligned}
\tag{3.35}
$$

and

$$
\begin{aligned}
C_{S3} =& \frac{2}{C_{Z0}\sqrt{C_{U0}C_{S0}}} \sum_{k,k'} \left(1+k^2+|R_2|^2\right) \Bigg\{ \left[\frac{\gamma_1}{\mathrm{Re}\left(\tau\right)|C_{iFj}|^2}\right]_{k'} \\
& \mathrm{Re}\Bigg\{ C_{2F1}^{(k,k')}\tau_{112}\Bigg[\left(C_{1F1}^{(k'',-k')}+C_{11F}^{(k'',k)}\right)\frac{\left[\mathrm{Re}\left(\tau\right)|C_{iFj}|\,|C_{Fmn}|\right]_{k_{ref}}}{\left[\mathrm{Re}\left(\tau\right)|C_{iFj}|\,|C_{Fmn}|\right]}e^{-i\phi} \\
& + \left(C_{2F2}^{(k,k')*}\right)\frac{\left[\mathrm{Re}\left(\tau\right)|C_{iFj}|\,|C_{Fmn}|\right]_{k_{ref}}}{\left[\mathrm{Re}\left(\tau\right)|C_{iFj}|\,|C_{Fmn}|\right]_{k''}}e^{i\phi''}\Bigg]\Bigg\}_{k_y=0} \\
& + \left[\frac{\gamma_1}{\mathrm{Re}\left(\tau\right)|C_{iFj}|^2}\right]_{k''} \\
& \mathrm{Re}\left\{ C_{21F}^{(k,k')}\tau_{112p}\Bigg[\left(C_{1F1}^{(k',-k'')}+C_{11F}^{(k',k)}\right)\frac{\left[\mathrm{Re}\left(\tau\right)|C_{iFj}|\,|C_{Fmn}|\right]_{k_{ref}}}{\left[\mathrm{Re}\left(\tau\right)|C_{iFj}|\,|C_{Fmn}|\right]}e^{-i\phi}\right. \\
& \left. + \left(C_{21F}^{(k,k')*}\right)\frac{\left[\mathrm{Re}\left(\tau\right)|C_{iFj}|\,|C_{Fmn}|\right]_{k_{ref}}}{\left[\mathrm{Re}\left(\tau\right)|C_{iFj}|\,|C_{Fmn}|\right]_{k'}}e^{i\phi'}\Bigg]\right\}_{k'_y=k_y}\Bigg\}
\end{aligned}
\quad . \tag{3.36}
$$

The nonlinear part of the zonal flow can be expressed as,

$$
\begin{aligned}
N_Z = & \sum_{k,k'} 2\mathrm{Re}\Bigg\{ \Bigg[\Bigg(C_{F12}^{(k,k')} \tau_{211} \left[\frac{\gamma_1}{\mathrm{Re}\left(\tau\right) \left|C_{iFj}\right|^2} \right] \\
& \Bigg[\left(C_{22F}^{(k'',-k')} + C_{2F2}^{(k'',k)} \right) \frac{\left[\mathrm{Re}\left(\tau\right) \left|C_{iFj}\right| \left|C_{Fmn}\right|\right]_{k_{ref}}}{\left[\mathrm{Re}\left(\tau\right) \left|C_{iFj}\right| \left|C_{Fmn}\right|\right]_{k'}} \left\langle \beta_1 \beta_2^* \right\rangle_{k_{ref}} \\
& + \left(C_{1F1}^{(k',k)} + C_{11F}^{(k',-k'')} \right) \frac{\left[\mathrm{Re}\left(\tau\right) \left|C_{iFj}\right| \left|C_{Fmn}\right|\right]_{k_{ref}}}{\left[\mathrm{Re}\left(\tau\right) \left|C_{iFj}\right| \left|C_{Fmn}\right|\right]_{k''}} \left\langle \beta_1 \beta_2^* \right\rangle_{k_{ref}} \\
& + \left(C_{1F2}^{(k',k)} + C_{12F}^{(k',-k'')} \right) \frac{\left[\mathrm{Re}\left(\tau\right) \left|C_{iFj}\right| \left|C_{Fmn}\right|\right]_{k_{ref}}}{\left[\mathrm{Re}\left(\tau\right) \left|C_{iFj}\right| \left|C_{Fmn}\right|\right]_{k''}} \left|\beta_{2ref}\right|^2 \\
& + \left(C_{2F1}^{(k'',k)} + C_{21F}^{(k'',-k')} \right) \frac{\left[\mathrm{Re}\left(\tau\right) \left|C_{iFj}\right| \left|C_{Fmn}\right|\right]_{k_{ref}}}{\left[\mathrm{Re}\left(\tau\right) \left|C_{iFj}\right| \left|C_{Fmn}\right|\right]_{k'}} \left|\beta_{1ref}\right|^2 \Bigg] \Bigg) \\
& + \Bigg(C_{F21}^{(k,k')} \tau_{211p} \left[\frac{\gamma_1}{\mathrm{Re}\left(\tau\right) \left|C_{iFj}\right|^2} \right] \\
& \Bigg[\left(C_{11F}^{(k'',-k')} + C_{1F1}^{(k'',k)} \right) \frac{\left[\mathrm{Re}\left(\tau\right) \left|C_{iFj}\right| \left|C_{Fmn}\right|\right]_{k_{ref}}}{\left[\mathrm{Re}\left(\tau\right) \left|C_{iFj}\right| \left|C_{Fmn}\right|\right]_{k'}} \left\langle \beta_1^* \beta_2 \right\rangle_{k_{ref}} \\
& + \left(C_{2F2}^{(k',k)} + C_{22F}^{(k',-k'')} \right) \frac{\left[\mathrm{Re}\left(\tau\right) \left|C_{iFj}\right| \left|C_{Fmn}\right|\right]_{k_{ref}}}{\left[\mathrm{Re}\left(\tau\right) \left|C_{iFj}\right| \left|C_{Fmn}\right|\right]_{k''}} \left\langle \beta_1 \beta_2^* \right\rangle_{k_{ref}} \\
& + \left(C_{2F1}^{(k',k)} + C_{21F}^{(k',-k'')} \right) \frac{\left[\mathrm{Re}\left(\tau\right) \left|C_{iFj}\right| \left|C_{Fmn}\right|\right]_{k_{ref}}}{\left[\mathrm{Re}\left(\tau\right) \left|C_{iFj}\right| \left|C_{Fmn}\right|\right]_{k''}} \left|\beta_{1ref}\right|^2 \\
& + \left(C_{1F2}^{(k'',k)} + C_{12F}^{(k'',-k')} \right) \frac{\left[\mathrm{Re}\left(\tau\right) \left|C_{iFj}\right| \left|C_{Fmn}\right|\right]_{k_{ref}}}{\left[\mathrm{Re}\left(\tau\right) \left|C_{iFj}\right| \left|C_{Fmn}\right|\right]_{k'}} \left|\beta_{2ref}\right|^2 \Bigg] \Bigg) \Bigg] \left|v_{zref}\right|^2 \Bigg\}_{k_y=0},
\end{aligned}
\tag{3.37}
$$

from which

$$
\begin{aligned}
C_{Z1} = & \frac{2}{C_{U0} C_{Z0}} \mathrm{Re}\Bigg\{ \Bigg(C_{F12}^{(k,k')} \tau_{211} \left[\frac{\gamma_1}{\mathrm{Re}\left(\tau\right) \left|C_{iFj}\right|^2} \right] \\
& \left(C_{2F1}^{(k'',k)} + C_{21F}^{(k'',-k')} \right) \frac{\left[\mathrm{Re}\left(\tau\right) \left|C_{iFj}\right| \left|C_{Fmn}\right|\right]_{k_{ref}}}{\left[\mathrm{Re}\left(\tau\right) \left|C_{iFj}\right| \left|C_{Fmn}\right|\right]_{k'}} \Bigg) \\
& + \Bigg(C_{F21}^{(k,k')} \tau_{211p} \left[\frac{\gamma_1}{\mathrm{Re}\left(\tau\right) \left|C_{iFj}\right|^2} \right] \\
& \left(C_{2F1}^{(k',k)} + C_{21F}^{(k',-k'')} \right) \frac{\left[\mathrm{Re}\left(\tau\right) \left|C_{iFj}\right| \left|C_{Fmn}\right|\right]_{k_{ref}}}{\left[\mathrm{Re}\left(\tau\right) \left|C_{iFj}\right| \left|C_{Fmn}\right|\right]_{k''}} \Bigg) \Bigg\}_{k_y=0},
\end{aligned}
\tag{3.38}
$$

$$
\begin{aligned}
C_{Z2} ={}& \frac{2}{C_{S0}C_{Z0}} \mathrm{Re}\Bigg\{ \Bigg(C_{F12}^{(k,k')} \tau_{211} \left[\frac{\gamma_1}{\mathrm{Re}\,(\tau)\,|C_{iFj}|^2} \right] \\
& \Big(C_{1F2}^{(k',k)} + C_{12F}^{(k',-k'')} \Big) \frac{[\mathrm{Re}\,(\tau)\,|C_{iFj}|\,|C_{Fmn}|]_{k_{ref}}}{[\mathrm{Re}\,(\tau)\,|C_{iFj}|\,|C_{Fmn}|]_{k''}} \Bigg) \\
& + \Bigg(C_{F21}^{(k,k')} \tau_{211p} \left[\frac{\gamma_1}{\mathrm{Re}\,(\tau)\,|C_{iFj}|^2} \right] \\
& \Big(C_{1F2}^{(k'',k)} + C_{12F}^{(k'',-k')} \Big) \frac{[\mathrm{Re}\,(\tau)\,|C_{iFj}|\,|C_{Fmn}|]_{k_{ref}}}{[\mathrm{Re}\,(\tau)\,|C_{iFj}|\,|C_{Fmn}|]_{k'}} \Bigg) \Bigg\}_{k_y=0} ,
\end{aligned}
\tag{3.39}
$$

and

$$
\begin{aligned}
C_{Z3} ={}& \frac{2}{C_{Z0}\sqrt{C_{U0}C_{S0}}} \mathrm{Re}\Bigg\{ \\
& \Bigg(C_{F12}^{(k,k')} \tau_{211} \left[\frac{\gamma_1}{\mathrm{Re}\,(\tau)\,|C_{iFj}|^2} \right] \Bigg[\Big(C_{22F}^{(k'',-k')} + C_{2F2}^{(k'',k)} \Big) \\
& \frac{[\mathrm{Re}\,(\tau)\,|C_{iFj}|\,|C_{Fmn}|]_{k_{ref}}}{[\mathrm{Re}\,(\tau)\,|C_{iFj}|\,|C_{Fmn}|]_{k'}} e^{-i\phi'} \\
& + \Big(C_{1F1}^{(k',k)} + C_{11F}^{(k',-k'')} \Big) \frac{[\mathrm{Re}\,(\tau)\,|C_{iFj}|\,|C_{Fmn}|]_{k_{ref}}}{[\mathrm{Re}\,(\tau)\,|C_{iFj}|\,|C_{Fmn}|]_{k''}} e^{-i\phi''} \Bigg] \Bigg) \\
& + \Bigg(C_{F21}^{(k,k')} \tau_{211p} \left[\frac{\gamma_1}{\mathrm{Re}\,(\tau)\,|C_{iFj}|^2} \right] \Bigg[\Big(C_{11F}^{(k'',-k')} + C_{1F1}^{(k'',k)} \Big) \\
& \frac{[\mathrm{Re}\,(\tau)\,|C_{iFj}|\,|C_{Fmn}|]_{k_{ref}}}{[\mathrm{Re}\,(\tau)\,|C_{iFj}|\,|C_{Fmn}|]_{k'}} e^{i\phi'} \\
& + \Big(C_{2F2}^{(k',k)} + C_{22F}^{(k',-k'')} \Big) \frac{[\mathrm{Re}\,(\tau)\,|C_{iFj}|\,|C_{Fmn}|]_{k_{ref}}}{[\mathrm{Re}\,(\tau)\,|C_{iFj}|\,|C_{Fmn}|]_{k''}} e^{i\phi''} \Bigg] \Bigg) \Bigg\}_{k_y=0} .
\end{aligned}
\tag{3.40}
$$

Acknowledgments

This work was supported by U.S. Department of Energy Grant DE-FG02-89ER53291. The data supporting the findings of this study is available from the authors upon reasonable request.

Bibliography

[1] W. Horton, Rev. Mod. Phys. **71**, 735 (1999).

[2] E.-j. Kim and P.H. Diamond, Phys. Rev. Lett. **90**, 185006 (2003).

[3] P.H. Diamond, Y.-M. Liang, B.A. Carreras, and P.W. Terry, Phys. Rev. Lett. **72**, 2565 (1994).

[4] S. Kobayashi, Ö. Gürcan, and P.H. Diamond, Physiscs of Plasmas **22** 090702 (2015).

[5] P. W. Terry, A. S. Ware, and D. E. Newman, Physics of Plasmas **1**, 3974 (1994).

[6] L. Schmitz, L. Zeng, T. L. Rhodes, J. C. Hillesheim, E. J. Doyle, R. J. Groebner, W. A.Peebles, K. H. Burrell, and G. Wang, Phys. Rev. Lett. **108**, 155002 (2012).

[7] L. Schmitz, Nuclear Fusion **57**, 025003 (2017).

[8] P. Terry, B. Faber, C. Hegna, V. Mirnov, M. Pueschel, and G. Whelan, Physics of Plasmas **25**, 012308 (2018).

[9] P. W. Terry, P.-Y. Li, M. J. Pueschel, and G. G. Whelan, Phys. Rev. Lett. **126**, 025004

[10] D. R. Hatch, P. W. Terry, F. Jenko, F. Merz, and W. M. Nevins, Phys. Rev. Lett. **106**,115003 (2011).

[11] P. W. Terry, K. D. Makwana, M. J. Pueschel, D. R. Hatch, F. Jenko, and F. Merz, Physicsof Plasmas **21**, 122303 (2014).

[12] C. Holland, P. Diamond, S. Champeaux, O. G. E. Kim, M. Rosenbluth, G. Tynan, N. Crocker,W. Nevins, and J. Candy, Nucl. Fusion **43**, 761 (2003).

[13] K. Makwana, P. Terry, and J.-H. Kim, Phys. Plasmas **19**, 062310 (2012).

[14] K. Makwana, P. Terry, M. Pueschel, and D. Hatch, Phys. Rev. Lett. **112**, 095002 (2014).

[15] D. Hatch, M. Pueschel, W. N. F. Jenko, P. Terry, and H. Doerk, Phys. Rev. Lett. **108**, 235002(2012).

[16] P.W. Terry, B.J. Faber, C.C. Hegna, V.V. Mirnov, M.J. Pueschel, and G.G. Whelan, Phys. Plasmas **25**, 012308 (2018).

[17] D.R Hatch, P.W. Terry, F. Jenko, F. Merz, and W.M. Nevins, Phys. Rev. Lett. **106**, 115003 (2011).

[18] P.W. Terry, K.D. Makwana, M.J. Pueschel, D.R. Hatch, F. Jenko, and F. Merz, Phys. Plasmas **21**, 122303 (2014).

Chapter 4

Saturation Physics of Threshold Heat-Flux Reduction

Abstract

The saturation physics of ion-temperature-gradient-driven turbulence is examined in relation to the temperature-gradient variation of the heat flux, which can exhibit an upshift of the critical gradient for significant flux relative to the linear instability threshold. Gyrokinetic measurements of saturation properties and spectral energy transfer (which will be defined in Sec. 4.2) are presented, indicating that the physics of saturation is fundamentally unchanged on either side of the upshifted gradient. To analyze heat transport below and above the upshifted critical gradient, a fluid model for toroidal ITG turbulence is modified to include the kinetic instability threshold. The model and the heat flux are rendered in the eigenmode decomposition to track the dominant mode-coupling channel of zonal-flow-catalyzed transfer to a conjugate stable mode. Given linear and nonlinear symmetries, the stable mode level and the cross correlation of the unstable and stable mode amplitudes are related to the unstable mode level via linear physics. The heat flux can then be written in terms of the unstable-mode level, which through a nonlinear balance depends on the eigenmode-dependent coupling coefficients and the triplet correlation time of the dominant coupled modes. Resonance in these quantities leads to suppressed heat flux above the linear threshold, with a nonlinear upshift of the critical gradient set by the resonance broadening of finite perpendicular wavenumber and collisionality. This work was carried out in collaboration with Paul W. Terry, Garth G. Whelan, and M.J. Pueschel.

In this chapter, we will describe how to use the saturation theory presented in chapter 2 to explain a long unanswered question about why the heat flux in various turbulent systems remains extremely low when the gradient is close to the linear critical gradient, but shoots up significantly at some nonlinear critical gradient. n this chapter, the triplet correlation time and eddy-turnover rate discussed in chapter 2 will be shown to be important in suppressing turbulence near criticality.

4.1 Introduction

Improving plasma confinement has remained a critical goal for magnetically confined fusion plasmas for decades [1]. A chief concern has been confinement losses associated with microturbulence. Despite significant progress in identifying and utilizing strategies for reducing losses associated with turbulence [2, 3, 4], new devices such as ITER and SPARC [5] have stringent specifications for transport relative to empirical benchmarks, and their achievement will require effort and skill on the part of experimenters. Beyond reaching overall confinement milestones, there is considerable advantage in being able to achieve transport control with selectivity relating to both location and time [4]. To achieve such advances, it will be necessary to thoroughly understand the plasma turbulence associated with confinement losses. Such understanding will furthermore enable transport reduction strategies through the design of three-dimensional magnetic fields in stellarator configurations [6], including those that seek lower transport levels by improving the efficiency of nonlinear energy transfer [7].

There is a well-known but poorly understood transport-reduction phenomenon whose study represents an opportunity to better understand the saturation of important micro-instabilities and physics that lowers transport rates. We refer to the so-called Dimits shift, the onset of significant heat transport at the nonlinear critical gradient (NLCG), a higher gradient than the linear instability threshold [11]. In the region below the NLCG but above the linear threshold, the heat flux is low relative to expectations based on linear drive strength but not zero, representing a gradient range of strongly but not completely suppressed transport. This phenomenon is observed in nonlinear simulations of ion-temperature-gradient-driven (ITG) turbulence with both gyrokinetic [9] and fluid models [21]. It also occurs for density-gradient-driven trapped electron turbulence [11]. We argue that the upshift is an integral part of the mechanism for saturation of ITG turbulence that has already been studied above the NLCG [30]. This mechanism involves the transfer of energy to stable modes through the zonal flow. When included in a model with the physics of the linear instability threshold, this mechanism reproduces many features of the critical-gradient upshift [21]. It is also consistent with detailed analyses of gyrokinetic simulations described in Sec. 4.2, which suggest that salient aspects of the saturated state are qualitatively the same on either side of the NLCG.

Despite numerous attempts to understand the critical-gradient upshift, none is considered definitive [13, 14, 15, 16, 15, 18, 19]. Suppression of transport below the NLCG by zonal-flow shearing has been a recurring theme, a notion that requires zonal-flow shearing to lose effectiveness above the NLCG [13, 14, 15, 16]. While zonal flows are excited in ITG turbulence and are known to reduce turbulence levels [11], they do this primarily by enabling energy transfer to stable modes [20, 17]. As shown in Sec. 4.2, the zonal-flow shearing hypothesis is at odds with a number of observations of the nonlinear turbulent state in gyrokinetics. Other mechanisms for the critical-gradient upshift involve adjustments of spatial fluctuation structure to inhomogeneous zonal flows with non-uniform shear [19], or aspects of mode coupling

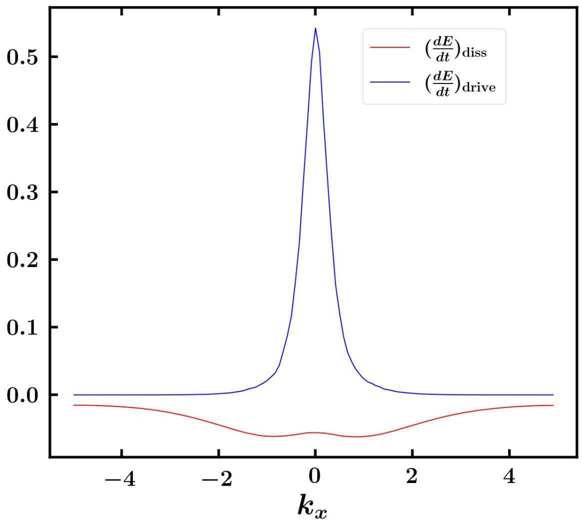

Figure 4.1: The energy drive and energy dissipation averaged over z and time, and summed over k_y as a function of k_x. Over the wavenumbers plotted, the energy dissipation rate is much larger within the unstable range than outside it. The absolute values of the total area under both curves are ≈ 4.78.

[22]. Numerous results have shown that the large-scale stable modes are critical in the saturation of ITG turbulence [30, 23, 24], however, those are not taken into consideration in these mechanisms.

ITG turbulence has been well characterized by observations from gyrokinetic and fluid simulations. While most observations are made above the NLCG, we will show in Sec. 4.2 that turbulence features remain similar below the NLCG. Key features include the following. 1) In the wavenumber range of instability there is a large removal rate of fluctuation energy by nonlinearly excited stable modes [25]), which can be seen in Fig. 4.1, where the result is derived from an adiabatic-electron Cyclone-Base-Case GENE simulation with $\omega_{T_\mathrm{i}} = 7$ (in units of R_0/L_{T_i}, the ratio of major radius and temperature gradient scale length). 2) Due to the stable modes, energy transferred toward small scales is mostly removed from the spectrum before reaching the largest wavenumber of the unstable range. This is demonstrated in Fig. 1 of Ref. [31], where it should be noted that inertial transfer, i.e., no energy removal by the stable modes, would yield constant transfer rates. The energy transfer rate will be explicitly defined in Sec. 4.2. 3) Energy transfer to the stable modes goes through the zonal flow, and its rate matches the energy input rate from the instability (see Fig. 9 of Ref. [20]). Net energy uptake by the zonal flow is small ($< 10\%$) in relation with the energy transferred to the stable mode. 4) The triplet decorrelation rate of the interaction of unstable mode, stable mode, and zonal flow, which mediates saturation, is a minimum relative to that of other interactions (see Fig. 13 of Ref. [20]). These features need to be accounted for in theories of the critical-gradient upshift.

These observations contradict foundational tenets of the shearing paradigm for zonal-flow regulation. Consider, for example, the wave-action-invariance argument of zonal-flow regulation via shearing [27]: shearing enhances energy transfer to $k_x > 1$ (here and throughout this chapter wavenumbers are all normalized with the ion sound gyroradius ρ_s); energy at these scales then lowers the wave frequency, which in turn lowers wave energy to maintain invariance of wave action; lower wave energy is then offset by an increase in zonal flow energy, which through its shearing perpetuates the process. The underlying premise of wave-action invariance is invalidated by the sizable large-scale dissipation seen in Fig. 4.1. The subsequent effects of the wave-action-invariance argument are contradicted by observation: most cascaded energy fails to reach even $k_x = 0.5$ before being removed from the system, the zonal flow only takes up a small fraction of transferred energy, and the nonlinear decorrelation rate is minimized, while in the shearing hypothesis it increases.

Our analysis of saturation below and above the NLCG starts with nonlinear simulations using the gyrokinetic code GENE [24]. We find that the heat flux below the NLCG increases slowly relative to the growth rate, then smoothly but rapidly increases its slope near the NLCG. The latter is not precisely defined or indicative of a bifurcation, as evident from continuously varying nonlinear energy transfer rates that set fluctuation levels. Both direct transfer in single sets of wavenumber triplets and cascading transfer through a series of triplets are qualitatively the same below and above the NLCG. Moreover, the character of this transfer will be shown in Sec. 4.2 to be consistent with saturation by stable modes accessed via zonal flows. Both the zonal-flow shearing rate and the ratio of shearing rate with linear growth rate are larger above the NLCG than below it.

Consistent with these results, we develop a theory for the heat flux that is valid below and above the NLCG [21]. Both regimes are nonlinear and will be called the low and high transport regimes, respectively. The theory is based on a tractable nonlinear fluid model [30] modified to recover the linear dispersion relation and instability threshold condition of a drift-kinetic calculation [29]. Low and high transport regimes naturally emerge from a single saturation mechanism — energy transfer through the zonal flow to stable modes. This interaction is nearly resonant, producing weak transport near threshold. Transport increases sharply at higher gradients due the gradient dependencies in resonance-broadening effects.

The heat flux depends on the fluctuation levels of unstable and stable modes, and the complex-valued cross-correlation of the two modes. We solve for these quantities using conjugate symmetry and nonlinear energy conservation. The relationship between levels of unstable and stable modes is consistent with dissipation-rate equipartition [24]. Because of nonlinear symmetry that leads to the cancellation of nonlinear terms affecting the eigenmode cross correlation, its phase depends mostly on linear physics. With these relationships, a single saturation balance suffices to determine the heat flux. This balance is solved accounting for all eigenmode levels and and explicitly handling wavenumber variation using a Markovian procedure.

The near-resonant effects that suppress the flux just above the linear threshold include a complex-wave-frequency resonance from the correlation time of the triplet interaction, a measure of the nonlinear interaction lifetime, of the unstable mode, zonal flow, and stable mode. In the limit that the collisionality and perpendicular wavenumber go to zero, the linear part of the correlation time goes to infinity, which allows a vanishingly small turbulence level to match the energy input of the instability, resulting in zero heat flux. The resonance is broadened by collisionality and the ion polarization drift, both of which give a small residual heat flux that increases with temperature gradient. The nonlinear coupling coefficient, which is a function of eigenmode frequency, also contributes to the small heat flux just above the linear critical gradient, and its eventual steep rise at larger gradient values.

This chapter is organized as follows. Section 4.2 describes gyrokinetic observations of turbulence in the low and high transport regimes. In Sec. 4.3, a fluid model for toroidal ITG turbulence is introduced, modified to match a kinetic dispersion relation and its critical gradient for instability, and transformed to the eigenmode decomposition. In Sec. 4.4, the relationships between eigenmode amplitudes and the eigenmode cross correlation are derived and used to obtain a succinct expression for the heat flux in terms of the unstable mode level. Statistical closure theory is applied in Sec. 4.5, and an expression for the eddy damping rate associated with zonal-flow-catalyzed transfer is derived. The nonlinear balance for the overall turbulence level is solved in Sec. 4.6 and used to obtain a heat flux expression valid in low and high transport regimes. Section 4.7 provides concluding remarks.

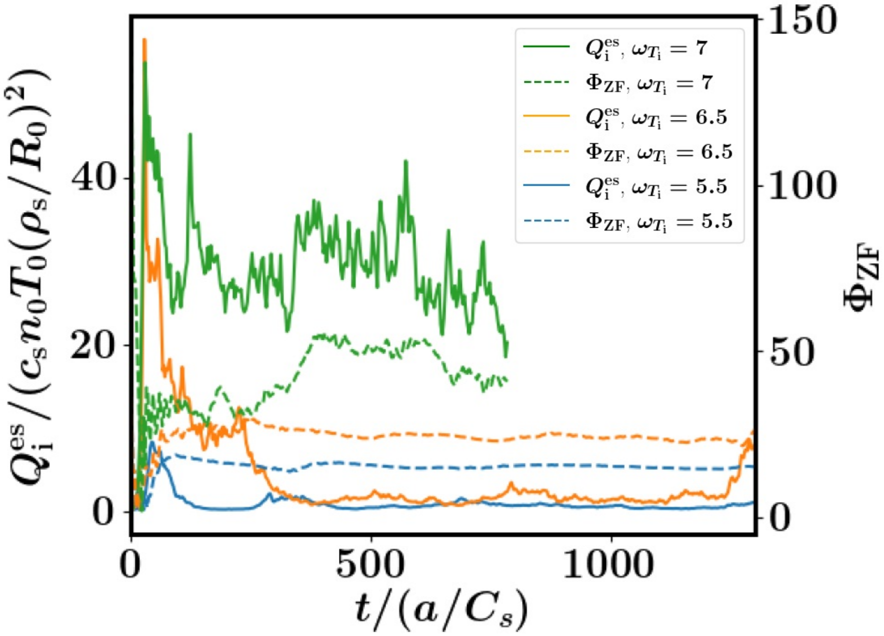

Figure 4.2: Time history of $Q_{\mathrm{i}}^{\mathrm{es}}$ and Φ_{ZF} for saturated ITG turbulence from gyrokinetic simulations for $\omega_{T\mathrm{i}} = 5.5$, $\omega_{T\mathrm{i}} = 6.5$, and $\omega_{T\mathrm{i}} = 7$. The NLCG is at $\omega_{T\mathrm{i}} \approx 6.5$.

4.2 Comparative Turbulence Analysis

While the heat flux and turbulence levels are small in the low-transport regime, they are not zero. This can be seen in Fig. 4.2, where the linear critical gradient is $\omega_{T\mathrm{i}} \approx 4.75$ and the NLCG is $\omega_{T\mathrm{i}} \approx 6.5$. Given these values, $\omega_{T\mathrm{i}} = 5.5$ is in the low-transport regime, $\omega_{T\mathrm{i}} = 6.5$ is around the NLCG, and $\omega_{T\mathrm{i}} = 7$ is above the NLCG. Gyrokinetic simulations show that in many respects, aside from overall levels, the turbulence in the low and high transport regimes is very similar. Figures 4.2–4.5 show results from analyses of gyrokinetic simulation data obtained with the turbulence code Gene [24] for the parameters of the collisionless adiabatic-electron Cyclone-Base-Case [11]. The Gene simulation details can be found in the appendix of Ref. [30]. In Fig. 4.3, the energy spectrum

$$E_k = \mathrm{Re}\left\{\sum_j \int \frac{n_{j0}T_{j0}}{F_{j0}}\left[g_{j,k} + \frac{q_j F_{j0}}{T_{j0}}\chi_{j,k}\right]^* g_{j,K}dzdv\right\}, \tag{4.1}$$

is plotted as a function of k_x and k_y, the radial and poloidal wavenumbers, respectively, where $g_{j,k}$ is the nonadiabatic distribution function for species j with wavenumber k, $\chi_{j,k}$ is the modified potential (which, in general, is comprised of both electrostatic and electromagnetic component), n_{j0} is the background density, $T_{j,0}$ is the background temperature, q_j is the charge, F_{j0} is the background Maxwellian, z is the parallel coordinate, and v is the velocity. The plots represent two values of the temperature gradient $\omega_{T\mathrm{i}}$, with $\omega_{T\mathrm{i}} = 5.5$ for a), while for b) $\omega_{T\mathrm{i}} = 7$. In a) the $k_y = 0$ energy is plotted at 0.01 of its actual value, while in b) the $k_y = 0$ energy is plotted at 0.1 of its actual value. The spectra are qualitatively similar. Below the NLCG the spectrum extent is somewhat more restricted in k_x and k_y, and the peak is shifted moderately to higher k_y. Both of these tendencies are well-matched to the growth rate spectra at the two values of $\omega_{T\mathrm{i}}$, which show reductions of peak growth rate and unstable range by a factor of ~ 2 for $\omega_{T\mathrm{i}} = 5.5$ relative to $\omega_{T\mathrm{i}} = 7$ [30].

In Fig. 4.4, spectral energy transfer rates $\langle T_{k,k'}\rangle$ are plotted, again for $\omega_{T\mathrm{i}} = 5.5$ and 7, where

$$T_{k,k'} = 2\mathrm{Re}\left\{\sum_j \int \frac{n_{j0}T_{j0}}{F_{j0}}\left[g_{j,k} + \frac{q_j F_{j0}}{T_{j0}}\chi_{j,k}\right]^* \left(k'_x k_y - k_x k'_y\right)\left[\chi_{j,k'} g_{j,k''}dzdv\right]\right\}, \tag{4.2}$$

the angle brackets represent the time average, and $k'' = k - k'$. The energy transfer rate into each grid cell is registered by color. Energy is transferred directly from the mode $(k_x, k_y) = (0, 0.2)$. Thus in Fig. 4.4 a) energy is removed from $(k_x, k_y) = (0, 0.2)$ and deposited into $(k_x, k_y) = (0.086, 0.2)$. Energy transferred from $(k_x, k_y) = (0, 0.2)$ to the cells with $k_x > 0.086$ and $k_y = 0.2$ is very small. In Fig. 4.4 a) energy

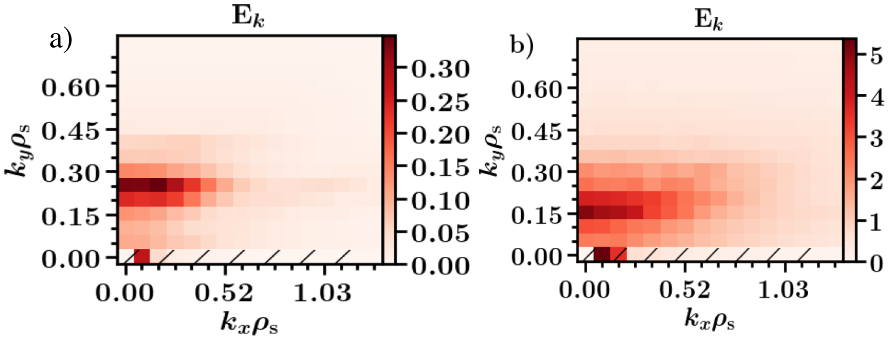

Figure 4.3: The time-averaged energy spectra of the ITG turbulence for saturated gyrokinetic simulations for a) $\omega_{T\mathrm{i}} = 5.5$ and b) $\omega_{T\mathrm{i}} = 7$. The NLCG is at $\omega_{T\mathrm{i}} \approx 6.5$. Both show strong band structure in the k_x direction, and modes are only strongly excited in the low-k regime. To better see how energy is distributed the $k_y = 0$ energy is plotted at 0.01 of its actual value in a), while the $k_y = 0$ energy is plotted at 0.1 of its actual value in b).

is removed from $(k_x, k_y) = (0, 0.2)$ and deposited into a number of cells to its right, with significant energy going into $(k_x, k_y) = (0.086, 0.2)$ and $(k_x, k_y) = (0.172, 0.2)$ and a much smaller quantity going to cells with $k_x > 0.172$ and $k_y = 0.2$. This prominent horizontal feature represents transfer to modes with $k_y = 0.2$ and various k_x, and requires coupling to the zonal modes $(k_x, 0)$. Its prominence reflects the fact that zonal-flow-catalyzed transfer is the dominant transfer channel. Transfer in the low and high transport regimes is similar; the greater extent of $\langle T_{k,k'} \rangle$ in k_y is consistent with a stronger and broader growth rate spectrum above the NLCG.

Fig. 4.5 shows the energy transferred from modes $(0, k_y)$ to wavenumbers on horizontal bands at different k_y through a sequence of interactions with the zonal flow $(0.086, 0)$. The sequence represents energy moving to higher k_x at a single $k_y = 0.2$ by increments of $\delta k_x = 0.086$, with color measuring the transfer in each step of the cascade, i.e., into a given cell from the cell immediately to its left. A tabular representation of the data involved in making a figure like Fig. 4.5 is given in Ref. [17] (Fig. 2). The energy measured is associated with the squared fluctuating

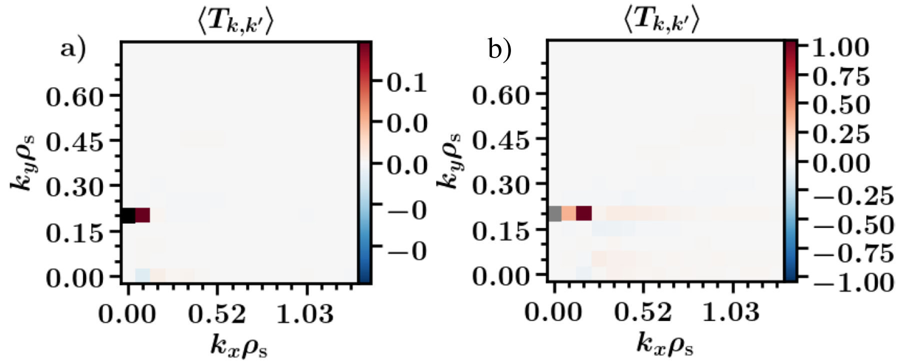

Figure 4.4: The time-averaged rate of direct energy transfer from $(k_x, k_y) = (0, 0.2)$ to grid cells for a) $\omega_{T\mathrm{i}} = 5.5$ and b) $\omega_{T\mathrm{i}} = 7$ at saturated state. The prominent horizontal bands for $k_y = 0.2$ represent the major energy transfer channel is the zonal-flow-catalyzed energy transfer.

distribution function $g_{j,k}$, a quantity that is sometimes called the entropy. The transfer rate is defined as

$$T^g_{k,k'} = 2\mathrm{Re}\left\{\sum_j \int \frac{n_{j0}T_{j0}}{F_{j0}} g^*_{j,k}\left(k'_x k_y - k_x k'_y\right)\left[\chi_{j,k'} g_{j,k''} dz dv\right]\right\}. \tag{4.3}$$

Panels a) and b) correspond to $\omega_{T\mathrm{i}} = 5.5$ and 7, respectively. This cascade analysis shows that energy is depleted with each step — a conservative (inertial-range) cascade mediated by zonal-flow interactions would show constant color across k_x. Evidently, a significant amount of energy is lost inside the unstable wavenumber band. This plot is nearly identical to Fig. 1 of Ref. [21], which shows energy cascaded to stable modes. Moreover, Fig. 1 of Ref. [31], which shows the zonal-flow-catalyzed energy transfer rate to the higher-k_x stable and unstable modes in the range $0 < k_x <\sim 0.25$ at $k_y = 0.4$, indicates that the stable modes within the unstable range remove ≈ 70% of the energy produced by the unstable modes. Therefore, the cascade depletion is caused by stable modes. Taken together, panels a) and b) show that energy cascade characteristics are similar in the low- and high-transport regimes, with differences primarily arising from the larger fluctuation level and broader growth rate spectrum for $\omega_{T\mathrm{i}} = 7$, which leads to a more robust cascade.

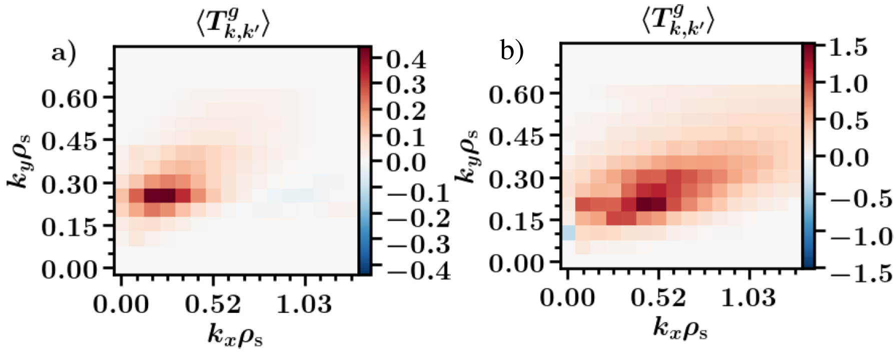

Figure 4.5: The time-averaged energy transfer in the zonal-flow mediated entropy cascade beginning at modes with $k_x = 0$ and different k_y to higher k_x for a) $\omega_{T\mathrm{i}} = 5.5$ and b) $\omega_{T\mathrm{i}} = 7$ at saturated state.

The zonal-flow shearing rate $\omega_\mathrm{s} = \sum_{k_x} k_x^2 |\Phi_\mathrm{ZF}|$, measured for $4.75 < \omega_{T\mathrm{i}} < 8$, is larger than the linear growth rate γ. The ratio $\omega_\mathrm{s}/\gamma \approx 3$ just above the linear threshold. As the gradient increases toward the NLCG the ratio slides to ~ 1.5, and then above the NLCG jumps to > 4. This behavior is shown in Fig. 2 of Ref. [21]. This is inconsistent with the notion that the larger fluctuation levels above the NLCG are due to a loss of efficacy of the shearing mechanism, and indicates that zonal flow shearing is not the primary arbiter of the gradient upshift.

Figs. 4.3–4.5 indicate that there is a range of strong energy removal embedded in the energy containing scales of ITG turbulence, but unlike collision-induced dissipation, energy removal is only accessed by the nonlinearity. This range of strong energy removal accounts for the well known observation that transport due to ITG turbulence is insensitive to enhanced resolution in scales beyond the unstable range. With respect to temperature gradient variation, Figs. 4.3–4.5 indicate that the energy balances that mediate saturation do not show obvious changes above the NLCG relative to below it, beyond those tied to the larger growth rates and fluctuation levels. Importantly, these figures illustrate each of the characterizations of ITG turbulence listed in Sec. 4.1. They show the large energy removal from stable modes at low wavenumber, the significant depletion of cascaded energy, and the role of the zonal flow in mediating energy transfer to stable modes. Critically, these features apply in both the low and high transport regimes. These results strongly suggest that zonal-flow-catalyzed transfer to stable modes mediates saturation in both regimes, and indicate that the theory previously developed for the strong-transport regime [30] should have features of the critical-gradient upshift if modified to account for the ITG instability threshold.

4.3 Threshold Fluid Model

We develop a fluid theory that is valid in both the low and high transport regimes. The theory is based on a reduced model for toroidal ITG turbulence that has been shown to capture the important properties of ITG turbulence discussed in the previous section [30]. This model yields solutions with strong zonal flows and provides insight about zonal-flow-catalyzed interactions, including the central idea that turbulence saturation is governed by the efficiency of energy transfer from the unstable modes to stable modes via nonlinear coupling with the zonal flow. The magnitude of the nonlinearity is determined by coupling coefficients, which quantify coupling strength between the linear eigenmodes; the eigenmode amplitudes; and the complex phases between coupled eigenmodes. The crucial complex phase for saturation is that of the cubic fluctuation correlation that governs energy transfer. With the nonlinearity described explicitly in these terms, the mechanism of turbulence saturation becomes more transparent.

The saturation theory was developed for a version of the model that does not include all necessary threshold physics associated with the onset of linear instability. As such it will not produce a reasonable description of the low and high transport regimes. Therefore, we reformulate the model to make its linear dispersion relation match that of a simplified drift-kinetic linear-instability calculation given by Hammett [29]. In the kinetic calculation, the ∇B and curvature drifts are retained in the equation for the perturbed ion distribution, yielding

$$(-i\omega+ik_\parallel v_\parallel+i\omega_{\mathrm{d}v})\tilde{f}_{\mathrm{i}} = -i\left\{-\frac{T_{\mathrm{i}}k}{eBL_n}\left[1+\eta\left(\frac{v_\parallel^2}{2v_{\mathrm{i}}^2}+\frac{\mu B}{v_{\mathrm{i}}^2}-\frac{3}{2}\right)\right]+\omega_{\mathrm{d}v}+k_\parallel v_\parallel\right\}\frac{e\phi}{T_{\mathrm{i}}}F_{\mathrm{i}0}\ , \tag{4.4}$$

where $\omega_{\mathrm{d}v} = \omega_d(v_\parallel^2+\mu B)/v_{\mathrm{i}}^2$ is the particle-velocity-dependent magnetic drift frequency, with $\omega_{\mathrm{d}} = -T_{\mathrm{i}}k/(eBR)(\cos y + \hat{s}y\sin y) = -T_{\mathrm{i}}k/(eBR)[1+\mathcal{O}(y^2)]$ for $y \ll 1$. Here, y is the ballooning angle (angular distance along the field), $\hat{s}$ is the magnetic shear, k is the poloidal wavenumber, $F_{\mathrm{i}0} = (n_0(x)/T_{\mathrm{i}0}(x)^{3/2})\,\exp[-m(v_\parallel^2/2+\mu B)/T_{\mathrm{i}0}(x)]$ is the equilibrium distribution, e is the ion charge, R is the major radius, and $n_0(x)$ and $T_{\mathrm{i}0}(x)$ are profiles of equilibrium density and ion temperature. Perpendicular velocity is expressed in terms of the magnetic moment $\mu = (1/2)v_\perp^2/B$, while $v_{\mathrm{i}} = (2T_{\mathrm{i}}/m_{\mathrm{i}})^{1/2}$ is the ion thermal velocity, $\eta = L_n/L_{T\mathrm{i}}$, and L_n and $L_{T\mathrm{i}}$ are the density and ion temperature gradient scale lengths, respectively.

The mode dispersion relation is obtained from the quasineutrality condition, $\tilde{n}_{\mathrm{i}} = \tilde{n}_{\mathrm{e}}$, with $\tilde{n}_{\mathrm{e}} = e\phi/T_{\mathrm{e}0}$ given by the adiabatic electron response, and $\tilde{n}_{\mathrm{i}} = \int d^3v\tilde{f}_{\mathrm{i}}$. Making the substitutions,

$$n_0\frac{e\phi}{T_{\mathrm{e}0}} = \int d^3v\frac{-\omega_{*v}^T+\omega_{\mathrm{d}v}}{\omega-\omega_{\mathrm{d}v}}F_{\mathrm{i}0}\frac{e\phi}{T_{\mathrm{i}0}}\ , \tag{4.5}$$

where, consistent with the toroidal ITG branch, we have assumed $k_\parallel v_\parallel \ll \omega$, $\omega_{\mathrm{d}v}$, ω_{*v}^T. The ion polarization contribution to the density has been neglected but will be introduced when the kinetic results are adapted to a fluid model. For ITG instability, it is possible to impose the approximation $\omega \gg \omega_{\mathrm{d}v}$, which allows expansion of the denominator in Eq. (4.5) and greatly simplifies the integration.

With this assumption, $(\omega-\omega_{\mathrm{d}v})^{-1}=\omega^{-1}[1+(\omega_{\mathrm{d}v}/\omega)+\ldots]$. Performing the velocity integrals, Eq. (4.5) reduces to

$$\frac{T_{\mathrm{i}0}}{T_{\mathrm{e}0}}=\frac{2\omega_{\mathrm{d}}}{\omega}-\frac{\omega_*}{\omega}+\frac{7\omega_{\mathrm{d}}^2}{\omega^2}-\frac{2\omega_{\mathrm{d}}\omega_*}{\omega^2}(1+\eta)\ , \tag{4.6}$$

where $\omega_*=-T_{\mathrm{i}0}k/(eBL_n)$. In the weak-density-gradient limit, where $\omega_*\ll\omega_*(1+\eta),\omega_{\mathrm{d}}$, solution of the quadratic dispersion relation yields

$$\omega=\left[\omega_{\mathrm{d}}\pm\sqrt{\omega_{\mathrm{d}}^2-\frac{T_{\mathrm{i}0}}{T_{\mathrm{e}0}}(2\omega_{\mathrm{d}}\bar{\omega}_{*\eta}-7\omega_{\mathrm{d}}^2)}\right]\frac{T_{\mathrm{e}0}}{T_{\mathrm{i}0}}\ , \tag{4.7}$$

where $\bar{\omega}_{*\eta}=\omega_*(1+\eta)$. Instability requires that $\bar{\omega}_{*\eta}$ exceed a threshold arising from the magnetic drift frequency, i.e., $\bar{\omega}_{*\eta}>(\omega_{\mathrm{d}}/2)(7+T_{\mathrm{e}0}/T_{\mathrm{i}0})$. For $L_{T\mathrm{i}}\ll L_n$ (i.e., $\eta\gg1$), this corresponds to a critical gradient given by $1/L_{T\mathrm{i}}>1/L_{T\mathrm{c}}=[1/(2R)](7+T_{\mathrm{e}0}/T_{\mathrm{i}0})$. Hereafter, we will assume $T_{\mathrm{e}0}/T_{\mathrm{i}0}=1$.

Both the kinetic calculation and the original fluid model for for the strong-transport regime [30, 15, 31] have quadratic dispersion relations. Therefore, it is possible to modify the fluid model so that it reproduces the kinetic dispersion relation. The reformulated fluid model is

$$\frac{dp_k}{dt}+\left[i\epsilon k_y\left(1+\sqrt{8}\right)+\chi k_\perp^4\right]p_k+ik_y\left(1+\eta\right)\phi_k=-\sum_{k'}(\mathbf{k}'\hat{\mathbf{z}}\cdot\mathbf{k})\phi_{k'}p_{k''}\ , \tag{4.8}$$

$$\begin{aligned}\left[\delta(k_y)+k_\perp^2\right]\frac{d\phi_k}{dt}-2i\epsilon k_y p_k+\left[ik_y+\nu k_\perp^2+ik_y\epsilon\left(1-\sqrt{8}\right)\right]\phi_k\\ =\frac{1}{2}\sum_{k'}(\mathbf{k}'\times\hat{\mathbf{z}}\cdot\mathbf{k})(k_\perp'^2-k_\perp''^2)\phi_{k'}\phi_{k''}\ ,\end{aligned} \tag{4.9}$$

where p_k and ϕ_k, respectively, are Fourier amplitudes of pressure and electrostatic potential, ν and χ are coefficients of collisional dissipation, and $\epsilon=L_n/R$. The wavenumber subscript k refers to the perpendicular wavevector $\mathbf{k}$, with a poloidal component k_y [denoted k in Eqs. (4.4)–(4.7)] and a radial component generated in the ballooning representation by shifts of the mode structure along the field line with respect to the outboard midplane. Aside from this shift required for the mode coupling $\mathbf{k}' \times \hat{\mathbf{z}} \cdot \mathbf{k}$, the eigenmodes are assumed to be strongly ballooning, making Eqs. (4.8) and (4.9) local in ballooning angle. The adiabatic electron response is $\delta(k_y)$, valid for all k_y, i.e., $\delta(k_y) = 0$ for $k_y = 0$, and $\delta(k_y) = 1$ for $k_y \neq 0$. In Eqs. (4.8) and (4.9), the parallel scale is normalized to L_n, and perpendicular scales are normalized to the sound gyroradius $\rho_{\rm s}$, rendering $\omega_{\rm d}$ as $k_y\epsilon$. The ion polarization drift has been included, producing $k_\perp^2 d\phi_k/dt$ and the nonlinearity in Eq. (4.9). The most important difference between this threshold model and prior versions in the literature [30, 15, 31] is the term $i\epsilon k_y(1+\sqrt{8})p_k$ in the pressure equation. Absent in prior versions, it provides the correct linear instability threshold. There are other less significant variations as follows. While $T_{\rm e0} = T_{\rm i0}$ is assumed in all models under discussion, in Ref. [31] ν and χ are not included and the factor $(1-\sqrt{8})$ in Eq. (4.9) is replaced by -2. In Refs. [30, 15] the vorticity equation has $-i\epsilon k_y p_k$ for the pressure term, and the term $ik_y\epsilon(1-\sqrt{8})\phi_k$ does not appear in any form.

Consistent with a low-wavenumber regime, we assume $\chi k_\perp^2 \ll \nu$, in which case the dispersion relation is given by

$$\begin{aligned}\omega_{1,2} \;=\; & \frac{1}{2\left(1+k_\perp^2\right)}\Bigg\{ k_y + k_y\epsilon\left[2+\left(1+\sqrt{8}\right)k_\perp^2\right] - i\nu k_\perp^2 \\ & \pm\sqrt{-8\epsilon k_y^2\left(1+\eta\right)\left(1+k_\perp^2\right) + \left[-k_y + \epsilon k_y\left(4\sqrt{2}+\left(1+\sqrt{8}\right)k_\perp^2\right) + i\nu k_\perp^2\right]^2}\,\Bigg\}\,,\end{aligned} \tag{4.10}$$

where ± distinguishes the unstable and stable branches $\omega_{1,2}$. There is no assumption of weak density gradient in Eq. (4.10). However, we recover an exact match to Eq. (4.7) for $T_{\rm e0} = T_{\rm i0}$ in the weak-density limit. Since the L_n dependence in Eq. (4.10) is hidden in normalizations, its weak-density limit is readily checked by replacing $L_n \to \infty$ with $k_y \to 0$, subject to $k_y(1+\eta) = \omega_{*\eta} \sim 1$, $\epsilon k_y = \omega_{\mathrm{d}} \sim 1$, and $k_\perp^2 \ll 1$.

To use Eqs. (4.8) and (4.9) for deriving the ITG heat flux in the low and high transport regimes, it is necessary to transform them to the eigenmode decomposition, which represents an arbitrary state p_k and ϕ_k as a finite-amplitude combination of the two linear eigenmodes, to whit,

$$\begin{pmatrix} p_k \\ \phi_k \end{pmatrix} = \beta_1(k) \begin{pmatrix} R_1(k) \\ 1 \end{pmatrix} + \beta_2(k) \begin{pmatrix} R_2(k) \\ 1 \end{pmatrix} . \tag{4.11}$$

Here, $[R_1(k), 1]$ and $[R_2(k), 1]$ are the eigenvectors of the unstable and stable modes, with eigenvector components R_1 and R_2 given by

$$R_{1,2}(k) = \frac{-\omega_{1,2}(1+k_\perp^2) + k_y[1+\epsilon(1-\sqrt{8})] - i\nu k_\perp^2}{2k_y\epsilon} . \tag{4.12}$$

The eigenmode amplitudes $\beta_1(k)$ and $\beta_2(k)$ are governed by nonlinear balances consistent with the transformation of Eqs. (4.8) and (4.9) by the decomposition, Eq. (4.11). These equations are

$$\begin{aligned} \dot\beta_l + i\omega_l\beta_l &= \sum_{k',k'_y\neq 0} C^{(k,k')}_{lmn}\beta'_m\beta''_n + \sum_{k'_x}\Bigg\{ \left[C^{(k,k')}_{lFn} v'_z\beta''_n + C^{(k,k')}_{lPn} p'_z\beta''_n \right]\Bigg|_{k'_y=0} \\ &\quad + \left[C^{(k,k')}_{lmF}\beta'_m v''_z + C^{(k,k')}_{lmP}\beta'_m p''_z \right]\Bigg|_{k'_y=k_y} \Bigg\} , \end{aligned} \tag{4.13}$$

$$\dot v_z + \nu v_z = \sum_{k'} C^{(k,k')}_{Fmn}\beta''_m\beta'_n\Big|_{k_y=0} , \tag{4.14}$$

$$\dot p_z + \chi k_x^2 p_z = \sum_{k'} C^{(k,k')}_{Pmn}\beta''_m\beta'_n\Big|_{k_y=0} , \tag{4.15}$$

where l, m, and n take the values 1 or 2, and repetition of these indices within a given term implies summation from 1 to 2, and F and P represent zonal flow and zonal pressure. Equations for the nonlinear coupling coefficients will be given below. In writing Eqs. (4.13)–(4.15), the zonal flow and zonal pressure, which are eigenmodes for $k_y = 0$, are written explicitly. A shorthand notation has been introduced for wavenumber dependence as follows: $\beta_j = \beta_j(k)|_{k_y \neq 0}$, $\beta_j' = \beta_j(k')|_{k_{y'} \neq 0}$, $\beta_j'' = \beta_j(k - k')|_{k_y'' \neq 0}$, $v_z = v_z(k)|_{k_y=0}$, $v_z' = v_z(k')|_{k_y'=0}$, $v_z'' = v_z(k-k')|_{k_y'=k_y}$, $p_z = p_z(k)|_{k_y=0}$, $p_z' = p_z(k')|_{k_y'=0}$, and $p_z'' = p_z(k-k')|_{k_y'=k_y}$, where $v_z = ik_x\phi_{k_y=0} = ik_x\phi_z$ is the zonal flow and p_z is the zonal pressure.

Figs. 2 and 3 indicate that the terms of the right-hand side of Eq. (4.13) with factors v_z' and v_z'' dominate the nonlinearities both below and above the NLCG in the corresponding gyrokinetic system. This result can be built into Eqs. (4.13)–(4.15) by introducing an ordering scheme previously used for saturation analysis above the NLCG [30]. For that ordering a small parameter $\hat{\epsilon}$ is introduced, and it is assumed that

$$k_y, k_\perp \sim \hat{\epsilon}^2 \ , \qquad v_z/p_z \sim \hat{\epsilon} \ , \qquad \beta_{1,2}/\phi_z \sim \hat{\epsilon}^2 \ . \tag{4.16}$$

These expressions reflect features observed in simulations, but also are rooted in physics. The first assumes that spectral energy transfer, fluctuation levels, and transport rates are dominated by long wavelengths, consistent with the large fraction of energy removed by stable modes at long wavelengths. The second is consistent with the long-wavelength assumption, given that p_z and ϕ_z are similar and $v_z \sim k_x\phi_z$. The third reflects the common observation that spectra peak at zonal wavenumbers. This is not the only ordering consistent with the dominance of the zonal-flow-catalyzed interaction, but is sufficient to produce it. When applied to Eqs. (4.13)–(4.15), the zonal pressure decouples, and the system reduces to

$$\dot{\beta}_l + i\omega_l\beta_l = \sum_{k_x'} \left\{ \left[C_{lFj}^{(k,k')} v_z' \beta_j'' \right]\Big|_{k_y'=0} + \left[C_{ljF}^{(k,k')} \beta_j' v_z'' \right]\Big|_{k_y'=k_y} \right\} \ , \tag{4.17}$$

$$\dot{v}_z + \nu v_z = \sum_{k'} \left[C_{Fmn}^{(k,k')} \beta_m'' \beta_n' \right]\Big|_{k_y=0} \ , \tag{4.18}$$

where l, m, and n are 1 or 2, and the coupling coefficients are given by

$$C_{lFn}^{(k,k')} = \frac{(-1)^{l-1}(-ik_y)}{2\left(R_1(k)-R_2(k)\right)}\left[R_n(k'') - \frac{R_{3-l}(k)[k_\perp''^2 - k_\perp'^2]}{1+k_\perp^2}\right] , \tag{4.19}$$

$$C_{lmF}^{(k,k')} = \frac{(-1)^{l-1}(-ik_y')}{2\left(R_1(k)-R_2(k)\right)}\left[R_m(k') - \frac{R_{3-l}(k)[k_\perp''^2 - k_\perp'^2]}{1+k_\perp^2}\right] , \tag{4.20}$$

$$C_{Fmn}^{(k,k')} = \frac{-ik_y'(k_\perp''^2 - k_\perp'^2)}{2} . \tag{4.21}$$

Equations (4.17) and (4.18) represent an energy-conserving reduction of the larger set of nonlinear interactions present in Eqs. (4.13)–(4.15). Consequently, these equations, which isolate zonal-flow-catalyzed transfer to the stable mode, give a realistic model of the physics that dominates saturation and transport in the ITG-driven system under investigation. The coupling coeefficients of Eqs. (4.19) and (4.20) combine the two nonlinearities of Eqs. (4.8) and (4.9). The first term in the square brackets represents the pressure nonlinearity of Eq. (4.8) and the second the vorticity nonlinearity of Eq. (4.9).

4.4 Relationships between Turbulent Correlations

The ion heat flux is given by $Q_\mathrm{i} = -\sum_k k_y \mathrm{Im}\langle\phi_{-k}p_k\rangle$, requiring a solution for the nonlinear correlation $\langle\phi_{-k}p_k\rangle$ consistent with steady state solutions of Eqs. (4.17) and (4.18). The first step is to render the flux in the eigenmode decomposition by substituting from Eq. (4.11), yielding

$$Q_\mathrm{i} = -\sum_k k_y \left[\mathrm{Im}R_1\,|\beta_1|^2 + \mathrm{Im}R_2\,|\beta_2|^2 + \mathrm{Im}(R_1+R_2)\mathrm{Re}\langle\beta_1\beta_2^*\rangle + \mathrm{Re}(R_1-R_2)\mathrm{Im}\langle\beta_1\beta_2^*\rangle\right] . \tag{4.22}$$

Noting that $\mathrm{Im}R_1$ is proportional to γ, the first term is essentially the quasilinear flux, assuming $|\beta_1|^2$ is supplied from a nonlinear simulation or a measurement. The remaining terms, which arise because of the nonlinear excitation of the stable mode, require solution for $|\beta_2|^2$ and $\langle\beta_1\beta_2^*\rangle$. There are also parametric dependencies in $|\beta_1|^2$ that can be missed in quasilinear theory and will be treated here, as well. Missed dependencies are illustrated by nonlinear finite-β electromagnetic stabilization, where the ITG heat flux decreases with β more strongly than the growth rate [32, 39]. The parameter β is the plasma pressure normalized by the magnetic pressure. This can be explained in part by an important scaling of $|\beta_1|^2$ with β arising from the nonlinear correlation time that mediates saturation [33, 34]. In the modeling of Refs. [33, 34], contributions to the heat flux from $|\beta_2|^2$ and $\langle\beta_1\beta_2^*\rangle$ were neglected. Here, they are retained and calculated to formulate a description of the critical-gradient upshift.

In saturation, $|\beta_j|^2$ and $\langle\beta_1\beta_2^*\rangle$ can be evaluated from energy evolution equations of statistical closure theory, as done in Ref. [30]. These equations are linearized when energy transfer is dominated by the interaction of unstable mode, stable mode, and zonal flow. The equations have robust parameter scalings, but their solution requires the inversion of a large matrix, and interpretation of individual roots is difficult. Here we utilize an approach based on nonlinear conservation properties and the nearly conjugate symmetry of unstable and stable modes for small ν. Conjugate symmetry carries over to the nonlinear couplings in the eigenmode decomposition, as seen in Eqs. (4.19) and (4.20). These symmetries produce relationships between $|\beta_2|^2$, $\langle\beta_1\beta_2^*\rangle$, and $|\beta_1|^2$ that for low collisionality, small wavenumber, and steady state are governed by linear physics. As a result, Eq. (4.22) can be expressed solely in terms of $|\beta_1|^2$. We derive these relationships in this section and solve a nonlinear balance for $|\beta_1|^2$ in Sec. 4.5.

We first consider the complex correlation $\langle\beta_1\beta_2^*\rangle$ and the physics of its cross phase, which have received limited attention. For turbulence governed by Eqs. (4.17) and (4.18), the phase is dominated by linear physics. Consider summing Eq. (4.17) over $l = 1, 2$, yielding

$$\begin{aligned} &\dot{\beta}_1 + \dot{\beta}_2 + i\omega_1\beta_1 + i\omega_2\beta_2 = \\ &\sum_{k'_x} \left[\left(C_{1F1}^{(k,k')} + C_{2F1}^{(k,k')} \right) \beta''_1 + \left(C_{1F2}^{(k,k')} + C_{2F2}^{(k,k')} \right) \beta''_2 \right] v'_z \bigg|_{k'_y=0} \\ &+ \sum_{k'_x} \left[\left(C_{11F}^{(k,k')} + C_{21F}^{(k,k')} \right) \beta'_1 + \left(C_{12F}^{(k,k')} + C_{22F}^{(k,k')} \right) \beta'_2 \right] v''_z \bigg|_{k'_y=k_y} . \end{aligned} \tag{4.23}$$

From Eqs. (4.19) and (4.20), it is readily found that

$$C_{1F1}^{(k,k')} + C_{2F1}^{(k,k')} = C_{1F2}^{(k,k')} + C_{2F2}^{(k,k')} = \frac{-ik_y}{2(1+k_\perp^2)}(k_\perp''^2 - k_\perp'^2) \; , \tag{4.24}$$

$$C_{11F}^{(k,k')} + C_{21F}^{(k,k')} = C_{12F}^{(k,k')} + C_{22F}^{(k,k')} = \frac{-ik'_y}{2(1+k_\perp^2)}(k_\perp''^2 - k_\perp'^2) \; . \tag{4.25}$$

In Eqs. (4.24) and (4.25), the pressure nonlinearity contributions cancel out, while the vorticity nonlinearity contributions add, generating the rightmost expressions. The cancellation occurs because energy removed from the unstable mode through the zonal flow by the pressure nonlinearity is deposited in total into the stable mode. On the other hand, the vorticity nonlinearity removes energy from both modes and deposits it into the zonal flow. It therefore does not cancel in a sum involving $\dot{\beta}_1$ and $\dot{\beta}_2$.

The vorticity nonlinearity is smaller than the pressure nonlinearity by a factor $k_\perp^2$. This is quantified under the ordering that describes the saturation energetics, $C_{lFn} \sim C_{lmF} \sim k \sim \hat{\epsilon}^2$ and $C_{Fln} \sim \hat{\epsilon}^6$, where $\hat{\epsilon}$ is the small ordering parameter. Because the pressure nonlinearity cancels in Eqs. (4.24) and (4.25),

$$\dot{\beta}_1 + \dot{\beta}_2 + i\omega_1\beta_1 + i\omega_2\beta_2 = \mathcal{O}(\hat{\epsilon}^6) \cdot v'_z \beta''_n \; . \tag{4.26}$$

The saturated value of v'_z is order unity, hence the right-hand side of Eq. (4.26) is much smaller than the left-hand side. Consequently, the cross phase of $\langle \beta_1 \beta_2^* \rangle$, which can be constructed from the left-hand side of Eq. (4.26), is dominated by linear physics.

Equation (4.26) indicates that, in the steady state, there is a fixed relation between β_1 and β_2. Accordingly, we adopt the ansatz $\beta_2 = \sqrt{\kappa}\exp(i\theta)\beta_1$, where the saturated mode amplitude ratio $\kappa \equiv |\beta_2|^2 / |\beta_1|^2$ will be determined from a separate relationship that will be introduced shortly. Substituting $\beta_2 = \sqrt{\kappa}\exp(i\theta)\beta_1$ into Eq. (4.26), with the right-hand side set to zero, we obtain

$$\left(1+\sqrt{\kappa}\mathrm{e}^{i\theta}\right)\dot{\beta}_1 + i\left(\omega_1+\omega_2\sqrt{\kappa}\mathrm{e}^{i\theta}\right)\beta_1 = 0\ . \tag{4.27}$$

We multiply Eq. (4.27) by β_1^* and sum it with its conjugate equation, obtaining

$$\left|\dot{\beta}_1\right|^2 - 2\mathrm{Im}\left(\frac{\omega_1+\omega_2\sqrt{\kappa}\mathrm{e}^{i\theta}}{1+\sqrt{\kappa}\mathrm{e}^{i\theta}}\right)|\beta_1|^2 = 0\ . \tag{4.28}$$

This is not an equation for $|\beta_1|^2$ or its evolution, because those require a nonlinear balance. Rather, it is an equation for θ consistent with Eq. (4.26). Having been constructed at the level of squared amplitudes, the imposition of a steady-state condition $|\dot{\beta}_1|^2 = 0$ represents the average of an energy-like quantity with the random phase of the raw amplitude β_1 removed. The stationary condition, aside from the trivial solution $|\beta_1|^2 = 0$, requires

$$\mathrm{Im}\left(\frac{\omega_1+\omega_2\sqrt{\kappa}\mathrm{e}^{i\theta}}{1+\sqrt{\kappa}\mathrm{e}^{i\theta}}\right) = 0\ , \tag{4.29}$$

which is the desired expression that sets the value of θ. Rationalizing the denominator, Eq. (4.29) implies that

$$\mathrm{Im}\left[\left(\omega_1+\omega_2\sqrt{\kappa}\mathrm{e}^{i\theta}\right)\left(1+\sqrt{\kappa}\mathrm{e}^{-i\theta}\right)\right] = \mathrm{Im}\left[\omega_1+\omega_1\sqrt{\kappa}\mathrm{e}^{-i\theta}+\omega_2\kappa+\omega_2\sqrt{\kappa}\mathrm{e}^{i\theta}\right] = 0\ . \tag{4.30}$$

To collect the θ dependence in a single term, we introduce the frequency difference $\Delta\omega = \omega_2 - \omega_1^*$ and write the two ω_2-dependent terms in the right-hand part of the above expression in terms of $\Delta\omega$. Solving the resulting expression for θ yields

$$\theta = -\tan^{-1}\left(\frac{\mathrm{Im}(\Delta\omega)}{\mathrm{Re}(\Delta\omega)}\right) + \sin^{-1}\left[\frac{\mathrm{Im}(\omega_1^* - \omega_2\kappa)}{\sqrt{\kappa}\,|\omega_2 - \omega_1^*|}\right] \ , \tag{4.31}$$

As previously stated, this expression supplies the angle θ in the correlations $\langle\beta_1\beta_2^*\rangle = \sqrt{\kappa}|\beta_1|^2\exp(-i\theta)$, $\mathrm{Re}\langle\beta_1\beta_2^*\rangle = \sqrt{\kappa}|\beta_1|^2\cos\theta$, and $\mathrm{Im}\langle\beta_1\beta_2^*\rangle = -\sqrt{\kappa}|\beta_1|^2\sin\theta$ that appear in Eq. (4.22).

The factor κ is a ratio of saturation levels. The levels for $|\beta_1|^2$ and $|\beta_2|^2$ individually depend on nonlinear balances. However, the similarity properties of nonlinear transfer associated with energy conservation suggest that the nonlinear transfer rates in equations for $|\beta_1|^2$ and $|\beta_2|^2$ are very similar. The ratio of $|\beta_1|^2$ and $|\beta_2|^2$ would then be governed by the ratio of rates of energy injection and removal. This is an observed feature in gyrokinetic simulations, where there are many stable modes [24]. For the conditions of Ref. [24], the energy damping rate of each stable mode is approximately equal for the 1200 modes with smallest damping rates, and their sum balances the energy injection rate. These rates are given by $\gamma_j|\beta_j|^2$. We revisit the tendency of equipartition of these rates for the present simpler system, formulating it from the properties of the equations instead of measuring it as an aspect of a simulation.

We assess the energy rates $\gamma_j|\beta_j|^2$ from the energy itself, which is given by

$$\begin{aligned} E \;=\; & \sum_{k_y\neq 0}\Big[\left(1+k_\perp^2+|R_1|^2\right)|\beta_1|^2 + \left(1+k_\perp^2+|R_2|^2\right)|\beta_2|^2 \\ & + 2\left(1+k_\perp^2\right)\mathrm{Re}\langle\beta_1^*\beta_2\rangle + 2\mathrm{Re}\langle R_1^*\beta_1^*R_2\beta_2\rangle\Big] + \sum_{k_y=0}\left[|p_k|^2 + k_\perp^2\,|\phi_k|^2\right] \end{aligned} \tag{4.32}$$

Because the nonlinear interactions of Eqs. (4.17) and (4.18) are conservative, dE/dt is governed solely by dissipative terms, i.e., the nonlinearities associated with time derivatives of $|\beta_j|^2$ and $\langle\beta_1^*\beta_2\rangle$ cancel each other. In steady state, dE/dt then describes the balance of energy injection and removal according to

$$\begin{aligned}\frac{dE}{dt} &= \sum_{k_y\neq 0}\Big\{2\mathrm{Im}(\omega_1)\left(1+|R_1|^2+k_\perp^2\right)|\beta_1|^2+2\mathrm{Im}(\omega_2)\left(1+|R_2|^2+k_\perp^2\right)|\beta_2|^2 \\ &\quad+2\left(1+k_\perp^2\right)\mathrm{Im}\left[\left(\omega_1^*-\omega_2\right)\langle\beta_1^*\beta_2\rangle\right]+2\mathrm{Im}\left[R_1^*R_2\left(\omega_1^*-\omega_2\right)\langle\beta_1^*\beta_2\rangle\right]\Big\} \\ &\quad-2\nu\sum_{k_x}|v_z|^2\big|_{k_y=0}=0\ . \end{aligned} \tag{4.33}$$

We first examine Eq. (4.33) in the collisionless limit, $\nu = 0$, where $\omega_1^* - \omega_2 = 0$ and $|R_1|^2 = |R_2|^2$. In this limit, we find that

$$\begin{aligned}\frac{dE}{dt} &= \sum_{k_y\neq 0}\left[2\mathrm{Im}(\omega_1)\left(1+|R_1|^2+k_\perp^2\right)|\beta_1|^2+2\mathrm{Im}(\omega_2\left(1+|R_2|^2+k_\perp^2\right)|\beta_2|^2\right] \\ &= \sum_{k_y\neq 0}\left[2\mathrm{Im}(\omega_1)\left(1+|R_1|^2+k_\perp^2\right)\left(|\beta_1|^2-|\beta_2|^2\right)\right]=0\ , \end{aligned} \tag{4.34}$$

i.e., the energy injected into turbulence by the unstable modes is removed totally by the stable mode. With $\gamma_1 = -\gamma_2$, this implies $|\beta_1(k)|^2 = |\beta_2(k)|^2$. This is a reflection of the complex-conjugate symmetry of the two eigenmodes when $\nu = 0$.

The collisionless limit is not strictly applicable for saturation with Eqs. (4.17) and (4.18), because collisionality balances the inverse energy transfer of the vorticity nonlinearity in Eq. (4.18). This gives rise to the last term of Eq. (4.33). We are nonetheless interested in the limit of small collisionality, noting that $\nu \neq 0$ makes $\omega_1^* \neq \omega_2$, $R_1^* \neq R_2$, and $|\beta_1|^2 \neq |\beta_2|^2$. To examine the effects of small collisionality on the ratio $\kappa = |\beta_2|^2/|\beta_1|^2$, we introduce ν into the ordering of Eq. (4.16) as $\nu \sim k^2 \sim \hat{\epsilon}^4$. Under this extended ordering, we return to Eq. (4.33) and examine each term. We note that $k_\perp^2$ does not break conjugate symmetry, i.e., for $\nu = 0$, the equality $\omega_1^* = \omega_2$ holds with terms of order $k_\perp^2$ included. However, ν itself is multiplied by $k_\perp^2$ in ω_j and R_j, raising the order of the symmetry-breaking contributions in the first four terms of Eq. (4.33). The last term requires special consideration, as discussed below.

From Eq. (4.10), we find that $\omega_1^* = \omega_2 + \mathcal{O}(\nu k_\perp^2) = \omega_2 + \mathcal{O}(\hat{\epsilon}^6)$, i.e., the first deviation of ω_2 from ω_1^* occurs at sixth order. From Eq. (4.12), we note that the breaking of conjugate symmetry in R_j resides in the term proportional to ω_j. Hence, $R_1^* = R_2 + \mathcal{O}(\nu k_\perp^2)$. The terms of Eq. (4.33) with dependence on the cross-correlation $\langle \beta_1^* \beta_2 \rangle$ have a factor $\omega_1^* - \omega_2$ and are therefore $\mathcal{O}(\nu k_\perp^2)$. The last term of Eq. (4.33) is proportional to $|v_z|^2$, hence its magnitude requires knowledge of saturation levels. The levels of $|\beta_1|^2$ and $|v_z|^2$ are given in Ref. [30] in terms of basic scalings, and are sufficient to estimate the order of the term $\nu|v_z|^2$ in Eq. (4.33). From Eqs. (33) and (40) of Ref. [30],

$$|v_z|^2 = \frac{2\gamma_1}{\nu b} \frac{|C_{F12}|}{|C_{1F2}|} |\beta_1|^2 , \tag{4.35}$$

where b is a constant of order unity in the $\hat{\epsilon}$ expansion.

With this expression, Eq. (4.33) can be written

$$2 \sum_{k_y \neq 0} |\beta_1|^2 \gamma_1 \left(1 + k_\perp^2 + |R_1|^2 - \frac{|C_{F12}|}{b|C_{1F2}|} \right) = 2 \sum_{k_y \neq 0} |\beta_2|^2 |\gamma_2| \left(1 + k_\perp^2 + |R_2|^2 \right) + \mathcal{O}(\nu k_\perp^2) , \tag{4.36}$$

where the contributions of $\mathcal{O}(\nu k_\perp^2)$ represent the terms proportional to $\langle \beta_1^* \beta_2 \rangle$. From this expression, we obtain

$$\kappa = \frac{|\beta_2(k)|^2}{|\beta_1(k)|^2} = \frac{\gamma_1 \left(1 + |R_1|^2 + k_\perp^2 - \frac{|C_{F12}|}{b|C_{1F2}|} \right)}{|\gamma_2| \left(1 + |R_2|^2 + k_\perp^2 \right)} + \frac{\mathcal{O}(\nu k_\perp^2)}{|\gamma_2| \left(1 + |R_2|^2 + k_\perp^2 \right)} , \tag{4.37}$$

where, in keeping with the strong localization of dominant energy transfer in the low wavenumber range, we have replaced the sum with evaluation at a representative wavenumber.

We now examine the order of the leading contribution to $|R_j|^2$, which from Eq. (4.12) is $-\omega_j(1+k_\perp^2)/(2k_y\epsilon) \sim \mp\sqrt{(1+\eta)\epsilon}$. Following Eq. (4.10) we compare the threshold dispersion relation to the results of Ref. [29], which assumes a flat density limit $L_n \to \infty$, and which was ordered as $(1+\eta)k_y \sim \mathcal{O}(1)$ and $\epsilon k_y \sim \mathcal{O}(1)$. The more appropriate limit is for a modestly peaked density profile with $\mathcal{O}(\hat{\epsilon}^2) \leq \epsilon < \mathcal{O}(1)$. Because $R_2|^2 = |R_1|^2 + \mathcal{O}(\nu^2 k_\perp^4)$, Eq. (4.37) can then be written

$$\kappa = \frac{\gamma_1}{|\gamma_2|}\left(1 - \frac{|C_{F12}|}{b|R_1|^2|C_{1F2}|}\right) + \frac{\mathcal{O}(\nu k_\perp^2)}{|\gamma_2|\,|R_1|^2} \ , \tag{4.38}$$

where for $\epsilon = \mathcal{O}(\hat{\epsilon}^2)$, this expression is valid to eighth order, and $\gamma_1/|\gamma_2|$ differs from unity in the sixth order.

The above analysis shows that equipartition of energy rates $\gamma_j|\beta_j|^2$ is followed to high order in this system, with small deviations arising from the breaking of conjugate symmetry in γ_1 and γ_2 by finite collisionality. The result is that κ deviates from unity by a small increment of order $\nu k_\perp^2$.

With these results, we return to the heat flux in Eq. (4.22), and write it up to order $\nu k_\perp^2 \sim \hat{\epsilon}^6$, yielding

$$Q_{\mathrm{i}} = \sum_k \frac{\gamma_1}{2\epsilon}(1 + k_\perp^2)\,|\beta_1|^2\,(1 - \kappa) \ . \tag{4.39}$$

This equation provides three pieces of important information. First, the heat flux is proportional to the growth rate of the instability, a standard result for drift-wave turbulence [35]. Second, the heat flux is proportional to the turbulence level. While this is also standard, the turbulence level is set by a saturation balance, which introduces dependencies on coupling coefficients and the triplet correlation time, with their tendency for resonance in a wave regime at low k. These dependencies are derived in the Sec. 4.5. The third important concept is that the heat flux is proportional to $1 - \kappa$, arising from $\mathrm{Im}(R_1)|\beta_2|^2 + \mathrm{Im}(R_2)|\beta_2|^2$. The high degree of conjugate symmetry for weakly collisional regimes puts the stable-mode amplitude on par with that of the unstable mode, significantly reducing the heat flux.

4.5 Nonlinear Saturation Relations

We turn now to the nonlinear physics that sets $|\beta_1|^2$. The level $|\beta_1|^2$ is governed by a saturation energy balance that depends on the triplet correlation time τ of the fluctuation interaction that mediates saturation. The triplet correlation time of interest in the present, zonal-flow-mediated case is essentially the reciprocal of the frequencies of the unstable mode, the zonal flow, and the stable mode, each at a wavenumber of the triplet interaction $k = k' + k''$. More precisely we write $\tau = -i[\omega_l(k'') + \omega_m(k') - \omega_n^*]^{-1}$, where l, m, and n respectively denote stable mode, zonal flow, and unstable mode. These frequencies have linear and nonlinear components, with the former given by Eq. (4.10). When the triplet correlation time is near resonance, the sum of the linear frequencies nearly vanishes, and the nonlinear frequencies become important. Hence, we also derive the nonlinear frequency, or eddy damping rate, as a function of turbulence levels. Both of these relationships are obtained from statistical closure theory. The statistical closure theory for Eqs. (4.17) and (4.18) was worked out in Ref. [30]. While that derivation was restricted to the strong-transport regime, it used the form and symbols of Eqs. (4.17)–(4.21) — one only need supply the correct threshold-model expressions for $R_{1,2}$ from Eq. (4.12) and $\omega_{1,2}$ from Eq. (4.10).

Statistical closure treats the nonlinear terms of energy evolution equations. For the zonal flow, the energy evolution equation is obtained from Eq. (4.18) and given by

$$|\dot{v}_z|^2 + \nu |v_z|^2 = 2\mathrm{Re} \sum_{k'} C_{Fmn}^{(k,k')} \left. \langle \beta''_m \beta'_n v_z^* \rangle \right|_{k_y=0} , \qquad (4.40)$$

where n and m can take the values of 1 or 2, and repetition of these indices in any single term indicates a sum from 1 to 2. The triplet correlation $\langle \beta''_m \beta'_n v_z^* \rangle$

governs nonlinear transfer, and it is calculated from its evolution equation, which from Eqs. (4.17) and (4.18) is given by

$$
\begin{aligned}
&\left[\tfrac{d}{dt} + i\omega''_m + i\omega'_n - i\omega^*_1\right] \langle \beta''_m \beta'_n v^*_z \rangle\Big|_{k_y=0} = \\
&\textstyle\sum_{k'''_x} \Bigg\{ \left[C^{(k'',k''')}_{mFl} \langle v'''_z \beta_l(k''-k''')\beta'_n v^*_z \rangle + C^{(k',k''')}_{nFl} \langle v'''_z \beta_l(k'-k''')\beta''_m v^*_z \rangle \right]\Big|_{k'''_y=0} + \\
&\left[C^{(k'',k''')}_{mlF} \langle \beta'''_l v_z(k''-k''')\beta'_n v^*_z \rangle\Big|_{k'''_y=k''_y} + C^{(k',k''')}_{nlF} \langle \beta'''_l v_z(k'-k''')\beta''_m v^*_z \rangle\Big|_{k'''_y=k'_y} \right] \Bigg\}\Bigg|_{k_y=0}
\end{aligned}
\qquad (4.41)
$$

where the nonlinearity that drives v^*_z has been neglected because it is smaller by a factor of $k^2_\perp$ than the nonlinearities of the right-hand side that drive β''_m and β'_n.

Equation (4.41) is inverted and substituted into Eq. (4.40). The fourth-order correlations of Eq. (4.41) are written as products of two second-order correlations, i.e., $\langle v'''_z \beta_l(k''-k''')\beta'_n v^*_z \rangle \rightarrow \langle \beta'^*_l \beta'_n \rangle |v_z|^2$, $\langle v'''_z \beta_l(k'-k''')\beta''_m v^*_z \rangle \rightarrow \langle \beta''^*_l \beta''_m \rangle |v_z|^2$, $\langle \beta'''_l v_z(k''-k''')\beta'_n v^*_z \rangle \rightarrow \langle \beta'^*_l \beta'_n \rangle |v_z|^2$, and $\langle \beta'''_l v_z(k'-k''')\beta''_m v^*_z \rangle \rightarrow \langle \beta''^*_l \beta''_m \rangle |v_z|^2$. Writing fourth-order correlations as products of second-order correlations assumes turbulence with a probability distribution function that is close to a Gaussian, which is valid for a randomized system, in which case the sum over k'''_x is dominated by $k'''_x = k_x$ in the first and second terms on the right-hand side of Eq. (4.41), by $k'''_x = k''_x - k_x$ in the third, and by $k'''_x = k'_x - k_x$ in the fourth.

The interaction of β''_m, β'_n, and v^*_z has a finite correlation time governed by the frequency mismatch $i\omega''_m + i\omega'_n - i\omega^*_1$. In a steady state, $\langle \beta''_m \beta'_n v^*_z \rangle$ is given by the right-hand side of Eq. (4.41) divided by $i\omega''_m + i\omega'_n - i\omega^*_1$. This means that $\langle \beta''_m \beta'_n v^*_z \rangle$ tends to be dominated by mode interactions for which $i\omega''_m + i\omega'_n - i\omega^*_1$ is minimal. Moreover, such interactions result in lower values of fluctuation levels for a given linear drive. Physically, $i\omega''_m + i\omega'_n - i\omega^*_1$ is the reciprocal of the triplet correlation time; when this time is large, energy transfer is more efficient, and the system saturates at lower turbulent amplitudes.

Consider couplings that make $i\omega''_m + i\omega'_n - i\omega^*_1$ minimal. By assignment, k is the wavenumber of the zonal flow, which we assume is a zero-frequency fluctuation with damping that is very small ($\nu \ll 1$). Then, if $m = 1$, a minimum occurs for $n = 2$, i.e., $|i\omega''_1 + i\omega'_2 - i\omega^*_1| \ll |i\omega''_1 + i\omega'_1 - i\omega^*_1|$. Similarly, for $m = 2$, a minimum occurs for $n = 1$, and $|i\omega''_2 + i\omega'_1 - i\omega^*_1| \ll |i\omega''_2 + i\omega'_2 - i\omega^*_1|$. This property follows from the near-conjugate symmetry of the unstable and stable modes. It also validates the assertion made in Sec. 4.1 that the nonlinear coupling is dominated by the interaction of the unstable mode, the zonal flow, and the stable mode. It is worth noting that if $\nu = k^2_\perp = 0$, $|i\omega''_1 + i\omega'_2 - i\omega^*_1|$ and $|i\omega''_2 + i\omega'_1 - i\omega^*_1|$ exactly vanish. This makes nonlinear frequencies important even in a weak-turbulence regime where the nonlinear frequency at a single k is small compared to its linear counterpart. Restricting three-wave coupling to the interaction of the unstable mode, zonal flow, and stable mode, the closed equation for $|v_z|^2$ is given by

$$\begin{aligned}\left[\tfrac{\partial}{\partial t} + 2\nu\right] |v_z|^2\Big|_{k_y=0} = \textstyle\sum_{k'} 2\mathrm{Re}\Bigg\{ & C^{(k,k')}_{F12}(i\omega'_2 + i\omega''_1 - i\omega^*_1)^{-1}|v_z|^2\Bigg[\\ & \left(C^{(k',-k'')}_{22F} + C^{(k',k)}_{2F2}\right)\langle\beta''_1\beta''^*_2\rangle \\ & + \left(C^{(k'',k)}_{1F1} + C^{(k'',-k')}_{11F}\right)\langle\beta'^*_1\beta'_2\rangle + \left(C^{(k'',k)}_{1F2} + C^{(k'',-k')}_{12F}\right)|\beta'_2|^2 + \Big(C^{(k',-k'')}_{21F} \\ & + C^{(k',k)}_{2F1}\Big)|\beta''_1|^2\Bigg] \\ & + C^{(k,k')}_{F21}(i\omega''_2 + i\omega'_1 - i\omega^*_1)^{-1}|v_z|^2\Bigg[\left(C^{(k',-k'')}_{21F} + C^{(k',k)}_{1F1}\right)\langle\beta''^*_1\beta''_2\rangle \\ & + \left(C^{(k',-k'')}_{12F} + C^{(k',k)}_{1F2}\right)|\beta''_2|^2 \\ & + \left(C^{(k'',k)}_{2F1} + C^{(k'',-k')}_{21F}\right)|\beta'_1|^2 + \left(C^{(k'',k)}_{2F2} + C^{(k'',-k')}_{22F}\right)\langle\beta'_1\beta'^*_2\rangle\Bigg]\Bigg\}\Bigg|_{k_y=0} .\end{aligned} \qquad (4.42)$$

Here, the notion of steady state that allows inversion of Eq. (4.41) with $(i\omega'_2 + i\omega''_1 - i\omega^*_l)^{-1}$ is, in fact, the Markovian assumption of the eddy-damped-quasi-normal-Markovian closure, commonly referred to as EDQNM [32], valid when the time scales of fluctuation correlations is slower than $(i\omega_2' + i\omega_1'' - i\omega_1^*)^{-1}$. In Sec. 4.6, we will solve this equation to obtain the saturated level of $|\beta_1|^2$ pursuant to an analytic expression for the heat flux.

As constructed in Eq. (4.41), the triplet correlation times $(i\omega_2' + i\omega_1'' - i\omega_1^*)^{-1}$ and $(i\omega_2'' + i\omega_1' - i\omega_1^*)^{-1}$ are made up of linear frequencies. However, in turbulent systems, any linear frequency has a nonlinear counterpart that describes the effect of nonlinear scattering on wave properties. These nonlinear frequencies are often referred to as eddy damping, because they lead to decorrelation at an amplitude-dependent rate. In turbulence with wave motion, these frequencies are complex, just like linear frequencies. As shown in Ref. [37], eddy damping arises from nonlinear interactions that are separate from those that converted the fourth-order correlations of Eq. (4.41) to products of second-order correlations, and the eddy damping can be formulated from those interactions [37].

We derive the complex eddy damping rate that renormalizes the linear frequency ω_l. Starting from Eq. (4.17), we observe that the nonlinearity involves products $v_z'\beta_j''$ and $\beta_j'v_z''$. Such products themselves satisfy a nonlinear evolution equation, which for $v_z'\beta_j''$ is constructed from Eqs. (4.17) and (4.18) and given by

$$\left[\tfrac{d}{dt} + i\omega_j'' + i\omega_1'\right] \beta_j''v_z'\Big|_{k_y'=0} = \textstyle\sum_{k_x'''}\left\{ C_{jFl}^{(k'',k''')} v_z'''\beta_l(k''-k''')v_z'\Big|_{k_y''',k_y'=0}\right.$$

$$\left. + \, C_{jlF}^{(k'',k''')} v_z(k''-k''')\beta_l'''v_z'\Big|_{k_y'''=k_y'',k_y'=0} + C_{Fml}^{(k',k''')}\beta_m'''\beta_l(k'-k''')\beta_j''\Big|_{k_y'=0}\right\} \quad (4.43)$$

To find contributions to the eddy-damping counterpart of ω_l from the sum over k_x''', we select wavenumbers that give the right-hand side of Eq. (4.43) the same phase as β_l. For the first term of the right-hand side of Eq. (4.43) this is accomplished with $k_x''' = -k_x'$, for the second term with $k_x''' = 0$, and for the third term with $k_x''' = k_x$

and $k_x''' = k_x' - k_x$. Consequently, in steady state, Eq. (4.43) becomes

$$\begin{aligned} v_z'\beta_j''\big|_{k_y'=0} &= \frac{1}{i(\omega_j'' + \omega_1')}\Bigg\{\left(C_{jFl}^{(k'',-k')} + C_{jlF}^{(k'',k)}\right)|v_z'|^2 \\ &\qquad + \sum_m \left[C_{Flm}^{(k',k)}\beta_m''^{*}\beta_j'' + C_{Fml}^{(k',-k'')}\beta_m''^{*}\beta_j''\right]\Bigg\}\Bigg|_{k_y'=0} \beta_l \ . \end{aligned} \tag{4.44}$$

We observe that, although the right-hand side of Eq. (4.44) is nonlinear, its phase is that of β_1, because $|v_z'|^2$ and $\beta_m''^{*}\beta_j''$ have zero phase for $m = j$, and for $m \neq j$ the phase is very small as seen from Eq. (4.31). Applying the procedure that produced Eq. (4.44) to $\beta_j' v_z''$, we obtain

$$\begin{aligned} v_z''\beta_j''\big|_{k_y'=k_y} &= \frac{1}{i(\omega_j' + \omega_1'')}\Bigg\{\left(C_{jFl}^{(k',-k'')} + C_{jlF}^{(k',k)}\right)|v_z''|^2 \\ &\qquad + \sum_m \left[C_{Flm}^{(k'',k)}\beta_m'^{*}\beta_j' + C_{Fml}^{(k'',-k')}\beta_m'^{*}\beta_j'\right]\Bigg\}\Bigg|_{k_y'=k_y} \beta_l \ . \end{aligned} \tag{4.45}$$

When these two expressions are substituted into Eq. (4.17) the factors multiplying β_l combine to produce a eddy turnover rate given by

$$\Delta\omega_l = 2\sum_{k_x'} \frac{C_{lFj}^{(k,k')}}{i(\hat{\omega}_j'' + \hat{\omega}_1')}\left[\left(C_{jFl}^{(k'',-k')} + C_{jlF}^{(k'',k)}\right)|v_z'|^2 + \left(C_{Flm}^{(k',k)} + C_{Fml}^{(k',-k'')}\right)\beta_m''^{*}\beta_j''\right] \ , \tag{4.46}$$

where the full frequency of β_l is written $i\hat{\omega}_l = i\omega_l - \Delta\omega_l$, and we note that the frequencies inside $\Delta\omega_l$ are themselves renormalized by eddy damping rates. The latter renormalization guarantees that $\hat{\omega}_l$ has low and high transport regimes, consistent with the observations depicted in Fig. 9 of Ref. [38].

While the eddy damping rate must have dimensions of the reciprocal of time and depend on amplitude, there is some ambiguity regarding the form of the nonlinear damping time $[i(\hat{\omega}_j' + \hat{\omega}_1'')]^{-1}$ in Eq. (4.46). For example, in Ref. [37] this time is the same as the nonlinear time that governs the three-wave interactions of the energy evolution equations. This puts three frequencies in the nonlinear damping time of

$\Delta\omega_l$ as given in Eq. (2) of Ref. [21]. As derived here, $\Delta\omega_l$ is the scattering rate associated with the frequency of a single-mode, three of which then enter the triplet correlation time. The single mode damping time has been measured in simulation and compared with analytic forms [38].

4.6 Heat Flux Solutions

To evaluate the nonlinear expression for heat flux in Eq. (4.22) we solve the zonal energy balance Eq. (4.42) for $|\beta_1|^2$, first simplifying its form. Consider the four terms of Eq. (4.42) whose spectral correlations are functions of k''. We exchange the wavenumbers k' and k'', which are assigned arbitrarily in the convolution generated by the Fourier transform of the nonlinearity. With the exception of the factors $C_{F12}^{(k,k'')}$ and $C_{F21}^{(k,k'')}$, this operation maps terms of Eq. (4.42) whose spectral correlations are functions of k'' into the terms whose spectral correlations are functions of k'. We then note that for $k_y = 0$, we have $C_{F12}^{(k,k'')} = C_{F21}^{(k,k')} = C_{F12}^{(k,k')} = C_{F21}^{(k,k'')}$, a property that can be readily verified from Eq. (4.21). Consequently, Eq. (4.42) becomes

$$\begin{aligned}\left[\frac{\partial}{\partial t} + 2\nu\right] |v_z|^2\bigg|_{k_y=0} = {} & 4\sum_{k'} \mathrm{Re}\Bigg\{ C_{F12}^{(k,k'')}\tau_{12F}\bigg[\Big(C_{1F1}^{(k'',k)} + C_{11F}^{(k'',-k')}\Big)\langle\beta_1'^{*}\beta_2'\rangle \\ & + \Big(C_{1F2}^{(k'',k)} + C_{12F}^{(k'',-k')}\Big)|\beta_2'|^2\bigg] + C_{F21}^{(k,k'')}\tau_{21F}\bigg[\\ & \Big(C_{2F2}^{(k'',k)} + C_{22F}^{(k'',-k')}\Big) \\ & \times\langle\beta_1'\beta_2'^{*}\rangle + \Big(C_{2F1}^{(k'',k)} + C_{21F}^{(k'',-k')}\Big)|\beta_1^{*}|^2\bigg]\Bigg\} |v_z|^2\bigg|_{k_y=0} \qquad (4.47)\end{aligned}$$

where $\tau_{21F} = (i\hat{\omega}_2'' + i\hat{\omega}_1' - i\hat{\omega}_1^{*})^{-1}$ and $\tau_{12F} = (i\hat{\omega}_1'' + i\hat{\omega}_2' - i\hat{\omega}_1^{*})^{-1}$ are the triplet correlation times for the zonal-flow-catalyzed triplet interaction. Defining amalgamated coefficients $C''_{mn} = C^{(k'',k)}_{mFn} + C^{(k'',-k')}_{mnF}$, the spectral balance acquires the succinct form

$$\begin{aligned}\left[\frac{\partial}{\partial t} + 2\nu\right] |v_z|^2\Big|_{k_y=0} \;=\; & 4\sum_{k'} \mathrm{Re}\Bigg\{\bigg[C^{(k,k'')}_{F12}\tau_{12F}\left(C''_{11}\langle\beta'^*_1\beta'_2\rangle + C''_{12}\left|\beta'_2\right|^2\right) \\ & + C^{(k,k'')}_{F21}\tau_{21F}\left(C''_{22}\langle\beta'_1\beta'^*_2\rangle + C''_{21}\left|\beta'_1\right|^2\right)\bigg]\left|v_z\right|^2\Bigg\}_{k_y=0} \qquad (4.48)\end{aligned}$$

We use $\beta_2 = \sqrt{\kappa}\exp(i\theta)\beta_1$ to write $|\beta'_2|^2$, $\langle\beta'^*_1\beta'_2\rangle$, and $\langle\beta'_1\beta'^*_2\rangle$ in terms of $|\beta'_1|^2$. Assuming a steady state ($\partial/\partial t \to 0$), the zonal energy cancels from the balance, leaving

$$\nu = 2\sum_{k'} \mathrm{Re}\left[C^{(k,k'')}_{F12}\tau_{12F}\left(C''_{11}\mathrm{e}^{i\theta} + C''_{12}\kappa\right) + C^{(k,k'')}_{F21}\tau_{21F}\left(C''_{22}\mathrm{e}^{-i\theta} + C''_{21}\right)\right]\left|\beta'_1\right|^2\Big|_{k_y=0} . \qquad (4.49)$$

Equation (4.49) is a rigorous version of the approximate saturation-level expression given by Eq. (31) of Ref. [30]. Both expressions have the same scalings with ν, C_{F12}, τ_{ijF}, C_{iFj} and C_{ijF}, but Eq. (4.49) also accounts for $|\beta'_2|^2$, $\langle\beta'^*_1\beta'_2\rangle$, and $\langle\beta'_1\beta'^*_2\rangle$, whose values are known up to $\mathcal{O}(\hat{\epsilon}^8)$ in the expansion for small k and ν.

In Eq. (4.49), $|\beta'_1|^2$ is part of a sum. Numerical solutions show that the coupling coefficients and τ factors vary slowly relative to $|\beta'_1|^2$, which because of energy removal by stable modes drops sharply over the unstable wavenumber range. The coupling coefficients and τ factors can then be extracted from the sum (a Markovian approximation) leaving a sum over $|\beta'_1|^2$, which produces a spectrum-averaged value over the unstable wavenumber range. With $|\beta'_1|^2$ understood to be this average, Eq. (4.49) can be expressed as

$$\left|\beta'_1\right|^2 \sim \frac{\nu}{\sum\limits_{k_x}\mathrm{Re}\left\{C^{(k,k'')}_{F12}\left[\tau_{21F}\left(C''_{21} + \sqrt{\kappa}C''_{22}\mathrm{e}^{-i\theta}\right) + \tau_{12F}\left(\kappa C''_{12} + \sqrt{\kappa}C''_{11}\mathrm{e}^{i\theta}\right)\right]\right\}} , \qquad (4.50)$$

where a sum over k_x is introduced to incorporate contributions from different zonal-flow wavenumbers. Note that in Ref. [21], the summation in Eq. (4.49) was approximated less consistently with spectrum features. However, because of the strong localization of fluctuation energy to the unstable wavenumber range, overall results are insensitive to these differences.

Equation (4.50) represents key aspects of ITG turbulence saturation. The factor ν in the numerator is the damping rate of the zonal flow. Larger zonal-flow damping requires stronger nonlinear energy transfer to the zonal flow to maintain the quasi-stationary state, leading to a higher turbulence level. The combination of the coupling coefficients and triplet correlation time in the denominator originates from the nonlinear energy transfer, which is proportional to the turbulence level. Larger values of the coupling coefficients and triplet correlation time produce more efficient nonlinear energy transfer and therefore lead to lower turbulence levels.

With $|\beta_1|^2$ given by Eq. (4.50), the heat flux as per Eq. (4.39) becomes

$$Q_\mathrm{i} = \sum_{k'''} \frac{\gamma(k''')(1+k_\perp'''^2)\nu(1-\kappa)}{4\epsilon \sum_{k_x}(k_\perp'^2 - k_\perp''^2)\mathrm{Re}\left\{ik_y'\left[\tau_{21F}\left(C_{21}'' + C_{22}''\sqrt{\kappa}\mathrm{e}^{-i\theta}\right) + \tau_{12F}\left(C_{12}''\kappa + C_{11}''\sqrt{\kappa}\mathrm{e}^{i\theta}\right)\right]\right\}}, \tag{4.51}$$

where $C_{F12}^{(k,k'')}$ is written explicitly using Eq. (4.21), thereby exposing a factor $(k_\perp'^2 - k_\perp''^2)$ in the denominator of Eq. (4.51). The combination of factors $\gamma(k''')/(k_\perp'^2 - k_\perp''^2)$ scales like the quasilinear heat flux. The remaining factors constitute a nonlinear correction to quasilinear scaling. Critical nonlinear corrections include the triplet correlation times τ_{21F} and τ_{12F}, the coupling coefficients C_{ij}'', and the parameters κ and θ from the contributions of $|\beta_2|^2$ and $\langle\beta_1^*\beta_2\rangle$. The factor $1-\kappa$ accounts for the up-gradient flux of the stable mode, in opposition to the down-gradient flux of the unstable mode.From Eq. (51), the heat flux is proportional to the zonal flow damping rate to a power 2 (since $\tau_{ijF} \propto \nu^{-1}$). The fact that the shearing paradigm of zonal-flow regulation [27] is also understood to produce a heat flux proportional to a positive power of ν [38] is coincidental. The latter requires a shearing rate that exceeds the nonlinear decorrelation rate by a sizable factor (10 when zonal flow fluctuate), enhancing energy transfer to small scale turbulent fluctuations by boosting the turbulent decorrelation rate to the shearing level [2]. In zonal flow catalyzed transfer, straining by the zonal flow (the threshold-less shearing process of ordinary mode coupling) enhances transfer to large scale turbulent fluctuations by reducing the decorrelation rate to its smallest possible value.

Fig. 4.6 shows the heat flux and growth rate as functions of the temperature-gradient parameter η. The heat flux is calculated from a numerical solution of Eqs. (4.8) and (4.9) in conjunction with the analytic formula of Eq. (4.51) for a case with parameters $\epsilon = 1.25$, $\nu = 0.001$, and $\chi = 0$. Simulations were performed on a grid of 2048×1024 points in (k_x, k_y), with $k_{x,\min} = 0.0125$ and $k_{y,\min} = 0.025$ in order to capture turbulent behavior for large η. A fourth order Runge-Kutta scheme was utilized. As for the heat flux evaluation from the analytic formula Eq. (4.51), k_x and k_y''' are summed over values from -0.25 to -0.15 and 0.25 to 0.4, respectively. The triplet correlation times τ_{21F} and τ_{12F} are evaluated with the linear frequencies only, i.e., the eddy-damping decrements $\Delta\omega_j$ were neglected. According to Eq. (4.37), $\kappa \sim 1 - \nu k_\perp^2/\gamma_2$ for $k_\perp$ and ν small, making $1-\kappa$ of order 10^{-4} in the low-k regime for η away from the linear threshold η_{crit}. In Fig. 4.6, the value $\kappa = 1 - 10^{-4}$ for higher η was assumed to represent η near threshold.

For comparison purposes, the scales of analytic and simulated heat fluxes in Fig. 4.6 are adjusted so that the two curves coincide at the highest value of η. We observe that both fluxes have positive curvature, in contrast to the negative curvature of the growth rate, giving a region above the threshold where heat flux increases slowly before turning up more sharply. The analytic flux has an unphysical spike just above the threshold which artificially raises its value relative to the simulated flux. This spike arises from a prompt increase of τ above the threshold

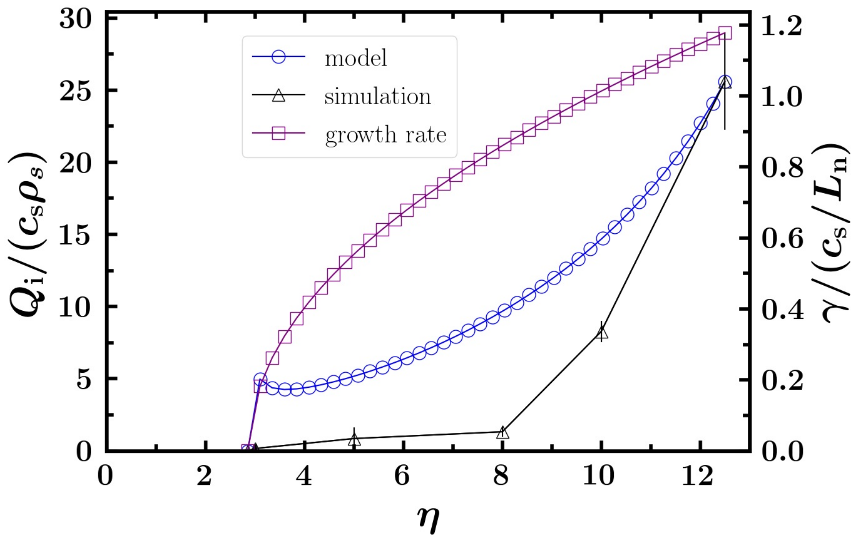

Figure 4.6: Growth rate at $\mathbf{k} = (0, 0.25)$ (magenta), analytic heat flux (blue) and simulated heat flux (black) as a functions of η for $\epsilon = 1.25$, $\nu = 0.001$ and $\chi = 0$. Eddy damping is neglected in the triplet correlation time factors of the analytic formula. The heat flux predicted from the analytic formula showing unphysical behavior close to the linear threshold.

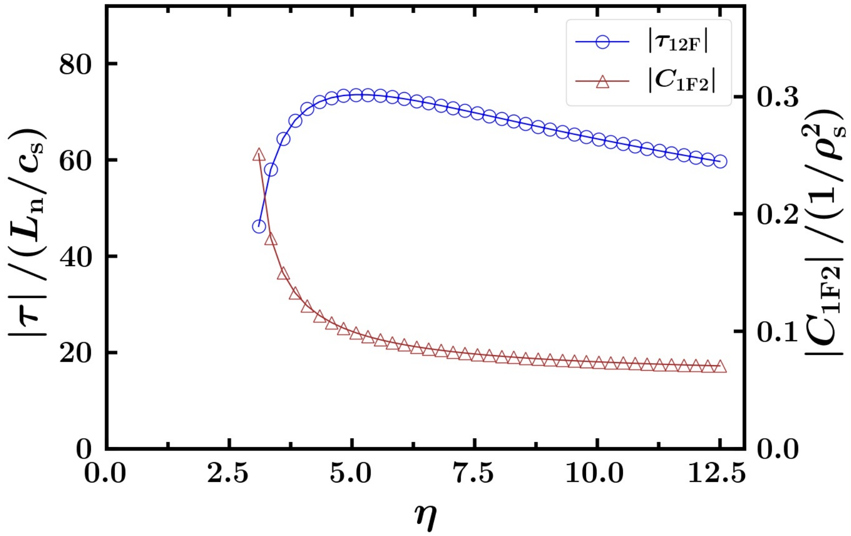

Figure 4.7: Triplet correlation time (blue) and coupling coefficient C_{1F2} (red) as a function of η for the same parameters as Fig. 4.6. Eddy damping is neglected in $|\tau|$. The triplet correlation time increases dramatically just above the linear threshold, which leads to the spike of the heat flux in close-threshold region.

followed by a slow slide off at higher η, as shown in the blue trace of Fig. 4.7. This behavior is unphysical because increasing η, which increases the dispersive components of frequencies and growth rates, necessarily *decreases* τ immediately above threshold. The source of the unphysical increase of τ is traced to the fact that the k dependence of the threshold puts multiple thresholds into τ from its frequencies at different wavenumber. This creates the spike region near the threshold in which the crossing of the identities of stable and unstable produce an increase in τ.

This sensitivity to a two-mode representation of the eigenmode space can be expected to be smoothed by eddy damping. This nonlinear frequency-broadening process is important near threshold, where resonance makes $\omega_2'' + \omega_1' - \omega_1^*$ much smaller than individual frequencies, bringing eddy damping into prominence even in the low-amplitude threshold regime. Moreover, Eq. (4.46) shows that the dominant component of the eddy damping $\Delta\omega$ is proportional to the product of $|v_z|^2$ and $C_{jFl}C_{jlF}$. The coefficient C_{1F2} is plotted in Fig. 4.7 as the red line, where it is seen that C_{1F2} is largest near the threshold. This behavior arises from the form $C_{1F2} \propto [\mathrm{Re}(\omega) + i\gamma]/\gamma$, which makes C_{1F2} strongest just above the threshold where $\mathrm{Re}(\omega) \gg \gamma$ and $C_{iFj} \propto \mathrm{Re}(\omega)/\gamma \gg 1$. At large η, the coupling coefficient C_{1F2} asymptotes to a smaller constant. The importance of eddy damping near resonance is amplified near threshold by this effect and therefore should not be ignored.

Fig. 4.8 shows that by adding the eddy damping rate $\Delta\omega$ of Eq. (4.46) to the τ factors of Eq. (4.51), the countering trends of τ in Fig. 4.6 are removed, thereby smoothing the unphysical behavior of Q_{i} around the instability threshold. The predicted heat flux now agrees much better with the simulation starting from the linear threshold. In Fig. 4.9, the triplet correlation time with eddy damping included is plotted as a function of η, showing that the triplet correlation time decreases

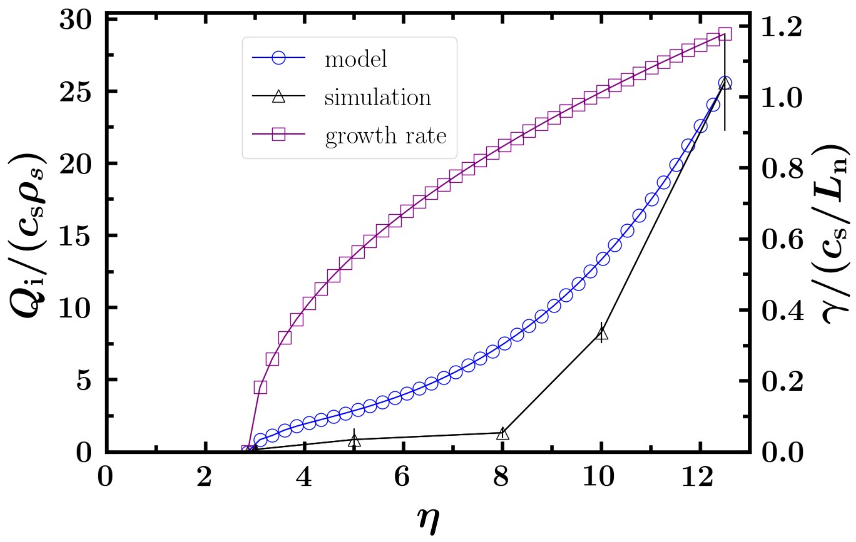

Figure 4.8: Growth rate (magenta), analytic heat flux (blue), and simulated heat flux (black) as functions of η for $\epsilon = 1.25$, $\nu = 0.001$, and $\chi = 0$, with eddy damping included in the analytic formula.

monotonically with η, as expected for nearly resonant frequencies that increase with η. This behavior represents a resonance in the standard sense of turbulent mode-coupling interactions. We note that the decrease of coupling coefficient with η, shown in Fig. 4.9 for comparison, is also pronounced, significantly contributing to the suppression of the heat flux immediately above the threshold. This effect can also be termed as resonant because it arises from the dependence of C_{1F2} on mode frequency, describing an enhancement of zonal-flow-mediated coupling between stable and unstable modes just above threshold.

The behavior depicted in Fig. 4.9 is broadly consistent with critical features of the Dimits shift. No bifurcation is observed, but rather a continuously increasing slope from a region near the instability threshold with very low flux. The match of the analytic flux with the simulated flux is not perfect, but the former generally tracks the variation of the latter. Both differ decidedly from the variation of the growth rate

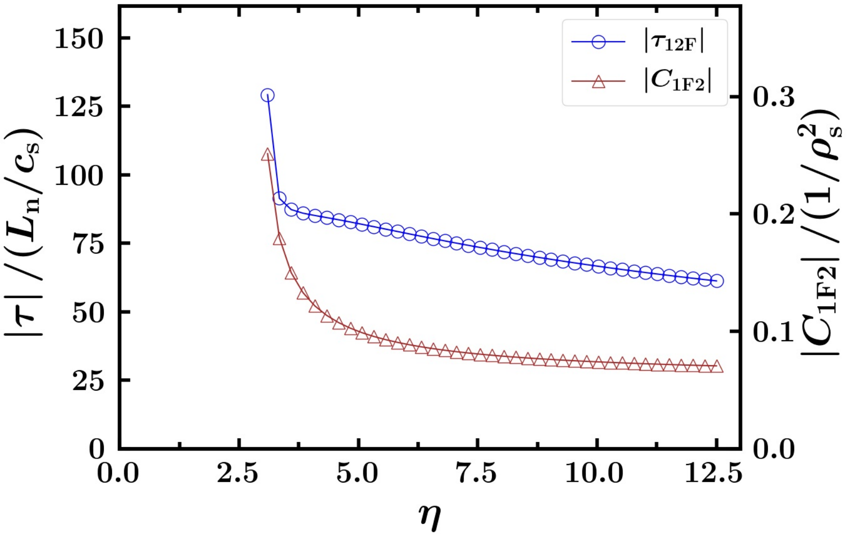

Figure 4.9: Triplet correlation time (blue) and coupling coefficient C_{1F2} (red) as a function of η for the same parameters as Fig. 4.4 with eddy damping included in τ. The triplet correlation time decreases monotonically as η increases, which eliminates the unphysical behavior.

with η. The features evident in Fig. 4.9 are replicated for other parameter values. Figure 4.10 shows the heat flux versus η for $\epsilon = 1.25$ and $\epsilon = 0.625$. As the magnetic curvature parameter, the threshold depends on ϵ. In Fig. 4.10, the simulated heat flux is actually larger than the analytic flux near the threshold for $\epsilon = 0.625$, and it is clearly evident that while there is noticeable upturn in slope of simulated heat flux at $\eta = 8$, the flux below that value is not zero. Variations with collisionality, which produce consistent effects in gyrokinetics and the present fluid model, will be described in a separate gyrokinetic study, along with other tests that directly broaden the resonance in the triplet correlation time. These modifications result in a increase in the heat flux and generally support the conclusion that resonance is an important aspect of the critical gradient upshift. The idea of resonant interactions has been used to modify quasilinear modeling, which in standard formulations does not capture the resonant aspects of saturation. The result is an improved quasilinear

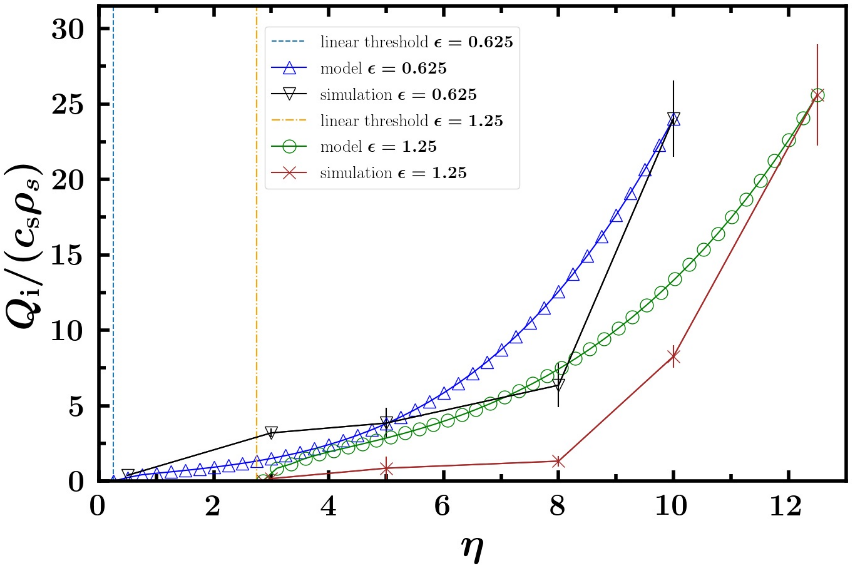

Figure 4.10: Heat flux as a function of η for $\epsilon = 0.625$ and $\epsilon = 1.25$ analytic theory (triangles and circles), numerical solution (inverted triangles and crosses).

model that is able to capture the critical gradient upshift in gyrokinetic simulations [40].

4.7 Conclusions

Physics central to the Dimits shift, a phenomenon where the ion heat flux becomes significant only at a larger temperature gradient than the critical gradient of linear instability, has been analyzed with approaches based on gyrokinetic simulation and fluid-model analytic theory. The simulations show that fluctuations and transport are not zero between the linear instability threshold and the nonlinear critical gradient (NLCG) where the flux rises sharply. Accordingly, turbulent transfer was investigated in the regimes of low and high transport on either side of the NLCG. Instantaneous nonlinear spectral energy transfer and scale-to-scale-cascaded energy transfer were found to be similar in both regimes, differing essentially in magnitude only. Energy transfer is governed by zonal-flow-catalyzed mode coupling — the interaction between the unstable mode, a stable mode, and the zonal flow at a triplet of wavenumbers.

A saturation theory based on this interaction was extended from the strong-transport regime for which it was originally developed to the weak-transport regime near the linear threshold by building the kinetic threshold of the ITG instability into the fluid model. The dominant mode coupling is resonant for $k_\perp^2, \nu \to 0$, i.e., the frequency mismatch of the triplet correlation time is zero because the stable mode forms a conjugate pair with the unstable mode and the zonal flow is a zero-frequency mode. This allows maximally efficient transfer to the stable-mode energy sink, yielding negligibly low levels of fluctuations and transport for a given instability growth rate. The resonance is broadened by finite ν, $k_\perp^2$, and eddy damping, producing a small heat flux near the instability threshold. The minimum value of the triplet correlation time produced by the broadening grows with temperature gradient, allowing the flux to become significant after a gradient range of latency set by the broadening.

Adequate description of this physics requires accounting for nonlinear transfer between eigenmodes, with the heat flux depending on the eigenmode auto and cross correlations $|\beta_1|^2$, $|\beta_2|^2$ and $\langle\beta_1^*\beta_2\rangle$. Expressions were derived for the relationship between these correlations. Because of the near conjugate symmetry in the regime $k_\perp^2$, $\nu \ll 1$, these relationships are dominated by linear physics in steady state. The contribution of $|\beta_2|^2$ to transport is significant and nearly cancels the quasilinear contribution from $|\beta_1|^2$, while $\langle\beta_1^*\beta_2\rangle$ makes a negligible contribution. The level of $|\beta_2|^2$ is set by equipartition of energy injection and removal rates $\gamma_1|\beta_1|^2$ and $\gamma_2|\beta_2|^2$.

The nonlinear balance for zonal-flow energy determines $|\beta_1|^2$ since the zonal energy drops out for zonal-flow-catalyzed mode coupling. This balance was solved inclusive of all eigenmode correlations by Markovianizing its nonlinear convolution and summing over wavenumber. The flux and $|\beta_1|^2$ are proportional to ν, the inverse of the triplet correlation time, and the inverse of a product of coupling coefficients. The eigenmode-frequency dependence of one of these coefficients gives it resonant behavior, i.e., it decreases sharply above the linear instability threshold. The heat-flux dependence on the nearly resonant triplet correlation time also explains to a substantial degree the nonlinear finite-β stabilization of ITG turbulence.

This theory does not account for all processes that may have bearing on the critical-gradient upshift. Turbulent fluctuations are intermittent just above the linear-instability threshold due to the relative paucity of mode coupling interactions available under the vanishing growth rate and instability range. Intermittency challenges the assumptions of closure calculations, although the one used here explicitly accounts for the weak-turbulence limit by retaining the resonance of three-wave interactions. This theory accounts only for the zonal-flow-catalyzed interaction. Well above the linear critical gradient, other nonzonal mode mode-coupling interactions may eventually become prominent. This theory does not apply when such interactions are dominant. Strongly ballooning modes in the ballooning representation of toroidal geometry are also assumed, limiting consideration of nonlinear eigenmode structure evolution not amenable to spectral representation. Non-adiabatic electrons have been omitted in keeping with the simplest realization of ITG physics. Non-adiabatic electrons are related to trapped electron mode (TEM) physics, where a critical gradient upshift has been noted in the density-gradient driven case [42]. Improvements of earlier work [43] on stable modes and zonal flows in TEM turbulence are under development and will be reported elsewhere. Mean flow shear has also been neglected. Its inclusion could be of interest for studying the interaction of the distinct processes of shear suppression by an externally maintained shear flow and saturation by zonal-flow-catalyzed transfer.

Acknowledgments

This work was supported by U.S. Department of Energy Grant DE-FG02-89ER53291. The data supporting the findings of this study is available from the authors upon reasonable request.

Bibliography

[1] W. Horton, Rev. Mod. Phys. **71**, 735 (1999).

[2] P.W. Terry, Rev. Mod. Phys. **72**, 109 (2000).

[3] E. J. Strait, L. L. Lao, M. E. Mauel, B. W. Rice, T. S. Taylor, K. H. Burrell, M. S. Chu, E. A. Lazarus, T. H. Osborne, S. J. Thompson et al., Phys. Rev. Lett. **75**, 4421 (1995).

[4] D.E. Newman, B.A. Carreras, D. Lopez-Bruna, P.H. Diamond, and V.B. Lebedev, Phys. Plasmas **5**, 938 (1998).

[5] J.W. Hughes, N.T. Howard, P. Rodriguez-Fernandexz, A.J. Creely, A.Q. Kuang, P.B. Synder, T.M. Wilks, R. Sweeney, and M. Greenwald, J. Plasma Phys. **86**, 865860504 (2020).

[6] H.E. Mynick, N. Pomphrey, and P. Xanthopoulos, Phys. Rev. Lett. **105**, 095004).

[7] C.C. Hegna, P.W. Terry and B.J. Faber, Phys. Plasmas **25**, 022511 (2018).

[8] A.M. Dimits, G. Bateman, M.A. Beer, B.I. Cohen, W. Dorland, G.W. Hammett, C. Kim, J.E. Kinsey, M. Kotschenreuther, A.H. Kritz et al., Phys. Plasmas, **7**, 969 (2000).

[9] D.R. Mikkelson and W. Dorland, Phys. Rev. Lett. **101**, 135003 (2008).

[10] P.W. Terry, P.-Y. Li, M.J. Pueschel, and G.G. Whelan, Phys. Rev. Lett. **126**, 025004 (2021).

[11] Z.R. Williams, M.J. Pueschel, P.W. Terry, and T. Hauff, Phys. Plasmas **24**, 122309 (2017).

[12] P.W. Terry, B.J. Faber, C.C. Hegna, V.V. Mirnov, M.J. Pueschel, and G.G. Whelan, Phys. Plasmas **25**, 012308 (2018).

[13] B.N. Rogers, W. Dorland, and M. Kotschenreuther, Phys. Rev. Lett. **85**, 5336 (2000).

[14] K. Miki, Y. Kishimoto, N. Miyato, and J.Q. Li, Phys. Rev. Lett. **99**, 145003 (2007).

[15] S.-I. Itoh and K. Itoh, Nucl. Fusion **56**, 106028 (2016).

[16] F. Rath, A.G. Peeters, R. Buchholz, S.R. Grosshauser, F. Seiferling, and A. Weikl, Phys. Plasmas **25**, 052102 (2018).

[17] C. Holland, P.H.Diamond, S. Champeaux, E. Kim, O. Gurcan, M.N. Rosenbluth, G.R. Tynan, N. Crocker, W. Nevins, and J. Candy, Nucl. Fusion **43**, 761 (2003).

[18] D.A. St-Onge, J. Plasma Phys. **83**, 905830504 (2017).

[19] H. Zhu, Y. Zhou, and I.Y. Dodin, Phys. Rev. Lett. **124**, 055002 (2020).

[20] K. Makwana, P.W. Terry, and J.-H. Kim, Phys. Plasmas **19**, 062310 (2012).

[21] K. Makwana, P.W. Terry, M.J. Pueschel, and D.R. Hatch, Phys. Rev. Lett. **112**, 095002 (2014).

[22] M. Stransky, Phys. Plasmas **18**, 052302 (2011).

[23] D.R Hatch, P.W. Terry, F. Jenko, F. Merz, and W.M. Nevins, Phys. Rev. Lett. **106**, 115003 (2011).

[24] P.W. Terry, K.D. Makwana, M.J. Pueschel, D.R. Hatch, F. Jenko, and F. Merz, Phys. Plasmas **21**, 122303 (2014).

[25] D.R. Hatch, P.W. Terry, F. Jenko, F. Merz, M.J. Pueschel, W.M. Nevins, and E. Wang, Phys. Plasmas **18**, 055706 (2011).

[26] G.G. Whelan, M.J. Pueschel, and P.W. Terry, Phys. Rev. Lett. **120**, 175002 (2018).

[27] P.H. Diamond, S.-I. Itoh, K. Itoh, and T.S. Hahm, Plasma Phys. Control. Fusion **47**, R35 (2005).

[28] F. Jenko, W. Dorland, M. Kotschenreuther, and B.N. Rogers, Phys. Plasmas **7**, 1904 (2000).

[29] G. Hammett, UCLA Winter School, Center for Multiscale Plasma Dynamics, Los Angeles, CA, Jan. 2007.

[30] G.G. Whelan, Ph.D. Dissertation, Univ. of Wisconsin-Madison, 2019.

[31] W. Horton, D.-I. Choi, and W.M. Tang, Phys. Fluids **24**, 1077 (1981).

[32] M.J. Pueschel and F. Jenko, Phys. Plasmas **17**, 062307 (2010).

[33] G.G. Whelan, M.J. Pueschel, and P.W. Terry, Phys. Rev. Lett. **120**, 175002 (2018).

[34] G.G. Whelan, M.J. Pueschel, P.W. Terry, J. Citrin, I.J. McKinney, W. Guttenfelder, and H. Doerk, Phys. Plasmas **26**, 082302 (2019).

[35] A.J. Wootton, M.E. Austin, R.D. Bengtson, J.A. Boedo, R.V. Bravenec, D.L. Brower, J.Y. Chen, G.Cima, P.H. Diamond, R.D. Durst et al., Plasma Phys. Control. Fusion **30**, 1479 (1988).

[36] S.A. Orszag, J. Fluid Mech. **41**, 363 (1970).

[37] R.H. Kraichnan, J. Fluid Mech. **5**, 497 (1959).

[38] P.W. Terry and W. Horton, Phys. Fluids **26**, 206 (1983).

[39] M.J. Pueschel, M. Kammerer and F. Jenko, Phys. Plasmas **15**, 102310 (2008).

[40] M.J. Pueschel, P.-Y. Li and P.W. Terry, Nucl. Fusion **61**, 054003 (2021).

[41] Z. Lin, T.S. Hahm, W.W. Lee, W.M. Tang, and P.H. Diamond, Phys. Rev. Lett. 83, 3645 (1999).

[42] D.R. Ernst, J. Lang, W.M. Nevins, M. Hoffman, Y. Chen, W. Dorland, and S. Parker, Phys. Plasmas **16**, 055906 (2009).

[43] R. Gatto, P.W. Terry, and D.A. Baver, Phys. Plasma **13**, 022306 (2006).

Chapter 5

The Role of Mode Resonances in Regulating Zonal-Flow-Moderated Plasma Microturbulence

Abstract

The onset of turbulent heat flux at a higher temperature gradient than the critical gradient of linear instability (known as the Dimits shift) is a well-known feature in fusion plasmas. It was shown in the saturation theory that resonance in the nonlinear coupling between the modes that dominate energy transfer in saturation can lead to suppression of turbulence and transport just above the linear critical gradient. Gyrokinetic simulations with ITG turbulence which has a Dimits shift have shown the clear coherence structure between streamers and sidebands coupled through zonal flow within the Dimits regime, which agree to the resonance picture. Furthermore, the resonance concept is also tested by use of artificial complex frequencies to break the resonance. By incorporating the more complete saturation physics described above, the quasilinear model for fast heat flux prediction is improved, in particular the triplet correlation time, the life time of the nonlinear interaction, which can be approximated from linear inputs. This work was carried out in collaboration with Paul W. Terry, Garth G. Whelan, and M.J. Pueschel.

In chapter 4, the triplet correlation time, eddy-turnover rate, and resonance picture are used to explain the Dimits shift. However, it is unclear whether it can be generalized to gyrokinetic simulations. In this chapter, we will discuss whether these ideas are still important in explaining Dimits shift in gyrokinetic simulations with numerical experiments. A quasilinear model is improved with this concept to predict heat flux for systems with and without Dimits shift. The performance of the improved quasilinear model will be described in the last section of this chapter.

5.1 Introduction

While much progress has been made over the years towards understanding instabilities, turbulence, and transport in fusion devices, key questions regarding the behavior of turbulent fluctuations remain. In order to predict with confidence the performance of next-generation fusion experiments as well as reactors, and to ensure that high-performance operation will be possible, a thorough understanding of turbulence is essential. One particularly important effect, understanding of which has eluded researchers for some time, is the upshift of the nonlinear critical gradient relative to the linear instability threshold, also known as the Dimits shift [27]. In this Dimits regime between the linear and nonlinear critical gradients, turbulence is dominated by strong zonal flows, which largely but not completely suppress turbulent transport. This phenomenon has been seen in both ion-temperature-gradientdriven (ITG) and trapped-electron-mode (TEM) turbulence [2, 26].

Due to the presence of strong zonal flows in systems with Dimits regimes, many studies on this topic have based their theories on transport suppression by zonal-flow shearing [1, 2, 3, 4, 5], with the zonal-flow shearing rate $\omega_{\mathrm{s}} = \sum_{k_x} k_x^2 \Phi_{k_y=0}$ an important means of quantifying this effect. Other proposed mechanisms have

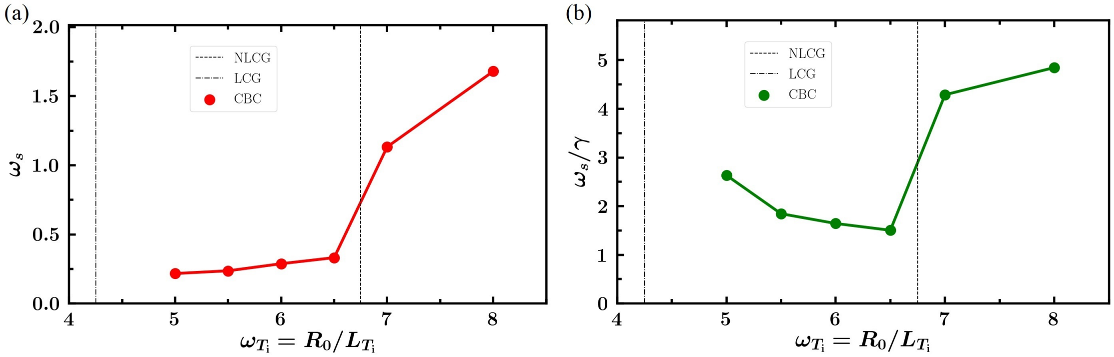

Figure 5.1: (a) Zonal flow shearing rate $\omega_s = \sum_{k_x} k_x^2 |\Phi_{ZF}|$ as a function of temperature gradient $\omega_{T\mathrm{i}}$. (b)Ratio of zonal flow shearing rate to growth rate of the most unstable mode γ as a function of $\omega_{T\mathrm{i}}$. Vertical lines denote the linear (dashed-dotted) and nonlinear (dashed) critical gradients. The shearing rate increases as ω_T increases, the shearing rate is always larger than the growth rate of the most unstable mode.

included tertiary instability and nonlinear suppression of energy transfer to the zonal flow [6, 7], impeding the zonal flow shearing and leads to inefficient turbulence suppression above the nonlinear critical gradient (NLCG). Generally, past theories fail to explain recent observations in gyrokinetic ITG turbulence simulations, where the zonal-flow shearing rate ω_s increases as the ion temperature gradient $\omega_{T\mathrm{i}}$ increases [8]. Relatedly, one may perform gyrokinetic ITG turbulence simulations with adiabatic electrons at Cyclone-Base-Case (CBC) parameters to show that the weakening zonal flow shearing picture cannot explain the to Dimits shift : Fig. 5.1 (a) shows the zonal flow shearing rate versus $\omega_{T\mathrm{i}}$, while Fig. 5.1 (b) shows the ratio of zonal flow shearing rate to growth rate γ of the most unstable mode as a function of $\omega_{T\mathrm{i}}$. The linear and nonlinear critical gradients are marked with the dashed-dotted and dotted lines, respectively. The shearing rate is much higher compared to the growth rate above the NLCG, suggesting the zonal flows are not weakened; instead, the stronger turbulence has driven the zonal flows to an even higher level. This can also be seen in Fig. 5.2, where the zonal field spectrum increases in amplitude and

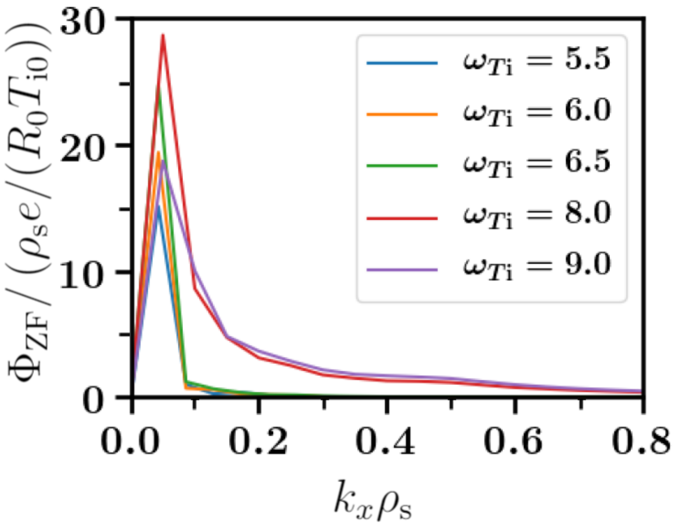

Figure 5.2: The zonal field spectrum for various $\omega_{T_{\mathrm{i}}}$ above and within the Dimits regime. The high-k_x zonal flow contributes nearly nothing to the shearing rate within in the Dimits regime. Note that k_x has the unit ρ_0^{-1}, the inverse of gyroradius

widens above the Dimits regime, corresponding to an increase of the shearing rate. Thus, other nonlinear mechanisms must underly the formation of the Dimits shift.

Histograms of heat-flux amplitudes are shown in Fig. 5.3. Above the Dimits regime, the excess kurtosis and skewness are closer to zero compared to within the Dimits regime, which means that the heat-flux histogram is much closer to a Gaussian distribution above the NLCG. Since the Gaussian distribution is also known as the indicator of randomness, looking like a Gaussian distribution implies that the system has a variety of nonlinear interactions excited, including the nonlinear interactions involving non-zonal-wavenumbers, which has been observed in Ref. [7]. On the other hand, the theory in Ref. [9, 28] points out that nonlinear interactions can modify mode frequencies, which can lead to higher heat flux due to detuning of resonances between the unstable and stable modes and less efficient energy transfer. It also states that because the magnitudes of the nonlinear effects depend on the

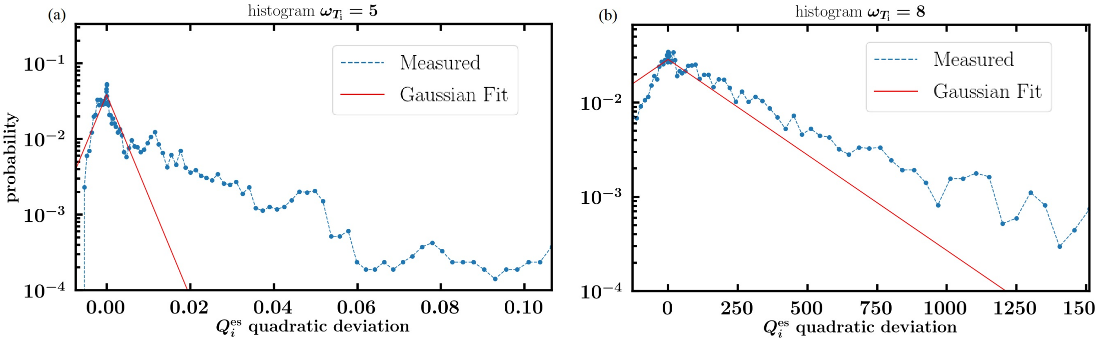

Figure 5.3: Histogram of heat fluxes in the quasi-stationary state for (a) $\omega_{T_\mathrm{i}} = 5$, with skewness = 1.446 and excess kurtosis = 1.219, and (b) $\omega_{T_\mathrm{i}} = 8$, with skewness = 0.681 and excess kurtosis = -0.97. The histogram above the Dimits regime is closer to a Guassian distribution, implying that the nonlinear interactions involving non-zonal wavenumbers are more excited above the Dimits regime.

turbulence level, the actual turbulence level therefore deviates significantly from the prediction based only on linear physics above the Dimits regime, which agrees to the gyrokinetic observations presented here so far.

In order to further examine the resonance concept between stable and unstable modes for Dimits shift, we performed a series of numerical examinations and observations, which will be presented in this chapter as follows. The underlying saturation theory and the ingredients leading to eigenmode resonance are explained in Sec. 5.2. Damped eigenmodes are shown to be a key player by using symmetry-breaking techniques in gyrokinetic simulations in Sec. 5.3. In Sec. 5.4, a series of gyrokinetic simulations comparing the frequency spectrum and coherence structure between the streamer and the sidebands above and below the NLCG are shown to be consistent to the saturation theory. Section 5.5 tests the resonance picture in the saturation theory by observing how the system reacts to the artificial modification of turbulent complex frequencies in gyrokinetic simulations. How the saturation theory can be used to improve quasilinear models will be addressed in Sec. 5.6, and thus-improved quasilinear transport estimates are then shown to recover nonlinear scalings for a number of parameter cases in addition to the cases shown in Ref. [14].

5.2 Saturation Theory for zonal-flow-Dominated Systems

In Ref. [11], a saturation theory was proposed based on a curvature-driven ITG fluid model. This model measures how efficiently energy injected by unstable eigenmodes can be transfered to the damped eigenmodes. The energy transfer rate away from the unstable modes can be influenced by several factors such as the amplitudes of the eigenmodes, the lifetime of the nonlinear interactions between eigenmodes, and the efficiency of the coupling between eigenmodes. The latter two can be quantified from linear calculations and were used to described the nonlinearity in the saturation theory. Note that in gyrokinetics, the nonlinearity is similar to that in the fluid model, allowing for the use of similar techniques to evaluate the gyrokinetic counterparts.

The gyrokinetic nonlinearity $N[g_{j,k}]$ for the distribution function $g_{j,k}$, where $\frac{dg_{j,k}}{dt} = L[g_{j,k}] + N[g_{j,k}]$ reads

$$N[g_{j,k}] = \sum_{k'} \int \left(k'_x k_y - k_x k'_y\right) \chi_{j,k'} g_{j,k''} dz dv \ . \tag{5.1}$$

The nonlinear transfer rate of energy to wavenumber $k = (k_x, k_y)$ can then be written as

$$T_k = 2\mathrm{Re}\left\{\sum_{k',j} \int \frac{n_{j0} T_{j0}}{F_{j0}} \left[g_{j,k} + \frac{q_j F_{j0}}{T_{j0}} \chi_{j,k}\right]^* \left(k'_x k_y - k_x k'_y\right) \chi_{j,k'} g_{j,k''} dz dv\right\} \ , \tag{5.2}$$

where $k'' = k - k' = (k_x - k'_x, k_y - k'_y)$, $g_{j,k}$ is the nonadiabatic perturbed distribution function for species j with wavenumber k, $\chi_{j,k} = \bar{\Phi} - v_{Tj} v_\parallel \bar{A}_\parallel$ is the modified potential, v_{Tj} is the thermal speed of species j, $\bar{\Phi}$ the electric potential, $A_\parallel$ being the parallel magnetic potential, $v_{\parallel}$ is the parallel velocity, n_{j0} is the background density, T_{j0} is the background temperature, q_j is the charge, F_{j0} is the background Maxwellian, z is the parallel coordinate, $v = (v_{\parallel,\mu})$ is the velocity vector. Because unstable modes drive turbulence, it is useful to track the energy delivered from these modes. Thus, one may project the energy transfer rate at k on the n-th unstable eigenmode to obtain the energy transfer rate $T_k^{n,\mathrm{ev}}$ for the eigenmode in question. To obtain the projection, the nonadiabatic distribution function $g_{j,k}$ is first decomposed into eigenmodes $g_{j,k} = \sum_o \beta_{o,k} v^{\mathrm{r}}_{o,k}$, where $\beta_{o,k}$ is the amplitude of o-th eigenmode at wavenumber k, and $v^{\mathrm{r}}_{o,k}$ is its corresponding right eigenvector. By taking advantage of the orthogonality of the right and left eigenvectors, that is, $\left\langle v^{\mathrm{l}}_{n,k}, v^{\mathrm{r}}_{o,k} \right\rangle = \delta_{no}$, where $v^{\mathrm{l}}_{n,k}$ is the left eigenvector of the n-th mode at wavenumber k and $\langle , \rangle$ denotes the inner product, or a numerical sum over $(z, v_{\parallel}, \mu)$, the eigenmode amplitude can be derived by calculating the inner product of its left eigenvector $v^{\mathrm{l}}_{n,k}(z, v_{\parallel}, \mu)$ and the nonadiabatic distribution function $g_{j,k}(z, v_{\parallel}, \mu)$ as $\beta_{n,k} = \left\langle v^{\mathrm{l}}_{n,k}(z, v_{\parallel}, \mu), g_{j,k}(z, v_{\parallel}, \mu) \right\rangle$. Similarly, the energy transfer rate to the n-th eigenmode can be obtained via the inner product of T_k and the left eigenvector $v^{\mathrm{l}}_{n,k}$, as $T_k^{n,\mathrm{ev}} = \left\langle v^{\mathrm{l}}_{n,k}, T_k \right\rangle$. By expanding $\chi_{j,k'}$ in the eigenmode basis and inserting it into $T_k^{n,\mathrm{ev}} = \left\langle v^{\mathrm{l}}_{n,k}, T_k \right\rangle$ along with $g_{j,k} = \sum_{o,k} \beta_{o,k} v^{\mathrm{r}}_{o,k}$, one can write

$$T_k^{n,\mathrm{ev}} = 2\mathrm{Re} \sum_{k',l,m} D^{n,l,m}_{k,k'} \beta^*_{n,k} \beta_{l,k'} \beta_{m,k-k'} \ , \tag{5.3}$$

where $D^{n,l,m}_{k,k'}$ is the nonlinear energy coupling coefficient for the triplet energy interaction between the n-th eigenmode at k, the l-th eigenmode at k', and m-th eigenmode at $k - k'$. In order to estimate the averaged $T_k^{n,\mathrm{ev}}$ based soley on linear properties, one must first understand the behavior of the ensemble-averaged $\beta^*_{n,k} \beta_{l,k'} \beta_{m,k-k'}$, as $\left\langle \beta^*_{n,k} \beta_{l,k'} \beta_{m,k-k'} \right\rangle$. One way to estimate this third-order moment is to look at how the it is affected by the beating between eigenmodes. This can be evaluated with help from the evolution equation of the n-th complex eigenmode amplitude $\beta_{n,k}$ at wavenumber k, which can be derived by doing the inner product between the evolution equation of $g_{j,k}$ and the left eigenvector $v^1_{n,k}$, reads

$$\dot{\beta}_{n,k} + i\omega_{n,k}\beta_{n,k} = \sum_{k',l,m} C^{n,l,m}_{k,k'} \beta_{l,k'}\beta_{m,k-k'} \ , \tag{5.4}$$

where $\omega_{n,k}$ is the eigenmode complex frequency, $C^{n,l,m}_{k,k'}$ is the nonlinear coupling coefficient for the triplet interaction. One may use Eq. (5.4) to compose a evolution equation for the third-order moment $\left\langle \beta_{l,k'}\beta_{m,k-k'}\beta^*_{i,k} \right\rangle$,

$$\frac{\partial \left\langle \beta_{l,k'}\beta_{m,k-k'}\beta^*_{i,k} \right\rangle}{\partial t} + i\left[\omega_{m,k-k'} + \omega_{l,k'} - \omega^*_{i,k}\right] \left\langle \beta_{l,k'}\beta_{m,k-k'}\beta^*_{i,k} \right\rangle \sim \left\langle \beta^4 \right\rangle \ , \tag{5.5}$$

where $\langle \beta^4 \rangle$ denotes the combinations of fourth-order moments. By applying a quasi-normal statistical closure described in Ref. [11] to Eq. (5.5), $\langle \beta^4 \rangle$ can be fully expressed by the combinations of the second-order moment $\langle \beta^2 \rangle$. With the help of the method of Green's function, the third-order moment can be expressed as

$$\left\langle \beta_{l,k'}\beta_{m,k-k'}\beta^*_{i,k} \right\rangle \sim \tau^{m,l,i}_{k,k'} \left\langle \beta^2 \right\rangle \left\langle \beta^2 \right\rangle \ , \tag{5.6}$$

where $\tau^{m,l,i}_{k,k'} = -i\left(\hat{\omega}_{m,k-k'} + \hat{\omega}_{l,k'} - \hat{\omega}^*_{i,k}\right)^{-1}$ is called the triplet correlation time, $\hat{\omega}_{i,k} = \omega_{i,k} + \Delta\omega_{i,k}$, and $\Delta\omega_{i,k}$ is the nonlinear complex frequency increment, stemming from nonlinearity. The triplet correlation time is the lifetime of the propagator in the Green's function approach, therefore, it also serves as a the measure of the lifetime of each nonlinear beatings of the triplet interaction $\left\langle \beta_{l,k'}\beta_{m,k-k'}\beta^*_{i,k} \right\rangle$. The life time of the triplet interaction $\left\langle \beta_{l,k'}\beta_{m,k-k'}\beta^*_{i,k} \right\rangle$ directly affects the magnitude of the total accumulated nonlinear interaction among the time history. With longer lifetime, the unstable modes can more strongly couple to the stable modes, and deliver energy more efficiently to the energy sink provided by the stable modes, thus removing it from the turbulence. This can be shown by inserting Eq. (5.6) into the ensemble-averaged Eq. (5.3), which yields

$$T_{k,k'}^{n,\mathrm{ev}} \sim \mathrm{Re} \sum_{k',l,m} A_k C_{k,k'}^{n,l,m} \tau_{k,k'}^{m,l,i} \left\langle \beta^2 \right\rangle \left\langle \beta^2 \right\rangle \ . \tag{5.7}$$

Equation (5.7) shows that by calculating the triplet correlation time, one can estimate the scalings of the nonlinear energy transfer rate. As saturation of ITG turbulence preferentially involves energy transfer from unstable modes to stable modes catalyzed by zonal flows[11, 24], it helps to focus on the triplet interactions that involve a zonal flow, an unstable and a stable mode, that is, $\beta_{n,k}$ and $\omega_{n,k}$ refer to an unstable mode, $\beta_{l,k'}$ and $\omega_{l,k'}$ refer to a zonal flow, while $\beta_{m,k-k'}$ and $\omega_{m,k-k'}$ refer to a damped mode. Note that in a more quiescent regime such as the Dimits regime, $\Delta\omega_{i,k}$ in $\tau_{k,k'}^{m,l,i}$ will be relatively small compared to $\omega_{i,k}$ due to the fact that the nonlinear frequencies are proportional to a positive power of the turbulence level. Therefore, $\hat{\omega}_{i,k} \approx \omega_{i,k}$, and the triplet correlation time can be expressed approximately with the linear frequencies $\tau_{k,k'}^{m,l,n} \approx -i \left(\omega_{m,k-k'} + \omega_{l,k'} - \omega_{n,k}^*\right)^{-1}$. Moreover, the pseudospectra of the linear frequency ω for stable modes is close to the complex conjugate of the frquency of the most unstable mode for low-collisionality ITG systems based on equipartition theory for the stable modes.[24] Taken together with the amplitude dependence of Delta omega, this implies that the linear frequencies in $\tau_{k,k'}^{m,l,n}$ for systems near the critical gradient will cancel out the lowest order terms and lead to large $\tau_{k,k'}^{m,l,n}$ and low heat flux. Thus, the energry-transfer resonance of the stable and unstable mode suppresses the turbulence. Conversely, in regimes where the nonlinear frequencies $\Delta\omega_{i,k}$ are large, the system is far away from resonance, which leads to much smaller triplet correlation times and less efficient nonlinear energy transfer. Figure 5.4 schematically illustrates these properties.

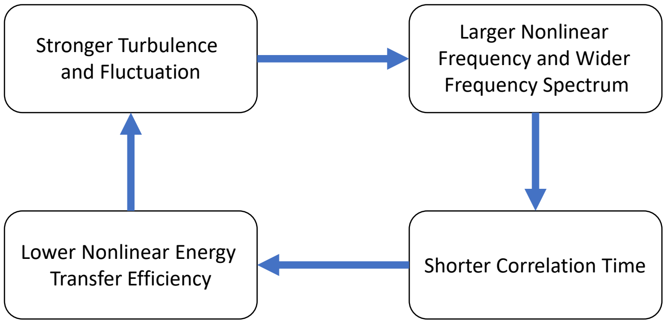

Figure 5.4: If we raise the gradient to induce larger fluctuation and stronger turbulence, the nonlinear frequency will also be enlarged, which will lead to smaller lifetime of the nonlinear energy transfer. The system will therefore end up at a more turbulent state, which deviates from the prediction based only on linear physics.

5.3 Symmetry breaking in ITG turbulence

The primary saturation channel in ITG turbulence involves an unstable mode, a large-scale stable mode, and a zonal flow. One simple way to show that stable modes are important is to observe how the heat flux changes as stable-mode damping is artificially enhanced while not modifying the growth rate of the unstable eigenmode. If the stable modes were unimportant, the heat flux would be expected not to change. However, assuming the stable modes do play an important in turbulence saturation, we would expect to observe a heat flux increase when stable modes are further damped, as they quickly remove energy injected by the instability and transfer it back to the background gradients, as opposed to that energy remaining available to the turbulent bath before it can slowly cascade to smaller scales.

For this work, simulations were performed with the nonlinear gyrokinetic Vlasov code GENE. Physical input parameters correspond to the kinetic-electron Cyclone Base Case (CBC)[12] with $\omega_{T_\mathrm{e}} = 0$ to ensure pure ITG turbulence, that is

$$\begin{aligned} &\omega_{T_\mathrm{i}} = 8, \quad \omega_{T_\mathrm{e}} = 0, \quad \omega_n = 3, \quad \hat{s} = 0.796, \\ &q_0 = 1.4, \quad \epsilon_\mathrm{t} = 0.18, \quad T_\mathrm{i}/T_\mathrm{e} = 1, \quad \beta = 0.5\% \end{aligned} \tag{5.8}$$

where $\omega_{T_\mathrm{j}} = R_0/L_{T_\mathrm{j}}$ is the normalized temperature gradient of species j, with R_0 being the major radius, $\omega_n = R_0/L_n$ is the normalized density gradient, $\hat{s}$ is the magnetic shear, q_0 is the safety factor, $\epsilon_\mathrm{t} = r_0/R_0$ is the inverse aspect ratio of the flux surface of interest, and T_j is the equilibrium temperature of species j. Both ions and electrons are treated kinetically, with a mass ratio of $m_i/m_e = 1836$.

In order to damp the stable modes while leaving the unstable modes unaffected, to show that the stable modes are important in ITG turbulence, one can utilize the fact that stable and unstable modes react in opposite ways to the temperature gradient ω_{T_i} but the same way to an artificial-damping operator $\propto D_{rad}$, the radiative damping.[28] The growth rates of the unstable modes in ITG turbulence increase as the temperature gradient increases; the growth rates of the stable modes become more negative when the temperature gradient is increased. On the other hand, artificial damping moves the whole growth rate spectrum downward, that is, smaller growth rates for unstable modes and stronger damping rates for the stable modes. Therefore, it is possible to increase the temperature gradient while concurrently adding radiative damping to achieve zero net chnage of the unstable growth rate and significant additional damping on the modes, as illustrated in Fig. 5.5. Figure 5.6 shows the growth rate spectrum of the unstable eigenmode with and without these modifications. The two spectra are nearly identical. Thus, one can indeed use this modified system to test whether stable modes impact saturation.

Figure 5.7 shows a 60% heat flux increase when adding artificial damping on the stable modes. In the linear stage, the heat fluxes of both simulations are identical, and the differences manifest only once saturation is achieved, when the stable modes

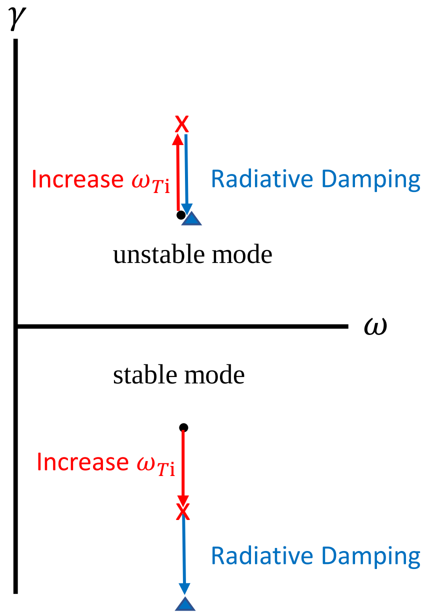

Figure 5.5: Schematic of how unstable and stable eigenvalues are affected by a combination of increased gradient drive (red) and radiative damping (blue): the original eigenvalue (black circles) experiences stronger growth/damping for the unstable/stable ITG mode due to increased $\omega_{T\mathrm{i}}$ (black crosses), while both modes are damped when adding the radiative damping term (blue triangles). These effects can be balanced to ensure close to no change of the unstable mode relative to the original eigenvalue.

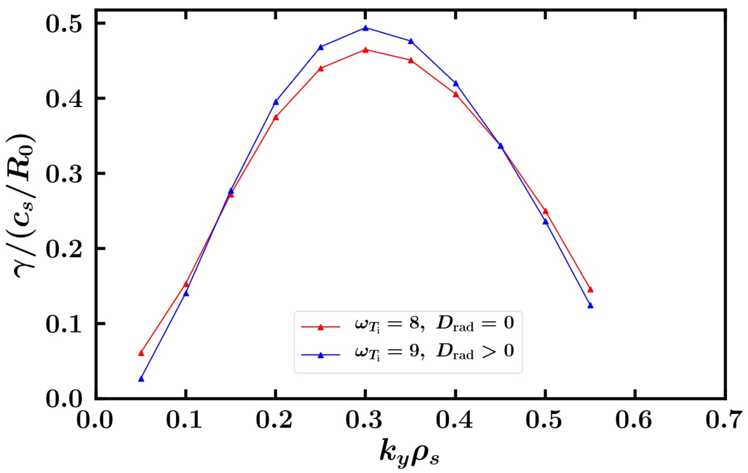

Figure 5.6: The red curve is the growth rate spectrum with $D_\mathrm{rad} = 0$ and $\omega_{T_\mathrm{i}} = 8$. The blue curve is the one with $D_\mathrm{rad} = 0.02338$, $\omega_{T_\mathrm{i}} = 8$, and second order hyper diffusion in y direction with magnitude $= 0.1338$ to suppress the growth rate in the high k regime. The growth rate spectra are nearly identical.

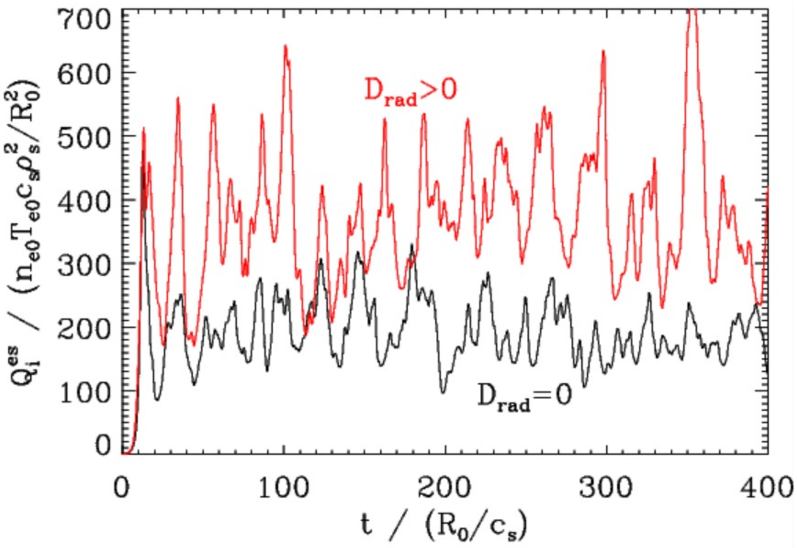

Figure 5.7: Time traces of ion electrostatic heat flux for a simulation with artificial radiative damping (red) and increased gradient drive, and for the reference simulation (black). Adding radiative damping leads to 60% more heat flux even though the linear growth rate spectrum is well matched between the two cases.

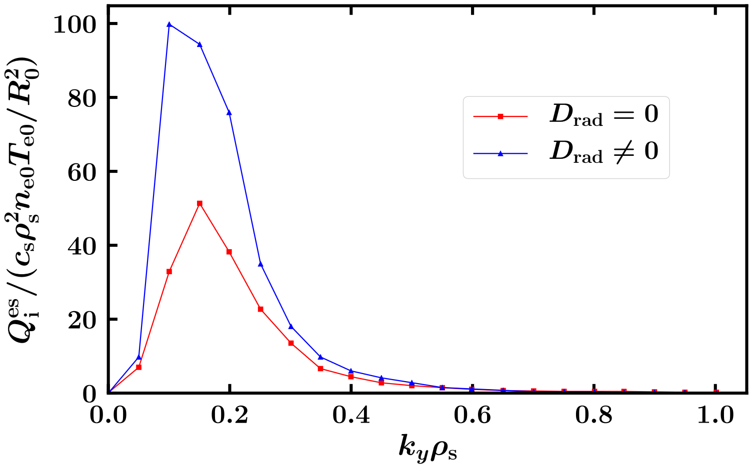

Figure 5.8: Heat flux spectra simulations with (a) $D_{\mathrm{rad}} = 0$ and (b) $D_{\mathrm{rad}} = 0.02338$. with matched growth rate spectra for the unstable ITG mode.

are excited to significant amplitudes. As can be seen in Fig. 5.8, the increase in the heat flux is primarily stemming from low-k modes, whereas the heat flux contributed by modes above $k_y = 0.4$ is hardly affected. As, for the purpose of tracking nonlinear dynamics, the collective stable modes can be replaced by the mirror modes of the unstable modes, i.e., with equal real frequency but close to the negative of the unstable modes' growth rate.[15, 16] The significant increase of heat flux at low k after the procedure confirms that the large-scale energy removal by the stable modes is important for turbulence saturation. When the approximate conjugate symmetry between low-k stable and unstable modes is broken, the turbulence will saturate through other, less efficient saturation mechanisms and produce higher amplitudes and fluxes.

5.4 Nonlinear frequency broadening

Resonance between linear eigenmodes can lead to effective energy transfer away from the unstable modes. Nonlinear modifications to the eigenvalues, however,

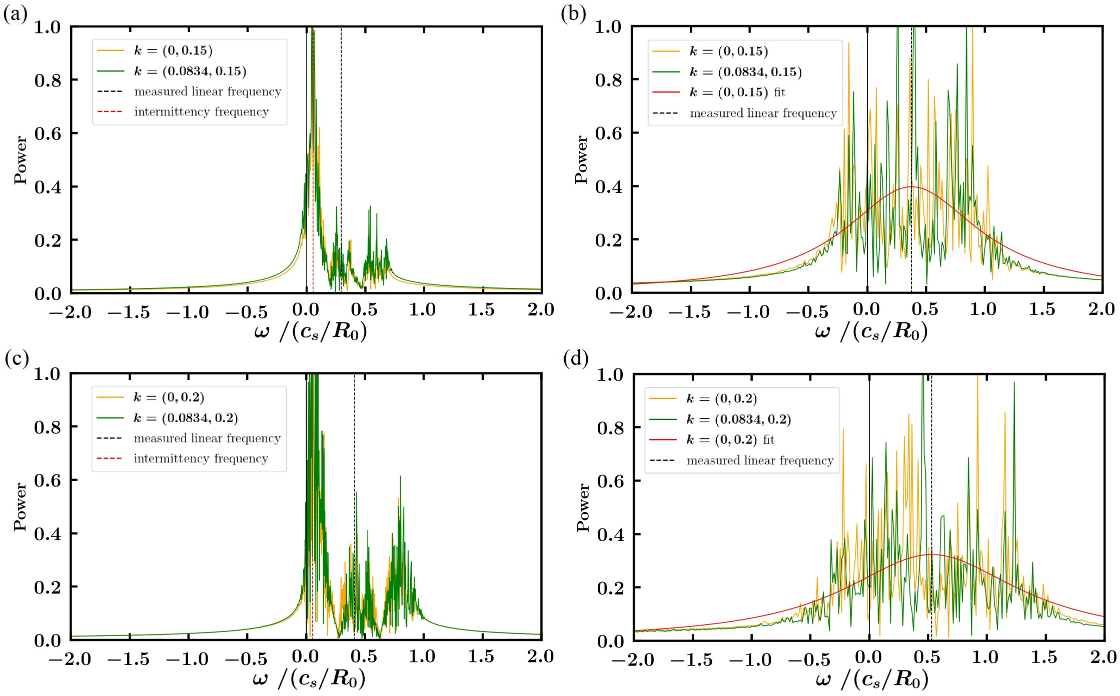

Figure 5.9: Frequency spectrum for (a) $\omega_{T_\mathrm{i}} = 5$ at $k_y = 0.15$, (b) $\omega_{T_\mathrm{i}} = 8$ at $k_y = 0.15$, (c) $\omega_{T_\mathrm{i}} = 5$ at $k_y = 0.2$, (d) $\omega_{T_\mathrm{i}} = 8$ at $k_y = 0.2$. Black dotted lines denote linear frequencies, whereas red dotted lines in (a) and (c) are intermittency frequencies obstained from nonlinear simulations. The red curve in (b) and (d) are Lorentzian fits to the frequency spectra. Frequency spectra are wider above the Dimits regime. The frequency spectra with same k_y are almost identical within the Dimits regime

can produce decoherence and resonance de-tuning of the eigenmodes.The frequency spectra above and in the Dimits regime for adiabatic-electron CBC parameters is shown Fig. 5.9. The frequency spectrum is derived by Fourier-transforming the auto-correlation function $R = \frac{1}{\mathrm{T}} \int_0^T \Phi_k^*(t)\Phi_k(t+\Delta t)dt$, where $[0, T]$ is an appropriate time interval in the quasi-stationary state, and $\Phi_k(t)$ is the electrostatic potentail at wavenumber k and time t. Note that the frequency spectrum is normalized with respect to its maximum value at the wavenumber $k = (k_x, k_y)$ in question.

Within the Dimits regime, the frequency spectra for $k = (0, 0.015)$ and $k = (0.0834, 0.15)$ are nearly identical, which can seen in Fig. 5.9(a). Figure 5.9(c) shows the same feature between the streamer and the sideband at $k_y = 0.2$. This suggests that eigenmodes with the same k_y are highly coherent within the Dimits regime, leading to strong zonal-flow-catalyzed interaction between these modes. Moreover, these are not Lorentzian nor subjected only to the linear frequency of the unstable mode; instead, an important feature in the Dimits-regime frequency spectra in both Fig. 5.9(a) and Fig. 5.9(c) is the intermittency frequency. Combining with the fact that the frequency spectra in Fig 5.9(a) are different from those in Fig. 5.9(c), strong zonal-flow-catalyzed interactions cause a strong resonance between the eigenmodes with same k_y. This amplifies the nonlinear energy transfer between eigenmodes, which leads to more efficient energy delivery to the heat sink comprised of the stable modes and to strongly reduced heat flux within the Dimits regime.

Above the Dimits regime, see Figs. 5.9(b) and 5.9(d), frequency spectra are much wider and can be fitted with a Lorentzian, which indicates that nonlinear interactions are more numerous and less coherent. A clear resonance between eigenmodes with the same k_y can thus no longer exist. Therefore, zonal-flow-catalyzed energy transfer is not as effective as it is within the Dimits regime.

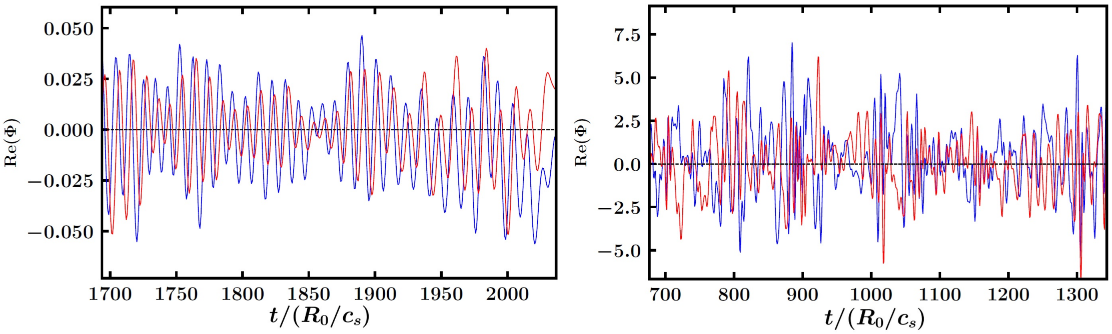

Figure 5.10: $\mathrm{Re}(\Phi_k)$ as a function of time for (a) $\omega_{T\mathrm{i}} = 5$ for $k = (0, 0.15)$ and $k = (0.0834, 0.15)$, and for (b) $\omega_{T\mathrm{i}} = 8$ for $k = (0, 0.15)$ and $k = (0.0834, 0.15)$. Modes above the Dimits regime are less coherent.

Another way to investigate the resonance is to relate time traces of the electrostatic potential at different wavenumbers. From Fig. 5.10, it is apparent that the phase between Φ_k at the same k_y but different k_x within the Dimits regime is remarkably constant, consistent with strongly resonant behavior. By contrast, above the Dimits regime, Φ_k at the same k_y are no longer coherent, and leading to less efficient energy transfer.

In order to quantify these observations, one can further calculate the cross-correlation function $C = \frac{1}{\mathrm{T}} \int_0^T \Phi_k^*(t)\Phi_{k'}(t + \Delta t)dt$ of Φ_k and $\Phi_{k'}$ for $k \neq k'$. In Fig. 5.11(a), where the system is within the Dimits regime, there exists a large peak of the cross-correlation function between two zonally coupled modes at $k = (0, 0.15)$ and $k = (0.0834, 0.15)$, while the non-zonally coupled modes at $k = (0, 0.15)$ and $k = (0, 0.2)$ shows no such thing. In order to understand how coherent Φ_ks are at two different k, one can measure the ratio of the magnitude the peak, the correlated signal, and the fluctuations of the decorrelated signal which is calculated via the standard deviation of portion of cross-correlation function for large Δt, which is also known as the peak signal-to-noise ratio in terms of signal processing. Therefore, it is apparent that the zonally coupled modes are strongly coherent, while the non-zonally coupled modes are uncorrelated. In Fig. 5.11(b), where the system is above the Dimits regime, there a peak still exists for the case with the same k_y, but with the decorrelated signal relatively stronger compare to Fig. 5.11(a). Besides, the non-zonally coupled modes remain uncorrelated above the Dimits regime. In Fig. 5.12, one observes that the coherency between $k = (0, 0.15)$ and $k = (0.0834, 0.15)$ decreases as ω_{T_i} increases. This means that the eigenmodes are less coherent above the Dimits regime, and thus, energy transfer is less efficient and the heat flux is significantly higher.

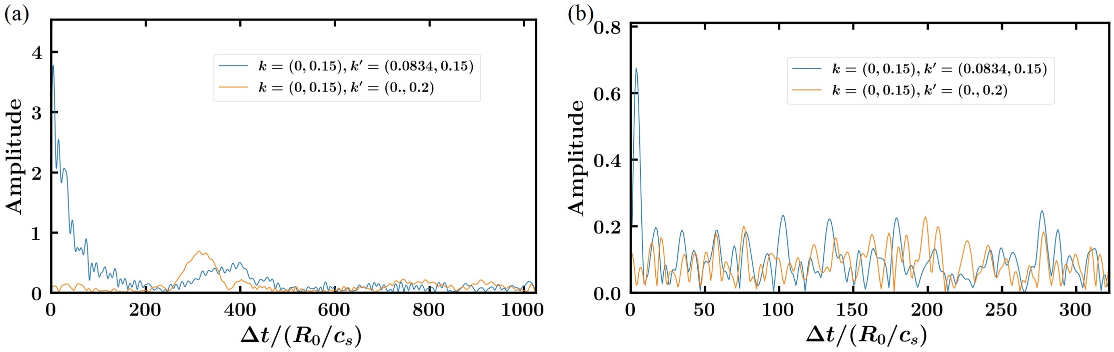

Figure 5.11: Cross-correlation functions C for modes at $k = (0, 0.15)$ and $k = (0.0834, 0.15)$, as well as $k = (0, 0.15)$ and $k = (0., 0.2)$, within the Dimits regime (a) $\omega_{T\mathrm{i}} = 5$ and above the Dimits regime (b) $\omega_{T\mathrm{i}} = 8$. Within the Dimits regime, C is extremely large at the correlated stage

5.5 Resonance breaking

As was demonstrated theoretically above, heat flux-suppression near criticality is due to resonance between unstable and stable modes in zonal-flow-catalyzed nonlinear interactions. Here, numerical experiments will be conducted to produce more direct evidence that the coherency and resonance between the eigenmodes is the cause of the reduction in heat flux, and that stable-mode properties are essential in

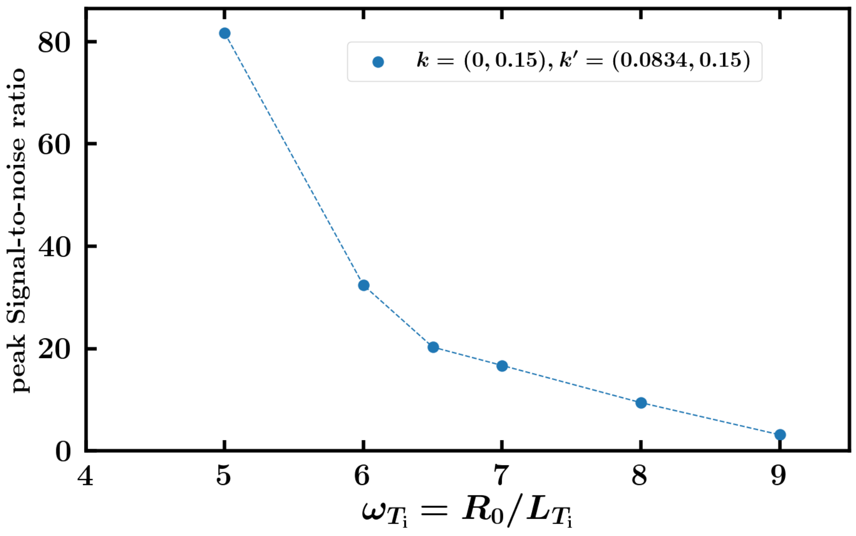

Figure 5.12: The ratio between the correlated signal and the decorrelated signal (peak signal-to-noise ratio) of the cross-correlation function versus $\omega_{T\mathrm{i}}$. The coherency between the electrostatic potential at two wavenumbers coupled through the zonal flow decreases as $\omega_{T\mathrm{i}}$ increases.

determining turbulent amplitudes and fluxes. In order to test the resonance picture,one may add an artificial complex frequency increment $\Delta\omega_{\mathrm{art}}$ to some of the eigenmodes and observe how the saturation level changes. The thus-modified triplet correlation time $\tau_{k,k'}^{l,m,n} = -i(\omega_l'' + \omega_m' - \omega_n^* + \Delta\omega_{\mathrm{nl}} + \Delta\omega_{\mathrm{art}})^{-1}$, will decrease if, before adding the artificial increment, the eigenmodes were at resonance $\omega_l'' + \omega_m' - \omega_n^* + \Delta\omega_{\mathrm{nl}}$. Since most of the energy transfer away from the unstable modes is through zonal-flow-catalyzed interactions with $\omega_m' = \omega'^{\mathrm{ZF}}$,one may choose to add the increment to the zonal flow and observe how the Dimits shift changes in response to this modification.

Figure 5.14 shows saturated heat fluxes for two different levels of artificial zonal dissipation. The red squares represent data from simulations with weaker zonal damping while the magenta circles represent data from simulations with stronger zonal damping. While the Dimits regime can be seen to shrink in either case, larger damping results in a lower NLCG. Moreover, above the Dimits regime, the heat

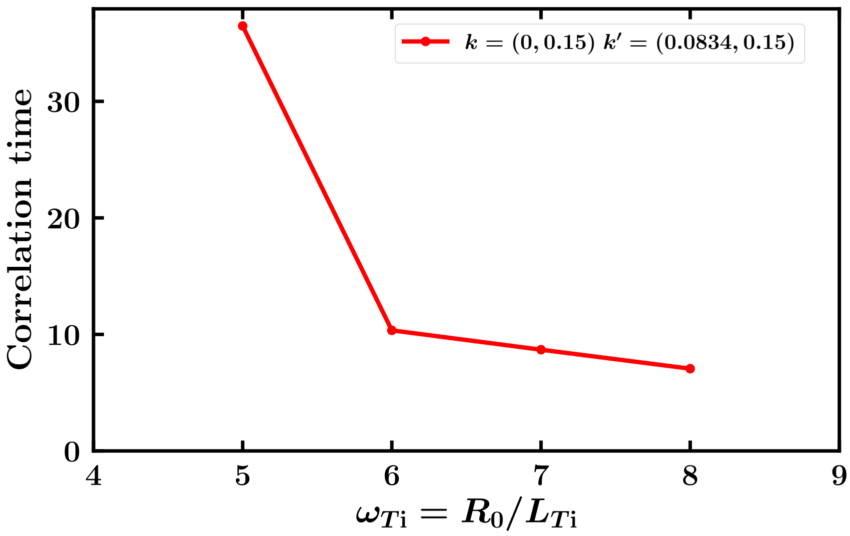

Figure 5.13: The correlation time measured from Fig. 5.11 as a function of $\omega_{T\mathrm{i}}$. The trend is about the same as Fig. 5.12, the correlation time decreases as $\omega_{T\mathrm{i}}$ increases.

fluxes for all three cases shown in Fig. 5.14 are rather similar. This result agrees with the picture that the heat flux is suppressed in the Dimits regime by a frequency resonance is broken. However, one might argue that since adding artificial zonal-flow dissipation weakens the zonal flow, the system will reach higher saturated turbulence levels due to reduced shearing efficiency. While this interpretation is contradicted by the lack of significant transport modification above the NLCG due to artificial zonal damping, one can demonstrate independently that it is indeed resonance breaking that is responsible, by imposing an artificial real frequency on the zonal distribution function, rather than damping. This is achieved by multiplying the distribution function in k space at $k_y = 0$ with $e^{i\Delta\omega_\mathrm{z}t}$ and $e^{-i\Delta\omega_\mathrm{z}t}$ for $k_x > 0$ and $k_x < 0$, respectively, where $\Delta\omega_\mathrm{z}$ is the real artificial zonal frequency.

Figure 5.15 shows the resulting heat fluxes for two different levels of artificial zonal frequencies $\Delta\omega_\mathrm{z}$. Similar to the situation with artificial zonal dissipation, the extent of the Dimits shift is reduced. The case with large zonal frequency is

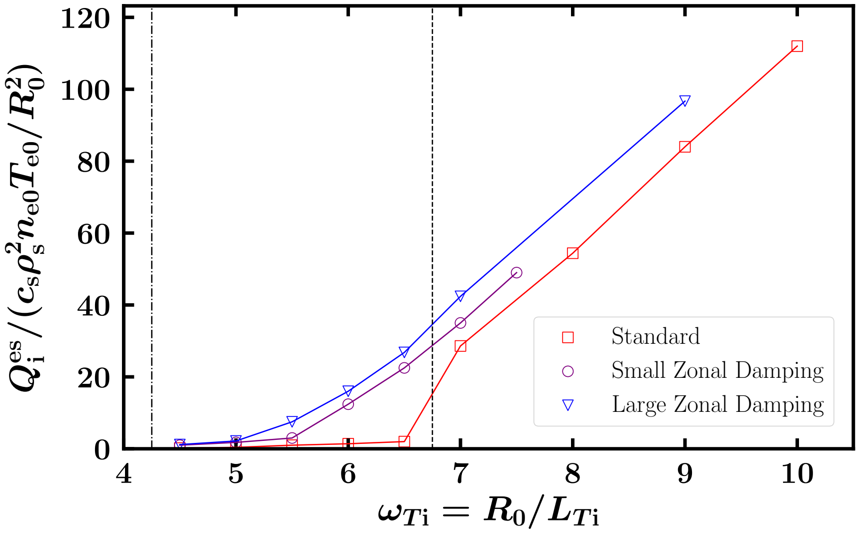

Figure 5.14: Heat flux as a function of temperature gradient for the standard scenario (blue), as well as for cases with artificially introduced weak (red) and strong (magenta) zonal dissipation. The dashed line is the NLCG and the dashed-dotted line is LCG.

designed to have a $\Delta\omega_\mathrm{z} = 0.25$ that approximately matches the eigenmode frequency at the wavenumber of strongest growth. This artificial frequency removes the Dimits shift almost entirely, and the heat flux above the Dimits regime increases only very moderately. The case with a much smaller zonal frequency $\Delta\omega_\mathrm{z} = 0.05$, also reduces the extent of the Dimits regime, but less strongly. Thus, the results agree precisely with the expectations from zonal-flow-catalyzed stable-mode saturation, but not with those from an inertial cascade associated with the shearing paradigm.

The analyses in this section show how breaking the resonance of the zonal-flow-catalyzed triplet interactionsin the Dimits regime dramatically reduces the NLCG. Exiting the resonant regime by increasing the driving temperature gradient can, in some situations, take a shape similar to a tertiary instability, which would deplete the zonal flow. Conversely, the resonance picture is *not* compatible with theories built on the assumption that a (near-)inertial cascade transfers energy to small

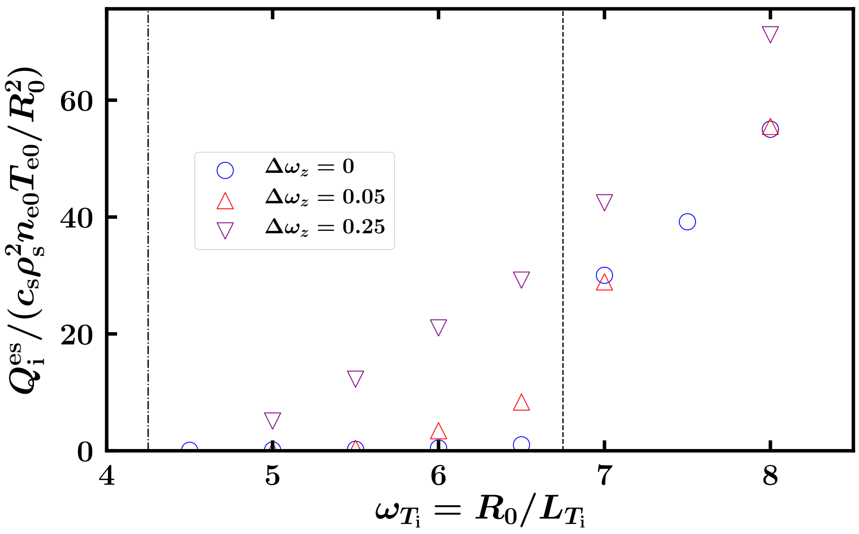

Figure 5.15: Heat flux for the standard Dimits shift scan (blue circle), as well as with two levels of zonal frequency $\Delta\omega_\mathrm{z}$, low (red triangle) and high (magenta triangle). Both cases with artificial zonal frequencies reduce the extent of Dimits shift. The case with strong artificial frequency removes the Dimits shift almost entirely. The dashed line is the NLCG and the dashed-dotted line is LCG.

scales. Setting aside that this assumption does not hold above the NLCG[20], the fact that in Fig. 5.16, smoothly is increased beyond the NLCG demonstrates that no a-priori critical zonal-flow weakening occurs.

5.6 Saturation theory in Quasilinear model building

The standard quasilinear model is derived from Fick's law $Q_\mathrm{i}^\mathrm{es} = \chi_\mathrm{i}^\mathrm{es}\omega_{T_\mathrm{i}}$, where $\chi_\mathrm{i}^\mathrm{es}$ is the ion electrostatic heat diffusivity. Using a mixing-length approach for the heat diffusivity, one arrives at

$$Q_\mathrm{i}^\mathrm{es} = C\omega_{T_\mathrm{i}} \sum_{k_y} \frac{w_k^\mathrm{lin}\gamma_k}{\langle k_\perp^2 \rangle} \, , \tag{5.9}$$

where $w_k^\mathrm{lin} = Q_\mathrm{i}^\mathrm{es}(k)|_\mathrm{lin}/\Phi^2(k)|_\mathrm{lin}$ is the quasilinear weight derived from linear eigenmodes, which includes the phase information relevant for transport, γ_k is the growth rate of the unstable mode, C is a calibration constant used to match the heat flux from one

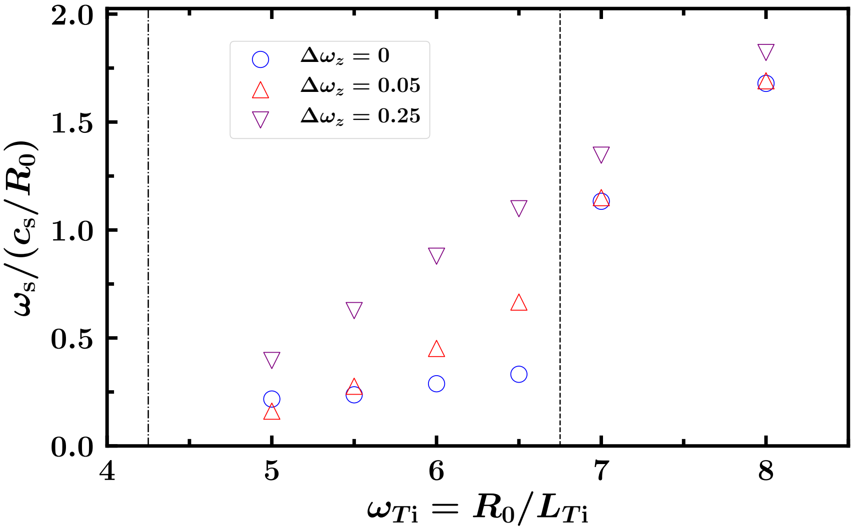

Figure 5.16: ω_s for the standard Dimits shift scan (blue circle), as well as with two levels of zonal frequency $\Delta\omega_{\rm z}$, low (red triangle) and high (magenta triangle). The artificial zonal frequency does not reduce the shearing rate. The dashed line is the NLCG and the dashed-dotted line is LCG.

reference nonlinear simulation, and $\langle k_\perp^2 \rangle$ is the effective wavenumber. The effective wavenumber is given by

$$\langle k_\perp^2 \rangle = \left\langle \frac{k_y^2[1 + [g^{xy} + \hat{s}\theta_0(k_x)g^{xx}]^2]}{g^{xx}} \right\rangle \tag{5.10}$$

where g^{ij} are metric coefficients, $\langle \dots \rangle$ is the average over the ballooning angle from -3π to 3π [13]. As the model is based on a mixing-length argument that relies on linear eigenmode information, it necessarily lacks any information about a possible resonance between the stable modes, unstable modes, and zonal flows. Therefore, to capture the relevant physics in the Dimits regime, it is necessary to expand the quasilinear model by incorporating the triplet correlation time $\tau_{k,k'} = -i[\hat{\omega}^{\rm sideband}_{\rm stable} + \hat{\omega}^{\rm ZF} - (\hat{\omega}^{\rm streamer}_{\rm unstable})^*]^{-1}$, arriving at the improved model

$$Q_{\rm i}^{\rm es} = C\omega_{T_{\rm i}} \sum_{k_y} \frac{w_k^{\rm lin}\gamma_k}{\langle k_\perp^2 \rangle {\rm Re}(\tau_{k,k'})} \,, \tag{5.11}$$

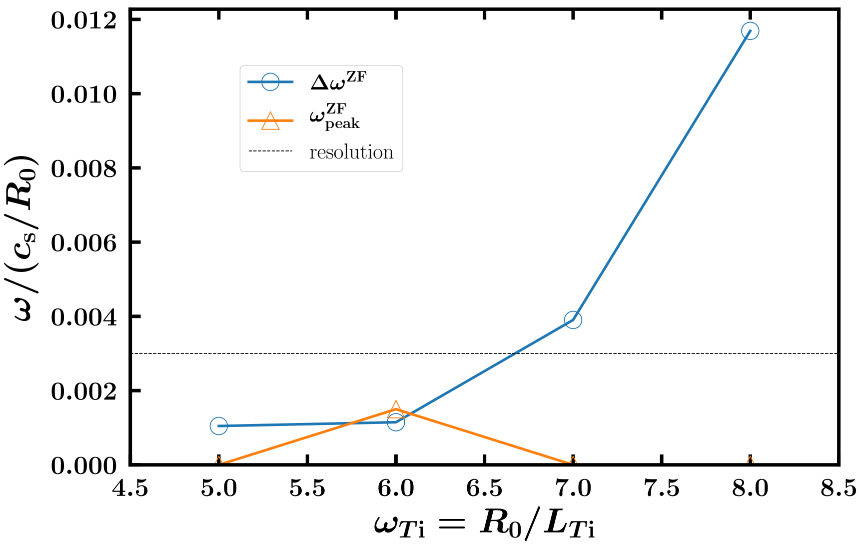

Figure 5.17: Zonal flow peak frequency $\omega^{\mathrm{ZF}}_{\mathrm{peak}}$ and half width $\Delta\omega^{\mathrm{ZF}}$ versus $\omega_{T_{\mathrm{i}}}$ at $k = (0.0834, 0)$. The zonal flow peak frequencies is much smaller than the instability frequency and growth rate. The same applies to the half width $\Delta\omega^{\mathrm{ZF}}$. The resolution is defined as two times the smallest increment of ω.

where $\hat{\omega}^{\mathrm{sideband}}_{\mathrm{stable}}$ is the complex frequency of the sideband stable mode, $\hat{\omega}^{\mathrm{ZF}}$ is the zonal flow complex frequency, and $\hat{\omega}^{\mathrm{streamer}}_{\mathrm{unstable}}$ is complex frequency of the streamer unstable mode, with the complex frequencies defined as $\hat{\omega} = \omega_{\mathrm{lin}} + \Delta\omega_{\mathrm{nl}}$, and the nonlinear complex frequency increment $\Delta\omega_{\mathrm{nl}}$. $\mathrm{Re}(\tau_{k,k'})$ originates from Eq. (5.7) by assuming the coupling coefficients to be close to constant and almost real, therefore, $\mathrm{Re}(C_{k,k'}\tau) \approx C_{k,k'}\mathrm{Re}(\tau)$. However, the triplet correlation time $\tau_{k,k'}$ contains nonlinear components and multiple wavenumbers, and thus a procedure to evaluate it with linear properties is required.[14] The first step is to assume the zonal flow complex frequency $\hat{\omega}^{\mathrm{ZF}} = 0$. This can be justified for collisionless systems, where the time scales of the zonal flow are much longer than those of the instability. The former can be quantified by measuring the peak frequency and the half width of the frequency spectrum of the zonal flow from nonlinear simulations. Figure 5.17 shows that the zonal flow peak frequency is essentially zero for adiabatic-electron CBC. The half width of the zonal flow spectrum $\Delta\omega^{\mathrm{ZF}}$ is only non-zero above the Dimits regime, but even there, its value $\Delta\omega^{\mathrm{ZF}} \sim 10^{-2}$ is much smaller than $\Delta\omega_{\mathrm{nl}} \sim \omega_{\mathrm{linear}} \sim 0.1 - 1$ Thus, one can approximate the zonal-flow complex frequency $\omega^{\mathrm{ZF}} \approx 0$, therefore the triplet correlation time $\tau_{k,k'} \approx -i(\hat{\omega}^{\mathrm{sideband}}_{\mathrm{stable}} - (\hat{\omega}^{\mathrm{streamer}}_{\mathrm{unstable}})^*)^{-1}$. For collisional case, more sophisticated zonal-flow-damping models could could be used in a straightforward manner in $\tau_{k,k'}$ to improve this approach.

The second step is to select the mirror mode of the unstable mode for the sideband complex frequency as the stable mode in the triplet interaction, that is, $\hat{\omega}^{\mathrm{sideband}}_{\mathrm{stable}} = \hat{\omega}^*_{\mathrm{unstable}}$. Even though there exists a sea of stable modes at each wavenumber, one can utilize pseudo-eigenmode analysis [15] to justify that the nonlinear interactions that couple the streamer instability and the zonal flow favor the sideband ITG mirror mode, even when it is not present in the linear eigenmode spectrum. The triplet correlation time can then be further simplified to $-i((\hat{\omega}^{\mathrm{sideband}}_{\mathrm{unstable}})^* - (\hat{\omega}^{\mathrm{streamer}}_{\mathrm{unstable}})^*)^{-1}$. Again, this approximation is valid for collisionless or low-collisionality systems, because substantial collsionality can make it more difficult for the system to access the mirror pseudo-eigenmode.

For the third step, consider the eddy turnover rate $\Delta\omega_{\mathrm{nl}}$, i.e., the nonlinear frequency arising from the sea of the nonlinear interactions. Its magnitude is governed by the number and magnitudes of the most strongly interacting eigenmodes. Meanwhile, the linear eigenmode spectrum is representative of the unstable range, as the temperature gradient $\omega_{T\mathrm{i}}$ is increased, the spectrum of linear energy injection broadens and the amplitudes of the eigenmodes increase. The linear eigemnode spectrum is used to capture the number of the nonlinear interactions and the eigenmode magnitudes and, therefore, track the effect of the eddy damping. As $\omega_{T\mathrm{i}}$ is lowered, it is possible for the linear spectrum at finite k_x to produce only negative growth rates, an effect termed sideband stablization. Note that in most cases, streamers will remain unstable longer than sidebands. Once the sideband is linear stable, energy transfered to it can be efficiently removed from the system. Therefore, the coupling of the streamer to a fully stable sideband through the zonal flow leads to highly efficient turbulence suppression. One may thus use the zonal wavenumber k_x' to measure whether the eigenmodes at a specific k_y are in the turbulent state; where it is not, i.e., where the sideband is stable, interactions are at resonance and one can set $\tau_{k,k'} = \infty$,

$$\frac{1}{\mathrm{Re}\left[\tau_{k,k'}\right]} \rightarrow \left\{ \begin{array}{cl} \mathrm{Re}\left[\tau_{k,k'}\right]^{-1} & \forall\ \gamma(k_x \neq 0) > 0 \\ 0 & \forall\ \gamma(k_x \neq 0) \leq 0 \end{array} \right. , \tau_{k,k'} = -i\left((\omega_{\text{unstable}}^{\text{sideband}})^* - (\omega_{\text{unstable}}^{\text{streamer}})^*\right)^{-1} , \quad . \tag{5.12}$$

The prescription of setting $\tau_{k,k'} = \infty$ for interactions involving stable sidebands originates from the fact that the eddy turnover rate $\Delta\omega_{\mathrm{nl}}$ is very small at low $\omega_{T\mathrm{i}}$, the eigenmodes coupled through the zonal flow can oscillate coherently with strong resonance and therefore transfer the energy efficiently to the stable region. At higher $\Delta\omega_{T\mathrm{i}}$, the sidebands become unstable, the eddy turnover rate $\Delta\omega_{\mathrm{nl}}$ builds up, and thus the eigenmodes are no longer exactly resonant and $\tau_{k,k'}$ becomes finite. As will be shown next, the approach given in Eq. (5.12) enables one to capture the heat flux for varius zonal-flow-dominated systems with the improved quasilinear model in Eq. (5.11).

First, consider CBC parameters with kinetic electrons at hydrogen mass ratio. Figure 5.18 shows the ion electrostatic heat fluxes calculated from the improved quasilinear model and nonlinear simulations versus temperature gradient ω_T, with identical ion and electron temperature profiles. Quasilinear fluxes match nonlinear ones well above $\omega_T = 5.5$. Furthermore, the improved prediction with $k_x' = 0.1$ tracks the nonlinear heat flux below the NLCG at $\omega_T = 5.5$, whereas the standard

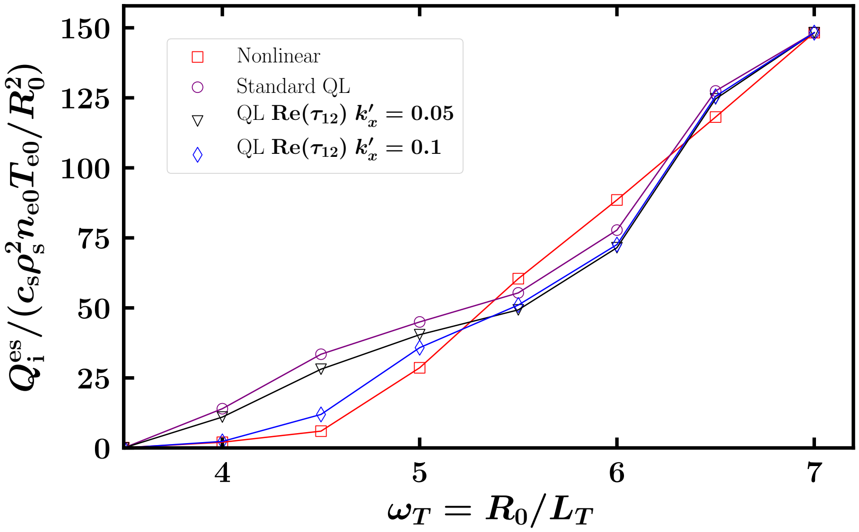

Figure 5.18: Quasilinear and nonlinear (red square) fluxes versus temperature gradient in kinetic-electron Cyclone Base Case. The standard quasilinear model (purple circle) overpredicts fluxes below $\omega_T \approx 5$, while the improved model using $\tau_{k,k'}(k'_x = 0.1)$ (blue diamond) recoversthe nonlinear heat flux in the Dimits regime.

quasilinear model fails to capture fluxes in the Dimits regime; the improved model with $k'_x = 0.05$ performs slightly better within the Dimits regime but still overpredicts fluxes there.

Note that this latter model is shown only for reference and is not expected to be predictive, as per the arguments laid out above. There is a range of zonal-flow wavenumbers that is decisive in whether coherency is avoided, which is determined by the energy transfer rate. If the width of growth-rate spectrum exceeds the dominating zonal flow wavenumber, the zonal-flow-catalyzed energy transfer can no longer deliver the energy effectively to the stable range, therefore the resonance will be gradually broken as $\omega_{T\mathrm{i}}$ is increased, which leads to larger heat fluxes.

Second, a scenario of ω_n-driven trapped-electron-mode (TEM) turbulence is considered in Fig. 5.19, of the Madison Symmetric Torus reversed-field pinch [26], which exhibits very strong zonal flows. The simulations are collisionless unless stated

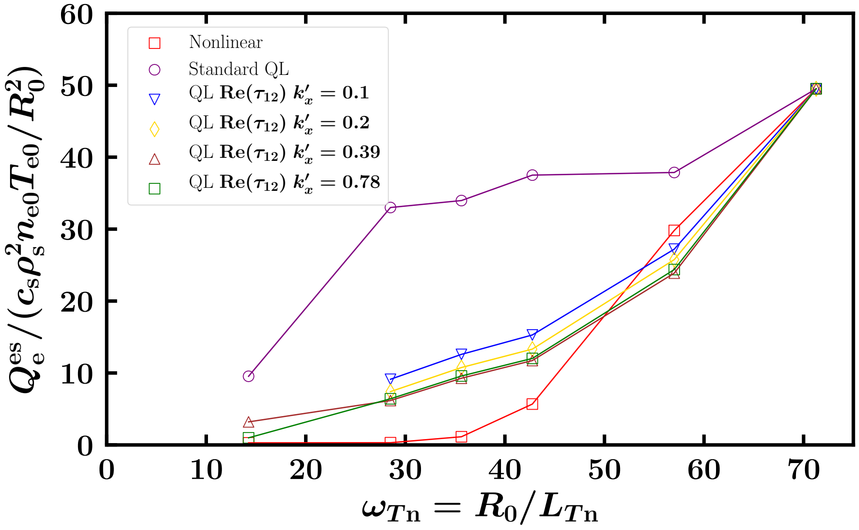

Figure 5.19: Quasilinear and nonlinear (red square) fluxes versus density gradient for a collisionless TEM case. The standard quasilinear model (purple circle) overpredicts fluxes greatly, while the τ factor improves the model significantly. The choice of k_x' is less relevant.

otherwise, with $\omega_T = 28.8$, $\beta = 0.0141$, $q_0 = 0.103$, $\hat{s} = 6.18$, and $\epsilon_t = 0.274$. The unstable range in the growth rate spectrum does not significantly change as ω_n is varied, the sidebands remain unstable even when ω_n drops below the nonlinear critical gradient. As is evident from the data shown, the improved model largely recovers nonlinear fluxes both in and above the Dimits regime, unlike the standard quasilinear model, which severely overpredicts fluxes below the NLCG. Furthermore, the notion that the precise choice of the zonal-flow wavenumber in the triplet correlation time is less relevant, the triplet correlation time solely captures the decoherence of the eigenmodes coupled through the zonal flow at higher density gradient produces little impact on the results.

A modified version of this parameter case, identical save for the experimental substantial collisionality, is shown in Fig. 5.19. The collision frequency in units of c_s/R_0 for this scenario is $\nu_c = 0.01262$. While the addition of the triplet correlation

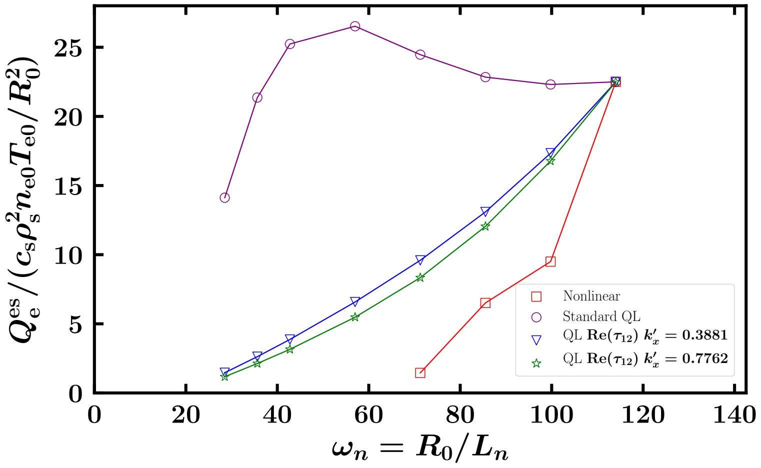

Figure 5.20: Quasilinear and nonlinear fluxes (red square) versus density gradient for a collisional TEM case. The standard quasilinear model (purple circle) hugely overpredicts fluxes, while the τ factor does improve the model significantly but the discrepancy remains.

time produces much-improved predictions relative to the nonlinear data, it cannot recover the Dimits shift. This result, however, is not surprising, since the introduction of a large collisionality breaks the symmetry of the stable and unstable modes, leading to the approximation of a symmetric unstable and mirror modes to fail. Additionally, the assumption of $\omega^{\mathrm{ZF}} = 0$ is no longer valid, as collisions now exert significant damping on the zonal flow. It can be concluded that cases with large collisionality $\nu_{\mathrm{ei}} \gtrsim \omega_{\mathrm{linear}}$ require a more involved treatment than is considered here.

Third, an analysis of ITG turbulence in JET [2] is shown in Fig. 5.21. The simulation uses $\omega_{n_{\mathrm{D}}} = 0.906$, $\beta = 10^{-5}$, $q_0 = 1.1392$, $\hat{s} = 0.1592$, $\epsilon_{\mathrm{t}} = 0.11592$, $\omega_{T\mathrm{i}} = \omega_{T\mathrm{e}}$, and a low collisionality $\nu_c = 0.7978 \times 10^{-4}$. The standard quasilinear model tracks the nonlinear heat flux to some degree, although it overpredicts fluxes by a factor of two at lower gradients; by comparison, the improved model tracks the nonlinear flux more closely. Even more importantly, these results demonstrate that in a case where the Dimits regime is largely nonexistent, the new model performs

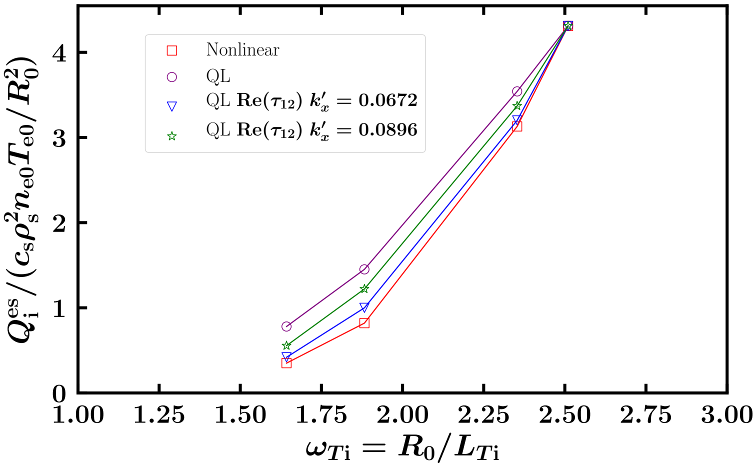

Figure 5.21: Quasilinear and nonlinear fluxes versus temperature gradient for a low collisionality ITG case for JET. The standard quasilinear model (purple circle) performs decently well, while the τ factor improves the model a bit more.

at least as well as the standard model.

As a fourth example, ITG turbulence is studied in the NCSX stellerator device, see Fig. 5.22. The simulation uses $\omega_{n_D} = 1$, $\beta = 5 \times 10^{-4}$, $q_0 = 1.789$, and $\hat{s} = -0.549$, with zero collisionality. This scenario turns out to be useful in illustrating the potential impact of the nonlinear coupling coefficients. The standard quasilinear model tracks the nonlinear heat flux closely, while the model with Re(τ) produces less accurate predictions. However, replacing Re(τ) with $|\tau|$, which was first proposed in the model for electromagnetic stabilization [16], performs very well in tracking the nonlinear heat flux. The assumption on which the use of Re(τ) is based is that the coupling coefficients $C_{k,k'}$ are almost real and do not vary rapidly. This assumption can be violated for systems with eigenmodes that vary strongly with control parameters, that the model with Re(τ) will be less predictive for such cases. On the other hand, the model that includes $|\tau|$ captures only the magnitude and discards the complex phase information. The model with $|\tau|$ outperforms its

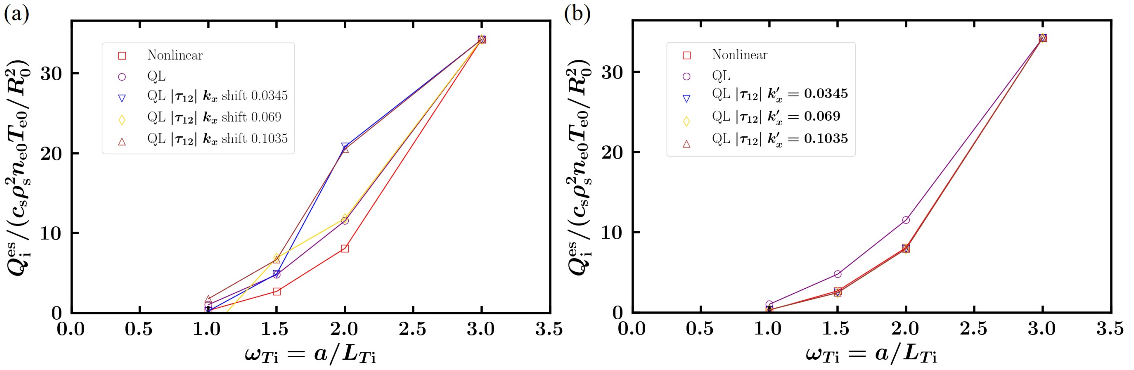

Figure 5.22: The quasilinear model with (a) Re(τ) and (b) $|\tau|$. The standard quasilinear model performs well in NCSX ITG case. The model with Re(τ) performs poorly. However, the model with $|\tau|$ tracks the nonlinear heat flux almost exactly.

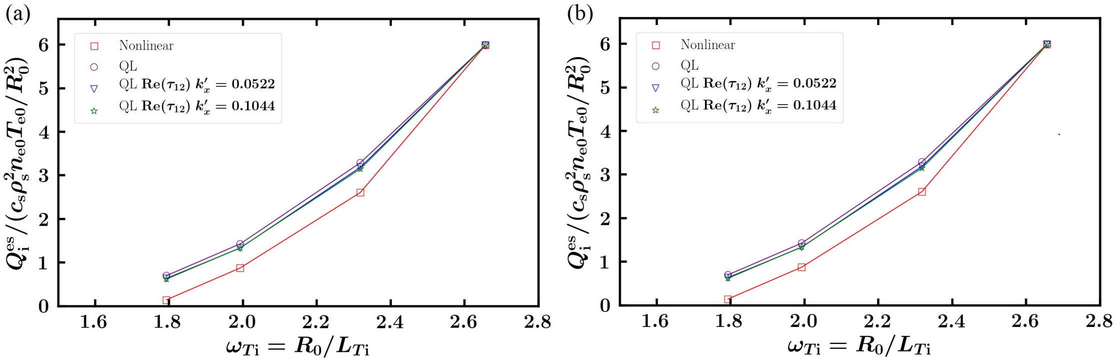

Figure 5.23: The quasilinear model with (a) Re(τ) and (b) $|\tau|$. The standard quasilinear model performs well in CMOD ITG case. Both models with Re(τ) or $|\tau|$ shows some but insignificant improvement.

competitor when the complex phase of the multiplication of τ and $C_{k,k'}$ does not vary a lot with control parameters. An investigation into the gyrokinetic coupling coefficients, their magnitudes and complex phases, is presently underway and will be reported in a separate publication, where it will be leveraged to further improve the quasilinear approach.

The fifth scenario analyzed here concerns ITG iturbulence in Alcator C-MOD, see Fig. 5.23. The simulation uses $\omega_{n_D} = 0.261$, $\beta = 1 \times 10^{-4}$, $q_0 = 1.17$, and $\hat{s} = 1.13$, with $\nu_c = 2 \times 10^{-3}$. The predicted heat fluxes from the standard quasilinear model

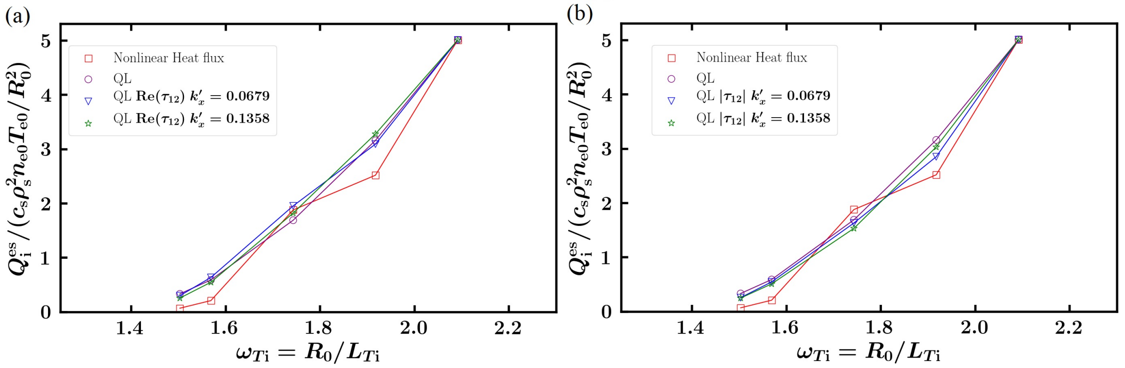

Figure 5.24: The quasilinear model with (a) $\mathrm{Re}(\tau)$ and (b) $|\tau|$. The standard quasilinear model performs well in SPARC ITG case. All models tracks the nonlinear result closely.

are close to the nonlinear values, and the same applies to the models with $\mathrm{Re}(\tau)$ and $|\tau|$. This again showcases that the improved model is able to predict fluxes as well as the standard quasilinear model even when the latter successfully recovers nonlinear scalings.

The final case, an ITG turbulence scenario for SPARC is shown in Fig. 5.24. Here, $\omega_{n\mathrm{D}} = 0.444$, $\omega_{n\mathrm{T}} = 0.457$, $\beta = 6.98 \times 10^{-3}$, $q_0 = 1.297$, $\hat{s} = 1.563$, and $\nu_c = 1.02 \times 10^{-4}$. The standard quasilinear model follows the nonlinear heat flux fairly well. Again, the models including the τ factor show little difference relative to the standard model.

5.7 Summary

The physical underpinnings of how the nonlinear critical gradient in zonal-flow-mediated plasma microturbulence – be it in an ITG or a ∇n-driven TEM regime – is increased beyond its linear counterpart, and how to predict this upshift using reduced models, have remained open questions for a long time. Prior attempts at explaining and predicting transport around this so-called Dimits regime have generally lacked applicability beyond narrow parameter points. The present work has demonstrated that one can leverage the ability of zonal flows to catalyze nonlinear energy transfer to large-scale stable eigenmodes; this transfer becomes resonant at the nonlinear critical gradient, and remains so throughout the Dimits regime, causing near-zero transport, as energy injected by the instability is immediately and resonantly removed from the system before it can contribute significantly to the turbulent bath of nonlinearly coupled modes.

Specifically, it is shown here that the energy transfer rate is governed by the magnitude of the zonal flow, the lifetime of the interaction, and the coupling strength between the three interacting eigenmodes in a given wavenumber triplet. However, the zonal-flow amplitude drops out of the overall balance, leaving the other two components, captured respectively by the triplet correlation time and the coupling coefficient. With the exception of one stellarator ITG turbulence scenario, where the complex phase of the coupling coefficient affects the result, the triplet correlation time τ is shown to be both the primary cause for and the primary ingredient in the prediction of the Dimits shift. In the cases studied – which range from the well-explored Cyclone Base Case to a reversed-field-pinch case to a JET discharge to a scenario for the upcoming SPARC device, a quasilinear model [see Eq. (5.11)] that includes the triplet correlation time as a correction factor is able to capture heat fluxes in the Dimits regime, whereas the standard quasilinear transport model fails to do so. In cases where the nonlinear system does not produce a significant Dimits shift, the corrected model accurately reflects its absence.

As next steps, a deeper analysis of the zonal-flow wavenumbers responsible for saturation will be conducted. Based on the present work, a value of $k_x\rho_\mathrm{s} \approx 0.1$ appears to be fairly general, but energy transfer analysis for the nonlinear simulations studied here may reveal a more widely applicable rule. Furthermore, the behavior of gyrokinetic coupling coefficients is presently the subject of investigation, and a broader understanding of its scaling properties will help improve the new quasilinear model further.

Acknowledgements

We would like to thank N. Howard for providing the SPARC parameter. Work is supported by U.S. Dept. of Energy.

Bibliography

[1] B. N. Rogers, W. Dorland, and M. Kotschenreuther, Phys. Rev. Lett. **85**, 5336 (2000).

[2] K. Miki, Y. Kishimoto, N. Miyato, and J. Q. Li, Phys. Rev. Lett. **99**, 145003 (2007).

[3] S.-I. Itoh and K. Itoh, Nuclear Fusion **56**, 106028 (2016).

[4] S. Kobayashi and B. N. Rogers, Physics of Plasmas **19**, 012315 (2012).

[5] R. Numata, R. Ball, and R. L. Dewar, Physics of Plasmas **14**, 102312 (2007).

[6] H. Zhu, Y. Zhou, and I. Y. Dodin, Phys. Rev. Lett. **124**, 055002 (2020).

[7] C. Holland, P. Diamond, S. Champeaux, E. Kim, O. Gurcan, M. Rosenbluth, G. Tynan,N. Crocker, W. Nevins, and J. Candy, Nuclear Fusion **43**, 761 (2003).

[8] T. Miura, T.-H. Watanabe, S. Maeyama, and M. Nakata, Physics of Plasmas **26**, 082304(2019).

[9] P. W. Terry, P.-Y. Li, M. J. Pueschel, and G. G. Whelan, Phys. Rev. Lett. **126**, 025004(2021).

[10] P.-Y. Li, P. W. Terry, M. J. Pueschel, and G. G. Whelan, (to be published)

[11] P. W. Terry, B. J. Faber, C. C. Hegna, V. V. Mirnov, M. J. Pueschel, and G. G. Whelan, Physics of Plasmas **25**, 012308 (2018). 33

[12] M. J. Pueschel and F. Jenko, Physics of Plasmas **17**, 062307 (2010).

[13] M. J. Pueschel, B. Faber, J. Citrin, C. Hegna, P. W. Terry, and D. Hatch, Phys. Rev. Lett. **116**, 085001 (2016).

[14] M. J. Pueschel, P.-Y. Li, and P. W. Terry, Nuclear Fusion **61**, 054003 (2021).

[15] D. Hatch, F. Jenko, A. B. Navarro, V. Bratanov, P. W. Terry, and M. Pueschel, New Journal of Physics **18**, 075018 (2016).

[16] G. G. Whelan, M. J. Pueschel, and P. W. Terry, Phys. Rev. Lett. **120**, 175002 (2018).

[17] F. Rath, A. G. Peeters, R. Buchholz, S. R. Grosshauser, F. Seiferling, and A. Weikl, Physics of Plasmas **25**, 052102 (2018).

[18] D. A. St-Onge, Journal of Plasma Physics 83, 905830504 (2017).

[19] D. R. Hatch, M. J. Pueschel, F. Jenko, W. M. Nevins, P. W. Terry, and H. Doerk, Phys. Rev. Lett. **108**, 235002 (2012).

[20] K. D. Makwana, P. W. Terry, M. J. Pueschel, and D. R. Hatch, Phys. Rev. Lett. **112**, 095002(2014).

[21] K. D. Makwana, P. W. Terry, and J.-H. Kim, Physics of Plasmas **19**, 062310 (2012).

[22] W. Horton, D. Choi, and W. M. Tang, The Physics of Fluids **24**, 1077 (1981).

[23] C. Holland, P. Diamond, S. Champeaux, E. Kim, O. Gurcan, M. Rosenbluth, G. Tynan,N. Crocker, W. Nevins, and J. Candy, Nuclear fusion **43**, 761 (2003).

[24] D. R. Hatch, P. W. Terry, F. Jenko, F. Merz, M. Pueschel, W. Nevins, and E. Wang, Physics of Plasmas **18**, 055706 (2011).

[25] Whelan, Garth G. (2019) Ph.D. Thesis, *Details of Ion-Temperature-Gradient-Driven instability saturation*

[26] Williams, Zachary R.. (2019) Ph.D. Thesis, *On the interactions of magnetic fluctuations, zonal flows, and microturbulence in fusion plasmas*

[27] A.M. Dimits, G. Bateman, M.A. Beer, B.I. Cohen, W. Dorland, G.W. Hammett, C. Kim, J.E. Kinsey, M. Kotschenreuther,

[28] A. E. Fraser1, M. J. Pueschel, P. W. Terry, and E. G. Zweibel, Physics of Plasmas **25**, 122303 (2018)

Chapter 6

The Coupling Coefficients

In previous chapters, it was shown that the triplet correlation time τ is important to saturation of the turbulence. However, the nonlinear coupling coefficients and tau in eigenmode amplitude evolution equations, under the right conditions, may equally exert influence on turbulence saturation and heat flux prediction. According to the saturation theory described in chapter 2, the heat flux $Q \sim \frac{1}{C_{Fmn}\tau C_{lFn}}$, where C_{Fmn} is the coupling coefficient for the zonal mode at k and two other eigenmodes at k' and k'', while C_{lFn} is the coupling coefficient for an eigenmode at k, the zonal mode at k', and another eigenmode at k''. Therefore, how the coupling coefficient varies with respect to the temperature gradient influences the overall result. While the coupling coefficients can be straightforwardly calculated analytically in fluid models, doing so becomes much more involved in the gyrokinetic framework, making it less appealing for use in simplified models. In this chapter, the coupling coefficients in gyrokinetics will be defined, and means of how they can be derived through numerical calculations will be discussed.

6.1 Coupling Coefficients in Analytic Form

For any set of differential equations $\mathcal{F}[f(\mathbf{x})]$, it is possible to express the operators in terms of linear operators $\mathcal{L}[f(\mathbf{x})]$ and nonlinear operators $\mathcal{N}[f(\mathbf{x})]$, that is,

$$\mathcal{F}[f(\mathbf{x})] = \mathcal{L}[f(\mathbf{x})] + \mathcal{N}[f(\mathbf{x})] \ , \tag{6.1}$$

where $\mathbf{x}$ is a vector and $f(\mathbf{x})$ is a scalar function. If there exists a set of functions $f_i(\mathbf{x})$, $i = 1,\ 2,\ 3, ...$ for $\mathcal{L}$ such that $\mathcal{L}\ [f_i(\mathbf{x})] = \lambda_i f_i(\mathbf{x})$, then $f_i(\mathbf{x})$ is the eigenfunction of the linear operator $\mathcal{L}$, commonly normalized to unity, and λ_i is the linear eigenvalue of the corresponding $f_i(\mathbf{x})$. The benefit of using the linear eigenfunction is that one can express any function $f(\mathbf{x})$ in the defined space in terms of the eigenfunctions $f_i(\mathbf{x})$ if the eigenfunction basis is complete, that is,

$$f(\mathbf{x}) = \sum_i \beta_i f_i(\mathbf{x}) \ , \tag{6.2}$$

where β_i are the eigenmode amplitudes. Also, if the linear operator $\mathcal{L}$ operates on the function $f(\mathbf{x})$, one simply obtains

$$\mathcal{L}[f(\mathbf{x})] = \sum_i \beta_i \lambda_i f_i(\mathbf{x}) \ . \tag{6.3}$$

This feature is particularly useful for time-evolving systems. For example, if $\frac{\partial f}{\partial t} = \mathcal{L}[f(\mathbf{x})]$, then

$$\frac{\partial f}{\partial t} = \mathcal{L}[f(\mathbf{x})] = \sum_i \beta_i \lambda_i f_i(\mathbf{x}) \ . \tag{6.4}$$

Because $f(\mathbf{x}) = \sum_i \beta_i f_i(\mathbf{x})$, and thus $\sum_i f_i \frac{\partial \beta_i}{\partial t} = \sum_i \beta_i \lambda_i f_i(\mathbf{x})\ \forall t$, it follows that

$$\beta_i(t) = C_i e^{\lambda_i t} \ . \tag{6.5}$$

where $\beta_i(t = 0) = C_i$. So,

$$f(\mathbf{x}) = \sum_i \beta_i(t) f_i(\mathbf{x}) = \sum_i f_i C_i e^{\lambda_i t} \ . \tag{6.6}$$

Now the time evolution of any function can be expressed simply as a linear combinations of the eigenfunctions multiplied by the time-evolving eigenmode amplitudes.

Typically, it is impossible to find the eigenfunctions of $\mathcal{F}[f(\mathbf{x})]$ if it includes a nonlinear operator $\mathcal{N}$. In plasma physics, a key quantity of interest is the distribution function in k space, that is, $f_k(\mathbf{v})$ at some wavenumber k, where $\mathbf{v}$ is the velocity vector. For time-evolving problems where $\frac{\partial f_k}{\partial t} = \mathcal{F}[f_k(\mathbf{v})]$, it is common to split f_k into the linear eigenfunctions $f_{k,i}$ and eigenmode amplitudes $\beta_{k,i}(t)$ and track how the eigenmode amplitudes evolve in time to recover $f_k(\mathbf{v}, \mathbf{t})$. In order to do that, one can define the projection operator $\mathcal{P}_i[f_k(\mathbf{v})] = \beta_{k,i}(\mathbf{v})$. The evolution equation for the i-th eigenmode amplitude $\beta_{k,i}$ can then be written as

$$\begin{aligned}\mathcal{P}_i\left[\frac{\partial f_k}{\partial t} - \mathcal{F}[f_k(\mathbf{v})]\right] &= \frac{\partial \beta_{k,i}}{\partial t} - \mathcal{P}_i\left[\mathcal{L}[f_k(\mathbf{v})] + \mathcal{N}[f_k(\mathbf{v})]\right] \\ &= \frac{\partial \beta_{k,i}}{\partial t} - \lambda_{k,i}\beta_{k,i} - \mathcal{P}_i\left[\mathcal{N}[f_k(\mathbf{v})]\right] = 0 \ ,\end{aligned} \tag{6.7}$$

where $\mathcal{P}_i\left[\mathcal{N}[f_k(\mathbf{v})]\right]$ describes how nonlinear interactions act on the eigenmode $\beta_{k,i}$. In fluid dynamics and plasma physics, nonlinearities are often dominated by second-order terms such as the Reynolds stress and $\mathbf{E} \times \mathbf{B}$ advection in the form of energy-conserving triplet interactions between k, k', and $k - k'$. This implies that the nonlinearity $\mathcal{N}[f_k(\mathbf{v})]$ can be written as $\sum_{k'} N_{k,k'} f_{k'} f_{k-k'}$, where $N_{k,k'}$ is a prefactor depending only on k and k'. One can further eigenmode-decompose $f_{k'}$ and $f_{k-k'}$, such that $\mathcal{N}[f_k(\mathbf{v})]$ can be wirtten as $\sum_{k',j,l} N_{k,k'} \beta_{k',j} f_{k',j} \beta_{k-k',l} f_{k-k',l}$, which corresponds to the sum of all eigenmode interactions that couple to the i-th eigenmode at k. Thus, one can define the coupling coefficients as the magnitude of the nonlinear interaction on $\beta_{k,i}$ from eigenmodes at k' and $k - k'$ per unit $\beta_{k',j}$ and $\beta_{k-k',l}$, that is,

$$C_{ijl}^{k,k'} = \mathcal{P}_i\left[N_{k,k'} f_{k',j} f_{k-k',l}\right] \ . \tag{6.8}$$

With this approach, Eq. (6.7) can be rewritten as

$$\frac{\partial \beta_{k,i}}{\partial t} = \lambda_{k,i}\beta_{k,i} + \sum_{k',j,l} C_{ijl}^{k,k'} \beta_{k',j}\beta_{k-k',l} \ . \tag{6.9}$$

In the context of the saturation theory presented in chapter 2, the coupling coefficients can be used to predict heat flux of the nonlinear systems. However, it can be challenging to evaluate the projection operator $\mathcal{P}_i$, making computing the coupling coefficient numerically expensive, as will be shown next.

6.2 Coupling Coefficient Numerical Calculation

Eigenvalue and eigenfunction calculations are often performed numerically with matrix solvers. The linear operator $\mathcal{L}$ will be written as a discretized matrix L, while the function f is written as a vector V. Expressing the evolution equation of f_k with a second-order nonlinearity in terms of the matrix elements, and using the Einstein summation convention,

$$\frac{\partial V_a}{\partial t} = L_a^l(k)V_l + N_a^{mn}(k', k'')V_m'V_n'' \ , \tag{6.10}$$

where L_a^l is the linear matrix operator, $N_a^{mn}(k', k'')$ is the nonlinear tensor operator, $V_m' = V_m(k')$ and $V_n'' = V_n(k - k')$. Let the i-th eigenvector be X^i, then the vector V_a can be expressed as $X_a^b\beta_b$, where $X = (X^1, X^2, ...)$, and β_b are the bth eigenmode amplitudes. Eq. (6.10) can be written as

$$\left(\delta_a^l \frac{\partial}{\partial t} - L_a^l\right) X_l^h \beta_h = N_a^{mn} {X'}^i_m \beta_i' {X''}^j_n \beta_j'' \ . \tag{6.11}$$

where δ_a^l is the Kronecker delta. Since X_l^h is the set of eigenvectors of L_a^l, $L_a^l X_l^h = X_a^l \Lambda_l^h$, where Λ_l^h is the diagonal eigenvalue matrix. After some matrix rearrangement, Eq. (6.11) can be written as

$$\left(\frac{\partial}{\partial t} - \Lambda_l^h\right) \beta_h = {X^{-1}}^a_h N_a^{mn} {X'}^i_m \beta_i' {X''}^j_n \beta_j'' \ . \tag{6.12}$$

The coupling coefficient defined in the previous section can therefore be expressed as

$$C^{k,k'}_{hmn} = X^{-1}{}^{a}_{h} N^{mn}_{a} X'^{i}_{m} X''^{j}_{n} \ . \tag{6.13}$$

While this formula takes an intuitive form, the inverse matrix $X^{-1}{}^{a}_{h}$ is not straight forward to calculate. Although X'^{i}_{m} and X''^{j}_{n} can be computed iteratively at a cost scaling as $\mathcal{O}(m^2)$, where m is the rank of the matrix, the calculation for the eigenvector matrix X itself requires $\mathcal{O}(m^3)$ of computation steps, the calculation of X^{-1} leads to a prohibitive amount of required computational time. Running nonlinear simulations is generally less expensive than a full-matrix eigenvalue run. An alternate way of calculating the coupling coefficients is to take advantage of the left eigenvectors. [1] The definitions of the right eigenvectors X_r and left eigenvectors X_l are $LX_r = \lambda_r X_r$ and $L^T X_l = \lambda_l X_l$, respectively. Therefore, $X_r^T L^T X_l = \lambda_r X_r^T X_l = \lambda_l X_r^T X_l$, that is

$$X_r^T X_l = 0 \quad \text{if } \lambda_r \neq \lambda_l \ . \tag{6.14}$$

This is known as the orthogonality of the right and left eigenvectors. The left eigenvector can therefore be used as the projection operator $\mathcal{P}_i$ in Eq. (6.8), and Eq. (6.13) can thus be expressed as

$$C^{k,k'}_{hmn} = (X_l^T)^{a}_{h} N^{mn}_{a} X'^{i}_{m} X''^{j}_{n} \ . \tag{6.15}$$

where $(X_l^T)^a_h$ is the h-th left eigenvector of the corresponding right eigenvector X^h_a. Unlike in Eq. (6.13), the coupling coefficient in Eq. (6.15) is less expensive to calculate because the left eigenvector can be calculated in the same way as the right eigenvectors, which costs much less than the approach in Eq. (6.13).

In the gyrokinetic turbulence code GENE, the iterative solvers are matrix-free, i.e., they use the gyrokinetic equations to calculate the distribution functions directly without storing the matrix. By turning the implicit calculator into an explicit one, one may use this infrastructure to calculate the left eigenvectors. The linear matrix operator $\mathcal{L}$ can be extracted by utilizing a test vector is chosen with only one non-zero entry to calculat each column separately. For example, by using the unit vector with only the j-th row being non-zero as the input vector, one obtains the j-th column of the matrix $\mathcal{L}$, and can ultimately construct the m by m linear matrix operator $\mathcal{L}$. The left eigenvectors then can be calculated with the built in solver and the transpose of the explicit matrix L^T.

Table 6.1 shows the absolute value of the coupling coefficients for different pairs of eigenmodes for the adiabatic-electron Cyclone Base Case between the most unstable mode for streamers at $k = (0, 0.3)$, the zonal flow at $k' = (0.083, 0)$, and the sideband at $k'' = (-0.083, 0.3)$, with dimensionality 114688. The most unstable mode at $k'' = (-0.083, 0.3)$ has larger coupling coefficients than the damped modes, which indicates that the most unstable mode for the sideband can be coupled to nonlinearly more efficiently than the damped modes. If one sets aside for a moment the possibility of coupling through mirror modes, which will be discussed below, this implies that eigenmode sea at the sideband can approximated by the single most unstable mode at $k'' = (-0.083, 0.3)$. There are three zonal eigenmodes that show large coupling coefficients with the most unstable mode of the sideband. However, focusing on the damping rate of these modes, the least damped is much closer to the zero-frequency approximation than the others, meaning resonant excitation is much more likely; this mode can therefore be identified as the key player for zonal-flow-catalyzed interactions.

From the above analysis, the dominant triplet interaction between the most unstable mode at $k = (0, 0.3)$, the zonal eigenmode at $k = (0.0834, 0)$, and the

γ_{side} γ_z	2.11×10^{-1}	-9.78×10^{-3}	-1.07×10^{-2}	-2.32×10^{-2}
-4.62×10^{-5}	4.45×10^{-2}	8.73×10^{-3}	5.63×10^{-3}	2.99×10^{-4}
-4.80×10^{-2}	8.76×10^{-2}	1.64×10^{-2}	9.59×10^{-3}	4.44×10^{-4}
-4.81×10^{-2}	8.96×10^{-2}	1.81×10^{-2}	1.23×10^{-2}	4.92×10^{-4}
-1.46×10^{-1}	1.99×10^{-5}	8.52×10^{-6}	1.40×10^{-5}	5.58×10^{-6}
-1.75×10^{-1}	1.39×10^{-5}	2.42×10^{-6}	3.74×10^{-6}	2.28×10^{-6}

Table 6.1: The absolute value of the coupling coefficients $|C|$ for different pairs of eigenmodes for the adiabatic-electron Cyclone Base Case between the most unstable mode at $k = (0, 0.3)$, the zonal mode at $k' = (0.083, 0)$, and the sideband at $k'' = (-0.083, 0.3)$, where γ_z and γ_{side} are the growth rates for the zonal modes and sidebands. Several coupling coefficients are orders of magnitudes larger than the others, allowing for a reduction of the problem dimension.

eigenmode at $k = (-0.0834, 0)$ will be that which involves the near-zero-frequency zonal mode and the most unstable mode for the sideband. However, it is essential to now consider the mirror mode for the sideband, which in theory can be more important than the most unstable mode. The mirror mode is generally not an eigenmode, but one can still derive its pseudo-eigenvector. One approach is to calculate the averaged eigenvalues and eigenvectors around the mirror mode. However, it can not be done numerically easily. The number of damped modes at each wavenumber is approximately the order of the resolution, there can be a lot of damped modes around the mirror mode which can prevent the eigenvalue solver from converging. An alternative approach is to derive an analytic formula of pseudo-eigenvector for the mirror mode to calculate the coupling coefficients, which will be left for future research.

Bibliography

[1] Burns, Keaton J. (2018) Ph.D. Thesis, *Flexible algorithms for simulating astrophysical and geophysical flows*

[2] Fraser, Adrian E. (2020) Ph.D. Thesis, *Role of stable eigenmodes in shear-flow instability saturation and turbulence*

Chapter 7

Conclusions and Future Work

7.1 Conclusions

In this thesis, the predictive capabilities and the limits of the ITG saturation theory proposed in Ref. [30] have been investigated in a fluid model, a predator-prey model, a modified fluid model with a linear gradient threshold, in gyrokinetic simulations, and in a quasilinear model. A predator-prey model is built from a more complicated fluid model by utilizing the saturation theory, which preserves the energy cascade and symmetry breaking between the stable and unstable modes. By utilizing this fundamental theoretical basis for model building, this aids in avoiding the need for heuristic assumptions and an excessive number of free parameters. The concept of the resonance between the stable and unstable modes derived from the saturation theory is used to explain the strong turbulence suppression in the Dimits regime, in agreement with gyrokinetic simulations. It is shown, by performing a resonance-breaking numerical experiment, that adding an artificial frequency to the zonal flow eliminates the Dimits regime in gyrokinetic simulations, as predicted by the resonance picture but not by other, earlier cascade-based theories. Lastly, the triplet correlation time has been added to the quasilinear transport model, making the model capable of predicting the heat flux near criticality for systems with or without a Dimits regime. With the above results, one can conclude that the saturation theory studied in this thesis captures the pertinent physics of ITG turbulence saturation, and highlights the role of the nonlinear interaction lifetime, or triplet correlation time, showing that it directly affects the energy transfer rate and turbulence level.

7.2 Future Work

Having shown that the triplet correlation time is indeed important in ITG turbulence and transport, the other ingredient of the underlying theory will be investigated, the nonlinear coupling coefficient, is also crucial to the energy transfer rate, which may also affect the turbulence saturation level. While a nonlinear coupling coefficient between quantities in k space depends only on wavevectors, assessing coupling between eigenmodes requires knowledge of the latter, and ideally obtaining the left eigenvectors of the system. Future work will improve the eigenvalue solvers in the Gene code and compute coupling coefficients for scenarios with kinetic electrons. One important application for the coupling coefficients is to go beyond quasilinear modeling to predict the heat flux for turbulence. The formula $Q \sim \omega_T \chi \sim \omega_T \frac{\gamma}{k_\perp^2}$ on which the quasilinear model is based originates from the mixing length theory, dimensional analysis, and Fick's law, which are heuristic and can break down under various conditions, for example, near the plasma edge, where large profile gradients are present. Instead, it is possible to use the saturation theory to predict the heat flux, because the theory is not subject to the same restrictions as the standard quasilinear model.

Calculating the heat flux, requires the eigenmode amplitudes β_l and the eigenvectors X_i^l of the dominant eigenmodes. The former can be predicted with the coupling coefficients and triplet correlation times, while the latter can be calculated by eigenvalue solvers. With the above ingredients, one can estimate the turbulent distribution function $g_i = \beta_l X_i^l$, and therefore the heat flux

$$Q_j = \frac{n_{0j} T_{0j}}{\int_{-\pi}^{\pi} J dz} \int_{-\pi}^{\pi} dz \sum_k J i k_y (\bar{\phi}_j - v_{Tj} v_\parallel \bar{A}_{1\parallel j}) \left(\pi B_0 \int dv_\parallel d\mu v^2 f_j(k) \right)^* . \qquad (7.1)$$

The primary question that still needs to be resolved is how left eigenvectors can be computed with a sufficiently high efficiency to make this approach competitive with other reduced models in transport solving.

Bibliography

[1] W. Horton, Rev. Mod. Phys. **71**, 735 (1999).

[2] J.D. Callen, Phys. Fluids B **2**, 2896 (1990).

[3] P. Helander, J.H.E. Proll, and G.G. Plunk, Phys. Plasmas **20**, 122505 (2013).

[4] N.T. Howard, C. Holland, A.E. White, M. Greenwald, and J. Candy, Nuclear Fusion **56**, 014004 (2016).

[5] D.R. Hatch, P.W. Terry, F. Jenko, F. Merz, M.J. Pueschel, W.M. Nevins, and E. Wang, Phys. Plasmas **18**, 055706 (2011).

[6] P.W. Terry, M. Greenwald, J.-N. Leboeuf, G.R. McKee, D.R. Mikkelsen, W.M. Nevins, D.E. Newman, and D.P. Stotler, Phys. Plasmas **15**, 062503 (2008).

[7] M. Greenwald, Phys. Plasmas **17**, 058101 (2010).

[8] R.E. Waltz, G.D. Kerbel, and J. Milovich, Phys. Plasmas **1**, 2229 (1994).

[9] C. Bourdelle, X. Garbet, F. Imbeaux, A. Casati, N. Dubuit, R. Guirlet, and T. Parisot., Phys. Plasmas **14**, 112501 (2007).

[10] B. Coppi, M.N. Rosenbluth, and R.Z. Sagdeev, Phys. Fluids **10**, 582 (1967).

[11] A.M. Dimits, G. Bateman, M.A. Beer, B.I. Cohen, W. Dorland, G.W. Hammett, C. Kim, J.E. Kinsey, M. Kotschenreuther, A.H. Kritz, et al., Phys. Plasmas **7**, 969 (2000).

[12] P. Helander, T. Bird, F. Jenko, R. Kleiber, G.G. Plunk, J.H.E. Proll, J. Riemann, and P. Xanthopoulos, Nucl. Fusion **55**, 053030 (2015).

[13] D. Carmody, M.J. Pueschel, J.K. Anderson, and P.W. Terry, Phys. Plasmas **22**, 012504 (2015).

[14] W. Horton, D.-I. Choi, and W.M. Tang, Phys. Fluids **24**, 1077 (1981).

[15] C. Holland, P.H. Diamond, S. Champeaux, E. Kim, O. Gurcan, M.N. Rosenbluth, G.R. Tynan, N. Crocker, W.M. Nevins, and J. Candy, Nuclear Fusion **43**, 761 (2003).

[16] K.D. Makwana, P.W. Terry, and J.-H. Kim, Phys. Plasmas **19**, 062310 (2012).

[17] K.D. Makwana, P.W. Terry, M.J. Pueschel, and D.R. Hatch, Phys. Ref. Lett. **112**, 095002 (2014).

[18] P.W. Terry, D.A. Baver, and S. Gupta, Phys. Plasmas **13**, 022307 (2006).

[19] M.J. Pueschel and F. Jenko, Phys. Plasmas **17**, 062307 (2010).

[20] G.G. Whelan, M.J Pueschel, P.W. Terry, J. Citrin, I.J. McKinney, W. Guttenfelder, and H. Doerk, Phys. Plasmas **26**, 082302 (2019).

[21] P.W. Terry, P.-Y. Li, M.J. Pueschel, and G.G. Whelan, Phys. Rev. Lett. **126**, 025004 (2021).

[22] M.J. Pueschel, P.-Y. Li, and P.W. Terry, Nuclear Fusion **61**, 054003 (2021).

[23] M.A. Beer and G.W. Hammett, Phys. Plasmas **3**, 4046 (1998).

[24] F. Jenko, W. Dorland, M. Kotschenreuther, and B.N. Rogers, Phys. Plasmas **7**, 1904 (2000).

[25] R.D. Sydora, J. Comp. Appl. Math. **109**, 243 (1999).

[26] M.N. Rosenbluth and F.L. Hinton, Phys. Rev. Lett. **80**, 724 (1998).

[27] J. Chowdhury, W. Wan, Y. Chen, S.E. Parker, R.J. Groebner, C. Holland, and N.T. Howard, Phys. Plasmas **21**, 112503 (2014).

[28] P.-Y. Li, P.W. Terry, M.J. Pueschel, and G.G. Whelan, submitted to Phys. Plasmas.

[29] J.A. Krommes, Annu. Rev. Fluid Mech. **44**, 175 (2012).

[30] P.W. Terry, B.J. Faber, C.C. Hegna, V.V. Mirnov, M.J. Pueschel, and G.G. Whelan, Phys. Plasmas **25**, 012308 (2018).

[31] G.G. Whelan, M.J. Pueschel, and P.W. Terry, Phys. Rev. Lett. **120**, 175002 (2018).

[32] S.A. Orszag, J. Fluid Mech. **41**, 363 (1970).

[33] R.H. Kraichnan, J. Fluid Mech. **5**, 497 (1959).

[34] R.H. Kraichnan, J. Fluid Mech. **88**, 355 (1978).

[35] R.Z. Sagdeev and A.A. Galeev, *Nonlinear Plasma Theory*, (Benjamin, New York, 1969).

[36] D.A. Baver, P.W. Terry, R. Gatto, and E. Fernandez, Phys. Plasmas **9**, 3318 (2002).

[37] D.R. Hatch, M.J. Pueschel, F. Jenko, W.M. Nevins, P.W. Terry, and H. Doerk, Phys. Plasmas **20**, 0112307 (2013).

[38] Z. Lin, T.S. Hahm, W.W. Lee, W.M. Tang, and P.H. Diamond, Phys. Rev. Lett. **83**, 3645 (1999).

[39] P.W. Terry, K.D. Makwana, M.J. Pueschel, D.R. Hatch, F. Jenko, and F. Merz, Phys. Plasmas **21**, 122303 (2014).

[40] C.C. Hegna, P.W. Terry, and B.J. Faber, Phys. Plasmas **25**, 022511 (2018).